UNIVERSITY OF CALIFORNIA, SAN DIEGO

# INVESTIGATION INTO MECHANICAL PROPERTIES OF BONE AND ITS MAIN CONSTITUENTS

A Dissertation submitted in partial satisfaction of the requirements for the degree of

Doctor of Philosophy

in

Materials Science and Engineering

by

Ekaterina Evdokimenko

Committee in charge:

Professor Joanna McKittrick (Chair)
Professor Vlado A. Lubarda (Co-Chair)
Professor Juan C. Lasheras
Professor Marc A. Meyers
Professor Shyni Varghese

2012

The dissertation of Ekaterina Evdokimenko is approved, and it is acceptable in quality and form for publication on microfilm and electronically:

_____

_____

_____

_____

Co-Chair

_____

Chair

University of California, San Diego

2012

DEDICATION

To Alex and Eugenia

## TABLE OF CONTENTS

SIGNATURE PAGE ..... iii

DEDICATION ..... iv

TABLE OF CONTENTS ..... v

LIST OF FIGURES ..... x

LIST OF TABLES ..... xix

ACKNOWLEGEMENTS ..... xx

VITA ..... xxiii

FIELD OF STUDY ..... xxiii

LIST OF PUBLICATIONS ..... xxiv

LIST OF PRESENTATIONS ..... xxviii

ABSTRACT OF THE DISSERTATION ..... xxxii

Chapter 1 INTRODUCTION AND BACKGROUND ..... 1

1.1 Biological Materials: Hierarchical Structure, Properties, Biomimicry ..... 1

1.2 Recent Advances on the Measurement and Calculations of the Elastic Properties of Cortical and Trabecular Bone ..... 8

1.2.1 Bone as a composite biological material: Main constituents, hierarchical structure, mechanical properties, and experimental methods to measure elastic modulus ..... 8

1.2.2 The elastic properties of bone ..... 20

1.2.3 Experimental methods to measure elastic modulus ..... 29

1.3 Importance of Bone Research: Osteoporosis, Artificial Bone, Orthopedic Implants and Bone Substitutes ..... 44

1.4 References ..... 46

Chapter 2 COMPRESSIVE ANISOTROPY OF BONE AND ITS MAIN CONSTITUENTS ..... 55

2.1 Compressive Anisotropy of Bovine Cortical Bone and its Main Constituents ..... 55

2.1.1 Introduction and background ..... 55

2.1.2 Materials and methods ..... 60

2.1.3 Results and discussion ..... 64

2.1.4 Conclusions ..... 76

2.2 Investigations into Partially Demineralized Cortical Bone ..... 77

2.2.1 Introduction and background ..... 78

2.2.2 Materials and methods ..... 79

2.2.3 Results and discussion ..... 80

2.2.3 Conclusions ..... 83

2.3 Initial Anisotropy in Demineralized Bovine Cortical Bone in Compressive Cyclic Loading-Unloading ..... 84

2.3.1 Introduction and background ..... 85

2.3.2 Materials and methods ..... 86

2.3.3 Results and discussion ..... 86

2.3.4 Conclusions ..... 95

2.3.5 References ..... 96

Chapter 3 MODELING OF THE ELASTIC PROPERTIES OF BONE ..... 101

3.1 Hierarchical Structure of Porosity in Cortical and Trabecular Bone ..... 101

3.1.1 Introduction and background ..... 101

3.1.2 Materials and methods ..... 102

3.1.3 Results and discussion ..... 103

3.1.4 Conclusions ..... 109

3.2 Correlation of Multi-Scale Modeling and Experimental Results for the Elastic Moduli of Cortical and Trabecular Bone ..... 109

3.2.1 Introduction and background ..... 110

3.2.2 Materials and methods ..... 111

3.2.3 Modeling procedure ..... 114

3.2.3 Results and discussions ..... 124

3.2.4 Conclusions ..... 142

3.2.5 References ..... 144

Chapter 4 COMPARATIVE STUDY OF YOUNG AND MATURE BOVINE CORTICAL BONE ..... 148

4.1 Introduction and Background ..... 148

4.2 Materials and Methods ..... 150

4.2.1 Sample preparation ..... 150

4.2.2 Mineral content ..... 150

4.2.3 Deproteinization and demineralization processes ..... 151

4.2.4 Structural characterization ..... 151

4.2.5 Image processing ..... 152

4.2.6 Compression testing ..... 153

4.2.7 Micro-hardness testing ..... 153

4.3 Results and Discussion ..... 154

4.4 Conclusions ..... 164

4.5 References ..... 165

Chapter 5 MODELING OF THE OSTEOPOTIC DEGRADATION OF ELASTIC PROPERTIES OF TRABECULAR BONE ..... 168

5.1 Introduction and Background ..... 169

5.2 Materials and Methods ..... 173

5.2.1 Sample preparation ..... 173

5.2.2 Demineralization and deproteinization process ..... 174

5.2.3 Compression testing ..... 174

5. 3. Results and Discussions ..... 175

5.3.1 Volume fractions and density relationships ..... 175

5.3.2 Young's moduli of elasticity ..... 177

5.3.3 Experimental data ..... 180

5.3.4 Osteoporotic degradation ..... 182

5.3.5 A simplified model of osteoporotic degradation ..... 184

5.3.6 Numerical evaluations ..... 185

5.4 Conclusions ..... 190

5.5 References ..... 193

Chapter 6 SUMMARY AND RECOMMENDATIONS FOR THE FUTURE RESEACH ..... 198

## LIST OF FIGURES

**Figure 1.1** Young's modulus as a function of density for biological materials, overlaid on a map indicating regions of synthetic materials. Taken from [1.1] and [1.2]. ..... 2

**Figure 1.2** Schematic representation of characteristic constraints/components in the study of biological systems. Modified from [1.3]. ..... 4

**Figure 1.3** (a) Structure of collagen fibrils. Collagen molecules twist together to form the tropocollagen molecule. The tropocollagen molecules are held together by covalent bonding and self-assemble to form a fibrous, periodic array consisting of a gap region (~ 40 nm) and an overlap region (~ 27 nm) between the staggered arrays. These staggered arrays form the collagen fibril, 10-200 nm in diameter. (b) Transmission electron microscopy (TEM) image of collagen, showing the characteristic banded pattern arising from the gap and overlap regions. Courtesy of P.-Y. Chen. ..... 12

**Figure 1.4** (a), (b) TEM micrographs of the mineral phase (hydroxyapatite) in cortical bovine femur bone. The platelets are ~ 20 x 50 nm in width and ~ 4 nm in thickness. Modified from [1.124]; (c) SEM micrograph of mineralized collagen fibers from bovine femur cortical bone. The globules are aggregates of hydroxyapatite. ..... 14

**Figure 1.5** Regions where hydroxyapatite is located in the mineralized collagen fibril, either intramolecular or extramolecular: (a) assembly of tropocollagen to form fibrils, (b) nucleation of intermolecular minerals in the gap region between the tropocollagen molecules, (c) extramolecular minerals nucleated outside of the tropocollagen. Taken from [1.47]. ..... 15

**Figure 1.6** Hierarchical structure of bone. Level I: The basic elements of bone, tropocollagen (300 x 1.5 nm) – a triple helix of α-collagen molecules and carbonated hydroxyapatite (platelets of 100 x 25 x 4 nm). Level II:

Tropocollagen assembles to form collagen fibrils and combine with hydroxyapatite, which is dispersed between (in the gap regions) and around the collagen, forming mineralized collagen fibrils. Level III: The fibrils are orientated into several structures, depending on the location in the bone (parallel, circumferential, twisted). Level IV: Cortical bone is lamellar – cylindrical and parallel plate lamella is found depending on location. Level V: Light microscope level showing osteons (organized cylindrical lamellae) with a central vascular channel and small lacunae (10-20 nm) interspersed between the lamellae. Level VI: Whole bone. Modified from [1.56]. ..... 17

**Figure 1.7** (a) Cross-section of cortical bone, showing vascular channels parallel and perpendicular to the growth direction; (b) The hierarchical structure of porosity of cortical bone. From left to right: spaces between wet collagen molecules, spaces between mineralized collagen fibers, canaliculi and lacuna spaces, vascular channels and resorption cavities. Modified from [1.98]. ..... 19

**Figure 1.8** Effect of mineral volume fraction on elastic modulus of bones from various animals (data plotted from ([1.19], [1.20], 1.57]). The Voigt, Reuss, Hashin-Shtrikman (H-S) upper and lower bounds and Hill model curves are shown. ..... 21

**Figure 1.9** Relative elastic modulus as a function of relative density for trabecular bone. Taken from [1.62]. ..... 23

**Figure 1.10** Tensile and compressive stress-strain curves for cortical bone in longitudinal and transverse directions. Adapted from [1.64]. ..... 25

**Figure 1.11** Compressive stress-strain curves for human cortical bone at varying strain rates. Taken from [1.66]..... 27

**Figure 1.12** Bone mineral density (BMD) from the lumbar spine as a function of age for: (a) young girls [1.71], and (b) older women [1.72]. ..... 28

**Figure 1.13** (a) Illustration of important measured nanoindentation parameters: maximum load ($P_{max}$), maximum displacement ($h_{max}$), and the elastic unloading stiffness (S). Taken from [1.85]. (b) Typical nanoindentation curves for cortical and trabecular bone samples. Elastic modulus is estimated from the slope (red lines) of the liner parts of unloading portions of the curves. Taken from [1.86]. ..... 34

**Figure 1.14** Backscattered electron (BSE) images showing cross-sectional microstructure of cortical bovine femur: secondary osteons surrounded by interstitial bone. Taken from [1.88]. ..... 35

**Figure 1.15** The probe assembly for bone diagnostic instrument. It consists of the reference probe and the test probe. Taken from Hansma *et al.* [1.91]..... 37

**Figure 1.16** Strain distribution across the height of the beam determined by electronic speckle pattern interferometry (ESPI) for four-point bending. Taken from Barak *et al.* [1.94]. ..... 38

**Figure 1.17** The bending moment distribution for: (a) three-point bending, and (b) four-point bending tests. ..... 40

**Figure 2.1** Schematic diagram of bone microstructure and sample orientations for three anatomical directions in cortical bone. Sample orientations: L = longitudinal, R = radial, T= transverse. ..... 61

**Figure 2.2** Photographs of untreated (UT), fully demineralized (DM) and fully deproteinized (DP) cortical bovine femur bone. The DM and DP samples are continuous, stand-alone structures that can be tested for mechanical properties (courtesy of Professor Paul Price, UCSD). ..... 64

**Figure 2.3** SEM images of (a) untreated (UT), (b) demineralized (DM), and (c) deproteinized (DP) bovine cortical bone (fracture surfaces). Os = osteons, La = lacuna spaces, Va = vascular channels. Images were taken from the different samples. ..... 65

**Figure 2.4** Stress-strain curves for untreated, deproteinized and demineralized cortical bovine femur bone tested in the longitudinal direction. Calculated weighted sum, shown in dots, clearly underestimates properties of untreated bone. ..... 67

**Figure 2.5** Representative compression stress-strain curves for the three anatomical directions for (a) untreated, (b) demineralized, and (c) deproteinized bone. ..... 69

**Figure 2.6** Weibull plots for ultimate compressive stress for untreated (n(L) = 20; n(R) = 10; n(T) = 10), and deproteinized (n(L) = 12; n(R) = 10; n(T) = 10) bone . Demineralized bone is 100% protein and Weibull analysis therefore was not applicable. ..... 70

**Figure 2.7** Optical micrographs showing the structure differences between (a) transverse, and (b) radial bone samples. Circumferential lamellae sheath is clearly shown at (b)..... 74

**Figure 2.8** Illustration of the preferentially oriented porosity level after collagen matrix removal for: (a) longitudinal, and (b) transverse/radial directions under compression for deproteinized cortical bone. ..... 76

**Figure 2.9** Master demineralization curves for the three anatomical directions. Demineralization was slightly faster in the radial and transverse directions as compared to the longitudinal direction. ..... 80

**Figure 2.10** Rate of demineralization as a function of time. The demineralized samples were from the steady state region (flat region). Modified from [2.29].... 80

**Figure 2.11** Stress-strain curves for untreated bone and different degrees of bone demineralization. It is clearly seen that even a small amount of mineral deficiency dramatically changes the stiffness and strength. ..... 83

**Figure 2.12** SEM image of demineralized cortical bone showing collagen fibers alignment along bone growth direction (shown by arrow). ..... 87

**Figure 2.13** Representative stress-strain curves during cyclic loading-unloading compression of demineralized samples in three different anatomical directions, showing first three consecutive cycles. L = longitudinal, R = radial, T = transverse. ..... 89

**Figure 2.14** Representative stress-strain, stress-time, and strain-time curves for cyclic loading-unloading compression (10 consecutive cycles) for demineralized cortical bone in different anatomical directions. L = longitudinal, R = radial, T = transverse. ..... 92

**Figure 2.15** The vanishing of the secant/tangent moduli ratio $E_s^{(i)}/E^{(i)}$ with the cycle number during first 10 loading-unloading compression cycles for longitudinal, radial, and transverse directions. ..... 94

**Figure 3.1** The hierarchical structure of the porosity in cortical and trabecular bone: (a) – nanoscale; (b) sub-microscale; (c) and (e) – microscale for cortical and trabecular bone, respectively; (d) and (f) – mesoscale for cortical and trabecualr bone, respectively. ..... 104

**Figure 3.2** Optical microscopy images of bone cross-section and porosity estimation (in red) for (a) cortical, and (b) trabecular bone. ..... 105

**Figure 3.3** μ-CT images of (a) untreated, (b) demineralized and (c) deproteinized cortical bone. The gold regions correspond to empty spaces (voids). Scale bar = 100 μm. ..... 106

**Figure 3.4** μ-CT images of (a) untreated, (b) demineralized, and (c) deproteinized trabecular bone. Gold regions correspond to bone tissue. Scale bar = 700 μm. ..... 107

**Figure 3.5** Schematic diagram of physiological and compressive loadings on a femur head, and the sample orientation for two directions: A and B. The samples are not shown to scale. Femur bone image was taken from avocadoexplosion.wordpress.com. ..... 112

**Figure 3.6** The hierarchical structure of cortical bone: (a) – nanoscale; (b) sub-microscale; (c) – microscale; (d) – mesoscale. ..... 116

**Figure 3.7** The hierarchical structure of trabecular bone: (a) – nanoscale; (b) sub-microscale; (c) – microscale; (d) – mesoscale. ..... 119

**Figure 3.8** Optical microscopy images of untreated (a), demineralized (b), and deproteinized (c) trabecular bone showing rod-like and plate-like elements. ..... 125

**Figure 3.9** Scanning electron microscopy images of the fracture surfaces of (a) untreated, (b) demineralized (continuous protein network), and (c) deproteinized (continuous mineral network) bovine trabecular bone. La = lacuna spaces. Arrows pointed out the preferential orientation of collagen fibers for demineralized bone (b), and minerals for deproteinized bone (c). Images were taken from different samples..... 126

**Figure 3.10** Scanning electron microscopy images of (a) untreated, (b) demineralized (continuous protein network), and (c) deproteinized (continuous mineral network) bovine cortical bone showing microstructural features: osteons (Os), lacuna spaces (Lac), Haversian channels (HC), and Volkmann's canals (VC). Images were taken from different samples. ..... 127

**Figure 3.11** μ-CT 3D isosurface images of untreated cortical bone showing (a) side view of canal network (red: Haversian, vertical; Volkmann's, horizontal) and osteocyte lacunae (yellow); the lacunae are preferentially oriented in vertical direction, indicating the long axis of bone, (b) side view of canal network only. A volumetric filter ($20 \times 20 \times 20\ \mu m^3$) was applied to separate canal network from lacuna spaces. ..... 128

**Figure 3.12** Micro-CT 3D isosurface images of trabecular bone for untreated (a) A-direction, (b) B-direction, demineralized (c) A-direction, (d) B-direction, and deproteinized (e) A-direction, (f) B-direction. Scale bar = 700 μm. 130

**Figure 3.13** Stress-strain curves for (a) untreated (UT), (b) demineralized (DM), and (c) deproteinized (DP) cortical bone for two anatomical directions. N = 10 for each curve. ..... 133

**Figure 3.14** Relative elastic modulus versus relative density for untreated, demineralized, and deproteinized trabecular bone for two anatomical directions. ..... 136

**Figure 3.15** Relative elastic modulus versus relative density for (a) untreated, (b) deproteinized, and (c) demineralized trabecular bone for two anatomical directions. ..... 136

**Figure 3.16** Comparison of the experimental and modeling results for (a) longitudinal, and (b) transverse elastic moduli of untreated (UT), demineralized (DM, magnified by 100X for clarity), and deproteinized (DP) cortical bone. The capped lines show the standard deviation for experimental data and the range for modeling results (due to range in porosity, see Table 3.3)..... 139

**Figure 3.17** Comparison of the experimental and modeling results for (a) A-direction, and (b) B-direction elastic moduli of untreated (UT), demineralized (DM, magnified by 100X for clarity), and deproteinized (DP) trabecular bone. The capped lines show the standard deviation for experimental data and the range for modeling results (due to range in porosity, see Table 3.4).141

**Figure 4.1** Photographs of cross-sections of (a) mature and (b) young bovine cortical bone. ..... 152

**Figure 4.2** Cross-sectional optical micrographs along with porosity analysis by ImageJ for (a) mature and (b) young. Interstitial bone regions, surrounded by secondary osteons, are enclosed in (a). Area with primary osteons is enclosed in (b). ..... 154

**Figure 4.3** Optical micrographs of (a) mature and (b) young bovine cortical bones in the medial and lateral areas. ..... 155

**Figure 4.4** Optical microscopy images of anterior, posterior, lateral, and medial quadrants of mature bovine cortical bone. ..... 157

**Figure 4.5** Optical microscopy images of anterior, posterior, lateral, and medial quadrants of young bovine cortical bone. ..... 158

**Figure 4.6** Porosity distribution around bone cross-section for mature and young bone. ..... 159

**Figure 4.7** Micro-harness data for different bone quadrants for mature and young bone. ..... 160

**Figure 4.8** Representative compressive stress-strain curves. Untreated mature (dashed) and young (solid) bones for (a) longitudinal and (b) transverse directions. Deproteinized mature (dashed) and young (solid) bones for (c) longitudinal and (d) transverse directions. Demineralized mature (dashed) and young (solid) bones for (e) longitudinal and (f) transverse directions. ..... 163

**Figure 4.9** Compressive stress-strain curves of untreated young bone in the (a) longitudinal and (b) transverse directions. Two distinct, visible regions were observed: undeveloped (yellow) and more organized (white). L1 and L2 samples were composed of both regions and L3-L5 consisted only of the yellow regions. ..... 164

**Figure 5.1** Photographs of cross-sections (5 x 5 mm) of trabecular bovine femur: (a) control/untreated (UT), (b) demineralized (DM), and (c) deproteinized (DP) bone samples (adopted from [5.24]). The volumes of the UT, DM, and DP samples are nearly the same, i.e., $= Vm = Vp$ . ..... 170

**Figure 5.2** The variation of the trabecular elastic modulus $E^*$ of trabecular bovine..... 181

**Figure 5.3** Trabecular bone structure: (a) normal, (b) osteoporotic. The osteoporotic bones contains larger holes as a result of the calcium being dissolved (from www.brsoc.org.uk/gallery, with permission from Prof. Alan Boyde, University of London, UK). ..... 183

**Figure 5.4** The time variation of the density ratio $\rho/\rho 0$, during 30 years of progression of osteoporosis, according to Eq. (5.18), with the rate coefficient r = 2.1 x $10^{-3}$(year)$^{-2}$..... 188

**Figure 5.5** The time variations of the elastic moduli ratios $E/E0$, $Em/Em0$ , $Ep/Ep0$ during their osteoporotic degradation, according to (5.23) – (5.25), corresponding to constant values of the morphological parameters $= 2.84$, $nm = 3.15$ and $np = 1.75$ with the rate coefficient $r = 2.1\ x\ 10 - 3$(year)$^{-2}$. ..... 189

**Figure 5.6** The time variation of the elastic moduli ratio of ftabecular bone $E/E0$ during odteoporosis degradation, according to (5.25), in the case when the morphological parameter $n = 2.84$ is constant, or equil to time dependent function $n1(t) = 2.84 - 0.008t3/2$ or $n2$(t) $= 2.84 - 0.0036t2 + 0.00006t3$..... 190

## LIST OF TABLES

**Table 1.1** Summary of the important parameters that affect the measurement of the elastic modulus of bone. ..... 30

**Table 1.2** Elastic modulus of cortical femoral bone..... 42

**Table 1.3** Elastic modulus of trabecular femoral bone..... 43

**Table 3.1** Porosity estimation by μ-CT and optical microscopy (OM) for untreated, demineralized, and deproteinized cortical and trabecular bone..... 108

**Table 3.2** Elastic properties and volume fractions of bone constituents employed in modeling. ..... 117

**Table 3.3** 3D bone morphometry results from μ-CT image analysis for UT = untreated, DM = demineralized, and DP = deproteinized cortical bone. ..... 129

**Table 3.4** Comparison of porosity estimation results from μ-CT imaging and the measured density for bovine trabecular bone. ..... 131

**Table 3.5** Normalizing parameters for untreated, demineralized, and deproteinized trabecular bone samples (used in Eq. (3.4)) obtained experimentally. All data averaged from [3.21] ..... 137

**Table 4.1** Hydrated density, volume % of minerals, compressive strength, and Young's modulus for untreated (UT), deproteinized (DP), and demineralized (DM) mature and young bovine femur bones for longitudinal (L) and transverse (T) directions..... 162

## ACKNOWLEGEMENTS

I am very grateful to my adviser, Professor Joanna McKittrick, for her excellent guidance, everyday support and amazing mentorship throughout my graduate study. I want to thank my co-adviser, Professor Vlado Lubarda, for his huge inspiration, support, and valuable insights to my dissertation work. I would like to thank all my committee members for their enthusiasm, smiles, and helpful guiding throughout of my graduate school years. I would also want to thank all my friends from Materials Science program and Mechanical and Aerospace department; without their everyday support and smiles my graduate school experience will never be so pleasant, productive and unforgettable. Research support from the National Science Foundation, Division of Ceramics Program (Grant DMR 1006931) is gratefully acknowledged.

I want to thank Alexei, Alexander and Eugenia Krista for their tremendous love and patience through these years. My family and friends have provided an enormous help and support without which none of these achievements would have been possible. I want to specially thank Rostislav Rokitski for his patient help with plural computer related tasks along these years.

This research would not be possible without the help and contribution from the collaborators. Professor Iwona Jasiuk, Elham Hamed and Jun Li provided the valuable theoretical insights about multiscale modeling of bone, their contribution is gratefully acknowledged.

I would also want to acknowledge Ryan Andersen from Nano3 facility at UCSD for his assistance with scanning electron microscopy.

Chapter 1, in part, is a reprint of the material as it appears in "Recent advances on the measurement and calculation of the elastic moduli of cortical and trabecular bone: A review," in Theoretical and Applied Mechanics, 38, 209-297, 2011. E. Novitskaya; P.-Y. Chen; E. Hamed; J. Li; V.A. Lubarda; I. Jasiuk; J. McKittrick. The dissertation author was the primary investigator and author of this paper.

Sub-chapter 2.1, in full, is a reprint of the material as it appears in "Anisotropy in the compressive mechanical properties of bovine cortical bone: Mineral and protein constituents compared with untreated bone," in Acta Biomaterialia, 7, 3170-3177, 2011. E. Novitskaya, A.B. Castro-Ceseña, P.-Y. Chen, S. Lee, G. Hirata, V.A. Lubarda, J. McKittrick. The dissertation author was the primary investigator and author of this paper.

Sub-chapter 2.2, in full, is a reprint of the material as it appears in "Investigations into demineralized cortical bone", in Materials Research Society Symposium Proceeding, Fall 2010, Volume 1301, Symposium NN1.7. E.E. Novitskaya; A.B. Castro-Ceseña; P.-Y. Chen; J. Vasquez; R. Urbaniak; S. Lee; G.A. Hirata; J. McKittrick. The dissertation author was the primary investigator and author of this paper.

Sub-chapter 2.3, in full, has been submitted for publication as it may appear in "Initial anisotropy in demineralized bovine cortical bone in compressive cyclic loading-unloading," in Materials Science and Engineering C, 2012. E.E. Novitskaya; S. Lee; V.A. Lubarda; J. McKittrick. The dissertation author was the primary investigator and author of this paper.

Sub-chapter 3.1, in full, is a reprint of the material as it appears in "Hierarchical structure of porosity in cortical and trabecular bones," in Materials Research Society Symposium Proceeding, Fall 2011. E. Novitskaya; E. Hamed; J. Li; Z. Manilay; I. Jasiuk;

J.McKittrick. The dissertation author was the primary investigator and author of this paper.

Sub-chapter 3.2, in part, is a reprint of the material as it appears in "Correlation of multiscale modeling and experimental results for the elastic moduli of cortical and trabecular bone," in Society for Experimental Mechanics Congress Proceedings, 2012. E. Novitskaya; E. Hamed; J. Li; I. Jasiuk; J. McKittrick. The dissertation author was the primary investigator and author of this paper.

Chapter 4, in part, has been submitted for a publication as it may appear in "A comparative study of young and mature bovine cortical bone," in Acta Biomaterialia, 2012. Z. Manilay; E.E. Novitskaya; E. Sadovnikov; J. McKittrick. The dissertation author was the primary investigator of this paper.

Chapter 5, in part, is a reprint of the material as it appears in "Elastic properties of cancellous bone in terms of elastic properties of its mineral and protein phase with application to their osteoporotic degradation," in Mechanics of Materials, 44, 139-150, 2012. V.A. Lubarda; E.E. Novitskaya; S.G. Bodde; J. McKittrick; P.-Y. Chen. The dissertation author was one of the primary investigator of this paper.

## VITA

| | |
|---|---|
| 1994 | St. Petersburg State University, Russia, Physics, B.S |
| 1997 | St. Petersburg State University, Russia, Physics, M.S. |
| 2012 | University of California, San Diego, Materials Science and Engineering Program, PhD |

## FIELD OF STUDY

Major: Material Science and Engineering with an emphasis on structure and properties of biological materials.

## LIST OF PUBLICATIONS

### Journal Publications

I. Gerlovin, Y. Dolgikh, V. Ovsyankin, Y. Efimov, I. Ignat'ev, **E. Novitskaya***, "Temperature-induced delocalization of excitations in GaAs/AlAs type-II superlattices,"*Physics of the Solid State*, **40** (6), 1041-1046, 1998

A.A. High, **E.E. Novitskaya***, L.V. Butov, M. Hanson, A.C. Gossard, "Control of exciton fluxes in an excitonic integrated circuit," *Science*, **321**, 229-231, 2008

L. Tombolato, **E.E. Novitskaya***, P.-Y. Chen, F. Sheppard, J. McKittrick, "Microstructure, elastic properties and deformation mechanisms of horn keratin," *Acta Biomaterialia*, **6** (2), 319-330, 2010

J. McKittrick, P.-Y. Chen, L. Tombolato, **E.E. Novitskaya***, M.W. Trim, G.A. Hirata, E.A. Olevsky, M.A. Meyers, M.F. Horstemeyer, "Energy absorbent materials and bioinspired design strategies: A review," *Materials Science and Engineering C*, **30**, 331-342, 2010

A.B. Castro-Ceseña, **E.E. Novitskaya***, P.-Y. Chen, G.A. Hirata, J. McKittrick, "Kinetic studies of bone demineralization at different HCl concentrations and temperatures," *Materials Science and Engineering C*, **31**, 523-530, 2011

S. Lee, **E.E. Novitskaya***, B. Reynante, P.-Y. Chen, L. Tombolato, J. Vasquez, R. Urbaniak, J. McKittrick, "Impact testing of structural biological materials," *Materials Science and Engineering C,* **31** (4), 730-739, 2011

**E. Novitskaya***, A. Castro-Ceseña, P.-Y. Chen, S. Lee, G. Hirata, V. A. Lubarda, J. McKittrick, "Anisotropy in the compressive mechanical properties of bovine cortical bone: Mineral and protein constituents compared with untreated bone," *Acta Biomaterialia,* **7***,* 3170-3177, 2011

**E. Novitskaya***, P.-Y. Chen, E. Hamed, J. Li, V. A. Lubarda, I. Jasiuk, J. McKittrick, "Recent advances on the measurement and calculation of the elastic moduli of cortical and trabecular bone: A review," *Theoretical and Applied Mechanics,* **38** (3), 209-297, 2011

E. Hamed, **E. Novitskaya***, J. Li, P.-Y. Chen, I. Jasiuk and J. McKittrick, "Elastic moduli of untreated, demineralized, and deproteinized cortical bone: Validation of a theoretical model of bone as an interpenetrating composite material," *Acta Biomaterialia,* **8***,* 1080-1092, 2012

V.A. Lubarda, **E.E. Novitskaya***, Sara G. Bodde, J. McKittrick, P.-Y. Chen, "Elastic properties of cancellous bone in terms of elastic properties of its mineral and protein phase with application to their osteoporotic degradation," *Mechanics of Materials,* **44**, 139-150, 2012

J. McKittrick, P.-Y. Chen, S.G. Bodde, W. Yang, **E.E. Novitskaya***, M.A. Meyers, "Structure, functions, and mechanical properties of keratin," *Journal of Materials,* **64**, 449-468, 2012

Z. Manilay, **E.E. Novitskaya***, E. Sadovnikov, J. McKittrick, "A comparative study of young and mature bovine cortical bone," accepted to *Acta Biomaterialia*, doi: 10.1016/j.actbio.2012.08.040

**E.E. Novitskaya***, S. Lee, V.A. Lubarda, J. McKittrick, "Initial anisotropy in demineralized bovine cortical bone in compressive cyclic loading-unloading," submitted to *Material Science and Engineering C*, 2012

M.M. Porter, **E. Novitskaya***, A.B. Castro-Ceseña, M.A. Meyers, J. McKittrick, "Fracture resistant bones: unusual deformation mechanisms protecting seahorses," submitted to *Nature*, 2012

A.B. Castro-Ceseña, **E.E. Novitskaya***, P.-Y. Chen, M. del Pilar Sanchez, G.A. Hirata J. McKittrick, "Comparison of the kinetics of the *in vitro* deproteinization of trabecular and cortical bone," submitted to *Bone*, 2012

**Conference Proceedings**

**E.E. Novitskaya***, A.B. Castro-Ceseña, P.-Y. Chen, J. Vasquez, R. Urbaniak, S. Lee, G.A. Hirata, J. McKittrick,"Investigations into demineralized cortical bone," Materials Research Society Symposium Proceeding, Fall 2010, Volume 1301, Symposium NN1.7.

A.B. Castro-Ceseña, **E.E. Novitskaya***, P.-Y. Chen, M.P. Sánchez-Saavedra, G.A. Hirata, J. McKittrick, "Comparison of demineralized and deproteinized bone," Materials Research Society Symposium Proceeding, Fall 2010, Volume 1301, Symposium NN1.8.

J. McKittrick, P.-Y. Chen, **E.E. Novitskaya***, D. Toroian and P.A. Price, "Deformation of demineralized and deproteinated bone," Proc. 16$^{th}$ US Natl. Cong. Theo. Appl. Mech., USNCTAM 2010, Pennsylvania State College, 2010.

**E. Novitskaya***, E. Hamed, J. Li, Z. Manilay, I. Jasiuk, J. McKittrick, "Hierarchical structure of porosity in cortical and trabecular bones," Mater. Res. Soc. Symp. Proc. Vol. 1420 © 2012 Materials Research Society DOI: 10.1557/opl.2012.488

S. Lee, M. Porter, S. Wasko, G. Lau, P.-Y. Chen, **E.E. Novitskaya***, A.P. Tomsia, A. Almutairi, M.A. Meyers, J. McKittrick,"Potential bone replacement materials prepared by two methods," Materials Research Society Symposium Proceeding, Fall 2011, accepted

**E. Novitskaya***, E. Hamed, J. Li, I. Jasiuk, J. McKittrick, "Correlation of multiscale modeling and experimental results for the elastic moduli of cortical and trabecular bone," Society for Experimental Mechanics Congress Proceedings, 2012, accepted

A.B. Castro-Ceseña, **E.E. Novitskaya***, A. Phadke, S. Varghese, J. McKittrick, "Isolation of collagen from cortical bovine bone for preparation of porous collagen sponges," Society for Experimental Mechanics Congress Proceedings, 2012, accepted

**Manuscrips in Preparation**

E. Hamed, **E.E. Novitskaya***, J. Li, P.-Y. Chen, I. Jasiuk, J. McKittrick, "Correlation of experimental and modeling results on predicting the elastic modulus of untreated, demineralized, and deproteinized trabecular bone."

P.-Y. Chen, **E.E. Novitskaya***, M.I. Lopez, M.A. Meyers, J. McKittrick, "Toward a better understanding of the microstructure of mineral constituents in bony tissues by complete deproteinization."

## LIST OF PRESENTATIONS

A. High, A. Hammack, **E. Novitskaya*,** L. Butov, L. Mouchliadas, A. Ivanov, M. Hanson, A. Gossard,"Control of exciton flux through tunable potential reliefs" (poster), Fundamental Optical Processes in Semiconductors, Big Sky, Utah, USA, July 23-27, 2007

**E. Evdokimenko**, L. Tombolato, P.-Y. Chen, F. Sheppard, and J. McKittrick "Structure and mechanical properties of horn keratin" (poster), Research Expo, UCSD, February 19, 2009

**E. Evdokimenko**, L. Tombolato, P.-Y. Chen, F.A. Sheppard, and J. McKittrick "Structure and mechanical properties of horn keratin" (poster), MRS Spring Meeting, San Francisco, California, USA, April 13-17, 2009

J. McKittrick, P.-Y. Chen, L. Tombolato, **E. Novitskaya***, Y.S. Lin, E.O. Olevsky, M.A. Meyers, "Structural biological materials," UC Riverside, USA, March 6, 2009

J. McKittrick, P.-Y. Chen, L. Tombolato, **E. Novitskaya***, M.A. Meyers, "Soft biological materials: role in the mechanical properties of biological composites", 1st International Conference on Soft Materials, Shanghai, China, May 25, 2009

J. McKittrick, P.-Y. Chen, **E. Novitskaya***, S. Lee, and M. Meyers, "Biological composites and bioinspired materials design: A materials science approach" (poster), Biomimicry Symposium, San Diego, California, USA, October 1-2, 2009

J. McKittrick, P.-Y. Chen, **E. Novitskaya***, 2nd International and Interdisciplinary Meeting on Nanoscience and Nanotechnology (NanoMex'09), Ensenada, Baja California, Mexico, November 10-11, 2009

**E. Evdokimenko**, L.Tombolato, J.Curiel, P.-Y.Chen, J.McKittick, "Why is horn so tough?" 3rd International Conference on Mechanics of Biomaterials and Tissues, Clearwater Beach, Florida, USA, December 13-17, 2009

**E. Evdokimenko**, L.Tombolato, Steve Lee, P.-Y.Chen, J.McKittick, "Microstructural features that toughen horn," TMS Meeting, Seattle, Washington, USA, February 14-18, 2010

**E. Evdokimenko**, Ana Castro-Ceseña, J. Vasquez, R. Urbaniak, P.-Y. Chen, J. McKittrick, "Mechanical and physical properties of demineralized and deproteinated compact bone" (poster), Research Expo, UCSD, April 15, 2010

S.G. Bodde, **E. Evdokimenko**, M.I. Lopez Fierro, "Biological materials: A materials science approach," Invited talk, Ensenada, Mexico, June 16, 2010

J. McKittrick, P.-Y. Chen, **E.E. Novitskaya***, D. Toroian, P. Price, "Deformation of demineralized and deproteinated bone," 16th US National Congress of Theoretical and Applied Mechanics, State College, Pennsylvania, USA, June 27 – July 2, 2010

J. McKittrick, P.-Y. Chen, **E.E. Novitskaya*,** "Kinetic and microstructural features of demineralized and deproteinated bone," The 7th Pacific Rim International Conference on Advanced Materials and Processing, Cairns, Australia, August 2-6, 2010

**E. Evdokimenko**, A. Castro-Cesena, P.-Y. Chen, J. Vasquez, R. Urbaniak, S. Lee. J. McKittrick, "Mechanical and physical properties of demineralized bone," MRS Fall Meeting, Boston, Massachusetts, USA, November 29-December 3, 2010

A.B. Castro, **E.E. Novitskaya***, P.-Y. Chen, M. del Pilar Sanchez, G. Hirata, J. McKittrick, "Kinetic studies of the demineralization and deproteination of bone," MRS Fall Meeting, Boston, Massachusetts, USA, November 29 - December 3, 2010

P.-Y. Chen, M.I. Lopez, **E.E. Novitskaya***, M.A. Meyers, J. McKittrick, "Structural characterization of the mineral phase in bony tissues: A comparative study," TMS Meeting, San Diego, California, USA, February 27 - March 3, 2011

A.B. Castro, **E.E. Novitskaya***, P.-Y. Chen, M. del Pilar Sanchez, G. Hirata, J. McKittrick, "Bone demineralization and deproteination studies: A biochemical-kinetic focus," TMS Meeting, San Diego, California, USA, February 27 - March 3, 2011

J. McKittrick, P.-Y. Chen, **E.E. Novitskaya***, M.I Lopez, I. Chen, M.A. Meyers, "Energy absorption in natural materials," TMS Meeting, San Diego, California, USA, February 27 - March 3, 2011

**E.E. Novitskaya***, J. Vasquez, R. Urbaniak, S. Lee, P.-Y. Chen, A. Castro, G. Hirata , J.McKittrick, "Quantitative and qualitative changes in the structure and properties of demineralized and deproteinated compact bone," TMS Meeting, San Diego, California, USA, February 27 - March 3, 2011

**E.E. Novitskaya***, P.-Y. Chen, S. Lee, E. Hamed, J. Li, V. A. Lubarda, I. Jasiuk, J. McKittrick, "Anisotropy in the compressive mechanical properties of bovine cortical bone," (poster) ASME International Mechanical Engineering Congress, Denver, Colorado, USA, November 11-17, 2011, Best Poster Award

**E.E. Novitskaya***, P.-Y. Chen, S. Lee, E. Hamed, J. Li, V. A. Lubarda, I. Jasiuk, J. McKittrick, "anisotropy in the compressive mechanical properties of bovine cortical bone and the mineral and protein constituents," (poster), 4th International Conference on Mechanics of Biomaterials and Tissues, Hawaii, USA, December 11-15, 2011

**E.E. Novitskaya***, P.-Y. Chen, V. A. Lubarda, J. McKittrick, "Modeling of the osteoporotic degradation of elastic properties of trabecular bone," (poster), 4th International Conference on Mechanics of Biomaterials and Tissues, Hawaii, USA, December 11-15, 2011

**E.E. Novitskaya***, P.-Y. Chen, S. Lee, V. A. Lubarda, J. McKittrick, "Viscoelastic properties of bone collagen," (poster), 4th International Conference on Mechanics of Biomaterials and Tissues, Hawaii, USA, December 11-15, 2011

**E.E. Novitskaya***, Z. Manilay, J. McKittrick, "A comparative study of the compressive mechanical properties of young and old bovine cortical bone," TMS Meeting, Orlando, Florida, USA, March 11-15, 2012

**E.E. Novitskaya***, E. Hamed, J. Li, I. Jasiuk, J. McKittrick, "The elastic modulus of trabecular bone: modeling and experiments," TMS Meeting, Orlando, Florida, USA, March 11-15, 2012

**E. Novitskaya***, E. Hamed, J. Li, Z. Manilay, I. Jasiuk, J. McKittrick, "Correlation of multiscale modeling and experimental results for the elastic moduli of cortical and trabecular bone," XXII Society for Experimental Mechanics Congress, Costa Mesa, California, USA, June 11-14, 2012

* Under the maiden name **Novitskaya**

ABSTRACT OF THE DISSERTATION

# INVESTIGATION INTO MECHANICAL PROPERTIES OF BONE AND ITS MAIN CONSTITUENTS

by

Ekaterina Evdokimenko

Doctor of Philosophy in Materials Science and Engineering

University of California, San Diego, 2012

Professor Joanna McKittrick, Chair

Professor Vlado A. Lubarda, Co-Chair

Bone is a hierarchically structured natural composite material, consisting of organic phase (type-I collagen), inorganic phase (hydroxyapatite), and water. Studies of the two main bone constituents, utilizing controlled demineralization and deproteinization, can shed light on mineral-collagen interaction which makes bone such a unique biological material. This knowledge is necessary for computational analysis of bone structure to identify preferential sites in the collagen matrix and mineral network

that degrade more easily. The main goal of this work is to develop a comprehensive picture of mechanical properties of bone and its main constituents.

Following the Introduction, Chapter 2 presents an investigation of microstructure and compressive mechanical properties of bovine femur cortical bone carried out on completely demineralized, completely deproteinized, and untreated bone samples in three anatomical directions. Anisotropic nature of bone was clearly identified in all cases. Extra levels of porosity along with microstructural differences for the three directions were found to be the main sources of the anisotropy.

In Chapter 3, a new theoretical model of cortical and trabecular bone as composite materials with hierarchical structure spanning from nanometer (collagen-mineral) level to millimeter (bone) level was developed. Compression testing was performed on untreated, demineralized, and deproteinized cortical and trabecular bovine femur bone samples to verify the model. The experimental data were compared with theoretical predictions; excellent agreement was found between the theory and experiments for all bone phases. Optical microscopy, scanning electron microscopy, and micro-computed tomography techniques were applied to characterize the structure of the samples at multiple length scales and provide further inputs for the modeling.

Chapter 4 presents a comparative study of mechanical properties, microstructure, and porosity of mature and young bovine femur cortical bone. It was found that the amount of porosity decreases, while the microhardness increases with maturation.

Osteoporotic degradation of trabecular bone elasticity, described in Chapter 5, was modeled using a cellular mechanics approach. Evolution equations for elastic modulus of bone in terms of those of mineral and protein trabeculae and in terms of

demineralized and deproteinized bones were formulated and verified by the analysis of compressive properties of bovine femur trabecular bone.

# Chapter 1 INTRODUCTION AND BACKGROUND

## 1.1 Biological Materials: Hierarchical Structure, Properties, Biomimicry

Solid mechanics has traditionally focused on modeling of materials and structures involving synthetic materials such as metals, ceramics, polymers, and composite materials. Natural biological materials are another class of materials which provide a wide spectrum of possibilities for mechanicians to apply existing theories and experimental techniques and develop new ones. Plants and animals have evolved over billions of years of evolution to become very efficient in utilizing materials for their desired functions. Thus, natural, including biological, materials have excellent properties for their applications. Biological materials are often porous, with cellular structures, which gives them light weight and energy-absorbing characteristics as well as high specific stiffness and strength. Such structures are present in trabecular bone and plant stems, for example. Mechanical property map showing Young's modulus as a function of density is shown in Fig. 1.1 [1.1, 1.2]. Densities of biological materials are low, generally less than 3 g/cm$^3$; whereas synthetic materials often have densities in the range of 4-15 g/cm$^3$. There is a broad range in Young's modulus, varying over orders of magnitude. Biological materials are also multifunctional and they adapt to changing environments and often have capacity to heal. Study of natural materials is needed to obtain fundamental understanding of their behavior to address problems in medicine and other fields. We can also look towards nature for ideas so we can adapt them to design superior synthetic materials for a wide range of engineering applications.

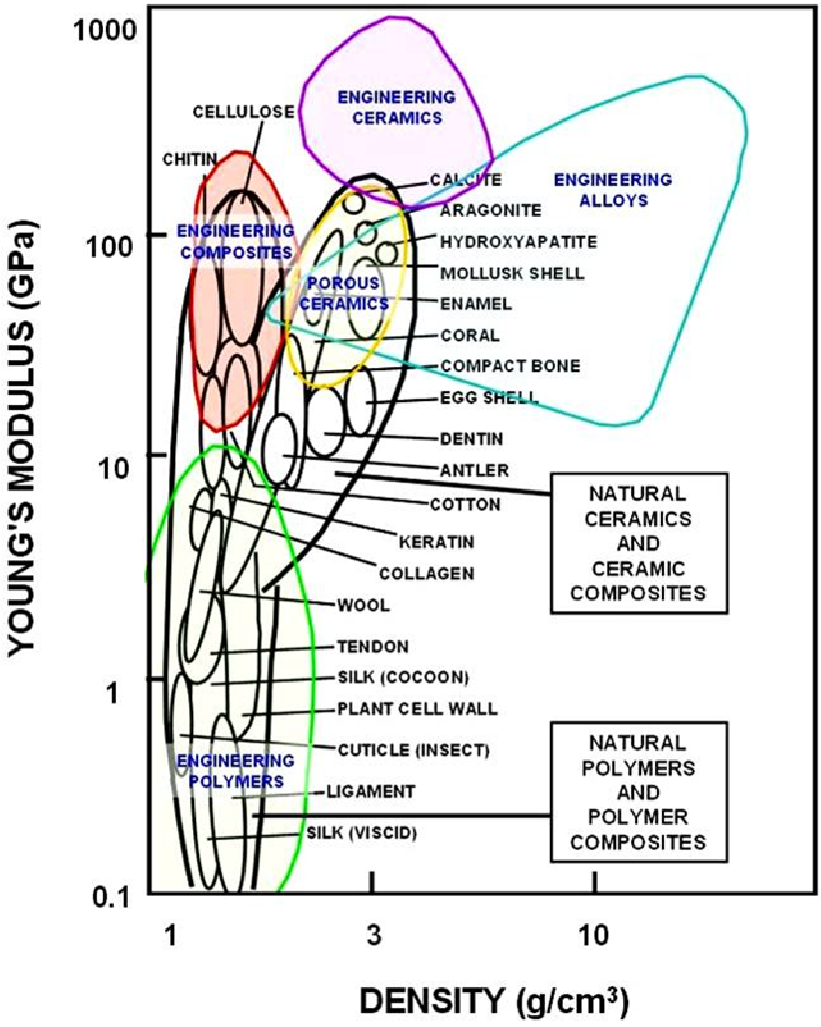


**Figure 1.1**Young's modulus as a function of density for biological materials, overlaid on a map indicating regions of synthetic materials. Taken from [1.1] and [1.2].

The unique structures and characteristics of biological materials are distinguished from synthetic counterparts. These are shown in Fig. 1.2, which are represented by six interrelated components:

- **Self-assembly** – the structures are assembled from the bottom-up, rather than from the top-down, due to the lack of a preexisting scaffold.

- **Functionality** – many components serve more than one purpose; for example, feathers provide flight capability, camouflage and insulation.
- **Hierarch***y* – there are different, organized scale levels (nano- to ultrascale) that confer distinct and translatable properties from one level to the next.
- **Hydration** – the properties are highly dependent on the level of water in the structure. There are some remarkable exceptions, such as enamel, but this rule applies to most biological materials and is of primary importance.
- **Mild synthesis conditions** – the majority of biological materials are fabricated at low temperatures and pressures and in an aqueous environment, a significant difference from synthetic materials fabrication.
- **Evolution, environmental constraints** – the limited availability of useful elements dictates the morphology and resultant properties.

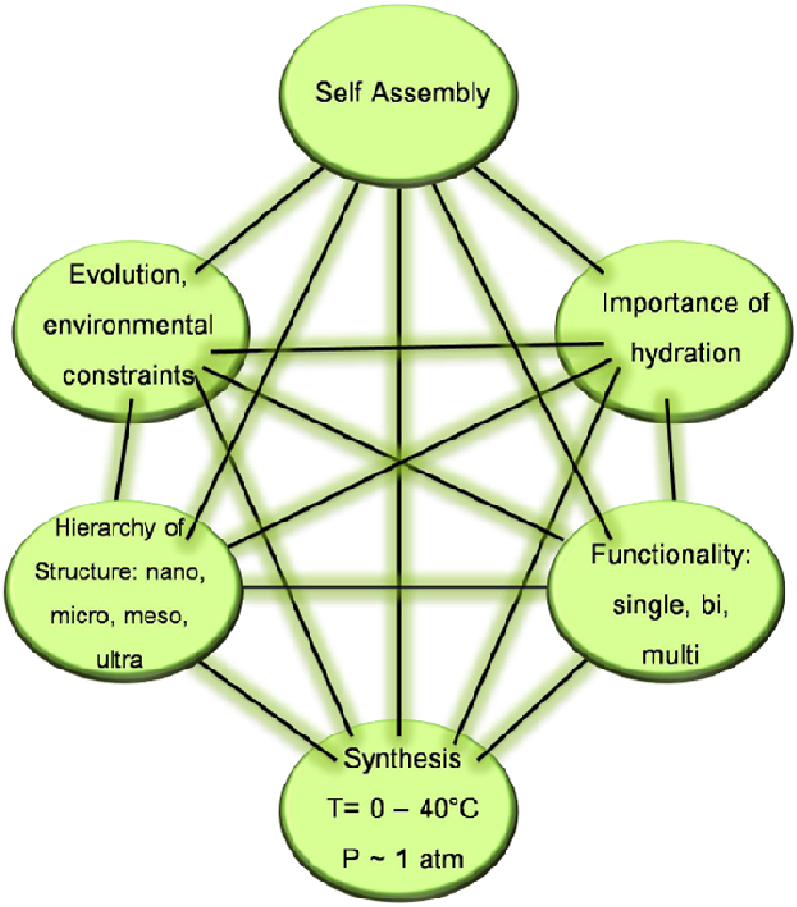


**Figure 1.2** Schematic representation of characteristic constraints/components in the study of biological systems. Modified from [1.3].

In terms of the hierarchical structure, there are several other defining features [1.4]:

- The presence of structural fibrous constituents (e.g. collagen, keratin, elastin, resislin) that display widely varying properties, depending on the function (e.g. collagen in tendon, skin, bone, heart muscles);
- The controlled orientations of the structural elements. For example, the minerals in bones are aligned with the collagen molecules, which are then

assembled into oriented mineralized fibrils, which are in turn, oriented into lamellar sheets;

- The ability for self-repair (bone, skin);
- The mutability of properties – they can adjust due to changes in ambient conditions (e.g. chemical and mechanical signals);
- The capacity for resiliency (energy absorbed during elastic deformation), toughness (energy absorbed during failure) and fatigue resistance, which are important for structural integrity.

Structural biological materials show a wide range of functions and forms. Teeth and tusks have the same chemical composition and microstructure, yet serve vastly different purposes. The same applies to bone and antler. Nature has optimized structural biological materials as functionally efficient composites. All natural biological materials are built under ambient conditions with only a few major elements (C, O, H, P, N, S, Ca, and Si). The main similarities between structural biological materials such as mollusk shells, diatoms, sea sponges, teeth, tusks, bone, antlers, crab exoskeletons and insect cuticles are that all structures are composites composed of a biopolymer (structural proteins such as collagen, keratin and elastin and/or polysaccharides such as cellulose and chitin) and a mineral phase (calcium carbonate, carbonated hydroxyapatite, or silica). Most structural biological materials are multifunctional, and bone is an excellent example. Skeletal bones support and shape bodies, serve as calcium and phosphorous stores, produce bone marrow and finally protect soft, critical organs exemplified by the ribs, skull and vertebrae.

Additionally, there is structural hierarchy that displays organization at all levels, from the nanoscale to the macroscale. The biopolymer imparts toughness and resilience while the biomineral increases hardness and stiffness. These biological materials usually serve several purposes such as protection (mollusk shell, bones), defense and aggression (claws, teeth, tusks, horns, and antlers), support (bones, mollusk shell, and hooves) and mastication (teeth). There is a synergistic effect between the biopolymer and mineral phases — both are greatly dependent on the presence of the other to impart the multi-objective mechanical properties. This is illustrated in the Wegst–Ashby plot (Fig.1.1), which shows that the Young's modulus is low and toughness is high for biopolymers while the stiffness is high but toughness is low for the mineral phase. However, toughness and stiffness values of biological composites are orders of magnitude higher than that of the pure mineral and pure biopolymer parts, respectively. From this observation, one can see that there are no rules of mixture in nature.

In order to understand structural biological materials, a few questions must be answered: What is (are) their function(s)? How are those functions optimally used? What loading conditions are present? For example, bones provide structural support and protection of internal organs. The largest natural stresses are compressive in the long leg bones and vertebrae. Failure can occur by many modes: torsion, bending, shear, compression, impact and fatigue loading. Trabecular (cancellous, spongy) bone appears in the skeleton where resistance to high impact loads is important — the skull, ribs, vertebrae and the head of the femur. They also ensure a higher flexural strength-to-weight ratio by forming the core of these bones, similar to sandwich panels. The multifunctional aspect of the trabecular bone must also be considered since it houses

bone marrow and vascular channels. The teeth must be able to bite and tear flesh and sustain high compressive loads. Tusks, which are long canine teeth that protrude from the mouth, are used for fighting and piercing. The horns from a big-horned sheep must be able to sustain large impact loads. The sheep do not shed their horns; they are a lifetime appendage. The average lifespan of a bighorn sheep is around 13 years; thus, the horns must be able to withstand repeated seasons of horn clashing without breakage. Hooves, found on ungulate mammals, transfer compressive loads to the skeleton, and in horses especially, undergo repeated high impact stresses.

A new paradigm for the fabrication of lightweight, impact resistant structures lies within the study of structural biological materials (biomimics). Bioinspired materials are synthetic materials that are fabricated to mimic the structure and mechanical properties of biological structural materials. Instead of using the limited library of elements and compounds available in nature, the task lies in mimicking the natural materials using high strength, high toughness engineering materials. The bioinspired design effort first involves the search for biological solutions in design. For example, antlers and horns are known to be impact resistant. Thus, designs based on these microstructures could be stronger and tougher than their natural counterparts because the components would be synthetically engineered materials (not biominerals and biopolymers). Determination of the mechanical properties and establishment of the relationship between the structure and function is the second step in the design of bioinspired materials. Finally, the application of engineering knowledge can be used to design new materials, using engineering ceramics, polymers and metals.

## 1.2 Recent Advances on the Measurement and Calculations of the Elastic Properties of Cortical and Trabecular Bone

Recent advances on the measurement and modeling of elastic properties of cortical and trabecular bone are reviewed. Bone is a multifunctional material which among its other functions serves as a support for other tissues in the body. As a structural material it is stiff, strong, tough, light weight and is adaptable. The excellent mechanical properties are due to its complex, composite and hierarchical structure. In this study the experimental approaches used to characterize bone's structure, composition and elastic properties at several different length scales are examined. The challenges and open issues in this area are then outlined.

### 1.2.1 Bone as a composite biological material: Main constituents, hierarchical structure, mechanical properties, and experimental methods to measure elastic modulus

Bone is a multifunctional material, which provides frame for body tissues, protects organs, manufactures blood cells, stores useful minerals, maintains pH in blood, detoxifies, and contributes to movement. As a structural material it has excellent mechanical properties: it is stiff, strong, tough and yet light. In addition, it is continuously adapting to loads and environment by growing larger and thicker when subjected to sufficient loads. Also, it has healing and regenerative characteristics as it heals its microcracks or fractures. The focus of this review is on bone as a structural material. The recent experimental and theoretical developments and challenges in

studies of elastic properties of bone were reviewed. Those techniques and ideas are generally also applicable to other biological materials. In addition, lessons learned from nature about bone's structure-property relations can give guidance on how to design novel bioinspired synthetic structural materials.

The excellent mechanics properties of bone are due to its complex composite and hierarchical structure. Bone is composed of three major constituents: an organic matrix (predominately type-I collagen), a mineral reinforcement (calcium phosphate) and water. A small amount of non-collagenous proteins (NCPs) (~ 10%) that surrounds the minerals and attaches the collagen molecules together are also found. There are two main types of bone: cortical (compact) and cancellous (trabecular or spongy). Cortical bone is the dense bone that forms outer core of bones and it makes up the majority of the skeleton whereas trabecular bone is sandwiched between cortical bone to give impact resistant properties (e.g., in skull, ribs, vertebrae) and at ends of long bones (e.g., femoral head) to distribute loads. Mammalian bone is made up of around 65 wt.% mineral phase, 25 wt.% organic, and 10 wt.% water. On a volumetric basis, this corresponds to ~ 33-43 vol.% minerals, 32-44 vol.% organic, and 15-25 vol.% water [1.5].

Cortical bone further consists of three subtypes, osteonal, interstitial, and plexiform. Osteonal bone consists of osteons that are made of thin (2-6 μm) lamellar sheets oriented into a concentric cylindrical structure. These osteons are 150-250 μm in diameter and align parallel along the long axis of bone. Interstitial lamellae (remnants after bone remodelling) occupy the space around the osteons. Periosteal bone consists of circumferential lamellae structure which is parallel to the bone surface and is made of

fibrolamellar bone. The periosteal bone is reported to be stronger and more highly anisotropic than osteonal bone [1.6]. The osteonal bone is made up of cylindrical structures (osteons) that span throughout the bone in the longitudinal direction. Osteons support nutritional needs and regeneration processes. The plexiform bone is made up of lamellar bone sheets that are perforated by a plexus of blood vessels. Plexiform bone is found in large, fast growing animals and is an indicator of non-human bone [1.6].

Trabeculae (trabecular wall material) of trabecular bone are composed almost exclusively of lamellar bone arranged in packets (hemiosteons). Trabecular bone is an open cell porous network consisting of rod- and plate-like elements (trabeculae, 50–300 μm thick and up to about 1 mm long), which provide room for blood vessels and marrow, and make the entire bone lighter [1.6].

There are several books that provide valuable insights into bone. In the 70's, J.D. Currey investigated a broad variety of mineralized biological materials and authored the well-known book Bones: Structure and Mechanics (Currey [1.6]). Other works of significance are Skeletal Tissue Mechanics (Martin [1.7]), Mechanical Testing of Bone and the Bone-Implant Interface (An, [1.8]), Bone Mechanics Handbook (Cowin, [1.9]), and Tissue Mechanics (Cowin, [1.10]). There have also been a number of overview articles presenting the field in a broad manner. Noteworthy among them are overviews in *Journal of Bone and Joint Surgery* (Reilly, [1.11]), *Annual Review of Materials Science* (Weiner, [1.12]), *Materials Science and Engineering R* (Olsza *et al*. [1.5]), and *Osteoporosis International* (Zysset, [1.13]).

There have been numerous experimental investigations into the evaluation of elastic modulus. Representative references include Currey [1.14 - 1.20], Bonfield and

Datta [1.21], Reilly *et al.* [1.22], Bonfield and Grynpass [1.23], Bonfield and Tully [1.24], Katz [1.25], Evans *et al.* [1.26], and Rho *et al.* [1.27]. The main findings are that elastic modulus is dependent on a variety of factors, including:

- type of bone (cortical or trabecular);
- taxa of bone (mammal, avian, reptile);
- skeletal location of the bone (femur, skull);
- amount of mineralization;
- degree of hydration (water content);
- porosity;
- orientation (longitudinal, transverse, radial);
- age;
- strain rate;
- testing method.

#### *1.2.1.1 Constituents of bone*

Protein structure (collagen)

At the molecular level, polypeptide chains (two $\alpha_1$ and one $\alpha_2$) twist together to form the triple helical collagen molecule, tropocollagen, that is ~ 300 nm in length and 1.5 nm in diameter, stabilized by numerous hydrogen bonds (Fig. 1.3a). A defining feature of collagen is the frequently occurring amino acid sequence of Gly-Pro-X or Gly-X-Hyp (Gly = glycine, Pro = proline, Hyp = hydroxyproline, X, Y = other amino acid residues). Glycine is a majority residue, which is the smallest amino acid and the

only one small enough to tuck into the twists along the triple helix. The tropocollagen molecules further self-assemble into fibrils that are ~ 100 nm in diameter and up to several microns in length. Collagen molecules, which are held together by covalent cross-linked bonds, organize into a staggered array. The interruption between the tropocollagen molecules gives rise to two important dimensions – the gap (~ 40 nm) and the overlap (~ 27 nm) regions that combine to form the characteristic banded structure of 67 nm spacing, observed in transmission electron microscopy (TEM), as shown in Fig. 1.3b. The collagen is also providing a template for mineral deposition, as the mineral crystals are aligned with the collagen fibril axis [1.9].

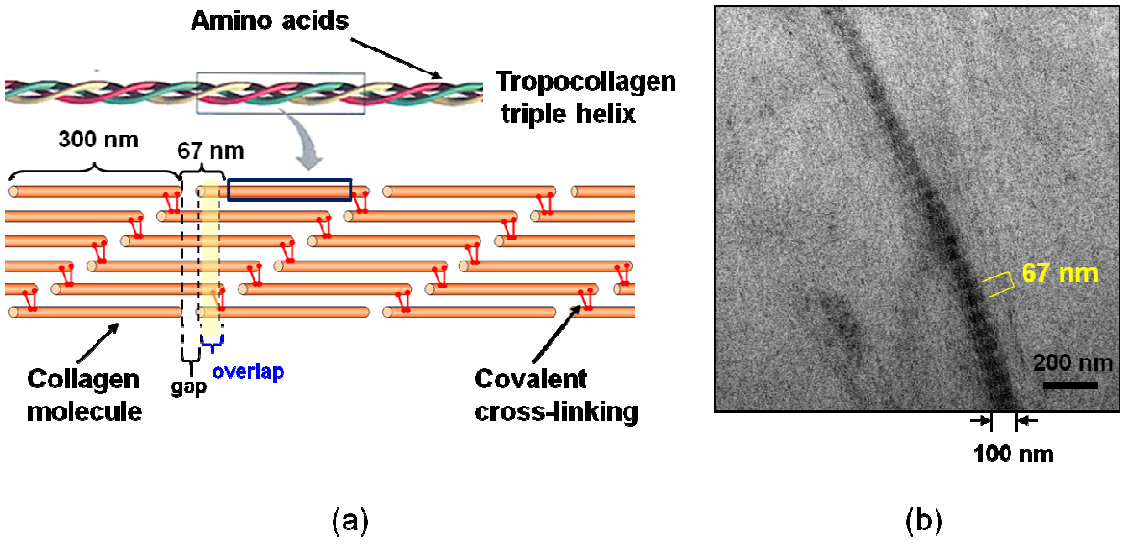


**Figure 1.3** (a) Structure of collagen fibrils. Collagen molecules twist together to form the tropocollagen molecule. The tropocollagen molecules are held together by covalent bonding and self-assemble to form a fibrous, periodic array consisting of a gap region (~ 40 nm) and an overlap region (~ 27 nm) between the staggered arrays. These staggered arrays form the collagen fibril, 10-200 nm in diameter. (b) Transmission electron microscopy (TEM) image of collagen, showing the characteristic banded pattern arising from the gap and overlap regions. Courtesy of P.-Y. Chen.

Mineral structure (hydroxyapatite)

Bone minerals consist of impure hydroxyapatite crystals, $Ca_{10}(PO4)_6(OH)_2$, with 4–6% of the phosphate groups replaced by carbonate groups, which provides stiffness and strength, while the biopolymer protein phase is composed of type-I collagen, which provides ductility of the bone and its toughness or ability to absorb energy before fracture [1.5]. Bone minerals consist of non-stoichiometric hydroxyapatite (HA) crystals (chemical formula, $Ca_5(PO_4)_3OH$, with 4-6% of the phosphate groups replaced by carbonate groups. The bone crystals are in the form of platelets approximately 40-60 nm in length and 20-30 nm in width. The thickness of bone crystals measured from TEM ([1.28] – [1.32]) and small angle X-ray scattering (SAXS) ([1.33], [1.34]) varies from 1.5 nm for mineralized tendon to 4 nm for some mature bones. Recent atomic force microscopy (AFM) studies found that the bone crystals are longer than those observed by TEM, with widths and lengths ranging from 30 to 200 nm ([1.35], [1.36]). This discrepancy may be due to breakage of the fragile crystallites during TEM sample preparation. Fig. 1.4 shows TEM and scanning electron microscopy (SEM) images of bone crystals. In the TEM micrographs, the plate-like structure of the minerals is observed that have dimensions of ~ 20-50 nm in width, and ~ 4 nm in thickness. The SEM image of mineralized collagen fibrils is shown with the bone crystals forming small aggregates of ~ 70 nm. The mineralized collagen fibril is the basic unit of all bones.

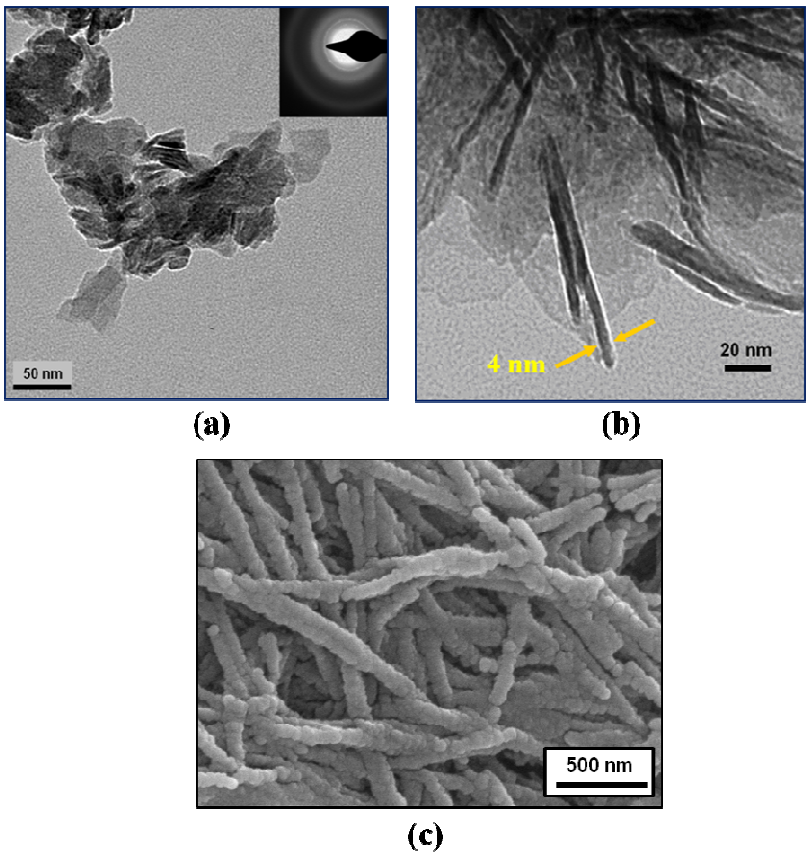


**Figure 1.4** (a), (b) TEM micrographs of the mineral phase (hydroxyapatite) in cortical bovine femur bone. The platelets are ~ 20 x 50 nm in width and ~ 4 nm in thickness. Modified from [1.124]; (c) SEM micrograph of mineralized collagen fibers from bovine femur cortical bone. The globules are aggregates of hydroxyapatite.

Figure 1.5 shows the mineralization process in bone. It is generally believed that crystals initially form within the gap region of the collagen fibrils, further proceed into the overlap region, and subsequently grow into the extrafibrillar space [1.37]. Consequently, minerals are found both within and outside the collagen fibrils, but the exact amount in each location is still a matter of contention ([1.38] - [1.42]). Landis and co-workers proposed a model for early stage mineralization based on the 3D TEM tomography ([1.43] – [1.45]). The staggered arrangement of collagen fibrils forms

extensive channels laterally through the arrays. Mineral crystals developed preferentially in length along the collagen long axes and in width within the spaces generated by the channel. Crystals are fused together and grow in length beyond gap and overlap regions, ranging 40-170 nm and in width to ~40 nm, well beyond that of individual collagen gap regions. However, the growth in thickness is limited to 4-6 nm. Ultimately, fused mineral crystals form thin parallel sheets throughout the assemblage of collagen fibrils. In the recent study on mineral crystals in embryonic chick bones, Landis *et al.* [1.46] have suggested that the mineral sheets may fuse to form a continuous mineral organization.

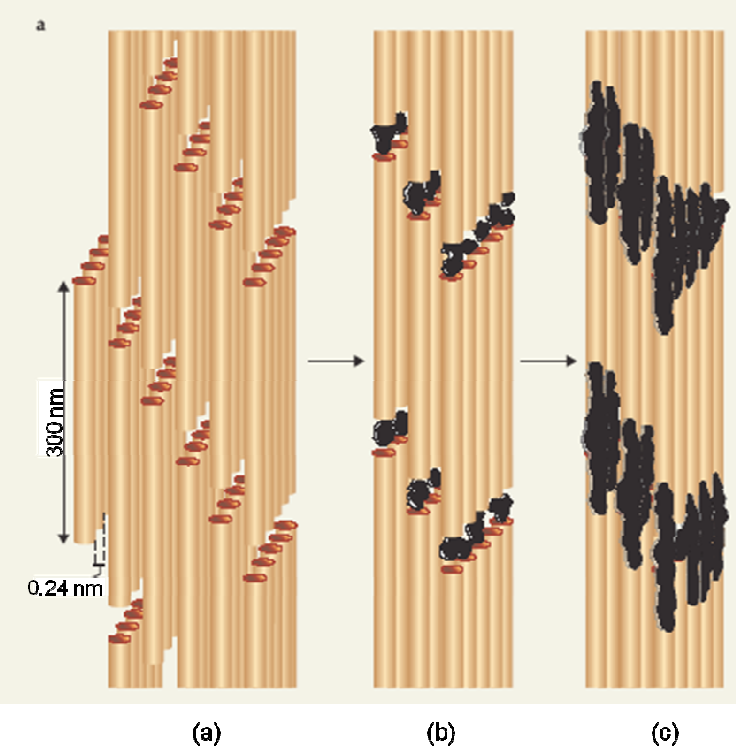


**Figure 1.5** Regions where hydroxyapatite is located in the mineralized collagen fibril, either intramolecular or extramolecular: (a) assembly of tropocollagen to form fibrils, (b) nucleation of intermolecular minerals in the gap region between the tropocollagen molecules, (c) extramolecular minerals nucleated outside of the tropocollagen. Taken from [1.47].

Water

Water is another significant phase in bone, which plays an important role in the bio-mineralization process and enhancing bone mechanical properties. Water is located at various hierarchical levels: within the porous regions, such as vascular channels, between the lamellae, inside the fibrils (gaps) and surrounding the triple helix tropocollagen molecules ([1.48] - [1.50]). Water also plays an important structural role in collagen fibrils. Hydration of the collagen fibril separates adjacent collagen molecules in the lateral plane by a water layer 0.7 nm thick, while not affecting the fibril's axial structure. This lateral fluidity of the fibril allows molecules up to the size of a 10 unit cell apatite crystal to diffuse within the fibril ([1.51], [1.52]). During mineralization, the water within the fibril is replaced by mineral [1.53], causing a loss of the freedom of collagen molecules to move. Water therefore helps to define the structural characteristics and physical properties of collagen.

#### *1.2.1.2 Hierarchical structure*

The hierarchical structure of bone is shown in Fig. 1.6. Level I represent the molecular arrangement of the collagen molecules – three α-helix chains twist to form the tropocollagen molecule. Level II (2-300 nm) has two basic units: the tropocollagen molecule and the mineral, hydroxyapatite. In Level III (0.1-5 μm), the tropocollagen molecules (300 nm length, 1.5 nm diameter) assemble to form collagen fibrils of ~ 100 nm in diameter. Hydroxyapatite (5 nm thickness, lateral dimension ~50-100 nm), is nucleated within and outside of the fibrils, which are held together by non-collagenous proteins [1.54]. In Level IV (10-50 μm), the fibrils further assemble into oriented arrays

of sheet-like structures (lamellae). In these lamellar structures reside lacunae (10-20 µm), which are connected by canaliculi channels (100 nm diameter). Bone cells (osteocytes) reside in lacunae. Level V represents cortical bone consisting of osteons with a central vascular channel and spongy trabecular bone. Level VI is whole bone (a femur).

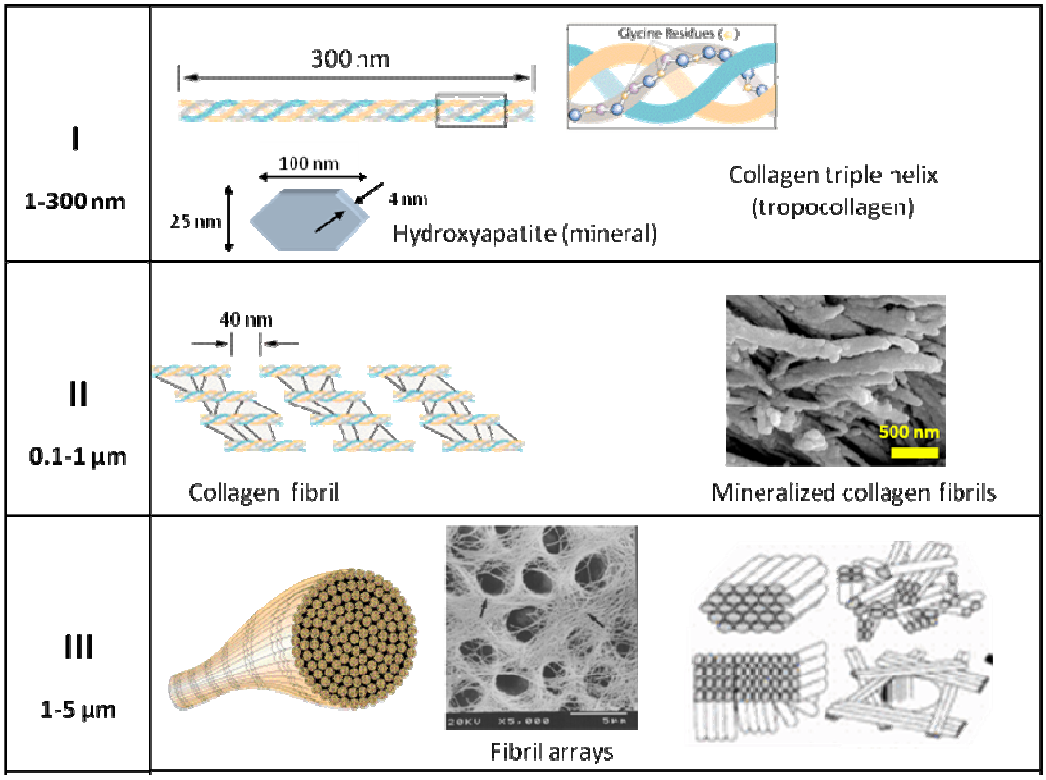


**Figure 1.6** Hierarchical structure of bone. Level I: The basic elements of bone, tropocollagen (300 x 1.5 nm) – a triple helix of α-collagen molecules and carbonated hydroxyapatite (platelets of 100 x 25 x 4 nm). Level II: Tropocollagen assembles to form collagen fibrils and combine with hydroxyapatite, which is dispersed between (in the gap regions) and around the collagen, forming mineralized collagen fibrils. Level III: The fibrils are orientated into several structures, depending on the location in the bone (parallel, circumferential, twisted). Level IV: Cortical bone is lamellar – cylindrical and parallel plate lamella is found depending on location. Level V: Light microscope level showing osteons (organized cylindrical lamellae) with a central vascular channel and small lacunae (10-20 nm) interspersed between the lamellae. Level VI: Whole bone. Modified from [1.56].

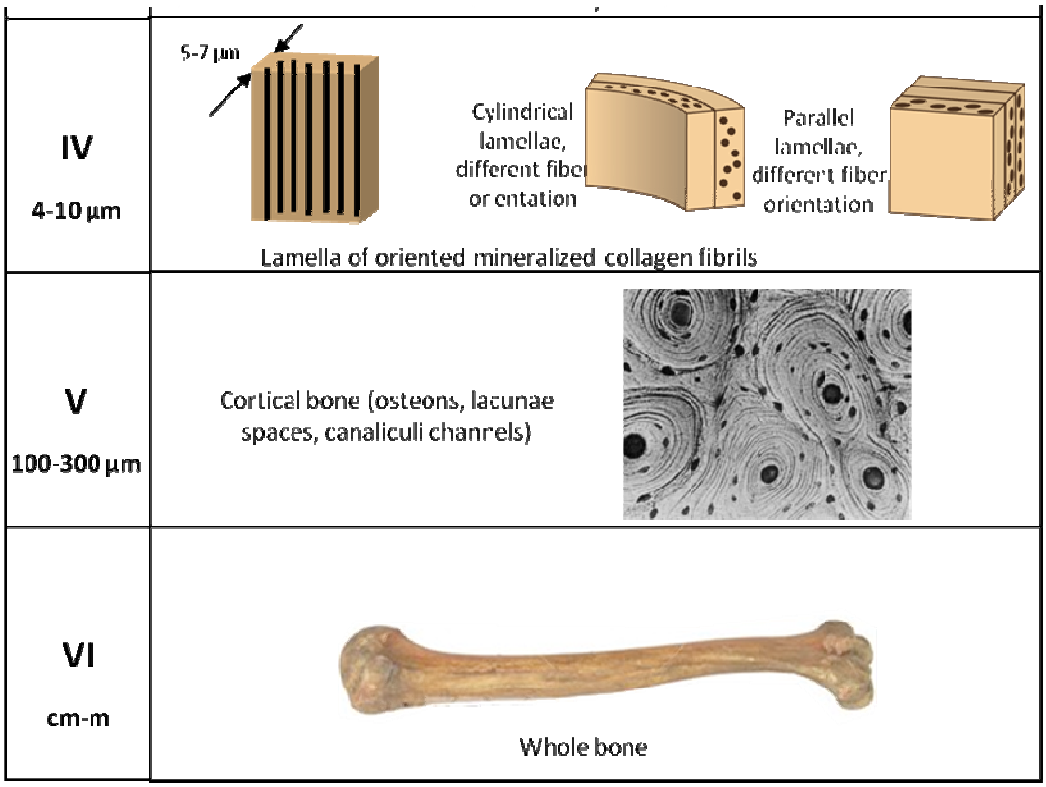


**Figure 1.6** Continued.

Figure 1.7a shows a cross-section of cortical bone, displaying more complexity due to vascular channels (Volkmann's canals) that extend perpendicularly to the main vascular channels (Haversian canals) aligned in the bone growth direction. This interconnected vascular network gives rise to oriented, tubular porosity throughout cortical bone. Additionally, bone is surrounded by a periosteal region, which is a tough, strong sheath that protects the interior bone.

Importance of porosity

The porosity in bone appears at varying hierarchical levels [1.55], as shown in Fig. 1.7b. At the molecular level, there exists space between adjacent collagen

molecules, where water and NCPs can be found. There are also spaces and gaps between mineralized collagen fibrils, in the order of 10 nm. The canaliculi, which are small tubules ~100 nm in diameter, interconnect lacunae spaces in different lamellae and transport nutrients and signals. The elliptically shaped lacunae spaces, where osteocytes reside, are 10-20 µm. The vascular channels (Haversian and Volkmann's canals) in the osteons, which are filled with blood, are 20-50 µm in diameter. Resorption cavities, ranging from 50 µm to 300 µm, can be observed during bone remodeling. Finally, the trabecular bone has pores that range from several hundred micrometers to several millimeters.

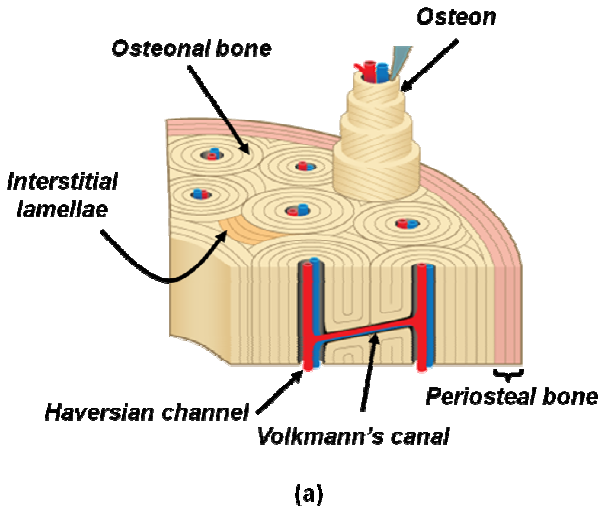


**Figure 1.7** (a) Cross-section of cortical bone, showing vascular channels parallel and perpendicular to the growth direction; (b) The hierarchical structure of porosity of cortical bone. From left to right: spaces between wet collagen molecules, spaces between mineralized collagen fibers, canaliculi and lacuna spaces, vascular channels and resorption cavities. Modified from [1.98].

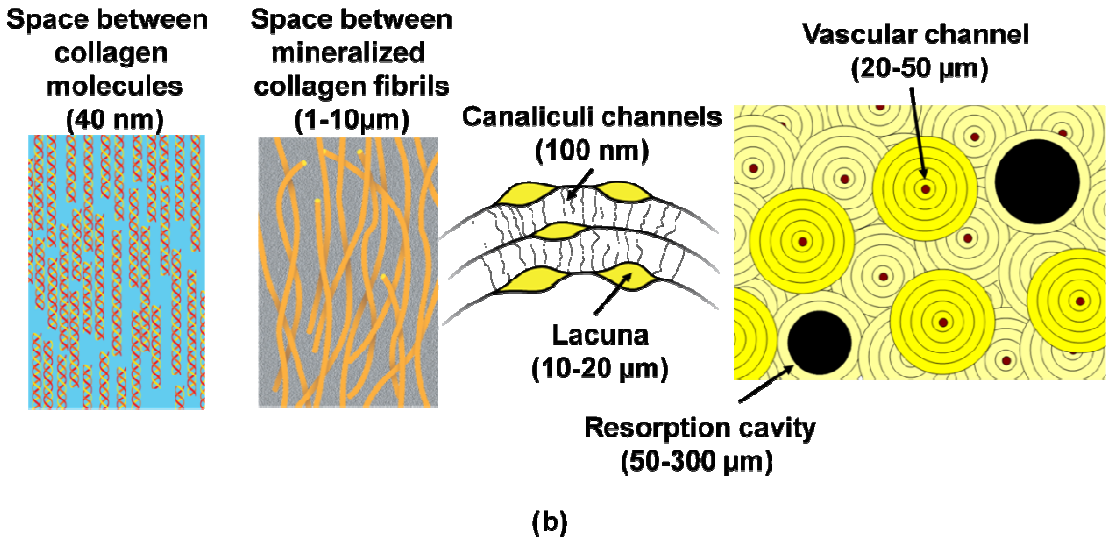


**Figure 1.7** Continued.

### 1.2.2 The elastic properties of bone

Given the complexity of the bone structure, it is not surprising that values of elastic modulus (E) reported in the literature range from 6-34 GPa. The modulus is highly dependent on the species, mineral content (Currey [1.15], [1.19], [1.20]), age (Currey [1.70], [1.76]; Kulin *et al.* [1.69]), the amount of hydration (Nalla *et al.* [1.65]), amount of porosity (Mackenzie [1.60], Carter and Hayes [1.58], Bonfield and Clark [1.59]), and anatomical location (e.g. rib vs. femur), Currey [1.19], [1.20].

#### *1.2.2.1 Effect of mineral content*

The correlation between mechanical properties and the DOM from a wide variety of animal mineralized tissues has been investigated by Currey [1.15], [1.19], [1.20]. Both the elastic modulus of bone and its toughness, measured by the area of the tensile stress-strain curve to failure, are strongly dependent on the degree of

mineralization (DOM), as evident in Fig. 1.8. In this plot, data from Currey [1.19], [1.20], taken from various mineralized tissues are plotted with data taken from McKittrick *et al.* [1.57] for some other mineralized materials. Various composite model curves are shown, demonstrating that these models do not adequately describe the elastic modulus. However, a general trend is observed with an increase in modulus with mineral content. The elastic modulus increases with mineral volume fracture in a roughly linear correlation. Antlers have a low DOM (left-hand side) with elastic modulus in the range of 7-10 GPa, while the elastic modulus for the highly mineralized whale bulla reaches 34 GPa. Interestingly, narwhal tusk cement is made of very loosely organized bone, which leads to the lower modulus (about 5.5 GPa), although it is more highly mineralized than the antlers. Human enamel has the highest DOM, and corresponding elastic modulus is about 80 GPa.

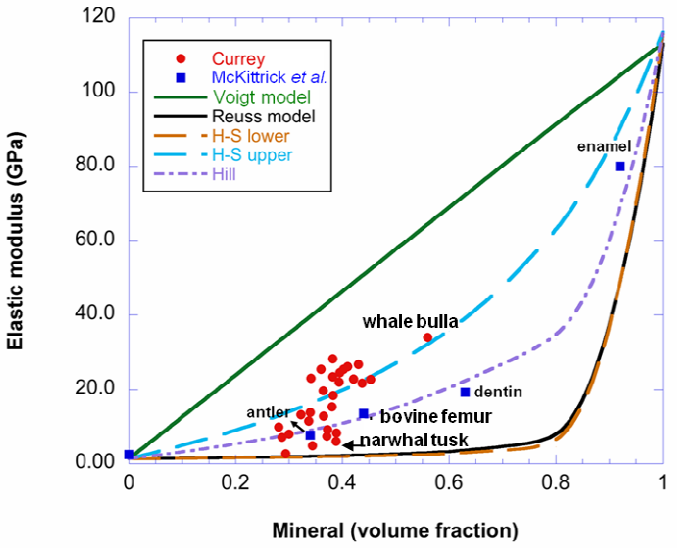


**Figure 1.8** Effect of mineral volume fraction on elastic modulus of bones from various animals (data plotted from ([1.19], [1.20], 1.57]). The Voigt, Reuss, Hashin-Shtrikman (H-S) upper and lower bounds and Hill model curves are shown.

### *1.2.2.2 Effect of porosity*

The elastic modulus of cortical bone is known to be reduced by porosity. Carter and Hayes [1.58] have proposed an expression for the elastic modulus that is proportional to the third power of the density,

$$E \alpha (1 - p)^3, \tag{1.1}$$

where $E$ is a measured elastic modulus and $p$ is volume fraction of porosity.

Bonfield and Clark [1.59] have expressed a modified Mackenzie [1.60] equation to account for porosity as:

$$E = E_o (1 - 1.9\, p + 0.9\, p^2), \tag{1.2}$$

where $E_o$ is the elastic modulus of compact bone containing no porosity. This model can be applied for estimating the under-evaluated elastic modulus due to porosity. For a compact bone containing 5% porosity, the absolute modulus $E_o$ is 10% higher than the measured modulus, $E$; for a compact bone containing 10% porosity, $E_o$ is ~ 22% higher than $E$. However, this model fails to explain the anisotropy of bone.

For trabecular bone, elastic modulus is highly dependent on the amount of porosity (Gibson [1.61]) and its architecture (rods versus plates, and their connectivity). Fig. 1.9 shows the relative elastic modulus $\left(E^* / E_s\right)$ as a function of the relative density $\left(\rho^* / \rho_s\right)$. $E_s$ and $\rho_s$ are taken as 18 GPa and 1.8 gm/cm$^3$, respectively [1.62]. The relative values are the measured ones $\left(E^*, \rho^*\right)$ divided by values for a non-porous solid $\left(E_s, \rho_s\right)$. The modulus fits the relationship:

$$\frac{E^*}{E_s} = C\left(\frac{\rho^*}{\rho_s}\right)^2, \tag{1.3}$$

for trabecular bone taken from the femur, tibia and vertebrae. Parameter C depends on the microarchitecture of trabecular bone, it equals to one for the ideal case of uniform isotropic cellular structure. This relationship demonstrates that the elastic modulus of trabecular bone is strongly dependent on density.

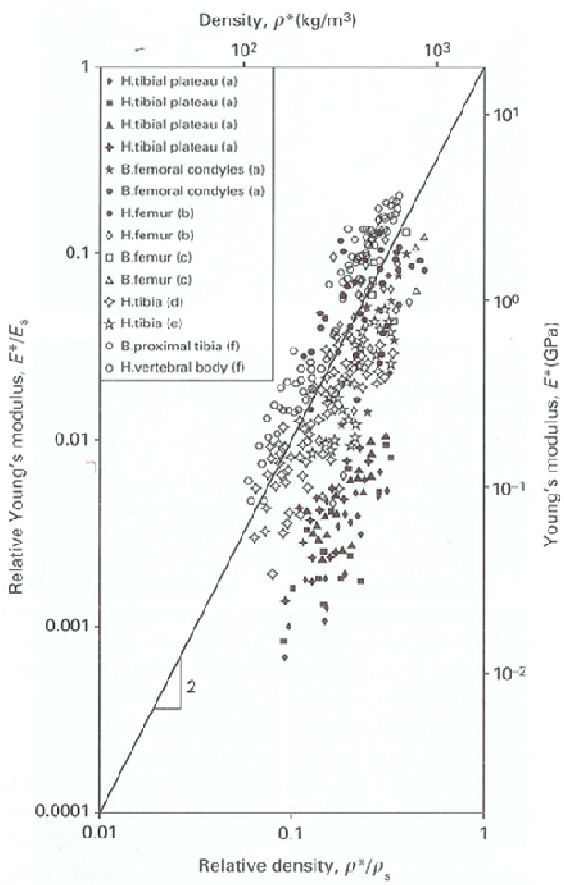


**Figure 1.9** Relative elastic modulus as a function of relative density for trabecular bone. Taken from [1.62].

### *1.2.2.3 Effect of orientation and anisotropy*

The structure of bone is highly anisotropic: apatite crystals, collagen fibers, and osteons are arranged in the longitudinal axis of lone bones. Therefore, bone exhibits anisotropic mechanical properties. The longitudinal elastic modulus and strength are higher than the transverse ones. The ratio of longitudinal/transverse elastic modulus varies from 1.6 to 2.4 (Bonfield and Clark [1.59]; Bonfield and Grynpas [1.23]; Currey [1.6]). The elastic modulus of human compact bone in the longitudinal direction is reported in the range of 16-23 GPa; whereas in the transverse direction is about 6-13 GPa (Rho *et al.* [1.63]). Bonfield and Grynpas [1.23] studied mechanical anisotropy of cortical bone at varying angles to the bone growth direction (longitudinal direction corresponded to 0°, transverse direction corresponded to 90°) by ultrasonic measurements. They found that elastic modulus gradually decreased with increasing angle (from 0° to 90°), and these was a plateau between 20° to 70°.

Figure 1.10 provides the tensile and compressive stress-strain curves for cortical bone in longitudinal and transverse directions [1.64]. The anisotropy is clearly visible. It also shows that bone is considerable stronger when loaded in compression than in tension. This plateau is produced, at the structural level, by the formation of shear zones, which are the result of localized buckling of the fibrils. Plastic microbuckling is a well-known phenomenon when composites are loaded along the fiber axis and was first described by Evans and Charles [1.115]. The angle of these buckling regions with the compression axis varies between 30° and 40°.

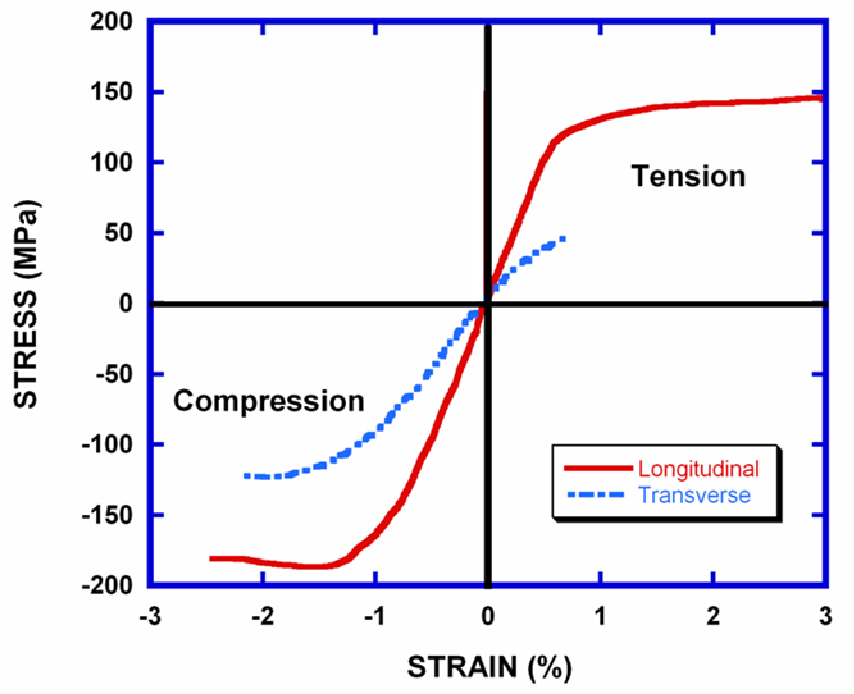


**Figure 1.10** Tensile and compressive stress-strain curves for cortical bone in longitudinal and transverse directions. Adapted from [1.64].

#### *1.2.2.4 Effect of hydration*

The amount of water present in bone is one of the most important determinants of its mechanical behavior. Bone is typically full of liquid, namely saline and blood, and the water in these mediums forms hydrogen bonds within the collagen structure. Bone has lower elastic modulus and strength yet higher strain to failure and toughness in hydrated state than in dry state. Bone can be re-hydrated with minimal effects on mechanical properties after drying [1.9]. Similar results were also observed for dentin, another collagen-mineral composite found in teeth [1.65]. Poorly mineralized bones, such as antler and tortoise femur, have higher water contents, whereas highly mineralized bones (whale bulla) have lower water contents. This relates to the

mineralization of the collagen fibrils, as minerals displace water within and around the gaps.

#### *1.2.2.5 Effect of strain rate*

The mechanical behavior of bone under dynamic loading has been of a great interest in the medical and engineering fields. Most bone fractures occur under dynamic loading, from auto accidents, sporting injuries, or other catastrophic events. Due to the large amount of collagen content (30-45 vol. %), bone is a highly viscoelastic material and its mechanical behavior is strain-rate sensitive. However, our understanding of the dynamic behavior of bone is far from complete. Most mechanical properties of bone found in literature were measured under quasi-static loading condition with a limited research performed dynamically. It is important to understand the mechanical properties of bone under dynamic loading.

One of the pioneers in the field of dynamic behavior of bone was McElhaney [1.66] who tested hydrated human compact bone in compression at strain rates varying from $10^{-3}$ to 1500 $sec^{-1}$. An air-gun type machine was used, capable of performing strain rates up to 4000 $sec^{-1}$. The compressive stress-strain curves showed that both elastic modulus and ultimate compressive stress increased with increasing strain rates while the strain to failure decreased (Fig. 1.11). Tennyson *et al.* [1.67] tested the dynamic response of bovine femur using the split-pressure Hopkinson bar (SPHB) at stain rates in the range of 10 - 450 $sec^{-1}$, in both hydrated and dehydrated conditions and found similar trends for both hydration states. Lewis and Goldsmith [1.68] measured the dynamic mechanical properties of bovine bone in compression, tension, and torsion by

using a biaxial split Hopkinson pressure bar combined with strain gages. The results showed further evidence of the viscoelastic behavior if bone. Kulin *et al*. [1.69] investigated the dynamic response of compact equine bone for the strain rates between $10^{-3}$ $sec^{-1}$ and $10^{3}$ $sec^{-1}$. Their results corroborated with the previous results of McElhaney [1.66] showing the increasing both elastic modulus and compressive strength with the strain rate.

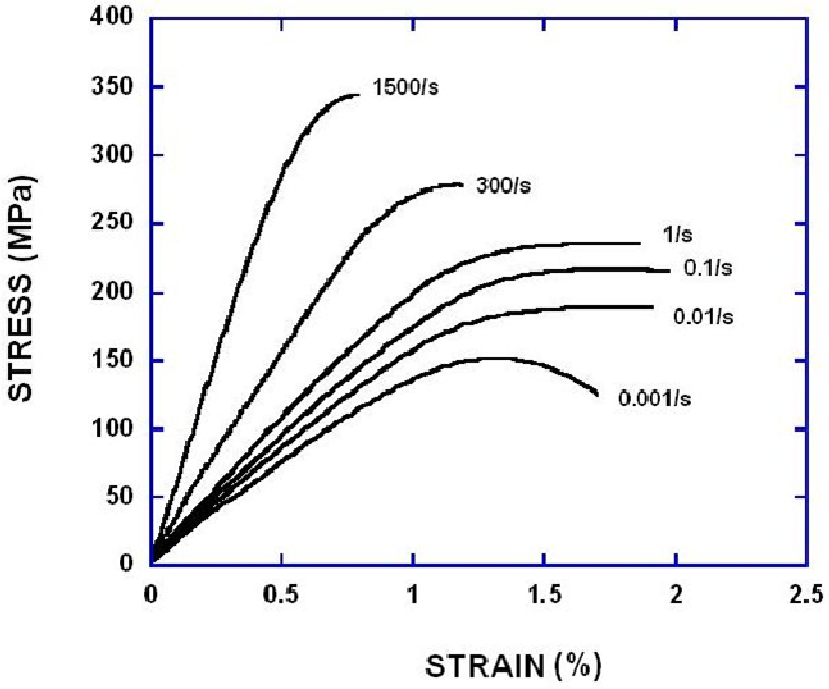


**Figure 1.11** Compressive stress-strain curves for human cortical bone at varying strain rates. Taken from [1.66].

### *1.2.2.6 Age effect*

The bone mineral density (BMD) changes significantly with age and the elastic modulus should change accordingly. Currey [1.70] showed that bone becomes more

mineralized with increasing age to a certain point, therefore getting more stiff and strong. For example, the elastic modulus of a human femur of 35-year old bone was twice that of 3-year old. Fig. 1.12a shows the BMD from the lumbar spine as a function of age for young girls [1.71], demonstrating that mineralization occurs steadily from 7 to 18 years, at which point the BMD levels out. In Fig. 1.12b, BMD is plotted for women from ages 20-80 [1.72], clearly showing the mineral fraction in bone is monotonically decreasing. This significant decrease is especially troublesome in middle age and older populations, where osteoporotic fracture can occur. Osteoporosis is a common disease that causes a lower bone mass density and mineral deficiency, causing bone to become less mineralized and more brittle (e.g., Bouxsein [1.73]; Lubarda *et al.* [1.74]).

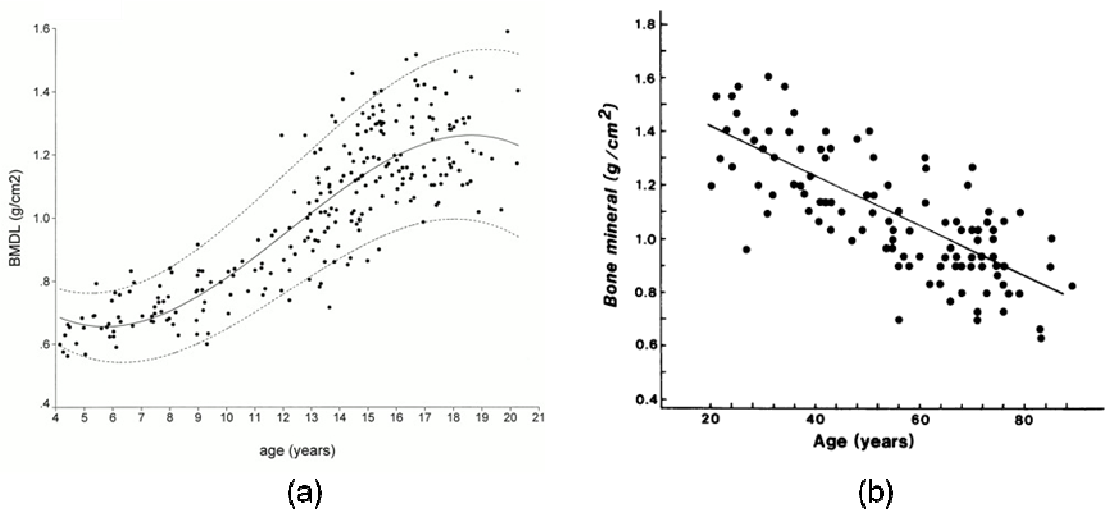


**Figure 1.12** Bone mineral density (BMD) from the lumbar spine as a function of age for: (a) young girls [1.71], and (b) older women [1.72].

It has been shown that several other factors, like degradation of collagen with age (Danielsen *et al.,* [1.75]), or larger density of un-remodeled microcracks (Currey *et al.*, [76]), could have an effect on the age-related mechanical properties. Several interesting results about the age related changes of bone microstructure and its influence on bone toughening mechanisms were reported by Nalla *et al*. [1.114], and Ritchie *et al.* [1.77]. They attributed the fracture receptivity of aged bones to an increasing density of Haversian systems and changes in collagen cross-linking at the nanoscale level.

A summary of the important parameters that affect the measurement of the elastic modulus of bone is given in Table 1.1, demonstrating that mechanical tests of bone are not as straightforward as testing of an isotropic solid.

### 1.2.3 Experimental methods to measure elastic modulus

There are many methods to investigate the mechanical properties of bone. Extrinsic parameters (e.g. fracture stress and strain) depend on the actual sample size and testing method, thus being different for the different sized samples. Intrinsic parameters, such as compressive stress and strain, are calculated based on the actual sample dimensions and are usually similar for the different sized samples.

Tests can be classified as non-destructive and destructive tests. The two main non-destructive methods are based on ultrasound and nanoindentation techniques. Compression, bending, torsion, and tension are the most widely used destructive tests.

**Table 1.1** Summary of the important parameters that affect the measurement of the elastic modulus of bone.

| **Parameter** | **Explanation** | **Effect** |
|---|---|---|
| Bone type | Trabecular, cortical, woven, intrafibular | Widely varying values (between 8.4 GPa for dolphin rib and 34.1 GPa for whale bulla (Currey, [1.20]). |
| Location | Femur, skull, tibia, rib, radius, ulna, antler, bulla. | Widely varying values depending on biological adaptation of the particular bone (Currey [1.19], [1.20]). |
| Taxa | Human, bovine, reptile, bird. | Proportionally higher for larger animals (Currey [1.19]; Erickson *et al*. [1.78]). |
| Hydration | Wet collagen fibers contribute to the whole bone mechanical response. | Hydration decreases elastic modulus. |
| Age | (a) Bone mineralization is progressively increasing until the full maturity, and after that starting to decrease.<br><br>(b) Changes in collagen cross-linking at nanoscale and increasing the density of secondary osteons with age. | (a) Elastic modulus progressively increased until full maturity (Currey *et al*. [1.76]), and started to decrease because of bone demineralization process.<br><br>(b) Fracture receptivity is increasing with age (Ritchie *et al*. [1.77]; Nalla *et al*. [1.114]). |
| Strain rate | Elastic modulus is different for quasi-static and dymnamic tests | Increasing strain rate increases elastic modulus (Zioupos *et al.* [1.79]; Hansen *et al.* [1.80]; Kulin *et al*. [1.69]). |
| Location along the same bone | Elastic modulus is slightly different for femur neck, femur midshaft, and femur head. | Different for different location along the same bone, depending on bone biological adaptation (Thurner [1.81]). |

### *1.2.3.1 Basic measurements*

One of the most important factors that should be considered before doing any mechanical testing is the specimen storage and preparation technique. Hydration plays an important role for all biological materials. Bone can be stored for periods of up to four weeks at ≤ 0˚C, although repeated freezing and thawing should be avoided (Sedlin and Hirsch [1.82]). Bone can be dried and rehydrated without significantly affecting its elastic properties; however, the toughness could be altered (Currey [1.83]). For all mechanical tests, bone needs to be tested in the hydrated condition. This involves soaking the specimens in an aqueous solution, such as Hank's buffered saline solution, for a period of several hours or overnight, depending on the size of the sample. Measurements on dry samples do not adequately reflect the nature of bone, since in the body bone is filled with fluid.

Before testing a bone, several basic experiments need to be performed: drying for water content and ashing for mineral content. Weighing the hydrated sample under ambient condition, then drying in an oven (~ 105 ˚C) to remove the water and subsequent re-weighing will give the weight fraction of water. Ashing involves baking the bone at higher temperature (~ 550 ˚C) to remove all of the organic material. The weight before and after ashing gives the weight fraction of the mineral phase. These are two key measurements that must be reported for experimental procedures.

Another basic measurement is density. Because the elastic modulus is extremely sensitive to the amount of porosity, density needs to be quantified. The density of collagen is 1.35 gm/cm$^3$ [1.122] and the density of hydroxyapatite is 3.15 gm/cm$^3$ [1.123], and with these numbers, the volume fraction of proteins, mineral and

water can be determined. Although the NCPs have a slightly different molecular weight than collagen, the volume fraction is low and estimates based on collagen only are adequate.

#### *1.2.3.2 Non-destructive methods*

Ultrasound

Ultrasound measurements involve the evaluation of the elastic modulus, which is proportional to the sample density ($\rho$) and the velocity of sound ($v$):

$$E = \rho v^2 \tag{1.4}$$

According to Cowin [1.9] this equation can be used if ultrasonic wavelength is greater than the cross-sectional dimension of the sample and characteristic dimension of the structure (for example, the size of the osteon), in order for the wave to propagate through the specimen. Another difficulty is related to the anisotropic and non-uniform bone properties. The density of bone samples varies depending on the anatomical position; therefore, estimation of the elastic modulus by ultrasound technique usually provides very scattered results for different bone locations. However, a great advantage of ultrasound technique is that it does not require expensive equipment (Turner and Burr [1.84]), and it does not destroy the specimen. The equipment usually involves ultrasonic pulse generator, oscilloscope, and wave transducers. An additional significant benefit of the ultrasound technique is that the anisotropic elastic properties can be measured at the same sample by propagating the waves along the different directions.

Nanoindentation

Nanoindentation is a technique in which a known load (in the 0.25 mN – 5 N range) from a pointed diamond indenter (tip radius ~ 100 nm) is applied onto the surface of the material. The hardness is related to the load ($P$) and indentation depth ($h$), but sensitive positioning sensors allow for measurement of the loading and unloading curve. The 'stiffness' ($S$) is given as the slope of the unloading curve ($dP/dh$), as shown in Fig. 1.13a. The reduced modulus, $E_r$, is calculated from:

$$E_r = \frac{1}{\beta}\frac{\sqrt{\pi}}{2}\frac{S}{\sqrt{A_p(h_c)}}, \tag{1.5}$$

where $\beta$ is a geometrical parameter that depends on tip geometry, and $A_p(h_c)$ is the projected area of indentation at contact depth $h_c$. The elastic modulus of the sample, $E_s$, is related to $E_r$ and the elastic constants of the diamond indenter ($E_i$ and $\nu_i$) by:

$$\frac{1}{E_r} = \frac{\left(1-\nu_s^2\right)}{E_s} + \frac{\left(1-\nu_i^2\right)}{E_i} \tag{1.6}$$

The indices $s$ and $i$ correspond to the sample and the indenter, respectively. The modulus $E_s$ can be evaluated from Eq. (1.6) after the reduced modulus calculated from Eq. (1.5). Despite the name, the indented boundaries are in the range of 1-10 μm. The osteonal and interstitial lamellar regions of bone can be probed separately.

Figure 1.13b shows the nanoindentation curves for cortical and trabecular bone. The elastic modulus is shown to be lower for trabecular than cortical bone samples, due to the high degree of porosity of the trabecular samples. In the figure, the red lines show the portion of the loading/unloading curve that is used for estimating $S$.

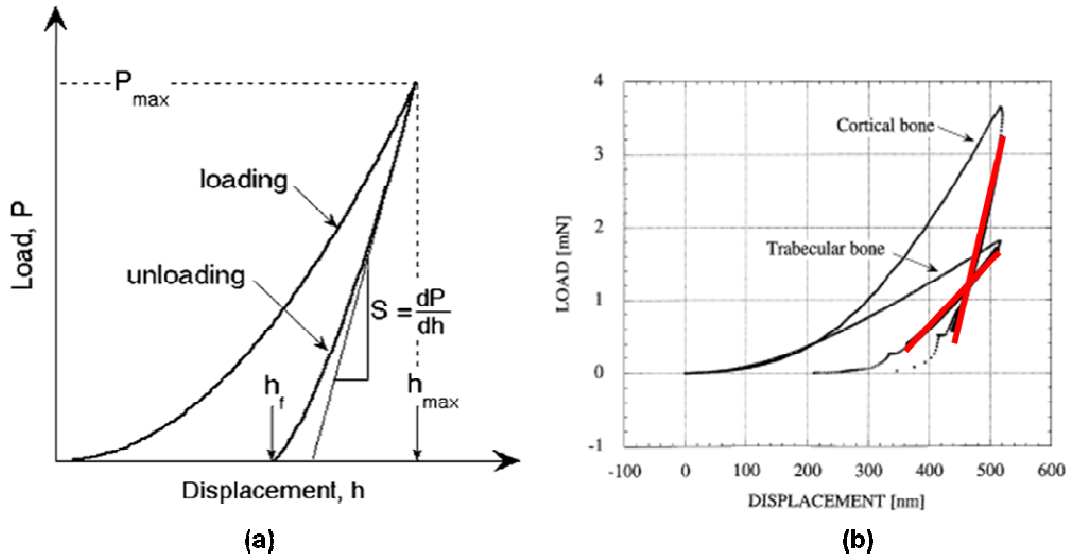


**Figure 1.13** (a) Illustration of important measured nanoindentation parameters: maximum load ($P_{max}$), maximum displacement ($h_{max}$), and the elastic unloading stiffness (S). Taken from [1.85]. (b) Typical nanoindentation curves for cortical and trabecular bone samples. Elastic modulus is estimated from the slope (red lines) of the liner parts of unloading portions of the curves. Taken from [1.86].

The elastic properties of microstructural components in human femur osteonal bone using nanoindentation have been investigated by several groups. Rho *et al.* [1.87] showed that elastic modulus of interstitial lamellae (~ 26 GPa) was higher than that of the osteons (~ 22 GPa) in the longitudinal direction for human femur cortical bone. Zysset *et al.* [1.86] investigated properties of cortical and trabecular human femoral bone at several locations. They pointed out that elastic modulus was higher for interstitial lamellae than for osteonal part for both diaphyseal and neck regions of femoral bone. The interstitial lamellae show a higher elastic modulus than the osteonal region due to the higher mineral content. This is clearly shown in the BSE SEM image in Fig.1.14, where the interstitial lamellae are brighter, indicating a higher calcium (mineral) content.

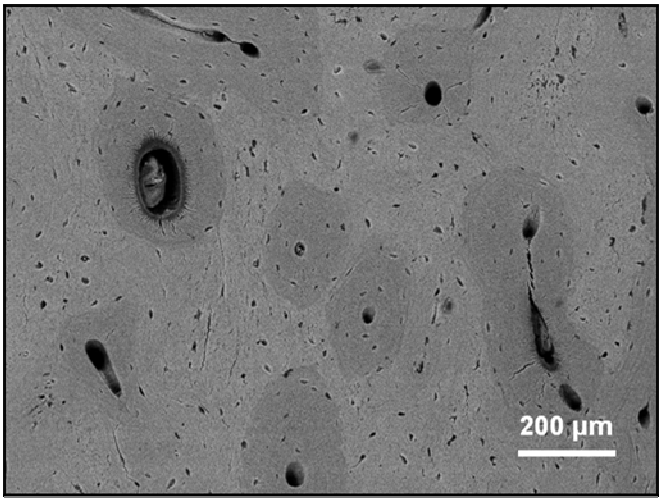


**Figure 1.14** Backscattered electron (BSE) images showing cross-sectional microstructure of cortical bovine femur: secondary osteons surrounded by interstitial bone. Taken from [1.88].

A comprehensive review of bone properties measured by nanoindentation technique was outlined by Thurner [1.81]. He summarized the results from the nanoindentation experiments of different human and animal bones, including tibia, femur, and vertebra. It was shown that although nanoindentation is a powerful method for the evaluation of elastic properties, hardness, viscosity and plastic deformation of bone, this procedure is very sensitive to a sample preparation technique and testing conditions. For example, according to Thurner [1.81], elastic modulus of human femur middle portion varied between 17 and 27 GPa, depending on sample hydration conditions, maximum applied force, tip type, and anatomical direction. Thus, it is crucial to report the exact experimental methods used to prepare bone for nanoindentation experiments.

The AFM can also be used as a nanoindenter ([1.89], [1.90]). The tip is made from silicon and is much finer and smaller than the diamond tips used for standard

nanoindentation methods (tip size ~ 15 nm). However the maximum load that can be applied is much smaller. This method has been used to determine the elastic modulus of cortical bone from various regions in one sample in which values from 2-30 GPa were measured [1.90]. This wide range was attributed to nanoscale irregularities, which were also proposed as the origin of bone toughness.

Microindentation

An interesting application of *in-vivo* indentation has been developed by Hansma *et al.* [91], [92]. Bone material properties can be measured directly on a patient through the skin or other soft tissue. The typical bone diagnostic instrument (BDI) invented by Hansma group is shown in Fig. 1.15. It consists of a reference probe and a test probe (with radius of 2.5 μm). A test probe is inserted into a bone through the skin and other connective tissues; an indented distance is usually about several microns, measured relatively to a reference probe. The whole test takes several minutes and requires only minor local anesthetization. The BDI provides the information about bone material properties *in vivo*, and moreover is able to measure the continuing damage that results from a repeated loading. BDI works in two different modes: force controlled and distance controlled. Penetration distance (corresponding to a fixed loading force), or force (corresponding to a fixed penetration distance) were measured for the patients with different expected fracture properties (based on the age). It was found that older bones were less capable of accumulating damage in form of microcracks and are associated with increasing risk of fracture.

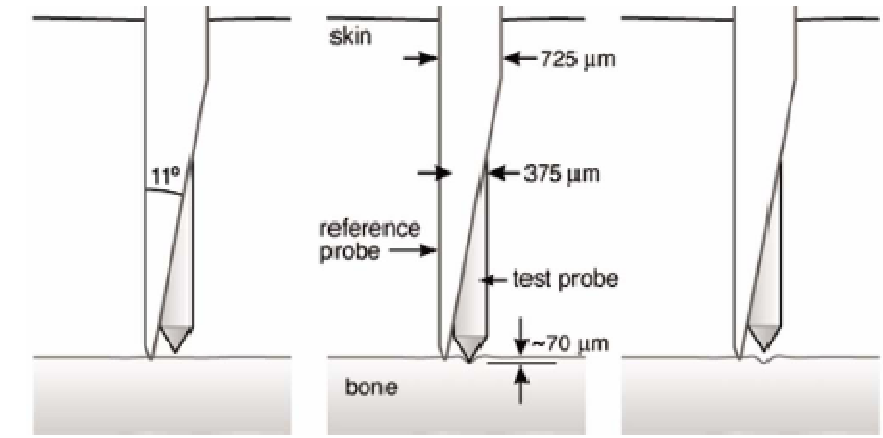


**Figure 1.15** The probe assembly for bone diagnostic instrument. It consists of the reference probe and the test probe. Taken from Hansma *et al.* [1.91].

Electronic speckle pattern interferometry (ESPI)

Zhang *et al.* [1.93] and Barak *et al*. [1.94] described an interesting method to evaluate the elastic properties of bone: electronic speckle pattern interferometry (ESPI). ESPI is an optical method that produces strain maps of the whole sample loaded in bending, as shown in Fig. 1.16. According to these authors this method is less sensitive to sample surface quality and provide excellent information about the bone elastic modulus. Barak *et al.* [1.94] used ESPI to precisely determine the tensile and compressive strains through the thickness of the cortical bone specimens tested in four-point bending. This information was used for the evaluation of the tensile and compressive elastic constants. It was found that tensile elastic modulus of mature equine osteonal bone is 6% higher than compressive elastic modulus. They mainly attributed their result to the structural inhomogeneities.

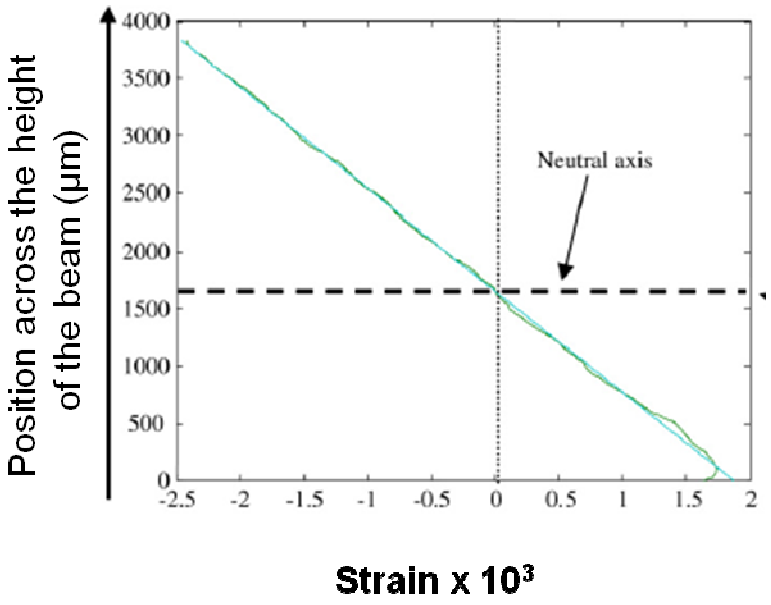


**Figure 1.16** Strain distribution across the height of the beam determined by electronic speckle pattern interferometry (ESPI) for four-point bending. Taken from Barak *et al.* [1.94].

#### *1.2.3.3 Destructive methods*

Turner and Burr [1.84] and Beaupied *et al.* [1.95] summarized the main destructive mechanical tests. They pointed out that in each case the mechanical test should be selected based on the bone nature (cortical or trabecular), its geometric parameters, and the loads that bone experiences *in vivo,* in order to minimize the errors in the determination of the mechanical properties.

Flexure

Flexure tests are widely used due to the ease of sample preparation. For three-point bending tests, the stress distribution is non-uniform across the thickness and along

the length of the bone sample (Fig. 1.17a). The elastic modulus $\left(E_{(3)}\right)$ can be extracted from this test as:

$$E_{(3)} = \frac{FL^3}{4\delta_{(3)} bh^3}, \tag{1.7}$$

where $F$ is the applied load, $L$ is the span between bending fixtures, $b$ is the sample width, $h$ is the sample height, and $\delta_{(3)}$ is the maximum deflection at the midpoint of the sample.

To avoid the non-uniform bending moment, several groups (Keller *et al.* [1.96]; Draper and Goodship [1.97]) employed a four-point bending test that is characterized by a constant bending moment between the applied loads (Fig. 1.17b). The elastic modulus $\left(E_{(4)}\right)$ is given by:

$$E_{(4)} = \frac{FL^3}{4\delta_{(4)} bh^3} \frac{a}{L}\left[3 - \left(\frac{2a}{L}\right)^2\right], \tag{1.8}$$

where $a$ is the distance between the fixture and the applied load. The elastic modulus obtained from the four-point bending test $E_{(4)}$ can be related to the elastic modulus obtained from the three-point bending test $E_{(3)}$ by:

$$\begin{aligned} E_{(4)} &= \kappa_v E_{(3)} \frac{\delta_{(3)}}{\delta_{(4)}} \\ \kappa_v &= \frac{a}{L}\left[3 - \left(\frac{2a}{L}\right)^2\right] \end{aligned} \tag{1.9}$$

Clearly, if $a = L/2$, the geometric factor $\kappa_v = 1$, because in this configuration the four-point bending test reduces to the three-point bending test, so that $\delta_{(4)} = \delta_{(3)}$.

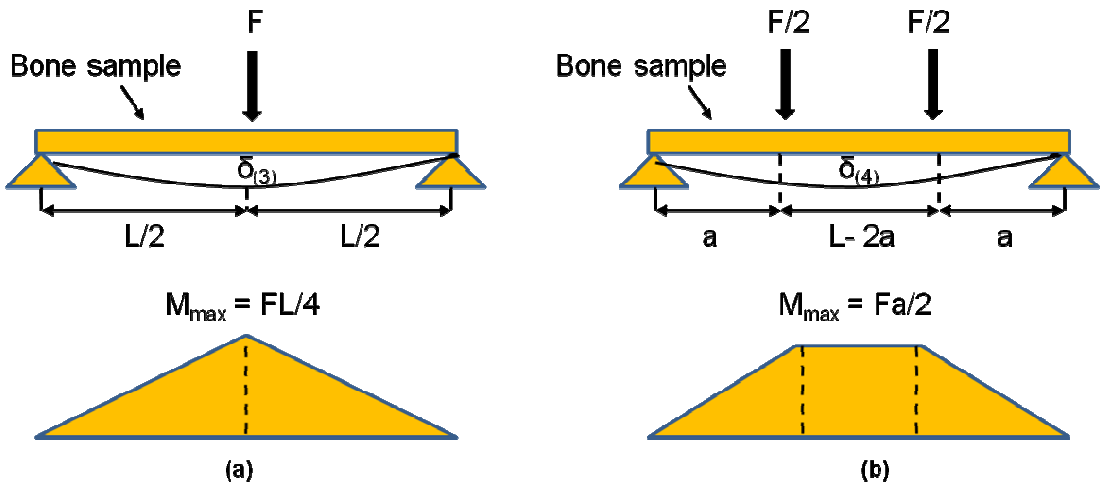


**Figure 1.17** The bending moment distribution for: (a) three-point bending, and (b) four-point bending tests.

Tension and compression tests

Bone is typically loaded in compression; however, bone is most likely to fracture by shear, in which failure is initiated by the tensile stresses. Thus, the elastic and plastic response of bone under a wide variety of loading conditions is of interest. Mechanical properties obtained from the tension and compression experiments are expected to be similar. Recently, however, Barack *et al.* [1.94] investigated the secondary osteonal equine bone properties obtained by ESPI and four-point bending tests, and found that the tensile elastic modulus was ~ 6% higher than compressive one. They attributed their result to the structural inhomogeneities (due to possible differences in mineralization and porosity concentration) of bone samples. On the other hand, these

results should be viewed by taking into account the size effect, because the structural hierarchy exists at all length scales, so that smaller samples are more sensitive to the presence of inhomogenieties.

The elastic modulus strongly depends on the bone anatomy (Currey [1.20], [1.70]). A comprehensive review of mechanical properties of femur bone from seven main vertebrate groups (including birds, reptiles, and mammals) from the evolutionary point of view was given by Erickson *et al.* [1.78]. They tested the whole femur bone of 69 species by three-point bending tests from different animal groups and analyzed their results in an evolutionary context using phylogenetic character analysis. The average elastic modulus was found to be 22.2 ± 6.7 GPa for all animals tested. It was concluded that material properties of femur bone were not changed much during evolution. On the other hand, Currey [1.19], [1.20], [1.70] found a wide variety of elastic moduli for different animal specimens that increased with the mineral fraction. Animal specimens for these studies, including such rare ones as whale bulla, dolphin ulna, tortoise bones, fish scale, and penguin bones, came from the different sources and anatomical locations (femur, tibia, radius, rib, bulla), so that the results show even wider range of values of the elastic modulus (between 2.7 GPa for dolphin ulna and 34.1 GPa for whale bulla).

Table 1.2 and Table 1.3 summarize the results of recent reported measurements of the elastic modulus obtained by different experimental techniques for cortical and trabecular bovine and human femur bone. The results obtained by non-destructive methods are higher than those from destructive methods. However, it should be pointed out that nanoindentation measures the local properties of bone samples close to the sample surface (Turner *et al.* [1.99]; Zysset *et al*. [1.86]), so that these results should not

be directly compared to those that measure bulk properties. Additionally, nanoindentation is not as influenced by porosity, as are the bulk measurements.

**Table 1.2** Elastic modulus of cortical femoral bone.

| Test method | Elastic modulus, GPa | Reference | Type | Condition |
|---|---|---|---|---|
| Compression | (16.2 - 17.0)[a] | Keller [1.102] | Human | Wet |
| | 19.9 ± 1.8 | Bayraktar *et al.* [1.100] | Human | Wet |
| | 22.6 ± 1.2 | Novitskaya *et al.* [1.98] | Bovine | Wet |
| Tension | 16.6 ± 1.8 | Dong and Guo [1.101] | Human | Wet |
| | 16.7[b] | Currey [1.70] | Human | Wet |
| | 24.5[b] | Currey [1.70] | Bovine | Wet |
| Torsion | 4.7 ± 0.7 (shear modulus) | Dong and Guo [1.101] | Human | Wet |
| 4-point bending | 12.3 ± 1.7 | Keller *et al.* [1.96] | Human | Wet |
| | 19.8[b] | Draper and Goodship [1.97] | c | Wet |
| 3-point bending | 17.3 ± 1.3 | Grimal *et al.* [1.103] | Human | Wet |
| | 13.5[b] | Currey [1.104] | Bovine | Wet |
| | 18.6 ± 1.9 | Cuppone *et al.* [1.105] | Human | Wet |
| | 24.2[b] | Zioupos *et al.* [1.106] | Bovine | Wet |
| | | | Bovine | Wet |
| Ultrasound | 13.9[b] | Rho *et al.* [1.107] | Human | Wet |
| | 32.5 ± 0.5 | Hunt *et al.* [1.108] | Human | Fresh |
| | 22.1 ± 1.1 | Grimal *et al.* [1.103] | Human | Wet |
| | 20.5 ± 0.2 | Turner *et al.* [1.99] | Human | Wet |
| | 41.0 ± 3.0 | Zimmerman *et al.* [1.109] | Bovine | Dry |
| Interferometry | 19.8 ± 1.1 | Zhang *et al.* [1.93] | Bovine | Wet |
| Nanoindentation | 20.1 ± 5.4 | Zysset *et al.* [1.86] | Human | Wet |
| | 23.5 ± 0.2 | Turner *et al.* [1.99] | Human | Wet |

[a] – only range reported
[b] – only number reported
[c] – the type was not reported

On the other hand, the good agreement between the results for different destructive methods for both cortical and trabecular bones is clearly seen from Tables 1.2 and 1.3. The average elastic modulus for all destructive methods was 17.5 ± 2.9 GPa for femur cortical bone, and 1.4 ± 0.8 GPa for femur trabecular bone. For non-destructive methods these numbers were 21.8 ± 5.2 GPa for femur cortical bone and 15.7 ± 3.0 GPa for femur trabecular one. The values of elastic modulus for destructive and non-destructive methods vary significantly for trabecular bone, but differ only by 20% for cortical bone. This could be explained by the more uniform density and porosity distributions in cortical as compared with trabecular bone.

**Table 1.3** Elastic modulus of trabecular femoral bone.

| Test method | Elastic modulus, GPa | Reference | Type | Condition |
|---|---|---|---|---|
| Compression | 1.4 ± 0.3<br>0.44 ± 0.27 | Lubarda *et al.* [1.74]<br>Lotz *et al.* [1.110] | Bovine<br>Human | Dry<br>Wet |
| Tension | 2.4 ± 0.8 | Morgan *et al.* [1.111] | Human | Wet |
| Torsion | 0.29 ± 0.18 (shear modulus) | Bruyere Garnier *et al.* [1.112] | Human | Wet |
| Ultrasound<br>Ultrasound + FEA* | 1.3[b]<br>17.5 ± 1.1<br>4.5 ± 0.7 | Rho *et al.* [1.107]<br>Turner *et al.* [1.99]<br>van Lenthe *et al.* [1.113] | Human<br>Human<br>Bovine | Wet<br>Wet<br>Wet |
| Nanoindentation | 11.4 ± 5.6<br>18.1 ± 1.7 | Zysset *et al.* [1.86]<br>Turner *et al.* [1.99] | Human<br>Human | Wet<br>Fixed |

[b] – only number reported
FEA* - microfinite element analysis

Mechanical properties of bone are usually measured under the wet condition (formalin, water, saline solutions), because bone is always wet *in vivo.* As mentioned

earlier, bone has lower elastic modulus and strength but higher strain to failure and toughness in hydrated state than in dry state [1.65], [1.109]. This is due to the wetting of collagen fibers that make a contribution to the whole bone behavior. Water plasticizes the collagen matrix, filling interior pores, and therefore decreases the elastic modulus of the whole bone (see ***Section 1.2.1.3***).

Differences in the elastic modulus measured by the same techniques, and even under the same hydration conditions, can be explained by the different microstructure between osteonal and other types of cortical bone, the age of the tissue, and the position of the sample along the femur bone (i.e. neck, head, or diaphysis).

## 1.3 Importance of Bone Research: Osteoporosis, Artificial Bone, Orthopedic Implants and Bone Substitutes

Bone tissue repair accounts for approximately 500,000 surgical procedures and more than $50 billion being spent on reconstructive biomaterials per year in United States [1.116], [1.117]. There is an increasing need for bone tissue replacement implants, growing at a rate of 7-12% per year [1.118]. Loss of bone (osteoporosis) and demineralization occur as bones age and are major causes of bone fracture. Understanding the mineral/collagen interaction is important to correctly predict the mechanisms of bone fracture. The entire complete perception of the structure and mechanical properties of natural bone is vital for developing new bioinspired bone implants. There is a need of synthetic and natural bone graft substitutes to heal osteoporotic bones, to repair periodontal defects, bone removal from tumor growth and

for oral implants [1.119-1.121].When synthesizing bioinspired materials for use as a bone implant/substitute, several important factors must be taken into consideration:

- Biocompatibility
- Biodegradability/resorbability
- Osteoconductivity
- Osteoinductivity
- Interconnected porosity
- Proper stiffness and strength

All biomaterials must be biocompatible to avoid a chronic immune response by the host. In some cases biodegradability or bioresorbability is desirable so that natural tissues eventually grow into and replace the implant, restoring full function back to the host. The materials for bone implants should be osteoconductive, such that mesenchymal stem cells and osteoblasts are attracted to the implant. The surface should also be osteoinductive, allowing for the formation of new osteoblasts and adequate bone ingrowth. Beyond biocompatibility, the mechanical stresses experienced by bone can greatly affect osteogenesis - the natural synthesis of new bone tissue by osteoblasts. A stiffness mismatch between the implant and bone, where the implant has a much higher stiffness, may cause a reduction in bone mass surrounding the implant over time. This phenomenon, known as stress shielding, is a result of the growth and remodeling of bone in response to external loading.

Based on all above, investigation of mechanical properties of bone and its main constituents (minerals and collagen) under varying loading conditions is of a great importance in the area of sport and reconstructive medicine.

**Acknowledgements:** Research support from the National Science Foundation, Division of Ceramics Program (Grant DMR 1006931) and Civil, Mechanical and Manufacturing Innovation (Grant 09-27909) is gratefully acknowledged.

Chapter 1, in part, is a reprint of the material as it appears in "Recent advances on the measurement and calculation of the elastic moduli of cortical and trabecular bone: A review," in Theoretical and Applied Mechanics, 38, 209-297, 2011. E. Novitskaya; P.-Y. Chen; E. Hamed; J. Li; V.A. Lubarda; I. Jasiuk; J. McKittrick. The dissertation author was the primary investigator and author of this paper.

## 1.4 References

[1.1] Ashby MF. On the engineering properties of materials. Acta Metall 1989;37:1273-1293.

[1.2] Wegst UGK, Ashby MF. The mechanical efficiency of natural materials. Phil Mag 2004;84:2167-2181.

[1.3] Arzt E. Biological and artificial attachment devices: Lessons for materials scientists from flies and geckos. Mater Sci Eng C 2006;26:1245-50.

[1.4] The National Academies Press, Hierarchical Structures in Biology as a Guide for New Materials, Washington, DC, NMAB-464, 1994.

[1.5] Olszta MJ, Cheng X, Jee SS, Kumar R, Kim Y-Y, Kaufman J, Douglas EP, Gower LB. Bone structure and formation: A new perspective Mater Sci Eng R 2007;58:77-116.

[1.6] Currey JD. Bones: Structure and mechanics, Princeton, Princeton University Press, 2002.

[1.7] Martin RB, Burr DB, Sharkey NA. Skeletal Tissue Mechanics, Springer Verlag, New York, 1998.

[1.8] An YH, Draughn RA. Mechanical testing of bone and the bone-implant interface, CRC Press, 1999.

[1.9] S.C. Cowin, Bone mechanics handbook, 2nd Edition, CRC Press, Boca Raton, 2001.

[1.10] Cowin SC, Doty SB, Tissue Mechanics, Springer, New York, 2007.

[1.11] Reilly DT, Burstein AH. The mechanical properties of cortical bone. J Bone Joint Surg Am 1974;56:1001-1022.

[1.12] Weiner S, Wagner HD. The material bone: Structure mechanical function relations. Ann Rev Mater Sci 1998;28:271-298.

[1.13] Zysset PK. Indentation of bone tissue: a short review. Osteoporos Int 2009;20:1049-1055.

[1.14] Currey JD. The relationship between the stiffness and the mineral content of bone. J Biomech 1969a;2:477-480.

[1.15] Currey JD. Mechanical consequences of variation in mineral content of bone. J Biomech 1969b;2:1-11.

[1.16] Currey JD. Effects of differences in mineralization on the mechanical properties of bone. Phil Trans Royal Soc Lond 1984;304:509-518.

[1.17] Currey JD. The evolution of the mechanical properties of amniote bone. J Biomech 1987; 20:1035-1044.

[1.18] Currey JD. The effect of porosity and mineral content on the Young's modulus of elasticity of compact bone. J Biomech 1988a;21:131-139.

[1.19] Currey JD, Brear K. Hardness, Young's modulus and yield stress in mammalian mineralized tissues. J Mater Sci Mater Med 1990;1:14-20.

[1.20] Currey JD. Mechanical properties and adaptations of some less familiar bony tissues. J Mech Behav Biomed Mater 2010;3:357-372.

[1.21] Bonfield W, Datta PK. Young's modulus of compact bone. J Biomech 1974;7:147-149.

[1.22] Reilly DT, Burstein AH, Frankel VH. The elastic modulus for bone. J Biomech 1974b;7: 271-276.

[1.23] Bonfield W, Grynpass MD. Anisotropy of Young's modulus of bone. Nature, 1977;270: 453-454.

[1.24] Bonfield W, Tully AE. Ultrasonic analysis of the Young's modulus of cortical bone. J Biomech 1982;4:23-27.

[1.25] Katz JL. Anisotropy of Young's modulus of bone. Nature 1980;283:106-107.

[1.26] Evans GP, Behiri JC, Currey JD, Bonfield W. Microhardness and Young modulus in cortical bone exhibiting a wide-range of mineral volume fractions, and in a bone analog. J Mater Sci Mater Med 1990;1:38-43.

[1.27] Rho JY, Ashman RB, Turner CH. Young's modulus of trabecular and cortical bone material-ultrasonic and microtensile measurements. J Biomech 1993;26:111-119.

[1.28] Jackson SA, Cartwright AG, Lewis D. The morphology of bone mineral crystals. CalcifTiss Res 1978 S;25:217-222.

[1.29] Weiner S, Price PA. Disaggregation of bone into crystals. Calcif. Tiss. Int., 39, (1986a), 365-375.

[1.30] Ziv V, Weiner S. Bone crystal sizes: A comparison of transmission electron microscopic and X-ray diffraction width broadening techniques. Connect Tiss Res. 1994;30:165- 175.

[1.31] Boskey A. Bone mineral crystal size. Osteoporos Int 2003;14:16-21.

[1.32] Rubin MA, Jasiuk I, Taylor J, Rubin J, Ganey T, Apkarian RP. TEM analysis of the nanostructure of normal and osteoporotic human trabecular bone. Bone 2003;33:270-282.

[1.33] Fratzl P, Groschner M, Vogl G, Plenk H, Eschberger J, Fratzl-Zelman N. Mineral crystals in calcified tissues: A comparative study by SAXS. J Bone Miner Res 1992;7:329-334.

[1.34] Watchtel E, Weiner S. Small-angle X-ray scattering study of dispersed crystals from bone and tendon. J Bone Miner Res 1994;9:1651-1655.

[1.35] Tong W, Glimcher MJ, Katz JL, Kuhn L, Eppell SJ. Size and shape of mineralites in young bovine bone measured by atomic force microscopy. Calc Tiss Inter 2003;72:592-598.

[1.36] Hassenkam T, Fantner GE, Cutroni JA, Weaver JC, Morse DE, Hansma PK. High-resolution AFM imaging of intact and fracture trabecular bone. Bone 2004;35:4-10.

[1.37] Siperko LM, Landis WJ. Aspects of mineral structure in normally calcifying avian tendon. J Struct Biol 2001;135:313-320.

[1.38] Katz EP, Li S. Structure and function of bone collagen fibrils. J Mol Biol 1973;80:1-15.

[1.39] Bonar LC, Lees S, Mook HA. Neutron diffraction studies of collagen in fully mineralized bone. J Mol Biol 1985;181:265-270.

[1.40] Pidaparti RMV, Chandran A, Takano Y, Turner CH. Bone minerals lies mainly outside collagen firbrils: predictions of a composite model for osteonal bone. J Biomech 1996;29:909-916.

[1.41] Sasaki N, Tagami A, Goto T, Taniguchi M, Nakata M, Hikichi K. Atomic force microscopic studies on the structure of bovine femoral cortical bone at the collagen fibril-mineral level. J Mater Sci Mater Med 2002;13:333-337.

[1.42] Nikolov S, Raabe D. Hierarchical modeling of the elastic properties of bone at submicron scales: The role of extrafibrillar mineralization. Biophys J 2008;94:4220-4232.

[1.43] Landis WJ, Song MJ, Leigh A, McEwen L, McEwen BF. Mineral and organic matrix interaction in normally calcifying tendon visualized in three dimensions

by high-voltage electron microscopic tomography and graphic image reconstruction. J Struct Biol1993;110:39-54.

[1.44] Landis WJ. The strength of a calcified tissue depends in part on the molecular structure and organization of its constituent mineral crystals in their organic matrix. Bone 1995; 16:533-544.

[1.45] Landis WJ, Hodgens KJ, Song MJ, Arena J, Kiyonga S, Marko M, Owen C, McEwen BF. Mineralization of collagen may occur on fibril surfaces: evidence from conventional and high-voltage microscopy and three-dimensional imaging. J Struct Biol 1996a;117:24-35.

[1.46] Landis WJ, Hodgens KJ, Arena J, Song MJ, McEwen BF. Structural relations between collagen and mineral in bone as determined by high voltage electron microscopic tomography. Microscopy Res Tech 1996b;33:192-202.

[1.47] Ritchie RO, Buehler MJ, Hansma P. Plasticity and toughness in bone. Phys Today 2009, 41-47.

[1.48] Fullerton GD, Amurao M. Evidence that collagen and tendon have monolayer water coverage in the native state. Cell Biol Intern 2006;30:56-65.

[1.49] Fullerton GD, Nes E, Amurao M, Rahal A, Krasnosselskaia L, Cameron I. An NMR method to characterize multiple water compartments on mammalian collagen. Cell Biol Intern 2006;30:66-73.

[1.50] Cameron IL, Short NJ, Fullerton GD. Verification of simple hydration/dehydration methods to characterize multiple water compartments on tendon type I collagen. Cell Biol Intern 2007;31:531-539.

[1.51] Ekani-Nkodo A. Size exclusion and diffusion of flouresceinated probes within collagen fibrils. Phys Rev E 2003;67:021909-7.

[1.52] Toroian D, Lim JL, Price PA. The size exclusion characteristics of type I collagen: implications for the role of non-collagenous bone constituents in mineralization. J Biol Chem 2007;282:22437-22447.

[1.53] Fratzl P, Fratzl-Zelman N, Klaushofer K. Collagen packing and mineralization: An X-ray scattering investigation of turkey leg tendon. Biophys J 1993;64:260-266.

[1.54] Fantner GE, Hassenkam T, Kindt JH, Weaver JC, Birkedal H, Pechenik L, Cutroni JA, Cidade GAG, Stucky GD, Morse DE, Hansma PK. Sacrificial bonds and hidden length dissipate energy as mineralized fibrils separate during bone fracture. Nature Mater 2005;4:612-616.

[1.55] Cowin SC. Bone poroelasticity, J Biomech 1999;32:217-238.

[1.56] Chen P-Y, Toroian D, Price PA, McKittrick J. Minerals form a continuum p hase in mature cancellous bone. Calcif Tiss Inter 2011;88:351-361.

[1.57] J. McKittrick, P.-Y. Chen, L. Tombolato, E.E. Novitskaya, M.W. Trim, G.A. Hirata, E.A. Olevsky, M.F. Horstemeyer, M.A. Meyers, Energy absorbent natural materials and bioinspired design strategies: A review. Mater Sci Eng C 2010; 30:331-342.

[1.58] Carter DR, Hayes WC. The compressive behavior of bone as a two-phase porous structure. J Bone Joint Surg Am 1977;59:954-62.

[1.59] Bonfield W, Clark EA. Elastic deformation of compact bone. J Mater Sci 1973;8:1590- 1594.

[1.60] Mackenzie JK. The elastic constants of solid containing spherical holes. Proc Phys Soc Lond B 1950; 63:2-11.

[1.61] Gibson LJ. The mechanical behaviour of cancellous bone. J Biomech 1985;18:317- 328.

[1.62] Gibson LJ, Ashby MF, Harley BA. Cellular Materials in Nature and Medicine. Cambridge University Press, Cambridge, UK, 2010.

[1.63] Rho JY, Kuhn-Spearing L, Zioupos P. Mechanical properties and the hierarchical structure of bone. Med Eng Phys 1998;20:92-103.

[1.64] Lucas GL, Cooke FW, Friis EA. A Primer on Biomechanics. Springer, New York, 1999.

[1.65] Nalla RK, Balooch M, Ager JW, Kruzic JJ, Kinney JH, Ritchie RO. Effects of polar solvents on the fracture resistance of dentin: role of water hydration. Acta Biomater 2005; 1:31-43.

[1.66] McElhaney JH. Dynamic response of bone and muscle tissue. J Appl Physiology 1966; 21:123.

[1.67] Tennyson RC, Ewert R, Niranjan V. Dynamic viscoelastic response of bone. Exper Mech 1972;12:502-507.

[1.68] Lewis JL, Goldsmith W. The dynamic fracture and prefracture response of compact bone by split Hopkinson bar methods. J Biomech 1975;8:27-40.

[1.69] Kulin RM, Jiang FC, Vecchio KS. Effects of age and loading rate on equine cortical bone failure. J Mech Behav Biomed Mater 2011;4:57-75.

[1.70] Currey JD. Tensile yield in compact bone is determined by strain, post-yield behaviour by mineral content. J Biomech 2004;37:549-556.

[1.71] Boot AM, de Ridder MAJ, Pols HAP, Krenning EP, de Muinck Keizer-Schrama SMPF. Bone mineral density in children and adolescents: Relation to puberty, calcium intake, and physical activity. J Clinical Endochrin & Metabol 1997;82:57-62.

[1.72] Riggs BL, Wahner HW, Dunn WL, Bazess RB, Offord KP, Melton III LJ. Differential changes in bone mineral densit of the appendicular and axial skeleton with aging. J Clin Invest 1981;67:328-225.

[1.73] Bouxsein ML. Biomechanics of age-related fractures. In: Marcus R, Feldman D, Nelson D, Rosen, CJ. (Eds.), Osteoporosis, 3rd ed. Elsevier, Inc., 2008, pp. 601–621.

[1.74] Lubarda VA, Novitskaya EE, McKittrick J, Bodde SG, Chen P-Y. Elastic properties of cancellous bone in terms of elastic properties of its mineral and protein phases with application to their osteoporotic degradation. Mech Mater 2012; 44:2012.

[1.75] Danielsen CC, Mosekilde Li, J. Bollerslev J, Mosekilde Le. Thermal stability of cortical bone collagen in relation to age in normal individuals and in individuals with osteopetrosis. Bone 1994;15:91-96.

[1.76] Currey JD, Brear K, Zioupos P. The effects of ageing and changes in mineral content in degrading the toughness of human femora. J Biomech 1996;29:257-260.

[1.77] Ritchie RO, Nalla RK, Ager III JW, Balooch G, Kinney JH. Fracture and ageing in bone: Toughness and structural characterization. Strain 2006;42:225-232.

[1.78] Erickson GM, Catanese J, Keaveny TM. Evolution of the biomechanical material properties of the femur. Anat Rec 2002;268:115-124.

[1.79] Zioupos P, Hansen U, Currey JD. Microcracking damage and the fracture process in relation to strain rate in human cortical bone tensile failure. J Biomech 2008;41:2932- 2939.

[1.80] Hansen U, Zioupos P, Simpson R. The effect of strain rate on the mechanical properties of human cortical bone. J Biomech Eng 2008;130:011011.

[1.81] Thurner PJ. Atomic force microscopy and indentation force measurement of bone. WILEY Interdisciplinary reviews-nanomedicine and nanobiotechnology 2009;1:624-649.

[1.82] Sedlin ED, Hirsch C. Factors affecting the determination of the physical properties of femoral cortical bone. Acta Ortop Scandinav 1966;37:29-48.

[1.83] Currey JD. The effects of drying and re-wetting on some mechanical properties of cortical bone. J Biomech 1988b;21:439-441.

[1.84] Turner CH, Burr DB. Basic biomechanical measurements of bone: a tutorial. Bone 1993; 14:595-608.

[1.85] Oliver WC, Pharr GM. Measurement of hardness and elastic modulus by instrumented nanoindentation: advances in understanding and refinements of the methodology. J Mater Res 2004;19:3-20.

[1.86] Zysset PK, Guo XE, Hoffler CE, Moore KE, Goldstein SA. Elastic modulus and hardness of cortical and trabecular bone lamellae measured by nanoindentation in the human femur. J Biomech 1999;32:1005-1012.

[1.87] Rho JY, II Roy ME, Tsui TY, Pharr GM. Elastic properties of microstructural components of human bone tissue as measured by nanoindentation. J Biomed Mater Res 1999;45:48-54.

[1.88] Skedros JG, Holmes JI, Vajda EG, Bloebaum RD. Cement lines of secondary osteons in human bone are not mineral-deficient: New data in a historical perspective. Anat Rec A 2006;286:781-803.

[1.89] Balooch G, Balooch M, Nalla RK, Schilling S, Filvaroff EH, Marshall GW, Marshall SJ, Ritchie RO, Derynck R, Allison T. TGF-beta regulates the mechanical properties and composition of bone matrix. Proc Natl Acad Sci 2005;102:18813–18818.

[1.90] Tai K, Dao M, Suresh S, Palazoglu A, Ortiz C. Nanoscale heterogeneity promotes energy dissipation in bone. Nature Mater 2007;6:455-462.

[1.91] Hansma PK, Turner P, Drake B, Yurtsev E, Proctor A, Mathews P, Lelujian J, Randall C, Adams J, Jungmann R, Garza-de-Leon F, Fantner G, Mkrtchyan H, Pontin M, Weaver A, Brown MB, Sahar N, Rossello R, Kohn D. The bone diagnostic instrument II: Indentation distance increase. Rev Sci Instrum 2008;79:064303.

[1.92] Hansma PK, Turner PJ, Fantner GE. Bone diagnostic instrument. Rev Sci Instrum 2006;77:075105.

[1.93] Zhang D, Arola DD, Rouland JA. Evaluating the elastic modulus of bone using electronic speckle pattern interferometry. Exp Tech 2001;25:32-34.

[1.94] Barak MM, Currey JD, Weiner S, Shahar R. Are tensile and compressive Young's moduli of compact bone different? J Mech Behav Biomed Mater 2009;2:51-60.

[1.95] Beaupied H, Lespessailles E, Benhamou C-L. Evaluation of macrostructural bone biomechanics. Joint Bone Spine 2007;74:233-239.

[1.96] Keller TS, Mao Z, Spengler DM. Young modulus, bending strength, and tissue physical properties of human compact bone. J Orthop Res 1990;8:592-603.

[1.97] Draper ERC, Goodship AE. A novel technique for four-point bending of small bone samples with semi-automatic analysis. J Biomech 2003;36:1497-1502.

[1.98] Novitskaya EE, Chen P-Y, Lee S, Castro-Ceseña A, Hirata G, Lubarda VA, McKittrick J. Anisotropy in the compressive mechanical properties of bovine cortical bone and the mineral and protein constituents. Acta Biomater 2011;**7**:3170-3177.

[1.99] Turner CH, Rho J, Takano Y, Tsui TY, Pharr GM, The elastic properties of trabecular and cortical bone tissues are similar: results from two microscopic measurement techniques. J Biomech 1999;32:437-441.

[1.100] Bayraktar HH, Morgan EF, Niebur GL, Morris GE, Wong EK, Keaveny TM. Comparison of the elastic and yield properties of human femoral trabecular and cortical bone tissue. J. Biomech., 37, ( 2004), 27-35.

[1.101] Dong XN, Guo XE. The dependence of transversely isotropic elasticity of human femoral cortical bone on porosity. J Biomech 2004;37:1281-1287.

[1.102] Keller TS. Predicting the compressive mechanical behavior of bone, J Biomech 1994:27:1159-1168.

[1.103] Grimal Q, Haupert S, Mitton D, Vastel L, Laugier P. Assesment of cortical bone elasticity and strength: Mechanical testing and ultrasound provide complementary data. Med Eng Phys 2009;31:1140-1147.

[1.104] Currey JD. What determines the bending strength of compact bone? J Exp Biol 1999;202:2495-2503.

[1.105] Cuppone M, Seedhom BB, Berry E, Ostell AE. The longitudinal Young's modulus of cortical bone in the midshaft of human femur and its correlation with CT scanning data, Calcif Tiss Inter 2004;74:302-309.

[1.106] Zioupos P, Currey JD, Casinos A. Exploring the effects of hypermineralisation in bone tissue by using an extreme biological example. Connect Tiss Res 2009;41:229-248.

[1.107] Rho JY, Hobatho MC, Ashman RB. Relations of mechanical properties to density and CT numbers in human bone. Med Eng Phys 1995;17:347-355.

[1.108] Hunt KD, O'Loughlin VD, Fitting DW, Adler L. Ultrasonic determination of the elastic modulus of human cortical bone. Med Biol Eng Comp 1998;36:51-56.

[1.109] Zimmerman MC, Prabhakar A, Chokshi BV, Budhwani N, Berndt H. The acoustic properties of normal and imbedded bovine bone as measured by acoustic microscopy. J Biomed Mater Res 1994;28:931-938.

[1.110] Lotz JC, Gerhart TN, Hayes WC. Mechanical properties of trabecular bone from the proximal femur: a quantitative CT study. J Comp Ass Tomog 1990;14:107- 114.

[1.111] Morgan EF, Yen OC, Chang WC, Keaveny TM. Nonlinear behavior of trabecular bone at small strains. J Biomed Eng 2001;123:1-9.

[1.112] Bruyère Garniera K, Dumasa R, Rumelharta C, Arlotb ME. Mechanical characterization in shear of human femoral cancellous bone: torsion and shear tests. Med Eng Phys 1999;21:641-649.

[1.113] van Lenthe GH, van den Bergh JPW, Hermus ARMM, Huiskes R. The prospects of estimating trabecular bone tissue properties from the combination of ultrasound, dual-energy X-ray absorptiometry, microcomputed tomography, and microfinite element analysis. J Bone Miner Res 2001;16:550-555.

[1.114] Nalla RK, Kruzic JJ, Kirmey JH, Ballooch M, Ager JW, Ritchie RO. Role of microstructure in the aging-related deterioration of the toughness of human cortical bone. Mater Sci Eng C 2006;26:1251-1260.

[1.115] Evans AG, Charles EA. Fracture toughness determinations by indentation. J Amer Cer Soc 1976;59:371.

[1.116] Geiger M, Lee RH, Fress W. Collagen sponges for bone regeneration with rhBMP-2. Adv Drug Deliv Rev 2003;55:1613-1619.

[1.117] Russias J, Saiz E, Nalla RK, Gyn K, Ritchie RO, Tomsia AP. Fabrication and mechanical properties of PLA/HA composites: A study of in vitro degradation. Mater Sci Eng C 2006;26:1289-1295.

[1.118] Hall MJ, Owings MF. National Hospital Discharge Survey. National Center for Health Statistics, Hyattsville, MD, 2002.

[1.119] Benke D, Olah A, Möhler H. Protein-chemical analysis of Bio-Oss bone substitute and evidence on its carbonate content. Biomaterials, 22, 1005-1012, 2001.

[1.120] Carter DH, Scully AJ, Heaton DA, Young MPJ, Aaron JE, Effect of deproteination on bone mineral morphology: implications for biomaterials and ageing. Bone 2002;31:389-395.

[1.121] Stavropoulos A, Karring TJ, Guided tissue regeneration combined with a deproteinized bone mineral (Bio-Oss) in the treatment of intrabony periodontal defects: 6 year results from a randomized-controlled clinical trial. J Clin Period 2010;37:200-210.

[1.122] Heidermann E, Riess W. Die Veranderungen Des Kollagens Bei Entwasserung Mit Aceton + Die Konsequenzen Dieser Veranderung Fur Die Kollagenstruktur. Hoppe-Seyler's Z Physiol Chem 1964;337:101.

[1.123] Potoczek M. Hydroxyapatite foams produced by gelcasting using agarose. Mater Lett 2008;62:1055-1057.

[1.124] Chen P-Y, Stokes A, McKittrick J. Comparison of the structure and mechanical properties of bovine femur bone and antler of the North American elk (Cervus elaphus Canadensis). Acta Biomater 2007;5:693-706.

# Chapter 2 COMPRESSIVE ANISOTROPY OF BONE AND ITS MAIN CONSTITUENTS

## 2.1 Compressive Anisotropy of Bovine Cortical Bone and its Main Constituents

This part will cover the investigations of compressive mechanical properties of bovine cortical bone for three anatomical directions. The mechanical properties of fully demineralized, fully deproteinized, and untreated cortical bovine femur bone were investigated by compression testing in three anatomical directions (longitudinal, radial, and transverse). The weighted sum of the stress-strain curves of the treated bones was far lower than that of the untreated bone, indicating a strong molecular and/or mechanical interaction between the collagen matrix and the mineral phase. Demineralization and deproteinization of the bone demonstrated that contiguous, stand-alone structures result, showing that bone can be considered as an interpenetrating composite material. Structural features of samples from all groups were studied by optical and scanning electron microscopy. The anisotropic mechanical properties were observed: the radial direction was found to be the strongest for untreated bone while the longitudinal one was found to be the strongest for deproteinized and demineralized bones. A possible explanation for this phenomenon is proposed that is attributed to the difference in bone microstructure in radial and longitudinal directions.

### 2.1.1 Introduction and background

The structure and mechanical properties of bone major constituents have been investigated by many research groups for several decades, including seminal works by Currey, Reilly and Burstein, Burstein *et al*., and Rho *et al*. [2.1-2.7]. The mechanical properties of cortical bone are highly anisotropic; therefore significant efforts have been

made to examine the properties of bone for different anatomical directions [2.2-2.10]. Figure 2.1 shows the orientation of longitudinal, radial, and transverse bone directions. One should keep in mind that measured strengths and stiffness numbers for bone are highly dependent on the test method, hydration condition, age, gender, histology, porosity, and a mineral content.

Reilly and Burstein [2.7] investigated anisotropic compressive and tensile properties of cortical bone, and found that the Young's modulus and maximum strength in the longitudinal direction are more than twice those in the transverse and radial directions. Bonfield and Grynpas [2.8] studied mechanical anisotropy of cortical bone at varying angles to the bone growth direction (longitudinal direction corresponded to 0°, transverse direction corresponded to 90°) by ultrasonic measurements. They found that Young's modulus gradually decreased with increasing angle (from 0° to 90°), and there was a plateau between 20° to 70°. Information on mechanical properties in radial direction was not reported. Bulk mechanical properties of bone are greatly affected by its microstructural features. Elastic properties of microstructural components in human and bovine osteonal bone using nanoindentation have been investigated by several groups. Rho *et al*. [2.11] showed that Young's modulus of interstitial lamellae (~ 26 GPa) was higher than that in the osteons (~ 22 GPa) in the longitudinal direction for human cortical bone. The average Young's modulus (including both osteon and interstitial lamellae) in the transverse direction was found to be ~ 17 GPa. Swadener *et al*. [2.12] and Fan *et al*. [2.13] proposed and verified methods to predict the nanoindentation moduli for different bone directions based on the previous ultrasound studies by Rho [2.14]. A possible mechanism for the bone anisotropy at the 10-100 μm

scale was suggested by Seto *et al*. [2.15]. They performed tensile experiments on relatively small samples (a fibrolamellar unit) obtained from periosteal region (see Fig. 2.1). An extremely high mechanical anisotropy in the Young's modulus (of the order 1:20) and tensile strength (of the order 1:15) between transverse and longitudinal directions in wet bovine femur bone was reported. Furthermore, they proposed the periodic presence of mechanically weak heterogeneous layers filled with soft organic constituents inside the fibrolamellar bone accounted for this high anisotropy. These weak interfaces act as damping elements, and suppress crack propagation on the 10-100 μm scale.

One of the main reasons for bone anisotropy is the preferential orientation of collagen fibers and mineral crystals along bone growth direction. This topic has been investigated by several groups [2.16-2.18]. Landis *et al*. [2.16] investigated the ultrasound interaction between collagen and mineral crystals in chicken bone by high voltage electron microscopic tomography, and found out that individual platelet-shaped mineral crystals were periodically arranged along collagen fibrils preferentially aligned along main bone axis. Martin *et al*. [2.17, 2.18] found out that longitudinal fiber orientation in cortical bone greatly contributed to increased elastic modulus and strength in four-point bending.

The mineral/protein interaction is important to understanding how bone constituents affect the mechanical properties. The mechanical properties of protein and mineral constituents can be investigated separately by demineralization and deproteinization, respectively. Mechanical testing results in compression and tension on deproteinized bone were summarized by Piekarski [2.19] and Mack [2.20], but

information on the orientation of bone was not provided. Burstein *et al.* [2.3] investigated tensile mechanical properties of partially demineralized bone using HCl solution at varying concentration. They found that bone in tension demonstrated plastic behavior: the yield point and maximum strength progressively decreased as demineralization proceeded, while slope of plastic region was the same for all demineralization stages. These findings demonstrated that bone stiffness in the plastic region is a function of collagen properties only. Contribution of the two main bone constituents to elastic anisotropy was investigated by Hasegawa *et al*. [2.9] and Iyo *et al*. [2.21]. Hasegawa *et al*. [2.9] performed acoustic velocity measurements on demineralized and deproteinized dog femur in the longitudinal and transverse directions. They found that the collagen matrix is highly isotropic and proposed that the minerals play the major role in the anisotropic behavior of the whole bone. Iyo *et al*. [2.21] investigated the effect of mechanical anisotropy on the Young's modulus relaxation. Their model consisted of a combination of two processes: a fast one, attributed to the relaxation of collagen matrix, and a slow one, attributed to the mixture of collagen and mineral phases. Moreover, they suggested that latter process, corresponding to both collagen and mineral constituents, was responsible for the anisotropic behavior of bone, in contrast to what was suggested by Hasegawa *et al*. [2.9]. Detailed examination of mechanical properties of the major bone constituents (mineral and collagen parts) in different anatomical directions is important to better understand the mechanical behavior of bone. Skedros *et al*. [2.22] used acoustic microscopy to evaluate elastic modulus of untreated, demineralized and deproteinized cortical bone of deer calcanei for different bone cortices. It was found that anisotropy

ratio, defined as a ratio between the acoustic velocity squared for longitudinal and transverse bone directions, was significantly different from one for both demineralized and deproteinized bone, demonstrating that not only untreated bone, but also the main bone constituents (mineral and collagen phases) were anisotropic. The anisotropy ratio was higher for cortices that were adapted for tension and compression, and were less for cortices that were adapted for a combination of compression/shear or tension/shear. These results clearly indicate that the degree of anisotropy of bone greatly depends on its functions and adaptations. Macione *et al*. [2.10] investigated properties of partially demineralized bone using ultrasound technique. They showed that the elastic modulus in the longitudinal direction could be predicted using ultrasound measurements on transverse and radial directions.

Mechanical properties of demineralized and deproteinized cancellous bone were recently studied by several groups. Chen *et al.* [2.23] developed and verified methods to fully demineralize and fully deproteinize cancellous bovine femur bone without altering microstructure. It was found that minerals form a continuous, stand-alone structure after removing all the protein, and mature cancellous bone is indeed an interpenetrating composite in agreement with Rosen *et al.* [2.24] who found well organized mineral structure in deproteinized bovine cortical bone. Compressive mechanical properties of demineralized and deproteinized cancellous bone were further investigated by Chen and McKittrick [2.25]. It was shown that both relative elastic modulus and compressive strength increase with relative densities. Moreover, strong synergistic effect between the mineral and protein phases was found and rule of mixture did not apply, proving a strong chemical bonding and interactions between the two phases. Lubarda *et al.* [2.26]

derived the elastic modulus of untreated cancellous bone based on measured properties of mineral and protein phases in order to understand osteoporotic degradation. Demineralization kinetics for cancellous and cortical bone was thoroughly studied by Castro-Ceseña *et al*. [2.27]. It was shown that mineral and protein phases of cortical bone are independent structures that can be mechanically tested, corroborated findings of Chen *et al.* [2.23], but mechanical testing was not performed.

Study on mechanical properties of demineralized and deproteinized cortical bone as a function of anatomical direction is the main goal of this research.

### 2.1.2 Materials and methods

#### *2.1.2.1 Sample preparation*

Bovine femur bone samples were obtained from a local butcher. The slaughter age of cattle was about 18 months. The bone was thoroughly cleaned with water. About 100 samples for compression testing (parallelepipeds 5 mm x 5 mm x 7.5 mm) were prepared from close locations of the bone in order to minimize variations in density and mineral content. The samples were first roughly cut by handsaw and then by a diamond blade with the surfaces as parallel as possible. Samples were cut in all three anatomical directions (Fig. 2.1). The longitudinal direction was chosen to be parallel to growth direction of the bone, the transverse direction was normal to the bone growth direction, and the radial one was orthogonal to both. Samples were stored in a refrigerator until chemical procedure and testing was performed.

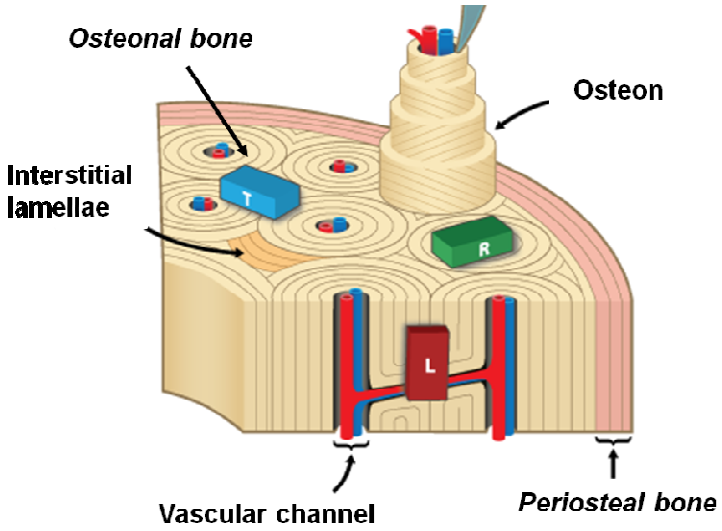


**Figure 2.1** Schematic diagram of bone microstructure and sample orientations for three anatomical directions in cortical bone. Sample orientations: L = longitudinal, R = radial, T= transverse.

### *2.1.2.2 Demineralization and deproteinization process*

Bone samples were demineralized (DM) by aging in 0.6N hydrochloric acid (HCl) at room temperature using the procedures outlined in Toroian *et al.* [2.28] and Chen *et al.* [2.23]. It should be noted that although EDTA (ethylenediaminetetraacetic acid) has been used to demineralize bone [2.29], complete demineralization may require one month or more at 37˚C, which thus may damage the gross structure of the matrix (possibly due to enzymatic autolysis). Consequently, we chose HCl as the demineralization media, since that process is much quicker at room temperature, minimizing damage of the protein structure. Acid solutions were changed every two hours in order to avoid saturation that can affect the demineralization process. The whole process took about 50 hours. The completeness of demineralization was verified by the mineral absence in the solution using the procedure described in Castro-Ceseña

*et al.* [2.27]. Bone samples were deproteinized (DP) by aging in a 5.6 wt. % sodium hypochlorite (NaOCl) solution at 37˚C, following the procedure outlined in Chen *et al.* [2.23]. The solutions were changed every 6 hours. The whole process took about two weeks.

#### *2.1.2.3 Compression testing*

Three different sets of the samples were prepared: 40 untreated (UT), 30 demineralized (DM) and 30 deproteinized (DP). Specimens from all groups were submerged in Hank's balanced saline solution for 24 hours before testing, and were tested in the hydrated condition. Compression testing of untreated bone samples was performed on universal testing machine equipped with 30kN load cell (Instron 3367 Dual Column Testing Systems, Norwood, MA). Compression testing of demineralized and deproteinized bone samples was performed on universal testing machine equipped with 500N load cell (Instron 3342 Single Column System, Norwood, MA). Compression testing for samples from all three groups was performed at a strain rate of $1x10^{-3}$ $s^{-1}$. An external deflectometer SATEC model I3540 (Epsilon Technology Corp., Jackson, WY) was used in order to measure the small displacement. All samples were loaded until compressive failure. Compressive failure is defined in the following sections for UT, DM and DP samples.

#### *2.1.2.4 Structural characterization*

Samples from the all groups were analyzed by optical microscopy using Zeiss Axio imager equipped with CCD camera (Zeiss Microimaging Inc., Thornwood, NY). Fracture surfaces of the specimens were investigated by scanning electron microscope

(SEM) equipped with EDS (FEI-XL30, FEI Company, Hillsboro, OR). DM samples were subjected to critical point drying procedure before SEM imaging in order to avoid excessive shrinkage. For SEM imaging all samples were mounted on aluminum sample holders, air dried and sputter-coated with chromium before imaging. Samples were observed at a 20kV accelerating voltage.

#### *2.1.2.5 Statistical analysis*

Since UT and DP bone samples fail in a brittle manner, containing preexisting flaw size distributions [2.30], the compressive strengths were analyzed by the Weibull probability distribution, which is a powerful method to analyze statistical variations in the strength of materials. The Weibull distribution function [2.31] provides the failure probability ($F$) that depends on the failure stress (f), according to:

$$F(\sigma_f) = 1 - \exp\left(\frac{\sigma_f}{\sigma_o}\right)^m, \tag{2.1}$$

where $\sigma_0$ is the characteristic strength of the material (stress at which 63.2% of the samples have failed – when $\sigma_f = \sigma_o$), and $m$ is the Weibull modulus. A larger value of $m$ indicates less variability in the strength distribution. The average compressive strength ($\bar{\sigma}$) was taken as the mean of the Weibull distribution, according to [2.32]:

$$\bar{\sigma} = \sigma_o \Gamma\left(1 + \frac{1}{m}\right), \tag{2.2}$$

$$\Gamma\left(1 + \frac{1}{m}\right) = \int_0^\infty x^{1/m} e^{-x} dx, \tag{2.3}$$

where Γ is the Gamma function, defined by the indicated improper integral, whose values are tabulated in [2.33].

### 2.1.3 Results and discussion

Figure 2.2 shows the photographs of untreated (UT), fully demineralized (DM) and fully deproteinized (DP) cortical bovine femur bone. Demineralization and deproteinization of cortical bone produced contiguous, stand-alone structures that can be tested for mechanical properties. Moreover, Fig. 2.2 demonstrates that cortical bone can be considered as a "two-phase" interpenetrating composite material, which according to Mack [2.20] achieves superb mechanical properties by interacting mineral and protein phases; that make bone's properties superior to the properties of its individual (mineral and protein) components as separate phases, corroborating the findings of Chen *et al.* [2.25] who reported the same for bovine femur cancellous bone.

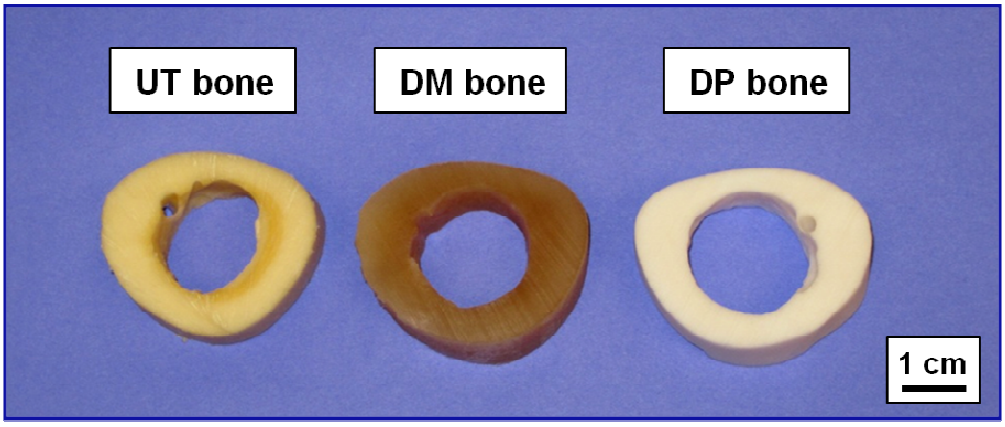


**Figure 2.2** Photographs of untreated (UT), fully demineralized (DM) and fully deproteinized (DP) cortical bovine femur bone. The DM and DP samples are continuous, stand-alone structures that can be tested for mechanical properties (courtesy of Professor Paul Price, UCSD).

Figure 2.3 shows SEM images of fracture surfaces for UT, DM, and DP bone. Images were taken from the different samples. SEM images of DM (Fig. 2.3b) and DP samples (Fig. 2.3c) showed that the collagen fibers in the former case, and minerals in the latter case, are aligned in a coherent manner, forming a continuous network. Moreover, microscopic features, such vascular channels (10-20 µm in diameter), lacuna spaces (5-10 µm in diameter) are preserved in both the DP and DM samples, in agreement with Chen *et al*. [2.23]. Well-defined osteonal structures are clearly observed in both the DP and DM images, as well as in UT image (Fig. 2.3a).

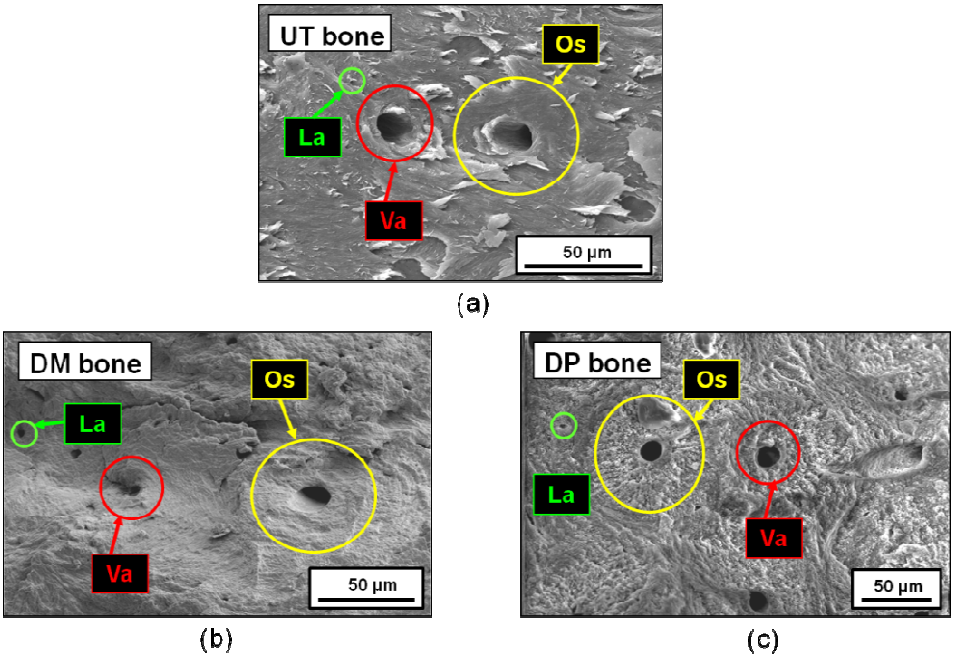


**Figure 2.3** SEM images of (a) untreated (UT), (b) demineralized (DM), and (c) deproteinized (DP) bovine cortical bone (fracture surfaces). Os = osteons, La = lacuna spaces, Va = vascular channels. Images were taken from the different samples.

Stress-strain curves for UT, DM, and DP bone for longitudinal direction are shown in Fig. 2.4. The weighted sum of the stress-strain curves ($\sigma_s$) for DM and DP samples is shown, based on the Voigt averaging scheme is:

$$\sigma_s = f_m\sigma_m + f_p\sigma_p = f_m\sigma_m + (1 - f_m)\sigma_p, \tag{2.4}$$

where $f_m$ is the volume fraction of the mineral phase, $\sigma_m$ and $\sigma_p$ are the stresses in mineral and protein phases, respectively. Using $f_m$ ~ 0.5, the Voigt average curve is far lower than that of the UT bone (Fig. 2.4). This indicates a strong molecular interaction or mechanical interlocking between the proteins and minerals. More involved models for determining the effective elastic properties of heterogeneous materials, or materials weakened by voids of different size and geometry, such as the self-consistent method or the differential scheme [2.34], could be utilized to account for some of interactions that takes place at higher concentration of collagen as a weaker phase, but this models are beyond the scope of this work. The UT and DP samples fractured in a brittle manner (Fig. 2.4 and Fig. 2.5a,c), while DM samples showed behavior typical for collagen with a long "toe-in" region at small strains (Fig. 2.4 and Fig. 2.5b).

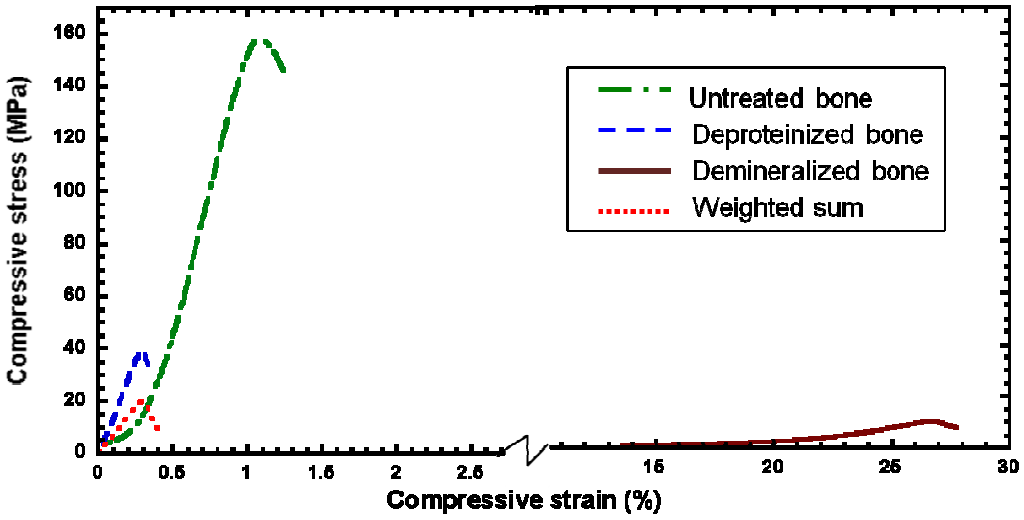


**Figure 2.4** Stress-strain curves for untreated, deproteinized and demineralized cortical bovine femur bone tested in the longitudinal direction. Calculated weighted sum, shown in dots, clearly underestimates properties of untreated bone.

Figures 2.5a-c shows the compression stress-strain curves for UT, DM and DP bone samples in the three anatomical directions, clearly exhibiting the highly anisotropic properties. The compressive strength was identified at fracture point for UT and DP samples, and as the maximum compressive stress for DM samples. The longitudinal direction is the strongest and stiffest for the DP and DM bone, while the radial one is the strongest for the UT bone. The porosity of DM and DP bone is much higher than of UT bone, and this increased porosity is due to the treatment generated pores, dominantly extended in the longitudinal direction. This yields the lower stiffness in radial and transverse directions than in the longitudinal direction. Additionally, the radial direction is the toughest (area under stress-strain curve) direction for UT bone. The collagen and mineral phases both play a significant role in bone mechanical

properties, therefore untreated bone has superior properties compared to either mineral or collagen parts. Therefore, when either phase is removed, the bonds between collagen and mineral phases are broken, which significantly affects the mechanical properties. Minerals preferentially orient in longitudinal direction [2.16], therefore this direction is the strongest and stiffest direction for DP bone. Furthermore, collagen fibers are also preferentially oriented in longitudinal direction [2.17, 2.18]; therefore the longitudinal direction is also the stiffest and strongest direction for DM bone. These findings supported the idea of Iyo *et al.* [2.21] and Skedros *et al.* [2.22] that both the mineral and the collagen constituents contribute to the anisotropic behavior of cortical bone. We have shown that bone is anisotropic not only for UT, but for DM and DP bones as well (see Table 2.1, Fig. 2.5).

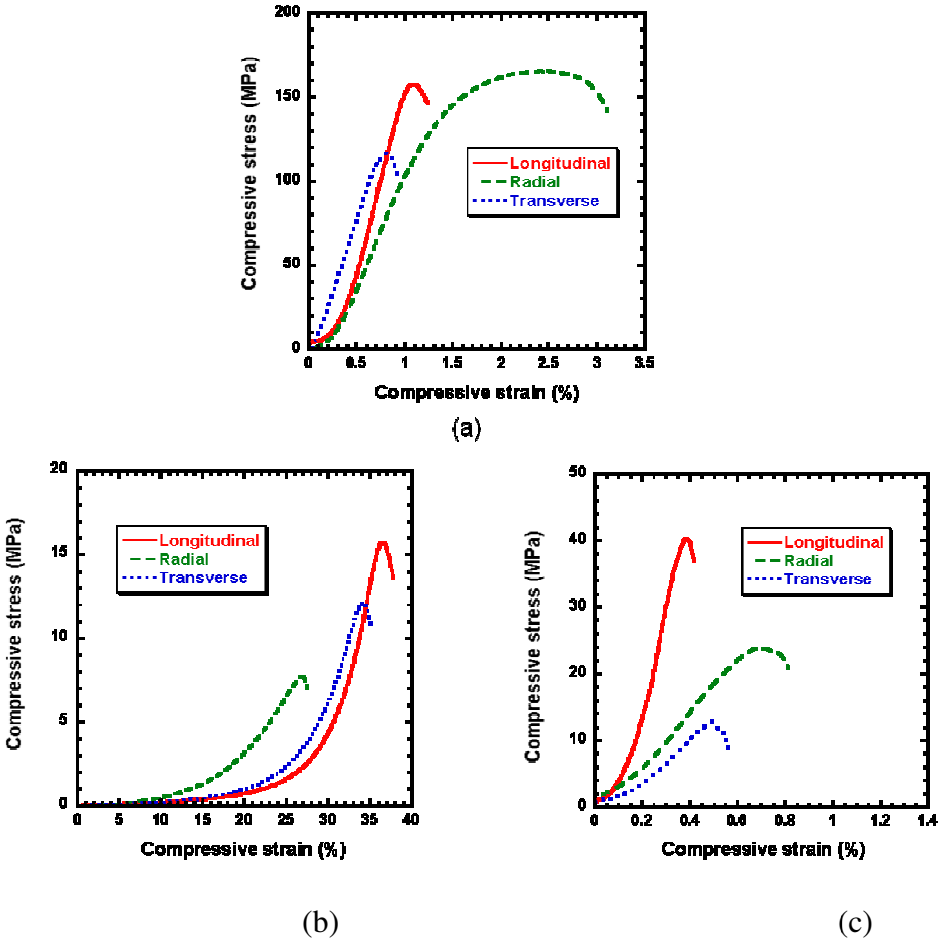


**Figure 2.5** Representative compression stress-strain curves for the three anatomical directions for (a) untreated, (b) demineralized, and (c) deproteinized bone.

Weibull distributions for compressive strengths of UT and DP bones (Fig. 2.6) clearly demonstrate that radial direction is the strongest direction for UT bone while the longitudinal one is the strongest for DP bone. A somewhat less perfect fit of the Weibull plot to experimental data for untreated bone in radial direction is a consequence of a less uniform microstructure of the samples used for testing in radial direction (see Fig. 2.7a for transverse direction and Fig. 2.7b for radial direction).

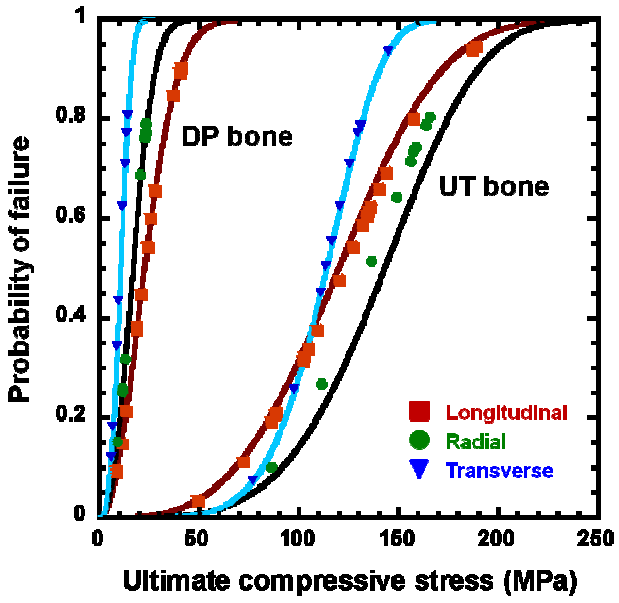


**Figure 2.6** Weibull plots for ultimate compressive stress for untreated (n(L) = 20; n(R) = 10; n(T) = 10), and deproteinized (n(L) = 12; n(R) = 10; n(T) = 10) bone . Demineralized bone is 100% protein and Weibull analysis therefore was not applicable.

Table 2.1 summarizes the hydrated density, average compressive strength, Young's modulus, and Weibull modulus for UT, DP, and DM bone in the three anatomical directions. The Weibull modulus listed only for UT and DP samples since DM samples did not break in a brittle manner. The average compressive strength was calculated according to Eq. (2.2) for UT and DP bone, and as the mean compressive strength for DM bone. The first observation is the density values: densities of the DM samples are much smaller than those of the DP samples because density of pure collagen (1.35 g/cm$^3$) [2.35] is almost three times smaller than density of pure hydroxyapatite (3.15 g/cm$^3$) [2.36]. These findings are well correlated with Chen *et al.* [2.25]. Another interesting observation was that the hydrated DP density values are very

close to the UT ones, which indicates that water fills all or nearly all of the empty voids created after protein removal (since density of the water (1 g/cm$^3$) is slightly lesser than the collagen density, hydrated DP sample density is slightly less than that of UT ones).

**Table 2.1** Hydrated density, Young's modulus, compressive strength and compressive strength Weibull modulus (*m*) for untreated (UT), deproteinized (DP) and demineralized (DM) bovine cortical bone in the three anatomical directions. Weibull modulus (*m*) is listed for UT and DP bone samples - the DM samples did not fracture. L = longitudinal, R = radial, T = transverse (Fig. 2.1). The average compressive strength was taken as a mean of Weibull distribution according to Eq. (2.2) for UT and DP bone. For DM bone the compressive strength was taken as a maximum stress from the stress/strain curves. The Young's modulus was estimated from the steepest portion of the stress/strain curves for all samples.

| **Sample** | **Orient-ation** | **Density (g/cm$^3$)** | **Young's modulus (GPa)** | **Average compressive strength (MPa)** | ***m*** |
|---|---|---|---|---|---|
| UT | L | 2.06 ± 0.01 | 22.6 ± 1.2 | 120 ± 9 | 3.32 |
| | R | 2.03 ± 0.05 | 12.4 ± 0.4 | 142 ± 13 | 4.22 |
| | T | 2.04 ± 0.04 | 16.2 ± 1.4 | 112 ± 7 | 5.68 |
| DP | L | 2.00 ± 0.01 | 9.2 ± 2.8 | 24 ± 4 | 2.04 |
| | R | 1.94 ± 0.01 | 2.6 ± 0.5 | 18 ± 3 | 2.32 |
| | T | 1.96 ± 0.01 | 2.2 ± 0.3 | 11 ± 1 | 2.95 |
| DM | L | 1.17 ± 0.01 | 0.232 ± 0.009 | 14 ± 1 | N/A |
| | R | 1.17 ± 0.01 | 0.060 ± 0.009 | 6 ± 1 | N/A |
| | T | 1.18 ± 0.01 | 0.132 ± 0.015 | 11 ± 1 | N/A |

Next, for the UT bone, there are clear differences in the stiffness values in the longitudinal, transverse and radial directions. The longitudinal and transverse stiffness values correlate well with that of human femur [2.37], and show that the longitudinal stiffness is 30% higher than that of the transverse one. This can be attributed to several

factors. First of all, the collagen is aligned in the longitudinal direction with coexisting mineral orientation in the same direction. Applying the Voigt and Reuss models of aligned fibrous composites, the stiffness in the longitudinal direction is predicted to be about 22 times higher than in the transverse direction. Another factor is the osteon structure, which is aligned in the longitudinal direction. The interior vascular channels are hollow cylinders that, when compressed in the transverse direction, will deform more easily than in the longitudinal direction.

In addition, the average longitudinal Young's modulus for UT, DP, and DM bone samples were 22.6 GPa, 9.2 GPa, and 232 MPa, respectively. These results indicate that the majority of the stiffness comes from the mineral contribution, as expected. The elastic modulus of DP bone was almost three times lower compared to UT bone, because of the significantly increased porosity (from 10 to 55 vol.%), induced by deproteinization process. The average Young's moduli for UT, DP, and DM radial and transverse samples show a similar trend, but with smaller differences in Young's modulus values between UT and DP cases. In addition, the average Young's modulus drops about 100 times between UT and DM samples for all three anatomical directions, proving that the majority of the bone stiffness comes from the mineral phase, and the collagen phase gives only a small contribution to the overall bone stiffness.

Furthermore, it is clear that the weighted sum of the compressive strength for pure mineral (DP samples) and pure protein phases (DM samples) is not even close to the compressive strength of UT samples for all three anatomical directions (Fig. 2.4). These findings are clearly supporting the conclusion that bone mechanical properties

should be evaluated as properties of an interpenetrating composite rather than being a simple sum of the properties of its two main components properties.

The Weibull modulus appears to be the highest for transverse direction for both UT and DP bone. This means that bone behaves in the most predictive way in this particular direction (strength is the most equally distributed in the bone volume for this direction). Strength in the longitudinal direction, on the contrary, appears to be the most scattered for the both cases. It can be attributed to the longitudinal alignment of collagen fibers and minerals, as well as the presence of vascular channels.

The difference in mechanical behavior between the radial and transverse directions for UT bone (Table 2. 1, Fig. 2.5a) is unexpected – they should be similar as the osteons are perpendicular to the loading direction in both cases. The cortical bone microstructure is shown in Fig. 2.7. The outer part of bone near the bone surface (periosteal part) consists of circumferential lamellae structure that is parallel to the bone surface [2.38]. This region has a thickness of ~ 600 μm, consisting of 15-20 lamellae. In addition, the mineralized collagen fibers in each of those lamella oriented at different angles, giving the bone extra strength in the radial direction. Optical micrographs of radial and transverse samples (cross-sectional view) are shown in Fig. 2.7. The outer part of the bone for radial sample consists of thin layer (Fig. 2.7b) that organizes differently than the rest the bone volume (Fig. 2.7a). Moreover, mineralized collagen lamellae in this thin outer layer are not developed cylindrical osteons, but are arranged smoothly in the longitudinal direction (Fig. 2.7b) creating outer sheath. This sheath contributed to the mechanical response of samples taken in radial direction, as the bone is too narrow in this direction to cut samples that do not contain this sheath, but it does

not contribute to the properties of transverse samples (Figs. 2.1, 2.7a). Therefore, the differences in mechanical properties between radial and transverse directions for untreated bone were attributed to existence of the radial sheath (periosteal bone with different microstructure). For the same reason, the untreated bone samples were found to be stronger in the radial than in longitudinal direction.

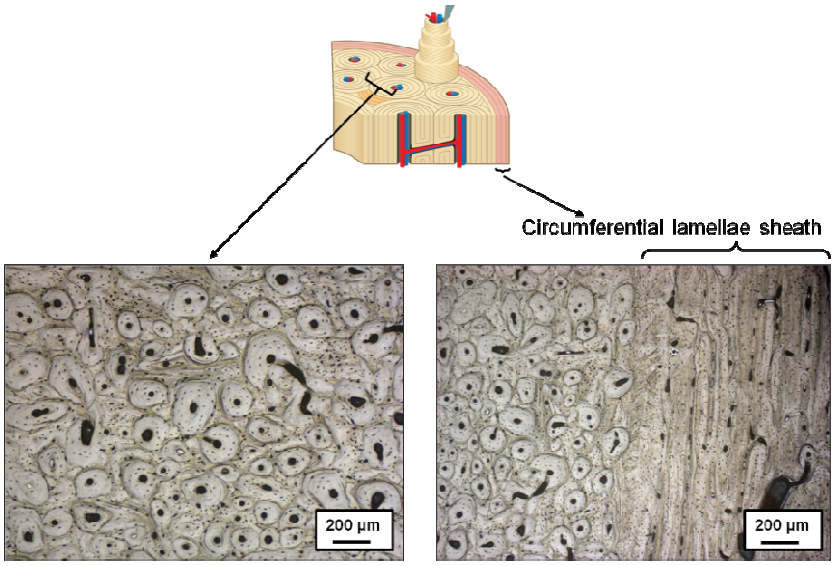


(a) (b)

**Figure 2.7** Optical micrographs showing the structure differences between (a) transverse, and (b) radial bone samples. Circumferential lamellae sheath is clearly shown at (b).

The fact that longitudinal direction appears to be the strongest direction for DP bone can be explained by consideration of the stress concentration factor. Compression of DP bone can be considered as compression of a solid with a preexisting micro flaw size distribution due to the high porosity (~ 55%). During the DP process, the voids (considered as interconnected ellipses in our 2D model sketched in Fig. 2.8) appear at the places previously occupied by the protein matrix. Since collagen fibers are

preferentially aligned in the bone growth direction (longitudinal), the voids are preferentially oriented in this direction. This additional porosity level for longitudinal and transverse (or radial) directions is shown in Fig. 2.8, which shows the ellipse major axis is parallel to the loading direction for the longitudinal orientation and is perpendicular for the transverse or radial orientation. Ignoring the void interactions effects [2.34], the stress concentration factor ($K$) for points A and B is about the same for the longitudinal direction, but greatly differ from each other for the transverse or radial directions, and is given by:

$$K_A = \sigma_a\left(1+2\frac{a}{b}\right), \tag{2.5}$$

$$K_B = \sigma_a, \tag{2.6}$$

where $\sigma_a$ is the applied stress, $a$ and $b$ are the lengths of major and minor axes, respectively, of the elliptically shaped void. As long as collagen phase is a continuous bone phase, there are some voids of smaller size and concentration that appear at the places of interconnectivity of collagen fibers, preferentially oriented in longitudinal direction. This additional porosity weakens DP bone in both longitudinal and radial/transverse directions, but the weakening effect is less pronounced in the longitudinal direction, which results in superior properties of DP bone in that direction, as predicted by Eqs. (2.5) and (2.6). Consequently, the longitudinal direction is the stiffest and strongest direction for DP bone, supporting the findings shown in Fig. 2.5c and Fig. 2.6.

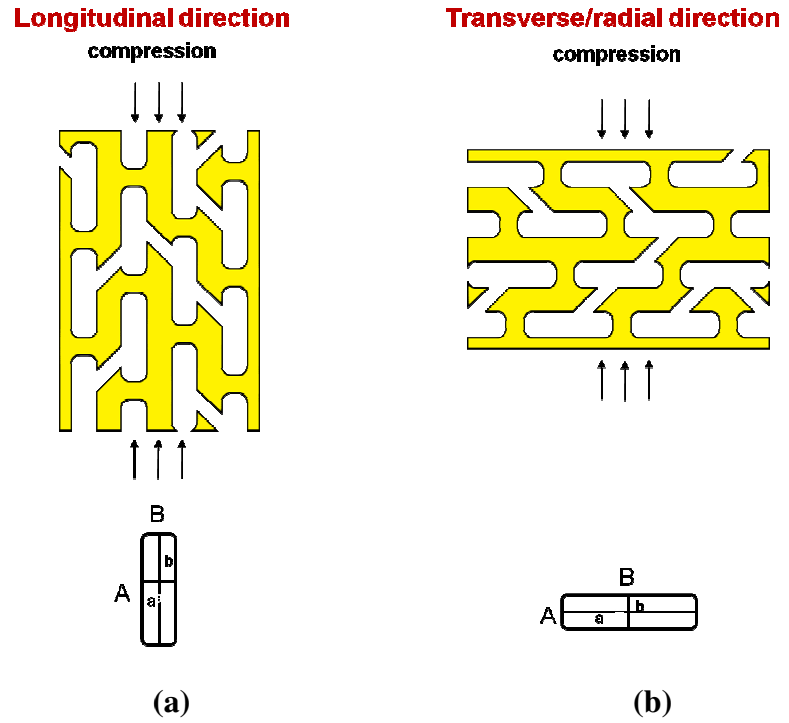


**Figure 2.8** Illustration of the preferentially oriented porosity level after collagen matrix removal for: (a) longitudinal, and (b) transverse/radial directions under compression for deproteinized cortical bone.

### 2.1.4 Conclusions

The mechanical properties and microstructure of untreated, demineralized (protein phase), and deproteinized (mineral phase) cortical bone for three anatomical directions were investigated. The main findings are:

- Untreated, demineralized and deproteinized cortical bovine femur bone all show anisotropic mechanical behavior.
  - The radial direction is the strongest for untreated bone due to existence of thin layer of circumferential lamellae (periosteal bone) that provides extra strength in this direction.

  - The longitudinal direction is the stiffest and strongest for demineralized and deproteinized bone due to preferential orientation of either the collagen fibers (demineralized bone) or minerals (deproteinized bone) in the longitudinal direction.

- The weighted sum of the deproteinized and demineralized strengths for all three anatomical directions does not equal to the strength of the untreated bone, proving the strong interaction between two main bone constituents.
- The Young's modulus decreases almost 100 times between untreated and demineralized bone samples indicating that the majority of the bone stiffness comes from the mineral contribution.
- Difference in Young's modulus between longitudinal and transverse/radial directions for deproteinized bone could be explained by the existence of the elliptically-shaped porosity oriented with the major axis parallel to the bone growth direction, causing different stress concentration for different directions.

### 2.2 Investigations into Partially Demineralized Cortical Bone

Partially demineralized (DM) bone is of interest due to its promising osteointegrative properties for advanced bone grafts. Structural features of partially DM (35 vol.%, 45 vol.% and 55 vol.% reduction), and untreated cortical bone samples were studied by scanning electron microscopy. Mechanical properties were investigated by compression testing in three anatomical directions at different stages of DM. The radial direction appears to be the stiffest and strongest bone direction for the all DM stages.

### 2.2.1 Introduction and background

Partially demineralized bone is of interest due to the excellent osteointegrative properties for advanced bone grafts [2.39-2.42]. Bone loss (osteoporosis) and demineralization occur as bones age and are a major cause of bone fractures. The mineral/collagen interaction is important in understanding how this affects bone fractures. Demineralization (DM) studies have been carried by several groups [2.43-2.46]. Broz *et al.* [2.43] investigated properties of partially DM (by ethylenediamine-tetraacetic acid) bone samples in three-point bending. They showed that specimens became less brittle with the increasing demineralization time. Lewandrowski *et al.* [2.44] provided an electron microscopy study of the DM process. They found that the DM process is described by advancing reaction front theory. Kotha *et al.* [2.45] summarized different techniques, which affect the bone mineral content, and found that sodium chloride solutions (NaCl) do not affect the mechanical properties of bone, while fluoride treatments (NaF) reduced the mechanical strength by converting some amount of bone mineral into calcium fluoride. The kinetics of cortical bone DM in 0.6N HCl was discussed in detail by Castro-Ceseña *et al.* [2.27]. The steady state DM reaction was found to be a first order reaction and kinetic parameters (activation energy and rate constant) were calculated. Since there are no systematic studies on mechanical properties of partially DM cortical bone, the main goal of this research is to find a correlation between mineral content during demineralization and the corresponding mechanical response.

### 2.2.2 Materials and methods

About 100 samples for compression testing (5mm x 5mm x 7.5mm) were cut out from the same portion of the bone in order to minimize variations in density and mineral content. Samples were prepared for all three anatomical directions (see Fig. 2.1). Bone samples were demineralized at different times through a controlled process by aging in 0.6N hydrochloric acid (HCl) at room temperature, following the procedure described in [2.28]. Acid solutions were changed every two hours in order to avoid saturation that can affect the process. The whole demineralization process took about 50 hours. The amount of mineral removed was calculated by measuring the Ca concentration in solutions extracted at set periods of time. The solutions were quantitatively analyzed by the inductively coupled plasma optical emission spectrometry (ICP-OES). Based on these results, master curves for DM were determined for all three anatomical directions (see Fig. 2.9). Complete DM was verified using the procedure outlined in [2.27]. Three conditions of DM were tested: 35 vol.%, 45 vol.% and 55 vol.% mineral removal from the untreated (UT) bone.

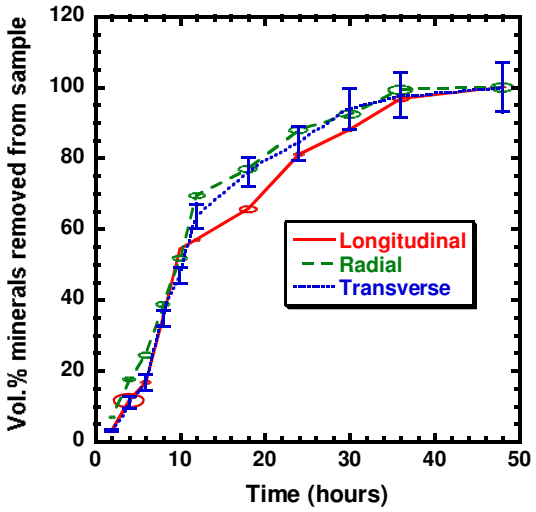


**Figure 2.9** Master demineralization curves for the three anatomical directions. Demineralization was slightly faster in the radial and transverse directions as compared to the longitudinal direction.

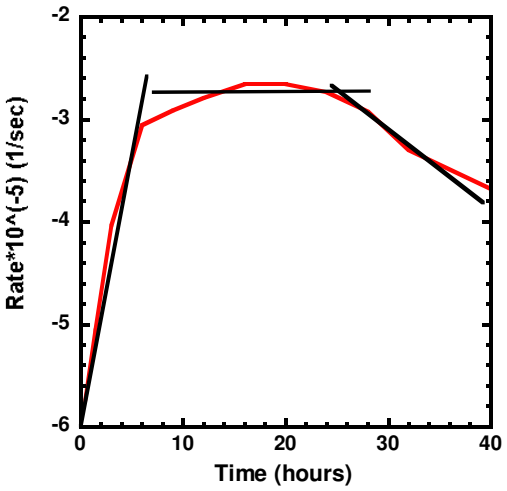


**Figure 2.10** Rate of demineralization as a function of time. The demineralized samples were from the steady state region (flat region). Modified from [2.29].

### 2.2.3 Results and discussion

The DM process occurred at a somewhat higher rate for the radial and transverse samples compared with longitudinal ones in the time range of 10 to 36 hours, as can be

observed in Fig. 2.9. The quickest way for the minerals to dissolve from the bone is along the vascular channels in the osteons, therefore, samples with the largest osteon surface area will demineralized slightly faster, as shown at Figs. 2.1 and 2.9.

It was shown by Castro-Ceseña *et al.* [2.27] that demineralization process went through three distinctive stages, corresponding to different demineralization rates. During the first stage, the rate constantly increased as acid solution demineralized the peripheral part of the sample. During the second stage DM occurred on a steady state that corresponds to DM of the central part of the bone sample. At the end of reaction (third stage) rate constant decreased, as mineral concentration in the bone became depleted (see Fig. 2.10). Based on these results, we used samples that were DM uniformly inside the steady state region. Three different degrees of DM were chosen inside this steady state region (35 vol.% DM, 45 vol.% DM, and 55 vol.% DM). Cortical bovine femur bone contains ~ 45 vol.% mineral – thus our samples had total bone mineral contents of ~ 16%, 20% and 25%.

Figure 2.11 shows the stress-strain curves for the different stages of DM and the three anatomical directions. For the UT bone, the radial direction has the highest toughness (area under the stress-strain curve) value while the longitudinal one is the stiffest, in agreement with [2.46]. Removal of the mineral shows a drastic change in the curves. First, what is noted is that there is now a 'toe' region, the low strain region. This indicates the larger influence of a protein phase (as the DM progressed). Usually this region is called physiological region where the tissue is normally functions [2.47]. Secondly, the maximum stress has been reduced significantly. Third, the elastic modulus – taken as the steepest portion of the stress-strain curve – was significantly

reduced, ~10 times, between the untreated state and 35 vol.% DM. It is clearly seen that the radial direction appears to be stiffest and strongest bone direction for all DM stages. Table 2.2 summarizes the elastic modulus and the peak stress under the various DM conditions.

One interesting feature is that there is a measurable difference between the radial and transverse directions for the all DM stages. From Fig. 2.1, it appears that there should be no difference, since the osteon orientation is perpendicular to the loading direction in both cases. However, the difference can be clearly seen at Fig. 2.11 and Table 2.2 for all DM stages. The radial direction is stiffer and stronger than the transverse one. This can be explained by consideration of the bone structure. The outer part of bone consists of a circumferential lamellar structure that is parallel to the bone surface [2.48]. This region has a thickness of ~ 200 μm, consisting of 5-10 lamellae. In addition, the mineralized collagen fibers in each lamella are oriented at different angles, forming an outer sheath and thus giving the bone extra strength in the radial direction.

**Table 2.2** Elastic modulus and peak stress from compressive stress-strain curves of untreated, 35 vol.% DM, 45 vol.% DM and 55 vol.% DM in the longitudinal (L), transverse (T) and radial (R) directions. *n* is the number of samples tested.

| | **Untreated** | | **35 vol.% DM** | | **45 vol.% DM** | | **55 vol.% DM** | |
|---|---|---|---|---|---|---|---|---|
| | **E (GPa)** | **$\sigma_p$ (MPa)** | **E (GPa)** | **$\sigma_p$ (MPa)** | **E (GPa)** | **$\sigma_p$ (MPa)** | **E (GPa)** | **$\sigma_p$ (MPa)** |
| **L** (*n* = 6) | 22 ± 2 | 138 ± 20 | 2.3 ± 0.3 | 51 ± 5 | 1.6 ± 0.1 | 45 ± 8 | 1.5 ± 0.3 | 40 ± 8 |
| **R** (*n* = 6) | 12 ± 1 | 145 ± 10 | 2.4 ± 0.1 | 75 ± 10 | 2.0 ± 0.1 | 69 ± 7 | 1.8 ± 0.1 | 64 ± 7 |
| **T** (*n* = 6) | 16 ± 2 | 124 ± 10 | 1.5 ± 0.3 | 50 ± 10 | 1.0 ± 0.2 | 42 ± 5 | 0.9 ± 0.1 | 29 ± 7 |

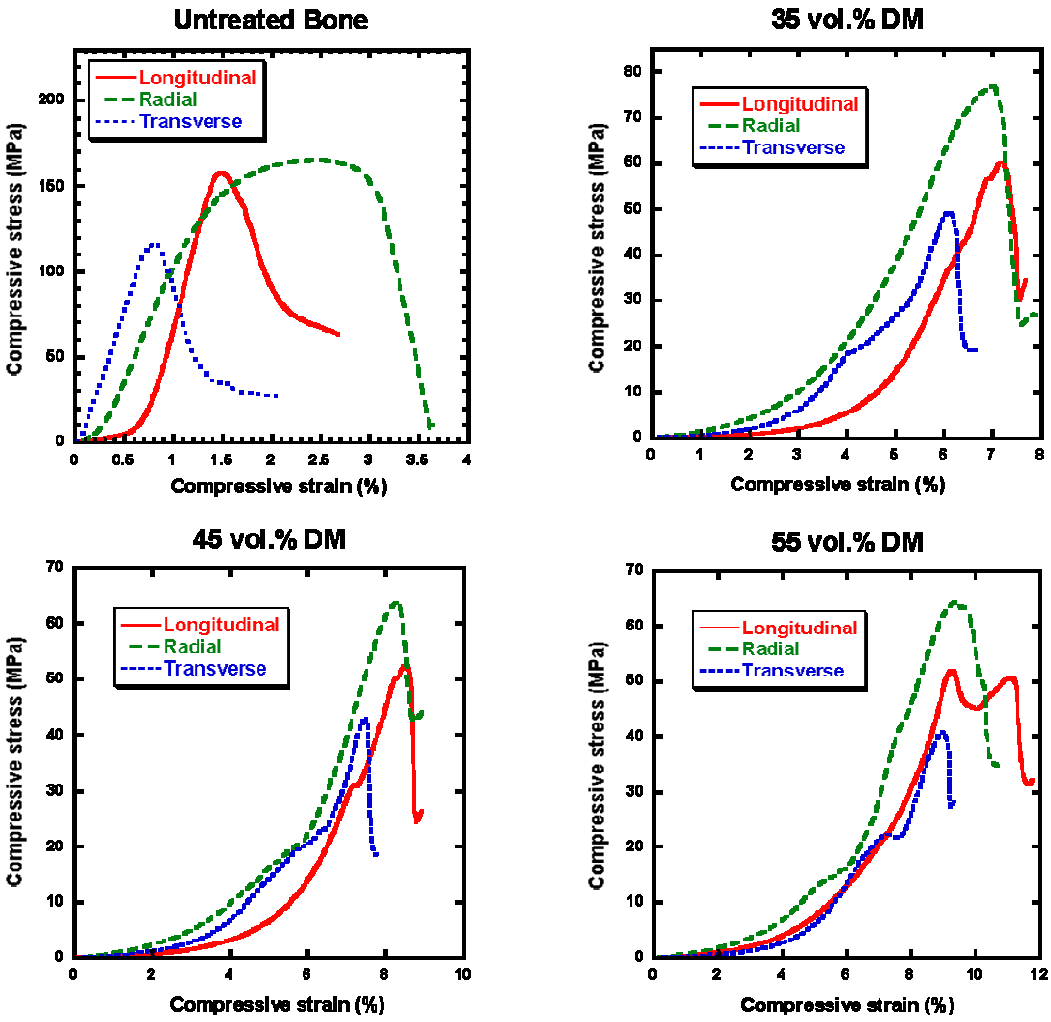


**Figure 2.11** Stress-strain curves for untreated bone and different degrees of bone demineralization. It is clearly seen that even a small amount of mineral deficiency dramatically changes the stiffness and strength.

### 2.2.3 Conclusions

This study is first to evaluate the compressive properties of partially demineralized cortical bone in three anatomical directions. It was found that the radial direction is the strongest and the stiffest for all demineralization stages due to existence of an outer circumferential lamellae sheath with mineralized collagen fibers oriented differently,

compared to the interior of the bone. Moreover, even a small mineral deficiency (16 vol.%) dramatically affects strength and stiffness of bone.

## 2.3 Initial Anisotropy in Demineralized Bovine Cortical Bone in Compressive Cyclic Loading-Unloading

The mechanical properties of demineralized bovine cortical femur bone were investigated by cyclic loading-unloading compression in three anatomical directions (longitudinal, radial, transverse) within the physiological strain range. The loading responses in the radial and transverse directions were nearly linear up to 2% strain, while the response in longitudinal direction was strongly non-linear in that range of strain. The unloading responses were non-linear for each anatomical direction, giving rise to overall loading-unloading hysteresis and cyclic dissipation of energy. The mechanical properties were observed to be anisotropic: the radial direction was found to be the most energy dissipative, while the longitudinal direction appeared to be the stiffest bone direction. The cyclic loading mostly affects the bone stiffness in the radial and transverse directions, while the longitudinal direction was found to be the least affected. These anisotropic properties can be attributed to the differences in collagen fibers alignment and different microstructural architecture in three different anatomical bone directions.

### 2.3.1 Introduction and background

Cyclic loading-unloading experiments on bone were performed by many groups [2.49-2.51] for cortical and trabecular bones. Keaveny *et al.* [2.49] performed compression loading up to 4% strain followed by the immediate unloading to a zero stress level and reloading up to approximately same strain level on a human vertebral trabecular bone. They reported percent of elastic modulus and strength reduction and concluded that occasional overloading of bone can increase the probability of bone fractures because of the mechanical degradation of a trabecular network. Pattin *et al.* [2.50] measured the fatigue properties of human femoral cortical bone, investigating the changes in secant moduli and cyclic energy dissipation during the load-controlled fatigue experiments. They reported that cortical bone loaded in tension up to $2.5x10^{-3}$ and in compression up to $4x10^{-3}$ strain recover to zero strain after unloading. Schaffler *et al.* [2.51] examined the fatigue properties of bovine cortical bone loaded up to strain magnitudes less than $2x10^{-3}$. They found that in these loading conditions cortical bone can withstand several millions of cycles without fatigue failure, and, moreover, after initial stiffness degradation of about 6%, bone stiffness does not significantly changes. These findings suggest that physiological loading conditions within the average lifetime number of cycles do not result in fatigue failure. All experiments mentioned above were performed on samples in longitudinal direction. Study of cyclic loading-unloading of demineralized cortical bone (pure bone protein matrix) for three anatomical directions is the main goal of this research.

Collagen based biomaterials are widely used to construct tissue engineering scaffolds and have found many applications from artificial bone substitutes [2.52] to

artificial skin [2.53]. For each of these, the analysis of mechanical behavior of bone collagen under different loading conditions is of great importance. This research is of medical interest since many groups (e.g., Hiraoka et al., 2003; Taira et al., 2006; Ratanavaraporn et al., 2008; Liu et al., 2010; Kane and Roeder, 2012) [2.54-2.58] have recently investigated collagen sponges structure and properties for prospective bone substitutes.

### 2.3.2 Materials and methods

About 60 samples for compression testing (parallelepipeds 5 mm x 5 mm x 7.5 mm, 20 for the each anatomical direction) were prepared (see Fig. 2.1). Samples were demineralized using the procedure described at **Section 2.2.2**. Compression testing was performed in loading-unloading conditions: samples were loaded under strain-controlled loading until 1% compressive strain, then unloaded at the same rate until zero stress was reached. Three consecutive cycles up to 1% compressive strain, followed by unloading, were performed in all three anatomical directions. In addition, ten consecutive cycles up to 2% compressive strain were performed for samples in three anatomical directions. The strain levels of 1% and 2% were chosen because they are within the physiological strain region of soft biological tissues [2.59].

### 2.3.3 Results and discussion

Figure 2.12 shows SEM images of a demineralized (DM) cortical bone, pointing out the preferential collagen fibers alignment along the bone growth direction. This preferential orientation plays a crucial role in the DM cortical bone response during the compression.

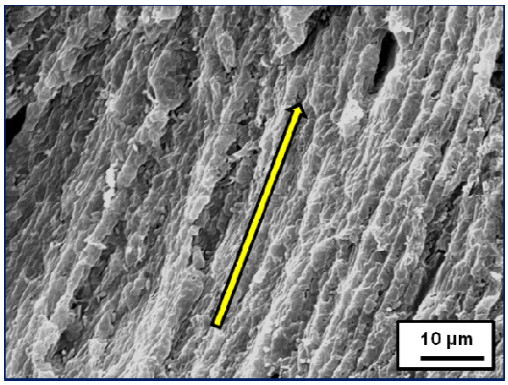


**Figure 2.12** SEM image of demineralized cortical bone showing collagen fibers alignment along bone growth direction (shown by arrow).

Table 2.3 summarizes the hydrated density, initial tangent modulus, secant modulus, and hysteresis areas for three consecutive cycles for DM cortical bone tested in three anatomical directions. The initial modulus was defined as a tangent modulus at the beginning of each cycle. The secant modulus of the $i^{th}$ cycle was defined as the ratio of the stress $\sigma^{(i)}$ at the end of the loading portion of that cycle and the recovered strain upon unloading during the previous cycle, i.e.,

$$E_s^{(i)} = \sigma^{(i)}/( \varepsilon_0 - \varepsilon_r^{(i-1)}), \quad (i = 1, 2, 3, \ldots), \tag{2.7}$$

where $\varepsilon_0$ is the maximum strain level during the loading, and $\varepsilon_r^{(0)} = 0$.

The experimentally observed small gradual increase of the secant modulus with the number of cycles can be attributed to gradual collagen compaction and rearrangement of its microstructure during repeated compressive loading.

**Table 2.3** density, initial tangent modulus, secant modulus, and hysteresis area for demineralized cortical bone under loading-unloading compression for different anatomical directions. Initial tangent modulus, secant modulus, and hysteresis area are presented for three consecutive cycles, shown in Figure 2.13. The notation is: D = anatomical direction, L = longitudinal (N = 10), R = radial (N = 10), T = transverse (N = 10).

| **D** | **Density ($g/cm^3$)** | **Initial tangent modulus, $E^{(i)}$ (MPa)** | | | **Secant modulus, $E_s^{(i)}$ (MPa)** | | | **Hysteresis area, x1000 ($J/m^3$)** | | |
|---|---|---|---|---|---|---|---|---|---|---|
| | | **1ST cycle** | **2nd cycle** | **3rd cycle** | **1st cycle** | **2nd cycle** | **3rd cycle** | **1st cycle** | **2nd cycle** | **3rd cycle** |
| L | 1.21 ± 0.02 | 5.1 ± 0.9 | 5.2 ± 0.5 | 5.3 ± 0.5 | 2.1 ± 0.4 | 2.2 ± 0.4 | 2.3 ± 0.5 | 3.7 ± 0.4 | 2.3 ± 0.4 | 2.0 ± 0.2 |
| R | 1.18 ± 0.02 | 3.6 ± 0.5 | 4.4 ± 0.5 | 4.5 ± 0.5 | 2.6 ± 0.4 | 3.5 ± 0.6 | 3.6 ± 0.6 | 10.1 ± 2.5 | 2.3 ± 0.6 | 1.3 ± 0.4 |
| T | 1.19 ± 0.01 | 2.3 ± 0.2 | 2.5 ± 0.2 | 2.6 ± 0.2 | 1.8 ± 0.1 | 2.0 ± 0.2 | 2.1 ± 0.2 | 3.2 ± 0.8 | 1.7 ± 0.2 | 1.2 ± 0.2 |

Figure 2.13 shows the representative stress-strain curves during cyclic loading-unloading compression of DM samples in three different directions for the first three consecutive cycles. The stiffness in the longitudinal direction was significantly larger compared to the radial ($p= 0.03$) and transverse ($p = 0.01$) direction, while there was no significant difference in stiffness between radial and transverse directions ($p = 0.24$). These findings are in agreement with the conclusions from **Section 2.1.4**, which reported the same trend for the bulk compression elastic modulus of DM cortical bone.

The criterion for statistical significance was $p < 0.05$. Furthermore, the loading portion of the stress-strain curve for the longitudinal direction was strongly non-linear, while it was nearly linear for the other two directions. The unloading responses were non-linear for each anatomical direction, giving rise to overall loading-unloading hysteretic response.

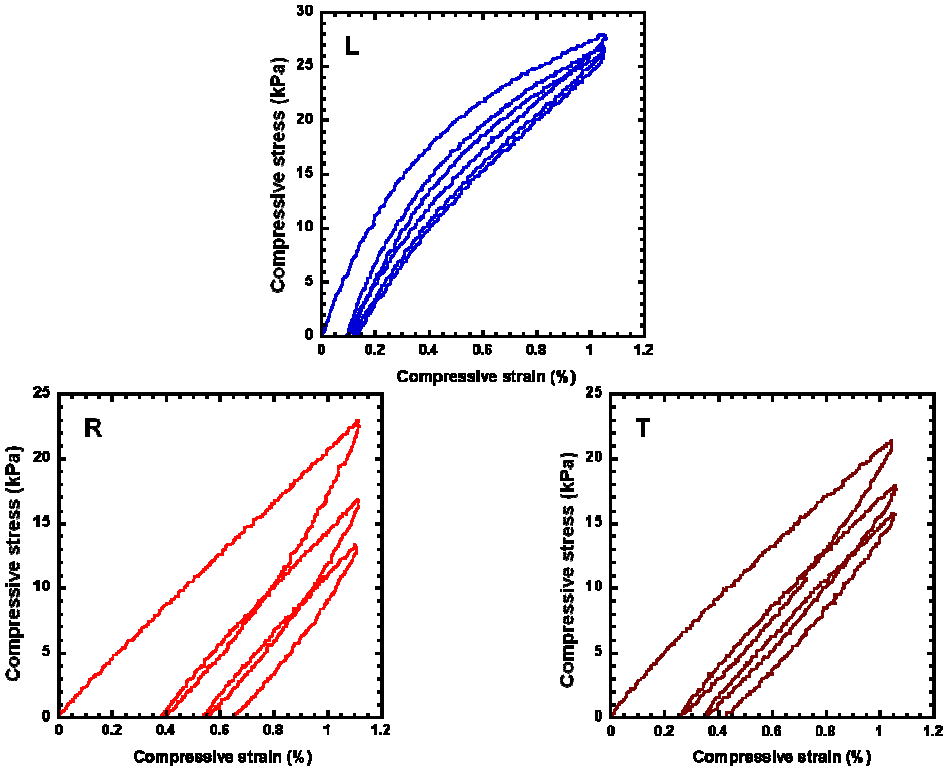


**Figure 2.13** Representative stress-strain curves during cyclic loading-unloading compression of demineralized samples in three different anatomical directions, showing first three consecutive cycles. L = longitudinal, R = radial, T = transverse.

A pronounced difference in hysteresis areas (dissipated energy) between longitudinal/transverse and radial directions, particularly for the first cycle, is reported

in Table 2.3. These results support the conclusion from **Section 2.1.4** on the importance of the periosteal sheath for mechanical properties of bone in the radial direction. In this sheath, the mineralized collagen lamellae do not form an osteonal structure, but are oriented smoothly in the longitudinal direction, making a significant contribution to the mechanical properties in this direction. As a result, cortical bone was found to be more energy absorbent in the radial direction. The results of present study show that radial direction is the most energy dissipative for DM cortical bone as well, demonstrating that bone internal microstructure plays the crucial role in both untreated and DM cortical bone.

#### *2.3.3.1 Secant and initial moduli*

The secant moduli were progressively larger in consecutive cycles for all three anatomical directions (Table 2.3). Additionally, the secant modulus was more than twice lower than the initial tangent modulus for longitudinal direction by the end of the third cycle, but there was a little difference between these two moduli for the radial and transverse directions. This means that DM bone was able to rearrange its internal structure in the radial and transverse directions to evenly support the stresses in three loading-unloading cycles, while it was unable to do so for the longitudinal direction, mainly because of collagen fibers preferential orientation in this particular direction. In addition, the relative change of secant modulus between the first two cycles was found to be the greatest for the radial direction. The initial and secant moduli for three consecutive cycles were found to be the most consistent in the transverse bone direction.

#### *2.3.3.2 Strain offsets*

The strain offsets (the residual strain upon unloading) reached equilibrium after the first three loading-unloading cycles for longitudinal direction, while there were progressively larger strain offsets for both radial and transverse directions (Fig. 2.13). Additional experiments for the strain-controlled cyclic loading-unloading compression up to ten cycles were performed to verify this assumption. Fig.2.14 shows representative stress-strain curves along with stress-time, and strain-time curves for these experiments. The difference between areas of hysteresis loops for cycles after the third cycle was negligibly small for the longitudinal direction, while the hysteresis loops were gradually becoming smaller all the way up to tenth cycle for the radial and transverse directions. These findings clearly demonstrate the anisotropic behavior of DM cortical bone in cyclic loading-unloading compression. As was mentioned above, difference in DM bone behavior between the radial and transverse directions is a consequence of the existence of the periosteal sheath with a different microstructure in the radial bone direction. Mineralized collagen lamellae are oriented differently in this sheath, so that the internal microstructure of radially oriented samples was not uniform, in contrast to rather uniform transversely oriented samples (see **Section 2.1.4**). The same conclusion applies to DM cortical bone, which explains the difference in cyclic loading-unloading compression behavior between the radial and transverse directions, reported in Figs 2.13, 2.14.

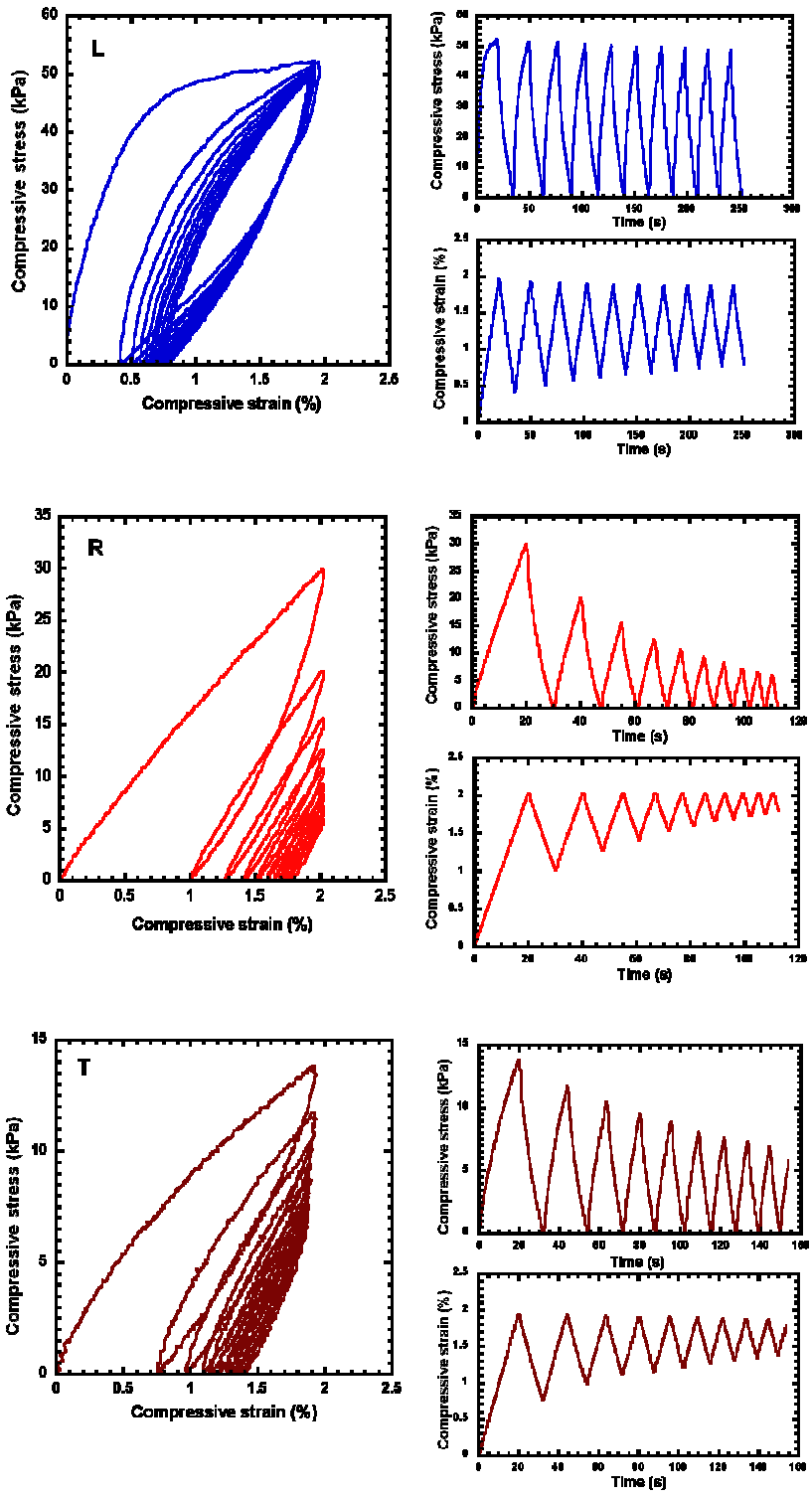


**Figure 2.14** Representative stress-strain, stress-time, and strain-time curves for cyclic loading-unloading compression (10 consecutive cycles) for demineralized cortical bone in different anatomical directions. L = longitudinal, R = radial, T = transverse.

The stresses versus time curves are different for all three anatomical directions (Fig. 2.14). The areas of the consecutive cycles are almost the same for the longitudinal direction, but are progressively smaller for the radial and transverse directions. Moreover, from the strain-time curves it can be seen that strain accumulation is larger for the radial and transverse directions, while it is least in the longitudinal direction.

#### *2.3.3.3 Cumulative damage*

A cumulative damage of cyclically loaded cortical bone involves bone inelasticity and viscoelasticity [2.60]. Cortical bone loaded in strain-controlled tension up to 1.1% strain, and unloaded at the same rate (the conditions similar to the conditions of the present study) demonstrated behavior similar to the DM bone behavior (Figs. 2.13 and 2.14). The unloaded curve of the first cycle crosses the zero stress level at the strain value that was approximately equal to the third of the maximum strain for all three anatomical directions tested. The main difference between cortical bone behavior described at [2.60] and DM cortical bone behavior from the present study, is that for DM cortical bone the initial (tangent) modulus at the beginning of each cycle remains nearly the same, while it drops significantly (about 30%) for untreated cortical bone. This supports the conclusion that DM cortical bone does not experience large stiffness degradation during the first 10 cycles of compressive cyclic loading-unloading within the physiological strain region.

It is worth mentioning that, after sufficient amount of time, the samples for all three anatomical directions returned back to their original shape and volume (in water at zero load) after the testing, proving that DM cortical bone did not experience permanent

or plastic deformation during first 10 cycles of cyclic loading-unloading in the considered strain range.

Figure 2.15 shows the vanishing of the secant/tangent moduli ($E_s^{(i)}/E^{(i)}$), scaled by the versus the cycle number *(i)* [2.51] for three anatomical directions. The results in Fig. 2.15 indicate that there was no significant difference in $E_s^{(i)}/E^{(i)}$ between the radial and transverse directions. Additionally, these results indicate that this ratio reached an equilibrium value for all three anatomical directions by the fourth cycle. The equilibrium value for the radial and transverse directions was close to 0.5, while for the longitudinal direction it was ~ 0.8, which means that the stiffness in the longitudinal direction is least affected by cyclic loading. The gradual increase of the secant modulus with the number of cycles can be attributed to gradual collagen compaction and rearrangement of its microstructure during repeated compressive loading.

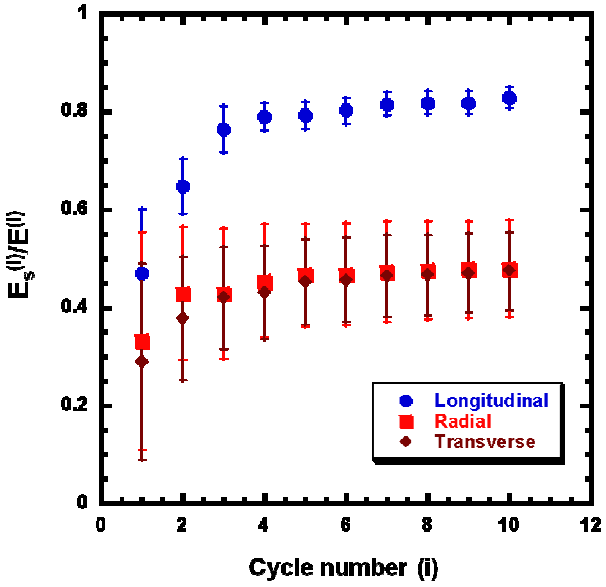


**Figure 2.15** The vanishing of the secant/tangent moduli ratio $E_s^{(i)}/E^{(i)}$ with the cycle number during first 10 loading-unloading compression cycles for longitudinal, radial, and transverse directions.

### 2.3.4 Conclusions

The mechanical properties under cyclic loading-unloading compression for strains up to 2% were investigated for demineralized (100% protein) bovine femur cortical bone in three anatomical directions. The main findings are:

- Demineralized bone shows anisotropic mechanical behavior.
- Demineralized bone is significantly stiffer in the longitudinal than in the radial and transverse directions due to preferential collagen fibers orientation.
- The radial direction is the most energy dissipative due to the periosteal sheath.
- There is no significant difference in the cyclic hysteresis area between the longitudinal and transverse directions due to uniform internal microstructure.
- The initial tangent modulus at the beginning of each loading cycle was little affected during first 10 cycles of compressive loading within the physiological strain range.
- Stiffness parameter was found to be the smallest for the longitudinal direction.
- There was no difference in stiffness parameter between the radial and transverse directions.

**Acknowledgements:**

Sub-chapter 2.1, in full, is a reprint of the material as it appears in "Anisotropy in the compressive mechanical properties of bovine cortical bone: Mineral and protein constituents compared with untreated bone," in Acta Biomaterialia, 7, 3170-3177, 2011. E. Novitskaya, A.B. Castro-Ceseña, P.-Y. Chen, S. Lee, G. Hirata, V.A. Lubarda, J.

McKittrick. The dissertation author was the primary investigator and author of this paper.

Sub-chapter 2.2, in full, is a reprint of the material as it appears in "Investigations into demineralized cortical bone", in Materials Research Society Symposium Proceeding, Fall 2010, Volume 1301, Symposium NN1.7. E.E. Novitskaya; A.B. Castro-Ceseña; P.-Y. Chen; J. Vasquez; R. Urbaniak; S. Lee; G.A. Hirata; J. McKittrick. The dissertation author was the primary investigator and author of this paper.

Sub-chapter 2.3, in full, has been submitted for publication as it may appear in "Initial anisotropy in demineralized bovine cortical bone in compressive cyclic loading-unloading," in Materials Science and Engineering C, 2012. E.E. Novitskaya; S. Lee; V.A. Lubarda; J. McKittrick. The dissertation author was the primary investigator and author of this paper.

### 2.3.5 References

[2.1] Currey JD. The mechanical properties of bone. Clin Orthop Relat Res 1970;73:210-231.

[2.2] Reilly DT, Burstein AH. The mechanical properties of cortical bone. J Bone Joint Surg Am 1974;56:1001-1022.

[2.3] Burstein AH, Zika JM, Heiple KG, Klein L. Contribution of collagen and mineral to the elastic-plastic properties of bone. J Bone Joint Surg Am 1975;57:956-961.

[2.4] Rho JY, Kuhn-Spearing L, Zioupos P. Mechanical properties and the hierachical structure of the bone. Med Eng Phys 1998;20:92-102.

[2.5] Currey JD. Bones: Structure and Mechanics. New York: Princeton University Press; 2002. pp. 12-21.

[2.6] Currey JD. Measurement of the mechanical properties of bone: A recent history. Clin Orthop Relat Res 2009;467:1948-1954.

[2.7] Reilly DT, Burstein AH. The elastic and ultimate properties of compact bone tissue. J Biomech 1975;8:393-405.

[2.8] Bonfield W, Grynpas MD. Anisotropy of the Young's modulus of bone. Nature 1977;270:453-454.

[2.9] Hasegawa K, Turner CH, Burr DB. Contribution of collagen and mineral to the elastic anisotropy of bone. Calcif Tissue Int 1994;55:381-386.

[2.10] Macione J, DePaula CA, Guzelsu N, Kotha SP. Correlation between longitudinal, circumferential, and radial moduli in cortical bone: Effect of mineral content. J Mech Behav Biol Mater 2010;3:405-413.

[2.11] Rho JY, Roy II ME, Tsui TY, Pharr GM. Elastic properties of microstructural components of human bone tissue as measured by nanoindentation. J Biomed Mater Res 1998;45:48-54.

[2.12] Swadener JG, Rho JY, Pharr GM. Effects of anisotropy on elastic moduli measured by nanoindentation in human tibial cortical bone. J Biomed Mater Res 2001;57:108-112.

[2.13] Fan Z, Swadener JG, Rho JY, Roy ME, Pharr GM. Anisotropic properties of human tibial cortical bone as measured by nanoindentation. J Ortho Res 2002;20:806-810.

[2.14] Rho JY. An ultrasonic method for measuring the elastic properties of human tibial cortical and cancellous bone. Ultrasonics 1996;34:777-783.

[2.15] Seto J, Gupta HS, Zaslansky P, Wagner HD, Fratzl P. Tough lessons from bone: extreme mechanical anisotropy at mesoscale. Adv Funct Mater 2008;18:1905-1911.

[2.16] Landis WJ, Hodgens KJ, Arena J, Song MJ, McEwen BF. Structural relations between collagen and mineral in bone as determined by high voltage electron microscopic tomography. Microsc Res Tech 1996;33:192-202.

[2.17] Martin RB, Boardman DL. The effects of collagen fiber orientation, porosity, density, and mineralization of bovine cortical bone bending properties. J Biomech 1993;26:1047-1054.

[2.18] Martin RB, Lau ST, Mathews PV, Gibson VA, and Stovert SM. Collagen fiber organization is related to mechanical properties and remodeling in equine bone. A comparison of two methods. J Biomech 1996;29:1515-1521.

[2.19] Piekarski K. Analysis of bone as a composite material. Int J Eng Sci 1973;11:557-565.

[2.20] Mack RW. Bone – a natural two-phase material. Tech Mem Biomech Lab, University of California, Berkeley 1964.

[2.21] Iyo T, Maki Y, Sasaki N, Nakata M. Anisotropic viscoelastic properties of cortical bone. J Biomech 2004; 37:1433-1437.

[2.22] Skedros JG, Sorenson SM, Takano Y, Turner CH. Dissociation of mineral and collagen orientations may differentially adapt compact bone for regional loading environments: Results from acoustic velocity measurements in deer calcanei. Bone 2006;39:143-151.

[2.23] Chen P-Y, Toroian D, Price PA, McKittrick J. Minerals form a continuum phase in mature cancellous bone. Calcif Tissue Inter 2011;88:351-61.

[2.24] Rosen VB, Hobbs LW, Spector M. The ultrastructure of anorganic bovine bone and selected synthetic hydroxyapatites used as bone graft substitute materials. Biomaterials 2002;23:921-928.

[2.25] Chen P-Y, McKittrick J. Compressive mechanical properties of demineralized and deproteinized cancellous bone. J Mech Behav Biomed Mater 2011;4:961-73.

[2.26] Lubarda VA, McKittrick J, Novitskaya EE, Chen PY. Elastic properties of cancellous bone in terms of elastic properties of its mineral and protein phase with application to their osteoporotic degradation. Mech Mater 2012;44:139-150.

[2.27] Castro-Ceseña AB, Novitskaya EE, Chen P-Y, Hirata GA, McKittrick J. Kinetic studies of bone demineralization at different HCl concentrations and temperatures. Mater Sci Eng C 2011;31:523-530.

[2.28] Toroian D, Lim JL, Price PA. The size exclusion characteristics of type-I collagen: implications for the role of non-collagenous bone constituents in mineralization. J Biol Chem 2007;282:22437-22284.

[2.29] Broz JJ, Simske SJ, and Greenberg AR. Material and compositional properties of selectively demineralized cortical bone. J Biomech 1995;28:1357-1368.

[2.30] Meyers MA, Chawla KC. Mechanical Behavior of Materials. New York: Cambridge University Press; 2009. pp. 449-457.

[2.31] Weibull W. A statistical distribution function of wide applicability. J Appl Mech 1951;18:293-297.

[2.32] Rinne H. The Weibull Distribution: A Handbook, Chapman and Hall/CRC; 2008.

[2.33] Abramowitz M, Stegun IA. Handbook of mathematical functions with formulas, graphs, and mathematical tables. New York: Dover publications; 1972.

[2.34] Gross D, Seeling T. Micromechanics and homogenization. In: Fracture mechanics with an introduction to micromechanics. New York: Springler; 2006. pp. 218-287.

[2.35] Heidermann E, Riess W. Die Veranderungen Des Kollagens Bei Entwasserung Mit Aceton + Die Konsequenzen Dieser Veranderung Fur Die Kollagenstruktur. Hoppe-Seyler's Z Physiol Chem 1964;337:101.

[2.36] Potoczek M. Hydroxyapatite foams produced by gelcasting using agarose. Mater Lett 2008;62:1055-1057.

[2.37] Wainwright SA, Biggs WD, Currey JD, Gosline JM. Mechanical Design in Organisms. New Jork: Wiley; 976. pp. 174-181.

[2.38] Fung YC. The anatomy of a long bone. In: Biomechanics: Mechanical Properties of Living Tissues. New York: Springer-Verlag; 1981. pp. 384-389.

[2.39] Actis AB, Obwegeser JA, Ruperez C. J Biomater Appl 2004;18:193.

[2.40] Frank JD, Balena R, Masarachia P, Seedor JG, Cartwright ME. Histochemistry 1993;99:295.

[2.41] Akbay A, Bozkurt G, Ilgaz O, Palaoglu S, Akalan N, Benzel EC. Eur Spine J 2008;17:468.

[2.42] Dodds RA, York-Ely AM, Zhukauskas R, Arola T, Howell J, Hartill C, Cobb RR, Fox C. J Biomater Appl 2010;25:195.

[2.43] Broz JJ, Simske SJ, Greenberg AR. J Biomech 1995;28:1357.

[2.44] Lewandrowski K-U, Tomford WW, Michaud NA, Schomacker KT, Deutsch TF. Calcif Tissue Int 1997;61:294.

[2.45] Kotha SP, Walsh WR, Pan Y, Guzelsu N. Bio-Med Mater Engin 1998;8:321.

[2.46] Rho J-Y, Kuhn-Spearing L, Zioupos P. Med Eng Phys 1998;20;92.

[2.47] Fung YC. Biomechanics: Mechanical properties of living tissues. New-York: Springer-Verlag; 1981. pp. 210-211.

[2.48] Fung YC. Biomechanics: Mechanical properties of living tissues. New-York: Springer-Verlag; 1981. pp. 387-388.

[2.49] Keaveny TM, Wachtel F, Kopperdahl DL. Mechanical behavior of human trabecular bone after overloading. J Orthop Res 1999;17:346-353.

[2.50] Pattin CA, Caler WE, Carter DR. Cyclic mechanical property degradation during fatique loading of cortical bone. J Biomech 1996;29:69-79.

[2.51] Schaffler MB, Radin EL, Burr DB. Long-term fatigue behavior of compact bone at low strain magnitude and rate. Bone 1990;11:321-326.

[2.52] Meinel L, Karageorgiou V, Fajardo R, Snyder B, Shinde-Patil V, Zichner L, Kaplan D, Langer R, Vunjak-Novakovic G. Bone tissue engineering using human mesenchymal stem cells: Effects of scaffold material and medium flow. Ann Biomed Eng 2004;32:112-122.

[2.53] Cen L, Liu W, Cui L, Zhang W, Cao Y, 2008. Collagen tissue engineering: Development of novel biomaterials and applications. Pediat Res 2008;63:492-496.

[2.54] Hiraoka Y, Kimura Y, Ueda H, Tabata Y. Fabrication and biocompatibility of collagen sponge reinforced with poly(glycolic acid) fiber. Tissue Eng 2003;9: 1102-1112.

[2.55] Taira M, Sasaki K, Saiton S, Nezu T, Araki Y. Preparation of highly pore-interconnected porous collagen sponges using chloroform and ammonia. J Oral Tissue Eng 2006;4:68-76.

[2.56] Ratanavaraporn J, Kanokpanont S, Tabata Y, Damrongsakkul, S. Effects of acid type on physical and biological properties of collagen scaffolds. J Biomater Sci, Polymer Edition 2008;19:945–952.

[2.57] Liu X, Huang C, Feng Y, Liang J, Fan Y, Zhongwei Gu Z, Zhang X. Reinforcement of a porous collagen scaffold withsurface-activated PLA fibers. J Biomater Sci 2010;21:963–977.

[2.58] Kane RJ, Roeder RK. Effects of hydroxyapatite reinforcement on the architecture and mechanical properties of freeze-dried collagen scaffolds. J Mech Behav BiomedMater 2012;7:41-49.

[2.59] Fung YC. Biomechanics: Mechanical Properties of Living Tissues. New-York: Springer-Verlag; 1981. pp. 196-260.

[2.60] Jepsen KJ, Davy DT, Akkus O. Observations of damage in bone. In: Cowin, S.C. (Ed.), Bone Mechanics Handbook. CRC press, New-York; 2001. 17-1–17-18.

# Chapter 3 MODELING OF THE ELASTIC PROPERTIES OF BONE

## 3.1 Hierarchical Structure of Porosity in Cortical and Trabecular Bone

In this chapter the amount and morphology of cortical and trabecular bone porosity was estimated using optical microscopy and micro-computed tomography technique. The hierarchical structure of porosity in cortical and trabecular bone at different structural scales spanning from nanoscale to trabecular or cortical bone levels was characterized and described. This study was conducted by using samples of untreated, deproteinized and demineralized bones, to obtain better insight into the bone structure and porosities. The motivation of this work is that the porosity in bone has a major effect on its mechanical response, yet it is often neglected in bone models. Investigations of the mechanical properties of bone and its main components (collagen and mineral phases), complemented by modeling, are of importance in orthopedics.

### 3.1.1 Introduction and background

The excellent mechanical properties of bone are a result of its multilayered hierarchical structure spanning from nano- to macro- levels. The bone porosity is also hierarchically arranged. Bone porosity has a significant effect on its mechanical properties. Therefore, its characterization is needed to better assess bone quality and evaluate bone strength and risk of fracture in elderly and osteoporotic patients. The relation between cortical bone porosity and its mechanical properties was obtained experimentally [3.1-3.3]. Recently, micro-computed tomography (μ-CT) and nano-computed tomography (nano-CT) techniques was used to characterize the structure and porosity of cortical [3.4-3.6] and trabecular bone [3.7-3.9] at different length scales. However, a systematic hierarchical characterization of bone porosity spanning several scales is not yet available.

Several models of the elastic properties of bone based on micromechanical and computational approaches were proposed [3.10-3.13]. Recently, the multi-scale model of cortical and trabecular bone as an interpenetrating composite material was developed by Hamed *et al.* [3.14, 3.15] and experimentally verified for cortical bone [3.16]. The hierarchical structure of the porosity in cortical and trabecular bone that was used as inputs in the above models is the main objective of this paper.

### 3.1.2 Materials and methods

#### *3.2.1.1 Sample preparation*

Bovine femur bone samples were obtained from a local butcher. The slaughter age of cattle was about 18 months. The bone was thoroughly cleaned with water, using water pick. The samples were first roughly cut by handsaw and then by a diamond blade. The samples were refrigerated in Hank's balanced saline solution until chemical procedures or structural characterization was performed. Ten cortical and trabecular samples were either demineralized (DM) by aging in HCl solutions using the procedures outlined in [3.17, 3.18] or deproteinized (DP) by aging in NaOCl solutions following the procedures in [3.18]. A special set of cortical and trabecular bone samples (six cubic samples ($1mm^3$)) was prepared for μ-CT scanning. Later on one cortical and one trabecular cubic samples were demineralized, and one cortical and one trabecular cubic samples were deproteinized.

#### *3.2.1.2 Structure characterization*

Polished surfaces of untreated cortical and trabecular specimens were investigated by optical microscopy (OM) using Zeiss Axio imager equipped with CCD camera (Zeiss Microimaging Inc., Thornwood, NY). To investigate the microstructure in 3D, the μ-CT imaging technique was performed at a nominal resolution of 1 μm. The scan produced around 1000 slices (1000x1000 image pixels per slice) resulting in a field of view of a $1mm^3$ cube. This procedure generates high-resolution 3D images without destruction the bone specimens. The μ-CT measurements were conducted in air using Xradia MicroXCT-200 (for UT and DP samples) and Xradia MicroXCT-400 (for DM samples) (Xradia Inc., Pleasanton, CA) instruments. Optical microscopy images were analyzed by ImageJ software program for the porosity estimation. The reconstructed μ-CT tomograms were post-processed using Amira (Visage Imaging, Inc., Berlin, Germany) to analyze 3D microstructures.

### 3.1.3 Results and discussion

Figure 3.1 shows the hierarchical structure of the porosity for cortical and trabecular bone. For both cortical and trabecular bone, the porosity at Level I (nanoscale) includes the spaces between collagen molecules and the spaces between mineralized collagen fibers (Fig. 3.1a). At Level II (sub-microscale), the porosity consists of lacuna spaces (a small space containing bone cells, osteocytes, 10-20 μm in diameter), and canaliculi channels (100-500 nm diameter), connecting the lacunae spaces (Fig. 3.1b). Level III (microscale) porosity in cortical bone takes into account vascular channels and Volkmann's canals that form a continuous network of blood vessels inside the bone

tissue that have diameters of 10-50 µm (Fig. 3.1c). Level IV (mesoscale) porosity in cortical bone consists of large resorption cavities (50-300 µm in diameter), the places where the bone remodeling process starts (Fig. 3.1d). Since trabecular bone does not have the osteonal structure, at micro- and mesoscales (Levels III and IV), a sophisticated trabecular network (between several hundred microns and several millimeters) provides the main contribution into trabecular bone porosity (Fig. 3.1e, f) at those levels.

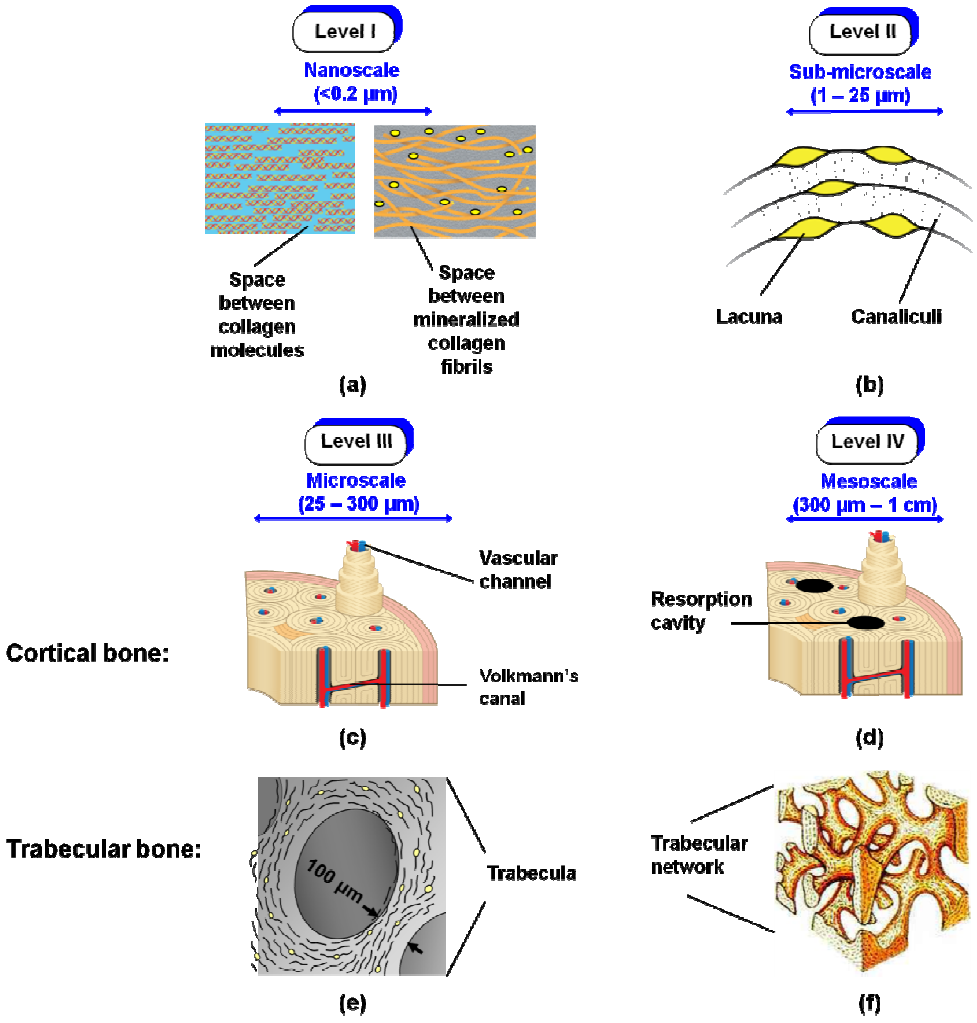


**Figure 3.1** The hierarchical structure of the porosity in cortical and trabecular bone: (a) – nanoscale; (b) sub-microscale; (c) and (e) – microscale for cortical and trabecular bone, respectively; (d) and (f) – mesoscale for cortical and trabecualr bone, respectively.

Representative optical microscopy images of bone cross-section along with ImageJ approximations are shown in Fig. 3.2a, b. Red areas correspond to bone porosity for cortical (Fig. 3.2a), and trabecular bone (Fig. 3.2b).

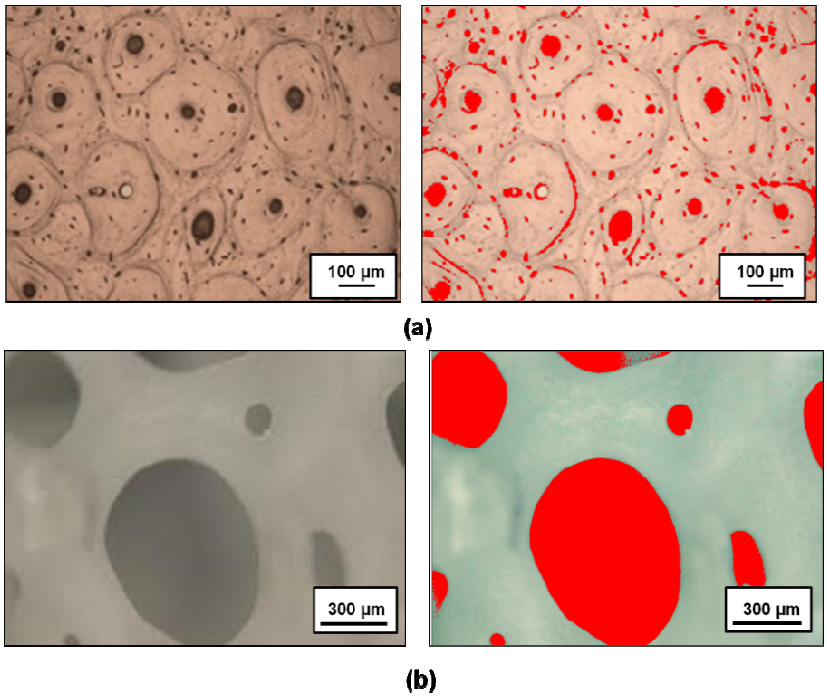


**Figure 3.2** Optical microscopy images of bone cross-section and porosity estimation (in red) for (a) cortical, and (b) trabecular bone.

Figure 3.3 shows µ-CT images for untreated (a), demineralized (b), and deproteinized (c) cortical bone samples. The gold regions correspond to empty spaces (voids). The corresponding porosity was estimated to be 8% for untreated, 52% for demineralized, and 57% for deproteinized cortical bone. The Haversian system (with vascular channels and Volkmann's canals) together with elliptically shaped little lacunae spaces are clearly seen in Fig. 3.3a. This image clearly confirms that µ-CT technique has

the ability not only to estimate the amount of bone porosity, but moreover to show its morphology and distribution. Images for demineralized (Fig. 3.3b) and deproteinized (Fig. 3.3c) cortical bone show both untreated bone porosity, and porosity due to the absence one of the corresponding phases together. Since the amount of collagen in the bone is slightly larger than amount of minerals, the estimated porosity for deproteinized case has the same trend (slightly higher compared to demineralized case). μ-CT images for both treated cases appear similar to each other, since the amount of minerals and collagen (that make a contribution into porosity of corresponded phase), are close to each other.

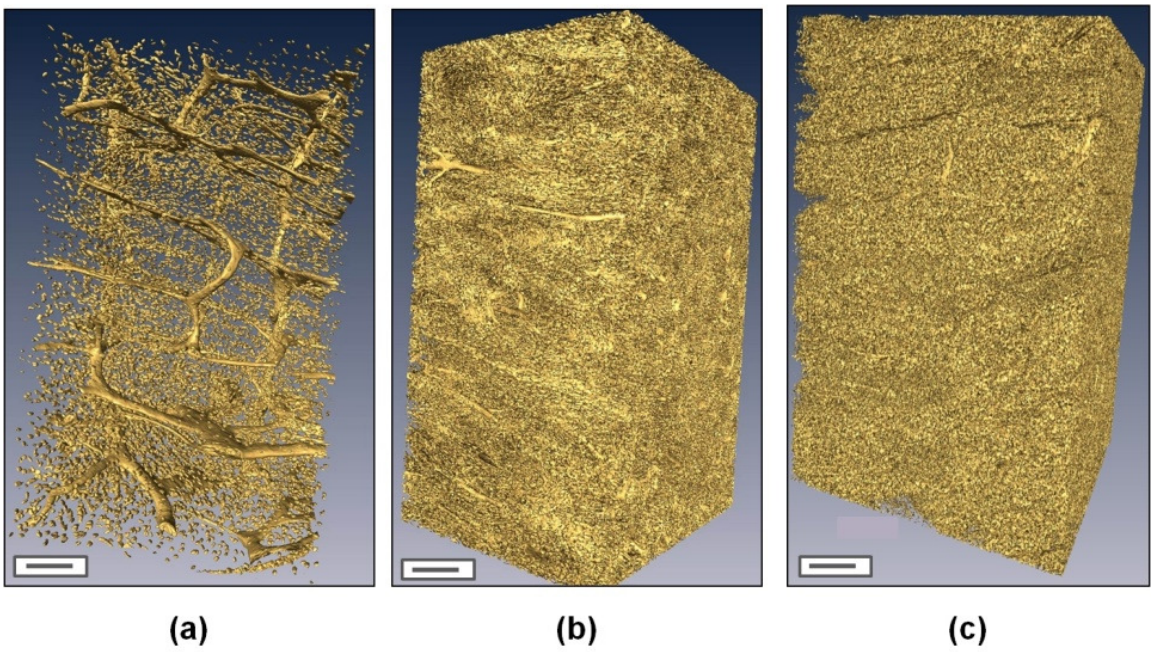


**Figure 3.3** μ-CT images of (a) untreated, (b) demineralized and (c) deproteinized cortical bone. The gold regions correspond to empty spaces (voids). Scale bar = 100 μm.

The trabecular network is clearly seen in the μ-CT images (Fig. 3.4) for untreated (a), demineralized (b), and deproteinized (c) trabecular bone samples. In this case, the gold regions correspond to bone tissue. Porosity was found to be 80% for untreated trabecular bone, to 94% for demineralized trabecular bone, and to 92% for deproteinized samples. Note, that trabecular bone porosity is highly dependent on the anatomical location and, as a result, on the bone's relative density [3.19]; untreated trabecular bone porosity can vary between 70% and 90%.

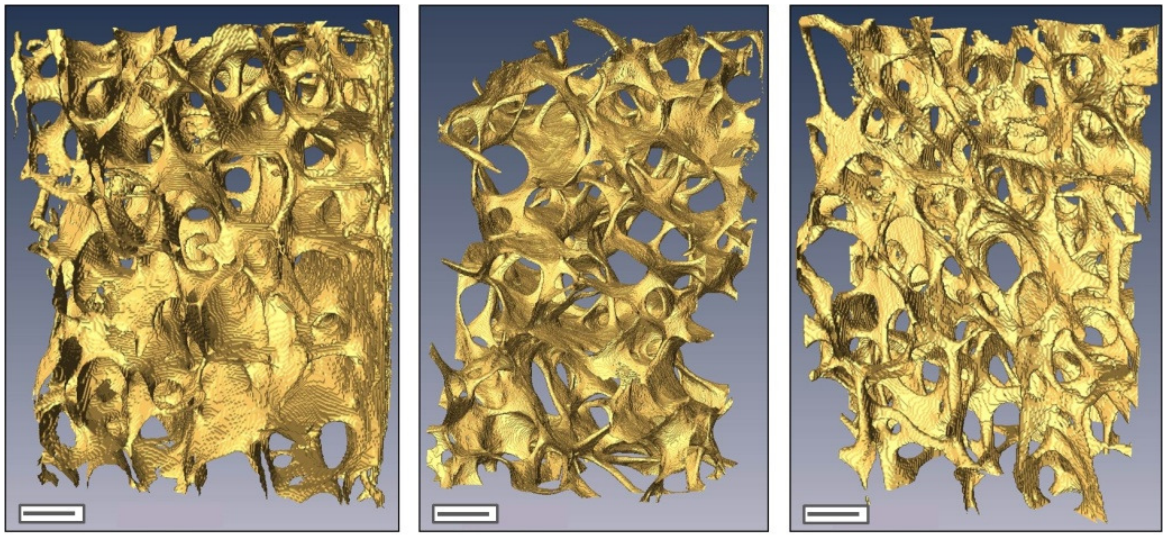


**Figure 3.4** μ-CT images of (a) untreated, (b) demineralized, and (c) deproteinized trabecular bone. Gold regions correspond to bone tissue. Scale bar = 700 μm.

Both treated cases (demineralized and deproteinized) have larger porosity values for cortical and trabecular bone due to absence of one or another corresponding phase. Data for porosity estimation for all three cases (untreated, demineralized, and deproteinized) for both cortical and trabecular bone were later used as input parameters

for multiscale modeling of bone as interpenetrating composite material [3.16]. All successive levels of this model [3.14, 3.15] contain its own amount and distribution of porosity; therefore, the above method on qualitative and quantitative porosity verification does provide important inputs for successful bone modeling.

The results for hierarchical porosity estimation of untreated cortical and trabecular bone, obtained using both methods, are summarized in Table 3.1. Keeping in mind that optical microscopy provides 2D information, while μ-CT gives 3D results; a good agreement between both techniques was found. Since sample preparation and testing method for optical microscopy is relatively simpler compared to μ-CT technique, preliminary reliable data on bone porosity can be collected by this method. However, μ-CT imaging technique should be used not only for more precise porosity estimation, but also for better visualization of its morphology and distribution. In particular, this method is useful to analyze the osteoporotic versus healthy bone architecture.

**Table 3.1** Porosity estimation by μ-CT and optical microscopy (OM) for untreated, demineralized, and deproteinized cortical and trabecular bone.

| **% porosity** | **Untreated** | | **Demineralized** | | **Deproteinized** | |
|---|---|---|---|---|---|---|
| | Trabecular | Cortical | Trabecular | Cortical | Trabecular | Cortical |
| μ-CT | 79.6 ± 1.5 | 7.9 ± 0.8 | 93.3 ± 0.5 | 51.5 ± 3.8 | 92.3 ± 1.1 | 57.1 ± 3.5 |
| OM | 70.4 ± 5.6 | 4.8 ± 1.1 | 91.2 ± 2.1 | N/A | 91 ± 2 | N/A |

### 3.1.4 Conclusions

The hierarchical structure of porosity for untreated, demineralized, deproteinized cortical and trabecular bovine femur bone was analyzed by optical microscopy and μ-CT scanning techniques. The main findings are:

- Bone has a hierarchical structure of porosity from nano- to mesoscale.
- Cortical and trabecular bone porosity were quantified from nano- to mesoscales.
- Optical microscopy provides reliable 2D data on bone porosity at micro- and mesoscales.
- μ-CT scanning technique provides accurate 3D information on bone porosity, its morphology and distribution from sub-microscale to mesoscale.

## 3.2 Correlation of Multi-Scale Modeling and Experimental Results for the Elastic Moduli of Cortical and Trabecular Bone

Cortical and trabecular bones were modeled as nanocomposite materials with hierarchical structures spanning from collagen-mineral level to cortical and trabecular bone levels. In order to verify theoretical models, the compression testing was done on cortical and trabecular bovine femur bone samples and the experimental data were compared with the theoretical results. The micro-computed tomography technique was used to characterize the porosities and structures of cortical and trabecular bones at different length scales, and to provide the inputs needed for the modeling. To obtain more insight on the structure of bone, especially on the interaction of the main constituents (collagen and mineral phases), both cortical and trabecular bone samples were

deproteinized and demineralized and, afterwards, tested mechanically in compression. This information was used to fine-tune our multi-scale model representing bone as an interpenetrating composite material. Very good agreement was found between the theory and experiments for the elastic moduli of untreated, deproteinized, and demineralized cortical and trabecular bones.

### 3.2.1 Introduction and background

Modeling the mechanical properties of bone has long been a challenging task due to the complexity of bone's hierarchical structure. Several models of the elastic properties of bone have been proposed based on analytical and computational approaches [3.10-3.13]. Recent studies [3.18, 3.21] showed that both cortical and trabecular bones are interpenetrating composite materials with continuous mineral and organic phases.

Multi-scale models of cortical and trabecular bones as interpenetrating composite materials were developed in [3.14, 3.15].The amounts and distributions of cortical and trabecular bones' porosities, which are major inputs to the theoretical model, were described in detail in **Section 3.1**. The correlation between the multiscale modeling and experimental results for elastic moduli of cortical and trabecular bones is the main objective of the present study. In this study, the elastic moduli of the UT, DM, and DP cortical and trabecular bone are investigated. A step-by-step modeling approach, involving four different hierarchical levels (Levels I to IV), is proposed and theoretical results at mesoscale level are compared with compression test data for both cortical and trabecular bones. The experimental observations on structure and composition of these three bone types (UT, DM, and DP) serve as inputs for the theoretical model. This multi-

scale model incorporates experimental observations of bone as an interpenetrating composite material composed of contiguous biopolymer and mineral phases.

### 3.2.2 Materials and methods

#### *3.2.2.1 Sample preparation*

Bovine femur bone samples were obtained from a local butcher. The slaughter age of cattle was about 18 months. The bone was thoroughly cleaned with water, using a water pick. About 60 samples (30 for cortical bone and 30 for trabecular bone, parallelepipeds 5x5x7.5 $mm^3$) were cut from mid-diaphysis and femoral head regions. The samples were first roughly cut by a handsaw and then by a diamond blade with prospective compressive surfaces as parallel as possible. Cortical bone samples were cut in the longitudinal and transverse directions. Longitudinal direction was chosen to be parallel to the bone growth direction, while transverse one was perpendicular to the longitudinal one (Fig. 2.1 page 61).

Trabecular bone samples were cut in two directions. The direction oriented along the femur neck axis was A-direction, while the direction normal to A-direction was B-direction (Fig. 3.5). Samples were stored in closed zip lock bags filled with Hank's balanced saline solution in refrigerator (T = 4˚C) for 1-2 days until chemical procedure and mechanical testing.

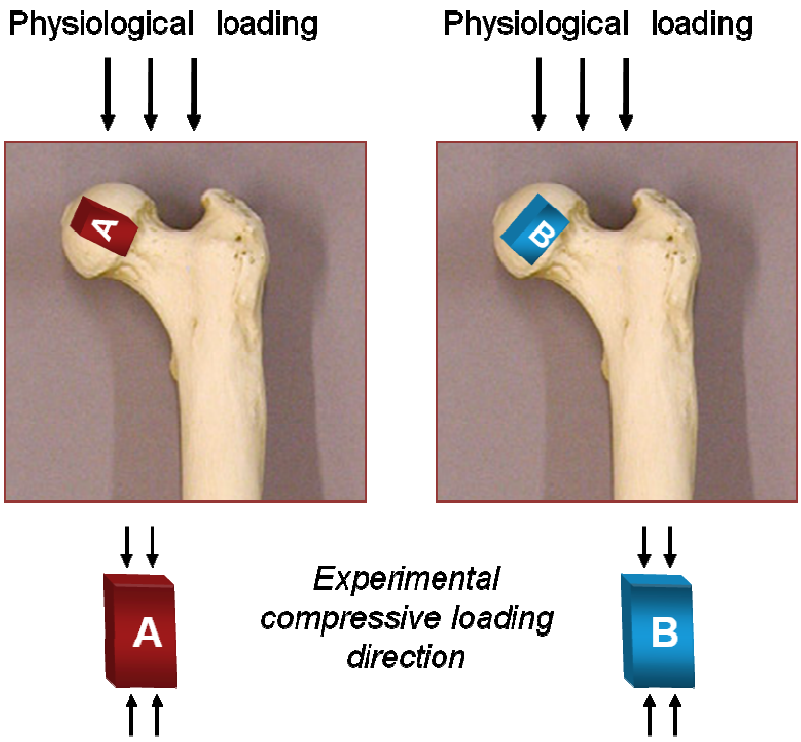


**Figure 3.5** Schematic diagram of physiological and compressive loadings on a femur head, and the sample orientation for two directions: A and B. The samples are not shown to scale. Femur bone image was taken from avocadoexplosion.wordpress.com.

### *3.2.2.2 Demineralization and deproteinization processes*

Cortical and trabecular bone samples were demineralized by aging in 0.6N hydrochloric acid (HCl) at room temperature following the procedures described in [3.17, 3.18]. Acid solutions were changed daily in order to avoid saturation that can affect the demineralization process. The complete demineralization process took about seven days. All solutions were quantitatively analyzed by inductively coupled plasma optical emission spectrometry (ICP-OES) to evaluate the Ca concentration. The completeness of demineralization was verified by the Ca absence in the solutions. Bone samples were deproteinized by aging in a 5.6 wt.% sodium hypochloride (NaOCl) solution at 37˚C,

following the procedures in [3.18]. The solutions were changed every 12 hours. The whole process took about two weeks. Full deproteinization was verified by subsequent demineralization, which resulted in the disappearance of the sample (deproteinization followed by demineralization). Previous work on bone demineralization and deproteinization showed that the amount of proteins left in the solution after subsequent demineralization of previously deproteinized samples is less than 0.001 wt.% [3.18]. A special set of cortical and trabecular bone samples were prepared for micro-computed tomography (μ-CT) scanning. One of each cortical and trabecular samples from this set were demineralized, and one of each cortical and trabecular samples were deproteinized.

#### *3.2.2.3 Compression testing*

Specimens from the three groups (UT, DM, and DP) were submerged in HBSS for 24 hours before testing and were tested in the hydrated condition (the time between taking the samples out from the solution and testing them was about one minute). Compression testing of untreated (UT) bone samples (cortical and trabecular) was done on a universal testing machine equipped with 30kN load cell (Instron 3367 Dual Column Testing Systems, Norwood, MA). Compression testing of demineralized and deproteinized bone samples (cortical and trabecular) was performed on a universal testing machine equipped with 500N load cell (Instron 3342 Single Column System, Norwood, MA). Compression testing for samples from all three groups was done at a strain rate of $1x10^{-3}$ $s^{-1}$. An external deflectometer SATEC model I3540 (Epsilon Technology Corp., Jackson, WY) was used to measure the small displacement.

#### *3.2.2.4 Structural characterization*

To investigate the internal microstructure of both cortical and trabecular bone samples in three-dimensions (3D), the μ-CT imaging technique was performed at a nominal resolution of 1 μm for cortical bone and 10 μm for trabecular bone, since for the latter one the interest was in porosity at a trabecular bone level. The scan produced around 1000 slices (1000x1000 image pixels per slice) resulting in a field of view of $1mm^3$ and $1cm^3$ cubes for cortical and trabecular bones, respectively. This procedure generates high-resolution 3D images without destruction of the bone specimens. The μ-CT measurements were conducted in air using Xradia MicroXCT-200 (for UT and DP samples) and Xradia MicroXCT-400 (for DM samples) (Xradia Inc., Pleasanton, CA) instruments. The reconstructed μ-CT tomograms were post-processed using Amira (Visage Imaging, Inc., Berlin, Germany) to analyze the 3D microstructures and porosities.

### 3.2.3 Modeling procedure

The multi-scale approach for modeling of cortical and trabecular bone is introduced which consists of successive homogenization steps from nano to mesoscale levels (Levels I-IV). The effective elastic properties of UT, DM, and DP cortical and trabecular bones at each structural level were found in a "bottom-up" fashion, using the results from a lower level as the inputs for a higher level. Continuum micromechanics methods and classical lamination theory of composite materials were employed to account for the microstructure of bone at different scales. The elastic properties and volume fractions of the constituents (collagen, hydroxyapatite, water, and NCPs) as well

as the amounts of porosities were the main inputs into the model. A wide range of values for the elastic moduli of collagen and hydroxyapatite has been reported in literature (see Table 1 in [3.14]). The properties for bone constituents for this study are tabulated in Table 3.2. For simplicity, in this model, all components were assumed to be linear elastic and isotropic.

The hierarchical structures of cortical and trabecular bones along with their main porosities and constituents are shown in Fig. 3.6 and Fig. 3.7, respectively. The hierarchical structure of bone along with the corresponding porosities (see **Section 3.1**) was studied in terms of four separate structural levels from nanoscale (up to 2 μm), through sub-microscale (1 - 25 μm) and microscale (25 – 300 μm) to mesoscale (300 μm – 1 cm).

Nanoscale (Level I), which ranges from few to several hundred nanometers, represents a mineralized collagen fibril level. A mineralized fibril has a composite structure made of organic and inorganic phases and water. Type I collagen, which is the major constituent of the organic phase, consists of triple helical tropocollagen molecules which are ~300 nm in length [3.22, 3.23] and ~1.5 nm in diameter [3.23, 3.24]. These molecules assemble into a staggered arrangement with a periodicity of 67 nm [3.25, 3.26], which includes gap and overlap regions. The inorganic phase consists of non-stoichiometric hydroxyapatite crystals ($Ca_{10}(PO_4)_6(OH)_2$), with 4-6% of the phosphate groups replaced by carbonate groups. The mineral crystals are in the form of platelets 40-60 nm in length, 20-30 nm in width, and 2-4 nm in thickness [3.27-3.31]. The remaining phase is water, which plays an important role in bio-mineralization. These constituents are combined into mineralized collagen fibrils (~ 100-200 nm in diameter [3.20, 3.32]),

which are the primary building blocks of bone. It is generally believed that crystals initially form within the gap regions of the collagen fibrils, further proceed into the overlap regions, and subsequently grow into the extrafibrillar space [3.33, 3.34]. Consequently, mineral is found both within and outside the collagen fibrils, but the exact amount in each location is still a matter of contention [3.35- 3.38].

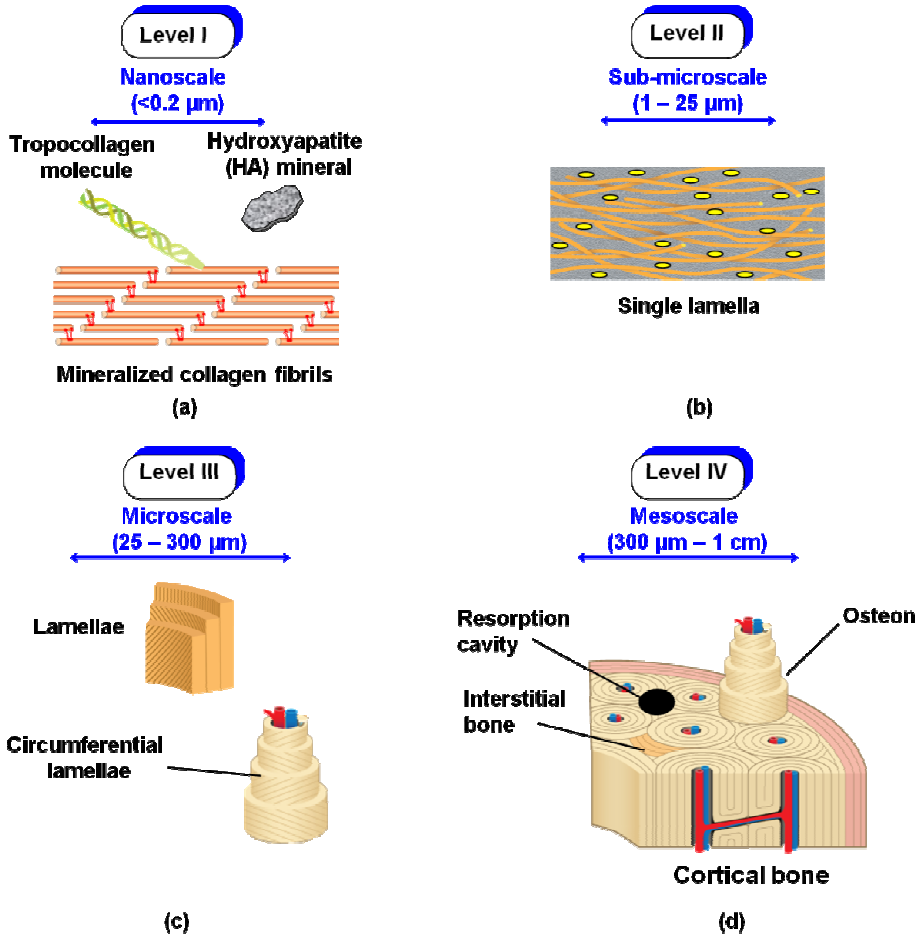


**Figure 3.6** The hierarchical structure of cortical bone: (a) – nanoscale; (b) sub-microscale; (c) – microscale; (d) – mesoscale.

Sub-microscale (Level II), which spans from one to tens of microns, represents a single lamella level. A lamella, having a thickness of 3-7 μm [3.27], is made of preferentially oriented mineralized collagen fibrils. At this length scale, the elliptical cavities called lacunae (typically 5-10 μm in width and 15-25 μm in length [3.39, 3.40]) can be observed. Connecting the lacuna are small channels (~ 100-500 nm in diameter [3.41]), called canaliculi.

Microscale (Level III), ranging from tens to hundreds of microns, denotes the lamellar structures, which are made of lamellae stacked together at different orientations, i.e. the fibrils in each lamella are oriented at a different angle with respect to the adjacent one [3.42, 3.43]. In cortical bone, several layers of the lamellae, arranged in concentric rings around the vascular channels, form osteons (Haversian system), while interstitial lamellae, which are remnants of old osteons, fill spaces between osteons.

**Table 3.2** Elastic properties and volume fractions of bone constituents employed in modeling.

| **Material** | **Young's modulus (GPa)** | **Poisson's ratio** | **Volume fraction (%)** |
|---|---|---|---|
| Collagen | 1.5 [3.44, 3.45] | 0.28 [3.23] | 41 [3.20] |
| Hydroxyapatite | 114 [3.46, 3.47] | 0.23 [3.48] | 42 [3.20] |
| Non-collagenous proteins | 1 [3.23] | 0.45 [3.23] | 4 |
| | Bulk modulus (GPa) | Poisson's ratio | Volume fraction (%) |
| Water | 2.3 | 0.49 | 13 [3.20] |

Mesoscale (Level IV), which spans from several hundred microns to several millimeters or more, depending on species, represents the cortical bone level. The cortical

bone is made of osteons embedded in interstitial lamellae with some resorption cavities, while trabecular bone consists of an interconnected network of pod/plate structures.

Given the Young's modulus, $E_r$, and Poisson's ratio, $\nu_r$, of a phase *r* with an isotropic elastic behavior, its elastic stiffness tensor, $\mathbf{C}_r$, is represented as:

$$\mathbf{C}_r = \frac{E_r}{(1+\nu_r)(1-2\nu_r)} \begin{pmatrix} 1-\nu_r & \nu_r & \nu_r & 0 & 0 & 0 \\ \nu_r & 1-\nu_r & \nu_r & 0 & 0 & 0 \\ \nu_r & \nu_r & 1-\nu_r & 0 & 0 & 0 \\ 0 & 0 & 0 & 1-2\nu_r & 0 & 0 \\ 0 & 0 & 0 & 0 & 1-2\nu_r & 0 \\ 0 & 0 & 0 & 0 & 0 & 1-2\nu_r \end{pmatrix}. \tag{3.1}$$

Young's moduli and Poisson's ratios of different phases (collagen, hydroxyapatite, and water and NCPs), which are given in Table 3.2, were substituted in Eq. (3.1) to obtain their corresponding elastic stiffness tensors.

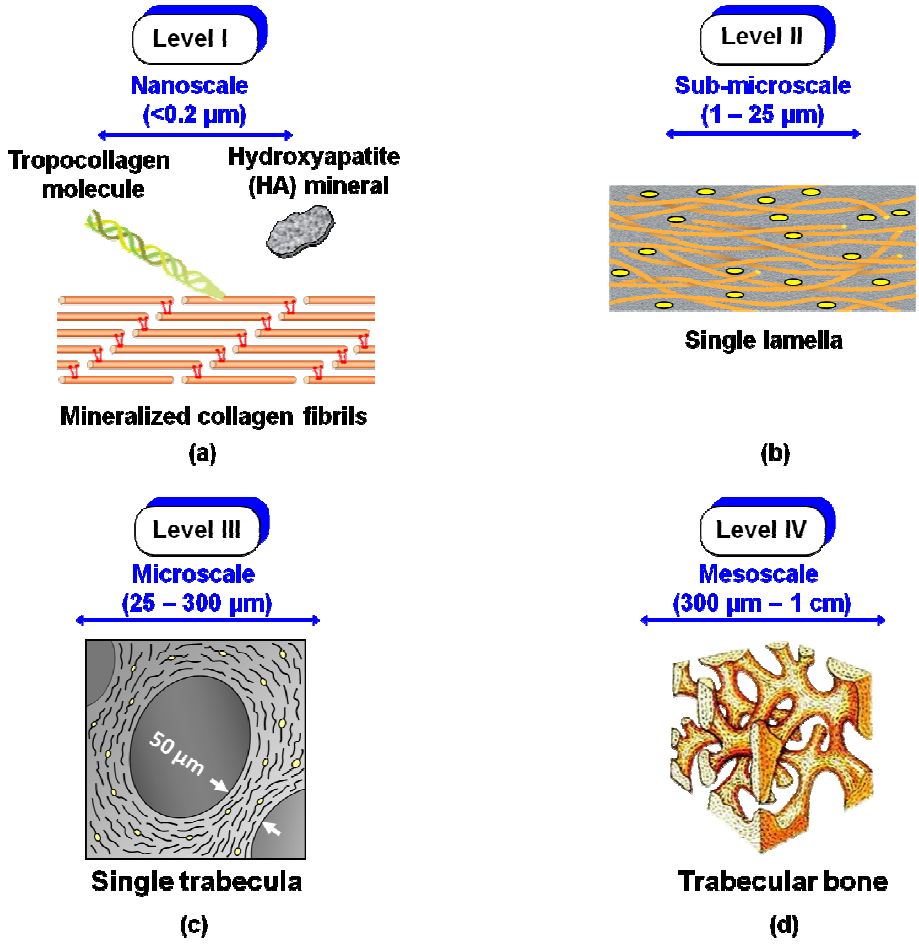


**Figure 3.7** The hierarchical structure of trabecular bone: (a) – nanoscale; (b) sub-microscale; (c) – microscale; (d) – mesoscale.

Each subsequent level shown in Figs. 3.6, 3.7 was modeled in a way that the outputs (stiffness tensor) from the previous level were used as the inputs for the next level along with a porosity evaluation for each level. All modeling assumptions and methods were the same for both cortical and trabecular bones at the first two levels (nano and sub-microscales). However, different modeling techniques were employed to capture the elastic behavior of cortical and trabecular bone at micro and mesoscales, due to different structures of these two bone types at higher scales. Two key equations were

used at different modeling steps: a self-consistent method for modeling a composite with interpenetrating phases and a Mori-Tanaka scheme for modeling a composite material with a matrix-inclusions structure. The general formulations for these two methods are given, respectively, in Eqns. (3.2) and (3.3):

$$\begin{aligned}\mathbf{C}_{compoaite} = &\{\Phi_1\mathbf{C}_1 : [\mathbf{I}+\mathbf{S}:\mathbf{C}^{-1}_{composite} : (\mathbf{C}_1 - \mathbf{C}_{composite})]^{-1} + \Phi_2\mathbf{C}_2 : [\mathbf{I}+\mathbf{S}:\mathbf{C}^{-1}_{composite} : (\mathbf{C}_2 - \mathbf{C}_{composite})]^{-1}\} \\ &: \{\Phi_1[\mathbf{I}+\mathbf{S}:\mathbf{C}^{-1}_{composite} : (\mathbf{C}_1 - \mathbf{C}_{composite})]^{-1} + \Phi_2[\mathbf{I}+\mathbf{S}:\mathbf{C}^{-1}_{composite} : (\mathbf{C}_2 - \mathbf{C}_{composite})]^{-1}\}^{-1},\end{aligned} \tag{3.2}$$

$$\mathbf{C}_{composite} = \mathbf{C}_1 + \Phi_2\{(\mathbf{C}_2 - \mathbf{C}_1) : [\mathbf{I}+\mathbf{S}:\mathbf{C}_1^{-1} : (\mathbf{C}_2 - \mathbf{C}_1)]^{-1}\} : \{\Phi_1\mathbf{I} + \Phi_2[\mathbf{I}+\mathbf{S}:\mathbf{C}_1^{-1} : (\mathbf{C}_2 - \mathbf{C}_1)]^{-1}\}^{-1}, \tag{3.3}$$

where $\mathbf{C}_r$ and $\Phi_r$ are, respectively, the elastic stiffness tensor and volume fraction of a phase *r*, I is the identity tensor, and S is the Eshelby tensor depending on the shape of the inclusion and elastic properties of the matrix. In the self-consistent formulation, Eqn. (3.2), phases 1 and 2 are two types of inclusions interpenetrating each other, and there is no matrix. In the Mori-Tanaka formulation, Eqn. (3.3), phase 1 is treated as a matrix, while phase 2 represents the reinforcing inclusions.

#### *3.2.2.1 Level I. Nanoscale*

A mineralized collagen fibril was modeled using the self-consistent method with two phases, namely collagen molecules and hydroxyapatite crystals, interpenetrating each other. Both phases were treated as inclusions, while no distinct matrix was considered. This was motivated by the recent findings of Chen et al. [3.18] which show that both collagen and minerals form continuous phases in bone.

#### *3.2.2.2 Level II. Sub-microscale*

Different experimental techniques confirmed the existence of randomly dispersed hydroxyapatite crystals on the outer surface of mineralized collagen fibrils. These extrafibrillar minerals can be represented by a porous polycrystal made of hydroxyapatite crystals and some pores in between them, filled with water and NCPs. The self-consistent scheme was used to obtain the effective elastic properties of that hydroxyapatite foam. Next, a coated fibril was modeled by assuming that the mineralized collagen fibrils and the extrafibrillar hydroxyapatite foam interpenetrate each other. Again, the self consistent homogenization method was used to obtain the effective elastic moduli of such coated mineralized fibrils. Finally, a single lamella was built by having the coated mineralized fibrils as a matrix and the osteocyte-filled lacunae as inclusions. Such geometry motivated the use of the Mori-Tanaka method to predict the elastic properties of a single lamella.

#### *3.2.2.3 Level III. Microscale*

Microscale represents the lamellar structures of bone: osteonal and interstitial lamellae in cortical bone, and trabecular packets and interstitial lamellae in trabecular bone. The lamellae can be arranged into orthogonal, rotated, and twisted motifs. However, the exact arrangement of fibrils from one lamella to the adjacent lamella is still a matter of contention. We made different assumptions on the fibril orientations in the neighboring lamellae of cortical and trabecular bone, which are described below.

3.3.2.3.1 Lamellar structures of cortical bone

To model an osteonal lamella, it was assumed that the single lamellae, having the elastic properties as obtained in **Section 3.2**, arrange in a twisted plywood pattern. The starting angle was chosen to be 0º degree for the innermost layer. Furthermore, it was assumed that the fibrils complete a 180º turn from the innermost to the outermost layer. As long as the layers are not orthogonal to each other, the angle change between successive layers has a negligible effect on the results. The elastic properties of the osteonal lamella were obtained by following the homogenization scheme of Sun and Li [3.49] developed for laminated composite materials.

The properties of an interstitial lamella were evaluated by following the same homogenization procedure as for the osteonal lamella. The osteons are generally less stiff and less mineralized than the interstitial lamella. In order to capture such behavior, one could use a higher degree of mineralization (DOM) for an interstitial lamella as compared to an osteonal lamella. However, here, for simplicity, both the osteonal and interstitial lamellae were assumed to have the same DOM and, therefore, the same elastic properties. Having found the elastic properties of an osteonal lamella, a generalized-self consistent method was used to calculate the effective elastic constants of an osteon, following the approach of Dong and Guo [3.50]. To this end, the osteon was modeled as a two phase composite with the osteonal lamella being a matrix and the Haversian canal being a cylindrical inclusion. The outputs of this level, which were the elastic stiffness tensors of an osteon, and an interstitial lamella, served as the inputs for the next level (mesoscale or cortical bone level). Note that the obtained properties for both osteon and interstitial lamellae were transversely isotropic.

3.2.2.3.2 Lamellar structures of trabecular bone

Elastic properties of a single trabecula were obtained by following the homogenization scheme of Sun and Li [3.49]. Since enough information is not available on the actual arrangement of lamellae in each trabecula, it was assumed, for simplicity, that the lamellae are oriented randomly, spanning whole set of directions, which gives rise to an isotropic response. In reality, trabeculae may be anisotropic and their properties may change from one trabecula to another. Again, for simplicity, it was assumed that the interstitial lamellae have the same DOM and elastic properties as trabecular packets.

### *3.2.2.4 Level IV. Mesoscale*

3.2.2.4.1 Cortical bone

Cortical bone consists of osteons embedded in the interstitial lamellae, with some resorption cavities. A hybrid Mori-Tanaka method, with the interstitial lamellae being a matrix and the osteons as well as resorption cavities being two types of inclusions, was used to obtain the transversely isotropic elastic constants of cortical bone.

3.2.2.4.2 Trabecular bone

Trabecular bone consists of a porous network of trabeculae. The analytical model proposed by Gibson and Ashby [3.51, 3.52] for cellular materials was applied to predicts the Young's modulus of trabecular bone as a function of its relative density

$$\frac{E^*}{E_s} = C\left(\frac{\rho^*}{\rho_s}\right)^2 \tag{3.4}$$

where $E^*$ and $\rho^*$ are the elastic modulus and density of trabecular bone, $E_s$ and $\rho_s$ are the corresponding values for a solid block of trabeculae, and $C$ is a coefficient of

proportionality. The relative density, $\rho^*/\rho_{s,}$ is equal to the bone volume fraction determined by μ-CT.

#### *3.2.2.5 Modeling of treated bones*

Modeling of treated (DM and DP) cortical and trabecular bones followed the same multiscale modeling procedure described in ***Sections 3.2.2.1*** to ***3.2.2.4***. The only difference was that in the case of treated bones, one phase was removed: collagen in the case of DP bone and hydroxyapatite in the case of DM bone. The material constants of the removed phase were set to be zero in all the modeling steps.

### 3.2.3 Results and discussions

Optical microscopy images of UT, DM, and DP trabecular bone samples shown in Fig. 3.8, illustrate a combination of both rod-like and plate-like elements. Additionally, it demonstrate that both DM and DP trabecular bones are contiguous structures, which can be mechanically tested in agreement with [3.57].

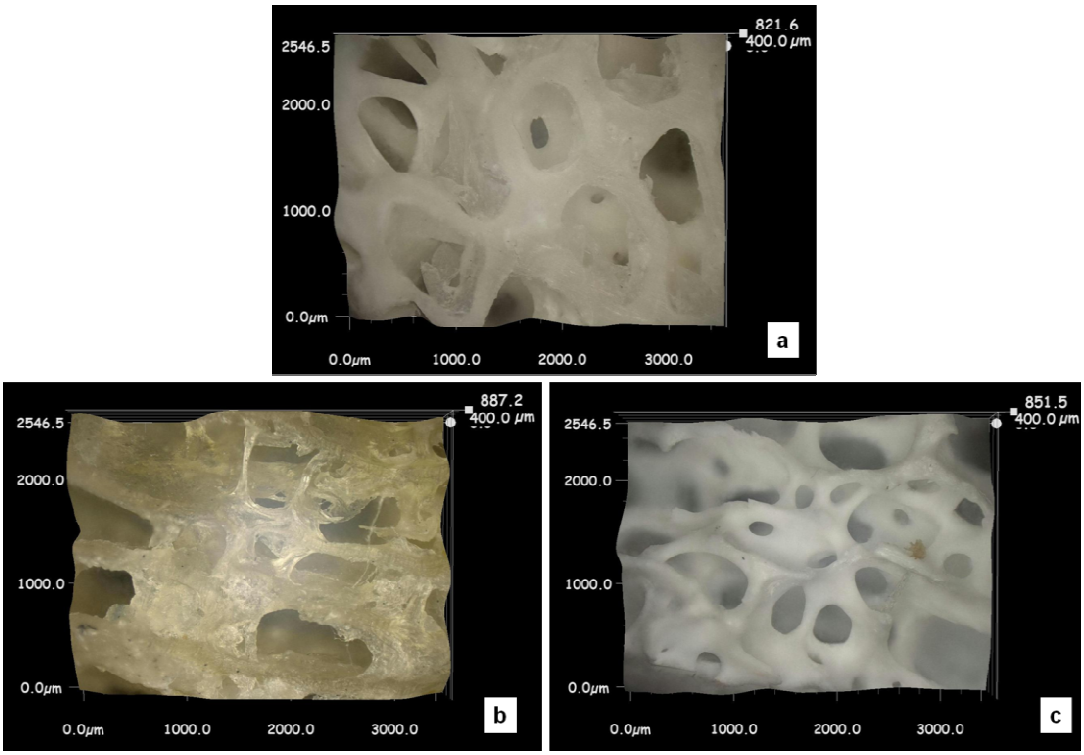


**Figure 3.8** Optical microscopy images of untreated (a), demineralized (b), and deproteinized (c) trabecular bone showing rod-like and plate-like elements.

SEM images of UT, DM, and DP trabecular and cortical samples are shown in Figs. 3.9 and 3.10, respectively. Fig. 3.9 proves that not only shape and volume of bone trabecular bone samples were preserved (as seen at Fig. 3.8) during demineralization and deproteinization processes, but moreover small microstructural features (such as lacuna spaces, La) were well defined as well in agreement with [3.53]. Moreover, it is clearly seen that both collagen fibers and minerals aligned in a preferential orientation, shown by arrows at Figs. 3.9b and 3.9c.

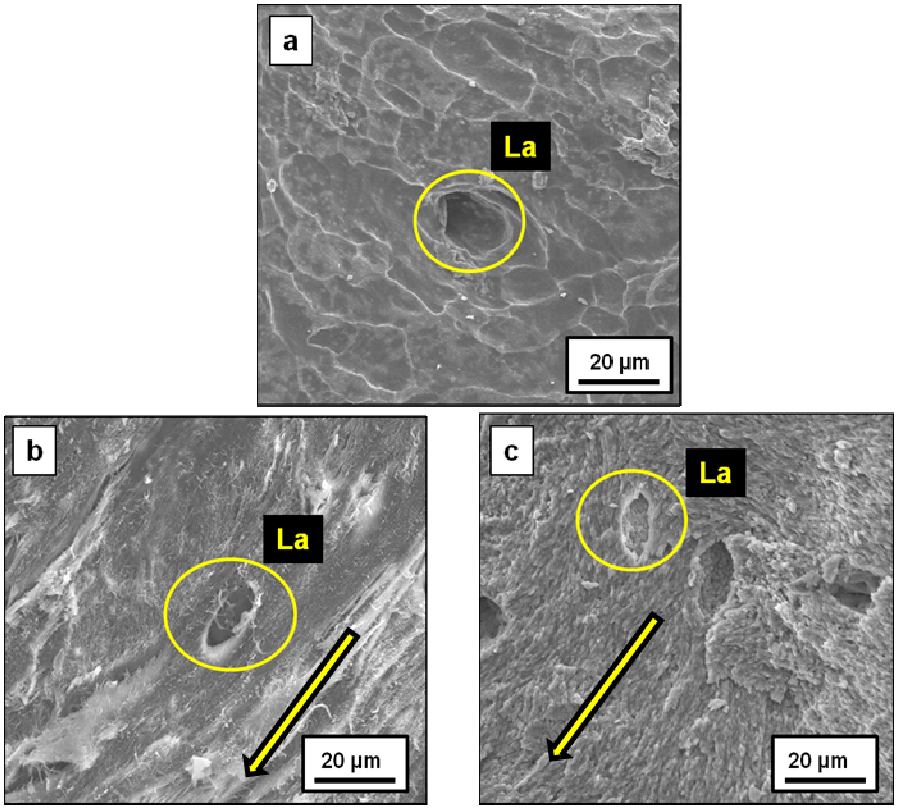


**Figure 3.9** Scanning electron microscopy images of the fracture surfaces of (a) untreated, (b) demineralized (continuous protein network), and (c) deproteinized (continuous mineral network) bovine trabecular bone. La = lacuna spaces. Arrows pointed out the preferential orientation of collagen fibers for demineralized bone (b), and minerals for deproteinized bone (c). Images were taken from different samples.

Figures 3.10a illustrates fracture surface of an UT cortical bone samples. Vascular channels are visible, and osteon structure is well defined. Figs. 3.10b and 3.10c demonstrate that DM and DP bones are contiguous, stand-alone structures (continuous protein network and continuous mineral network). Similar to trabecular bone samples, all microstructural features is very well preserved for the cortical bone samples during the demineralization and deproteinization processes. Microscopic features, such as the Haversian channels (HC), 20-40 µm in diameter, and Volkmann's canals (VC), are

preserved in DM and DP samples in agreement with [3.18]. Moreover, a well-defined osteonal structure is clearly seen in both types of treated cortical bone.

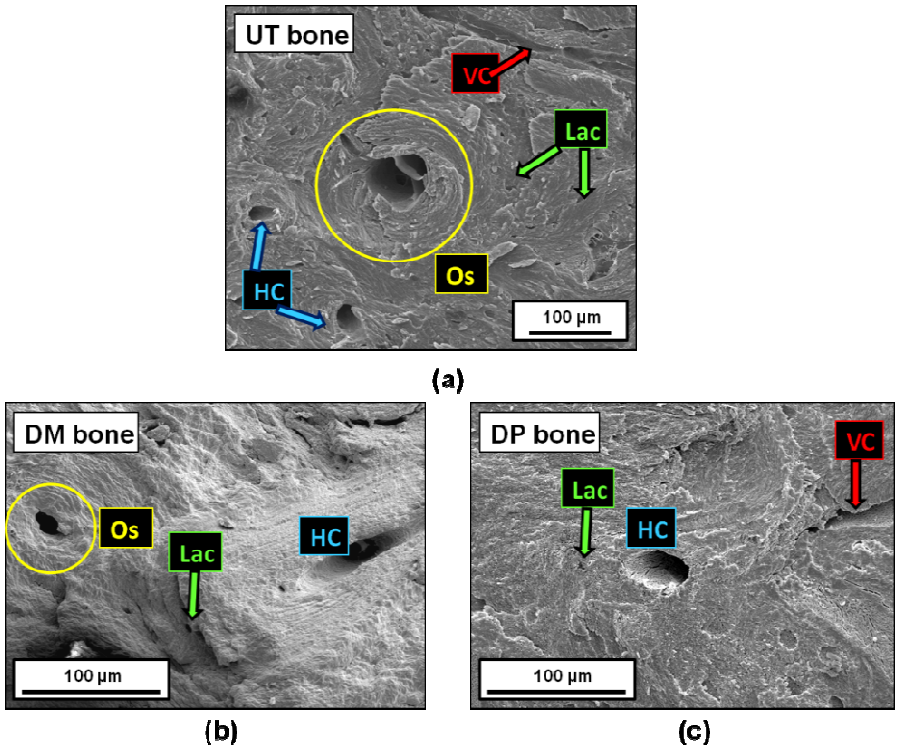


**Figure 3.10** Scanning electron microscopy images of (a) untreated, (b) demineralized (continuous protein network), and (c) deproteinized (continuous mineral network) bovine cortical bone showing microstructural features: osteons (Os), lacuna spaces (Lac), Haversian channels (HC), and Volkmann's canals (VC). Images were taken from different samples.

Figure 3.11 shows the 3D isosurface overview of all voids in the UT cortical bone sample from µ-CT imaging. The two types of porosity in sub-microscale to microscale levels, the osteocyte lacunar system (golden parts) and canal network (red parts), are clearly observed at Fig. 3.11a. It was verified that in the cortical bone the lacunae have ellipsoid shapes that are oriented in the longitudinal direction. The canal network without the lacuna spaces is shown at Fig.3.11b. It is clear that both the vascular channels

(oriented along long axis of bone) and the Volkmann's canals (oriented angularly to the long axis of bone) are visible in this image. The quantification of the amount of lacuna spaces and canals was then performed on four samples per each group and the results are presented in Table 3.3, which lists means and standard deviations.

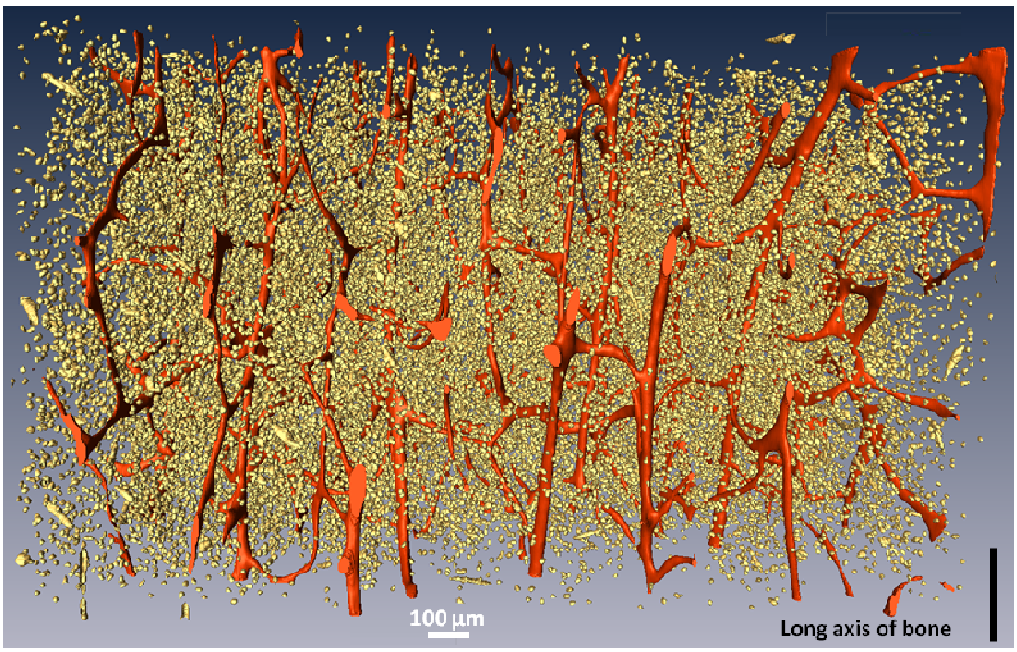


**Figure 3.11** µ-CT 3D isosurface images of untreated cortical bone showing (a) side view of canal network (red: Haversian, vertical; Volkmann's, horizontal) and osteocyte lacunae (yellow); the lacunae are preferentially oriented in vertical direction, indicating the long axis of bone, (b) side view of canal network only. A volumetric filter (20 × 20 × 20 $\mu m^3$) was applied to separate canal network from lacuna spaces.

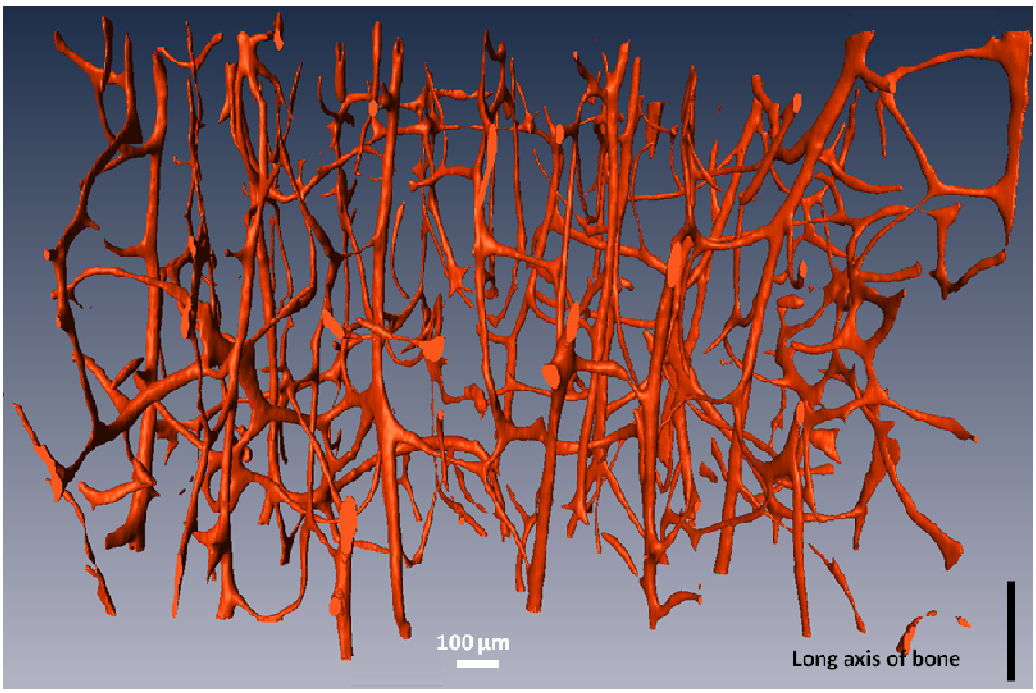


(b)

**Figure 3.11** Continued.

**Table 3.3** 3D bone morphometry results from µ-CT image analysis for UT = untreated, DM = demineralized, and DP = deproteinized cortical bone.

| **Porosity** | | | **Canals (UT samples only)** | | **Lacunae (UT samples only)** | | |
|---|---|---|---|---|---|---|---|
| UT sample (%) | DM sample (%) | DP sample (%) | Volume fraction (%) | Mean width (µm) | Volume fraction (%) | Mean length (µm) | Mean width (µm) |
| 7.9±0.81 | 51.5±3.8 | 57.1±3.5 | 4.4±0.15 | 54.2±4.8 | 3.6±0.68 | 16.6±2.8 | 7.0±0.3 |

Figure 3.12 shows the 3D isosurfaces overview of bone material for untreated (Fig. 3.12a,b), demineralized (Fig. 3.12c,d), and deproteinized (Fig.3.12e,f) trabecular bone samples. A sophisticated trabecular network composed of plates and rods is clearly

seen on these images. The amount of porosity for each bone types was estimated and presented in Table 3.4 along with porosity estimated from the bone density measurements; nice agreement was found between these values.

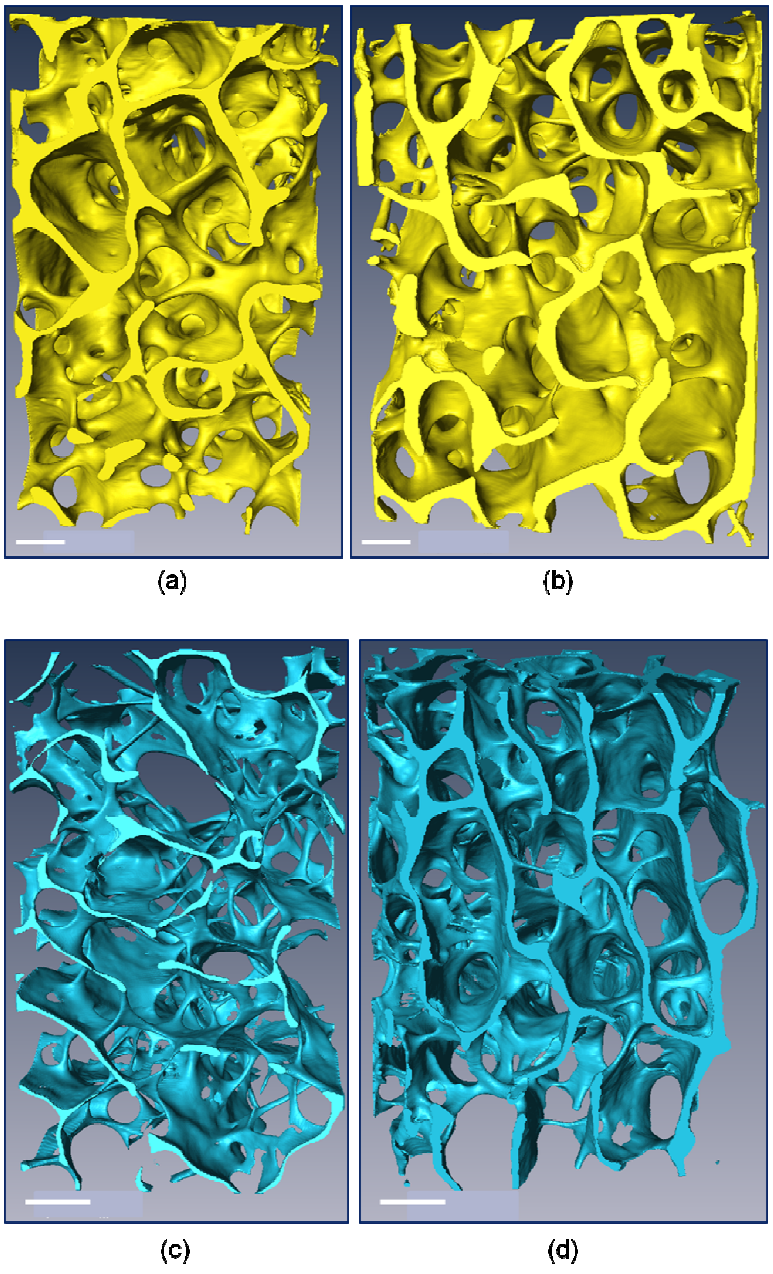


**Figure 3.12** Micro-CT 3D isosurface images of trabecular bone for untreated (a) A-direction, (b) B-direction, demineralized (c) A-direction, (d) B-direction, and deproteinized (e) A-direction, (f) B-direction. Scale bar = 700 µm.

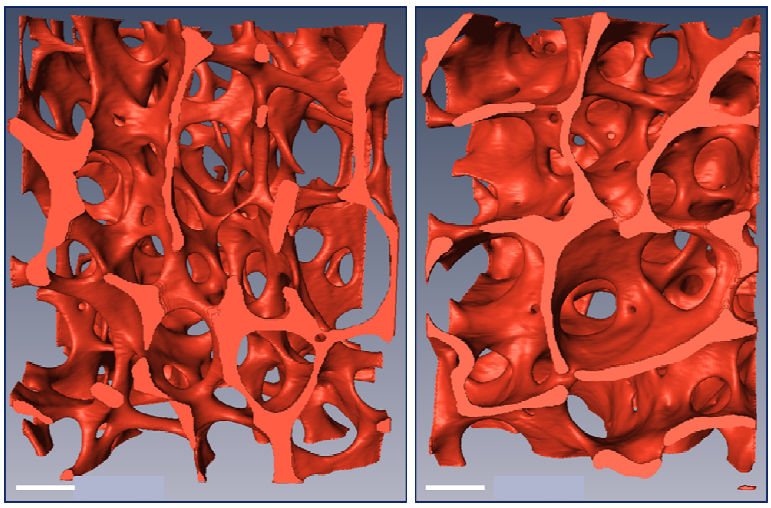


**Figure 3.12** Continued.

**Table 3.4** Comparison of porosity estimation results from μ-CT imaging and the measured density for bovine trabecular bone.

| **Bone type (direction)** | **UT (L)** | **UT (T)** | **DM (L)** | **DM (T)** | **DP (L)** | **DP (T)** |
|---|---|---|---|---|---|---|
| **Resolution (μm)** | 10.8 | 10.8 | 5.8 | 5.5 | 5.8 | 5.4 |
| **Porosity by Micro-CT** | 83.9 ± 3.3% | 83.2 ± 4.6% | 91.6 ± 1.4% | 90.6 ± 1.6% | 89.1 ± 1.1% | 86.9 ± 2.2% |
| **Porosity by density calculations** | 84 ± 3% | 80 ± 6% | 91 ± 2% | 91 ± 2% | 89 ± 2% | 84 ± 3% |

Porosity evaluations summarized in Tables 3.3 and 3.4 were incorporated into model as one of the input parameters along with volume fractions, Young's modulae, and Poisson's ratios of bone main constituents (summarized in Table 3.2).

Fig. 3.13 shows the experimental stress-strain curves for UT, DM, and DP cortical bones measured in longitudinal and transverse directions. UT and DP samples showed a well-defined initial linear elastic region, while DM samples showed the behavior typical for biopolymers with long "toe in" region in the initial part of the stress-strain curve. For UT bone, the longitudinal direction (with elastic modulus of 22.76 ± 1.79 GPa) is stiffer and stronger then the transverse direction (with elastic modulus of 16.20 ± 1.44 GPa), in good agreement with results of other researchers [3.54]. Removal of the mineral or protein phase resulted in a drastic change in the stress-strain curves. First, for the DM samples (Fig. 3.13b), the elastic modulus was calculated using the steepest portions of the curves and the modulus in the longitudinal direction (0.23 ± 0.01 GPa) was found to be larger than in the transverse direction (0.13 ± 0.02 GPa). As pointed out by Gibson and Ashby [3.52], the elastic modulus of a polymer foam is highly dependent on the density and large deformations can be accommodated. The difference between the behavior in the longitudinal and transverse directions can be explained by the preferential orientation of the osteons, among other factors (see [3.55, 3.56]). Secondly, the DP samples (Fig. 3.13c) appear to behave as a classic cellular solid, demonstrating a linear elastic region up to a peak stress, after which a plateau region is sustained. The longitudinal elastic modulus (9.23 ± 2.82 GPa) is larger than the transverse one (2.45 ± 0.78 GPa). This again can be attributed to the alignment of osteons in the longitudinal direction. As a side note, it is clear that a rule of mixtures law (Voigt average) does not apply here – the volume fraction averaged elastic modulus of the mineral and protein constituents (~ 4.6 GPa in longitudinal direction) is not close to that of the untreated bone.

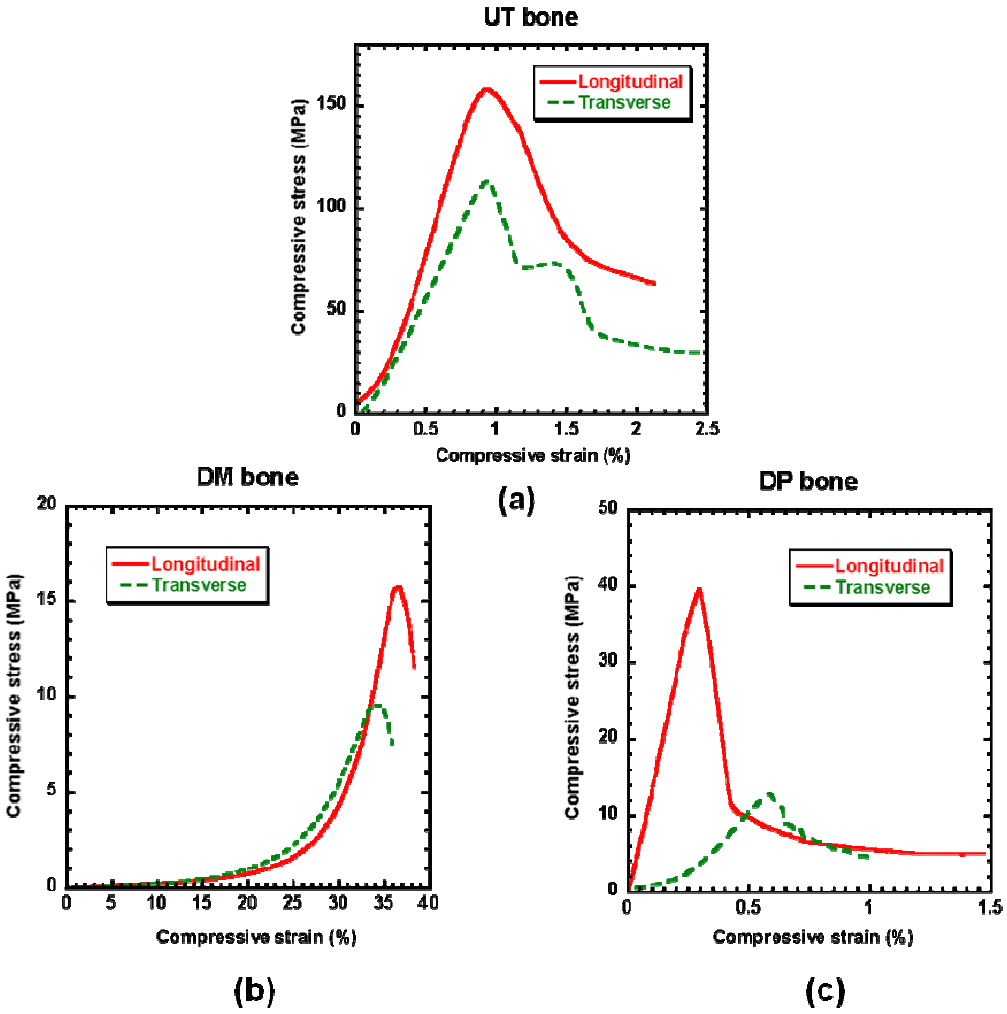


**Figure 3.13** Stress-strain curves for (a) untreated (UT), (b) demineralized (DM), and (c) deproteinized (DP) cortical bone for two anatomical directions. N = 10 for each curve.

Trabecular bone samples relative densities ($\rho_{bone}/\rho_{trabecula}$) were calculated and plotted against relative elastic modulus ($E_{bone}/E_{trabecula}$) for all three trabecular bone phases for two anatomical directions tested (Fig. 3.14). The normalizing parameter $\rho_{trabecula}$ is a density of the cell wall material, and $E_{trabecula}$ is an elastic modulus of the cell wall material. These parameters were different for UT, DM, and DP samples (Table 3.5),

and were averaged between three anatomical directions (longitudinal, radial, and transverse) from [3.21] due to relatively random orientation of trabeculae in each particular trabecular bone sample. For UT samples, the normalizing parameters were the Young's modulus and density of cortical bone. For DM samples, the parameters are the Young's modulus and density of DM cortical bone, and for DP samples, the parameters are the Young's modulus and density of DP cortical bone. All these normalizing parameters were taken from [3.21]. Most of the data points fall between two lines with slopes equal to 1 and 3 (Fig.3.14) in agreement with [3.52], demonstrating that not only UT bone, but both DM and DP trabecular bone can be modeled as a cellular solid with properties described by the Eq. (3.4). The fact that the majority of the data points were close to the line with slope equal to 3 support the assumption that according to [3.51] the relation between relative elastic modulus and relative density of trabecular bone is strongly depends on cells geometry and a load orientation. Due to different load distribution, trabecular bone cells could be equiaxed (if load is similar for all principal directions). In a condition of a non-uniform stress distribution, cell walls tend to align in some prevalent direction to accommodate this non-uniformity of stress. Trabecular bone forms a some kind of perforated plates oriented in B-direction (direction with presumably larger stress, see Figs. 3.12b,d), due to our choice of the sample orientations (B-direction is more optimized for everyday loading condition (see Fig. 3.6) that means that stress in this particular direction is higher compare to A-direction. Thin rods that act as a spacers are forms in the direction perpendicular to that perforated plates. According to [3.52] stress applied normal to these plates (in A-direction) made them bend, data points for this kind of loading should fall close to the line with slope 3 (see Fig. 3.14). In the case of

stress applying parallel to those plates (B-direction), data points should be close to the line with slope 1 (as seen at Fig. 3.14).

Data points corresponded to DP and DM cases (for both anatomical directions) were shifted along x-axis. The collagen fibers saturation with water is one of the possible reasons for this shift for DM samples, since water contributes significantly not only into DM bone density measurements, but into the DM trabecular bone mechanical behavior as well. According to [3.52], mechanical properties of cellular solids strongly depend on their relative density. Since the mechanical testing of all samples was performed in the wet condition, some water could possibly stacked in-between of trabecular network and made a contribution to the corresponding bone mechanical response; data shift for DP samples can be explained by this fact.

Data for each particular bone type (UT, DP, and DM) are summarized on Fig. 3.14. Parameters $n$ (slope of the curve) and $C$-value (the intercept between the data line and y-axis) for Eq. (3.4) can be estimated from these plots. It is clear that for the untreated trabecular bone $n$ is equal to 2, and $C$-values fall in between of 0.1 and 0.2; for the deproteinized one $n$ is equal to 3, while $C$-value is equal to 0.4. For the demineralized case $n$ is equal to 1 for A-direction and to 2 for B-direction, while $C$-value is equal to 0.005 for A-direction and 0.013 for B-direction. This information provides new supplemental information for the modeling of elastic properties of bovine femur trabecular bone and its main constituents.

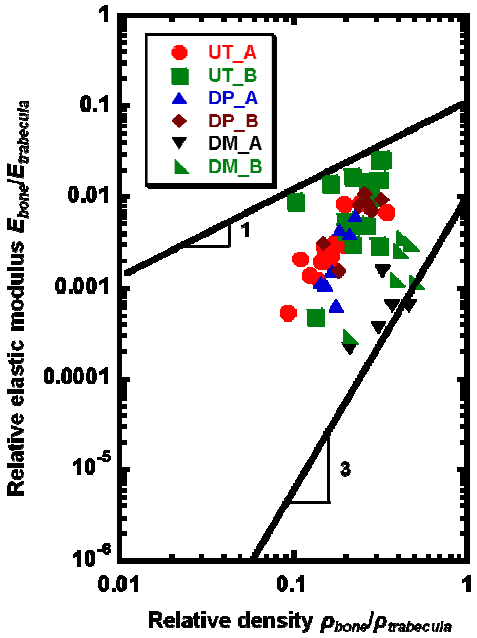


**Figure 3.14** Relative elastic modulus versus relative density for untreated, demineralized, and deproteinized trabecular bone for two anatomical directions.
UT_A = untreated bone, A-direction, UT_B = untreated bone, B-direction
DM_A = demineralized bone, A-direction, DM_B = demineralized bone, B-direction
DP_A = deproteinized bone, A-direction, DP_B = deproteinized bone, B-direction

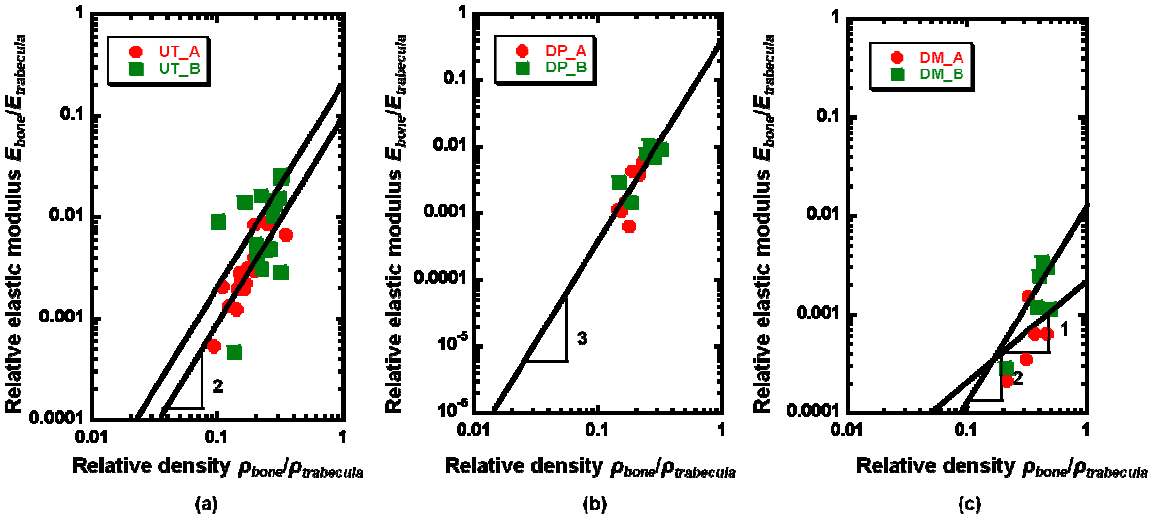


**Figure 3.15** Relative elastic modulus versus relative density for (a) untreated, (b) deproteinized, and (c) demineralized trabecular bone for two anatomical directions.

Figures 3.8 and 3.12 clearly show that trabecular bone samples for UT, DM, and DP cases are mostly consists of rod-plate-like structures with corresponded relative densities slightly larger than 0.2, therefore data points for all cases tested are closer to the line with slope equal to 3 (Fig. 3.14) according to [3.51]. Additionally, cell shapes and sizes were not the same for all samples tested; moreover, some samples show the prevalent orientation of the cells (Figs. 3.8c, 3.12d, 3.12f) along one direction. To some extend this type of structure could be evaluated as parallel prismatic cell structure, which behaves differently depending on the load conditions. Loaded along the prism axes, the relative elastic modulus depends linearly on the relative density, while loaded across the prism axes the relation between those parameters is cubic.

**Table 3.5** Normalizing parameters for untreated, demineralized, and deproteinized trabecular bone samples (used in Eq. (3.4)) obtained experimentally. All data averaged from [3.21]

| **Bone type** | $\rho_{trabecula}$, **g/cm$^3$** | $E_{trabecula}$, **GPa** |
|---|---|---|
| Untreated (UT) | 2.05 | 19.4 |
| Demineralized (DM) | 1.18 | 0.182 |
| Deproteinized (DP) | 1.98 | 5.9 |

Elastic modulus was found to be about three times higher for B-direction compare to A-direction for all UT, DM and DP bone cases. The largest difference in the elastic modulus appeared between the two anatomical directions for UT samples. Our choice of sample orientations (Fig. 3.6) shows that the B-direction was more optimized for physiological loading conditions; this could be the reason why the elastic modulus for these samples was found to be higher compare to the A-oriented ones. Somewhat large

difference in the elastic modulus was found between A and B directions for DM and DP samples. This fact supports the idea that bone minerals as well as collagen fibers preferential orientation contributes significantly into bone stiffness in agreement with [3.21].

Figure 3.16 illustrates the experimental results, obtained from compression testing, for the longitudinal and transverse (in the circumferential direction) elastic moduli of UT, DP, and DM cortical bones and compares them with modeling results. The mean values reported for theoretical results (Fig. 3.16) were calculated by averaging over the different values of porosity (see Table 3.3). The bars in Fig. 3.16 represent the standard deviation and the range, respectively, for the experimental and modeling data. Experimental and modeling results are in very good agreement and in most cases their discrepancies, whenever present, are mainly due to simplifying assumptions and selections made at different stages of modeling. The main discrepancy between experiments and modeling occurs for the transverse elastic modulus of UT cortical bone. One possible reason may be that in our model, for simplicity, all osteons were assumed to be aligned along the long axis of bone. However, there are some drifting osteons in bone with off-axis, rather than the longitudinal, alignment [3.57]. The transverse elastic modulus of UT bone is underestimated by neglecting the presence of those misaligned osteons in the model. In addition, as mentioned in **Section *3.3.2.3.1***, in our model the osteonal and interstitial lamellae were assumed to have the same DOM (42% mineral volume fraction [3.58]). The modeling results reported in Fig. 3.16 are based on that assumption. In reality, however, this is not the case and the interstitial lamellae are more mineralized than the osteonal lamellae. Our model can easily handle different mineral

contents for interstitial and osteonal lamellae. In order to address this issue, first, the average mineral volume fraction was assumed to be 37% for osteon and 43% for interstitial lamella, following Gupta *et al*. [3.59], and the modeling steps were repeated for UT bone. In this case, the longitudinal and transverse elastic moduli were found to be, respectively, 19.63 GPa and 8.91 GPa. Clearly, the values were lower compared to our previous results since the overall mineral content became lower. Next, the case of 42% mineral volume fraction for osteons and 48% mineral volume fraction for interstitial bone was considered. The longitudinal elastic modulus of UT bone increased to 24.42 GPa, while the transverse modulus increased to 11.65 GPa. However, no experimental references support inputs of such higher mineral content. Ideally, the actual mineral content specific to our bone type should be used in the model, but such measurements are not available for our samples.

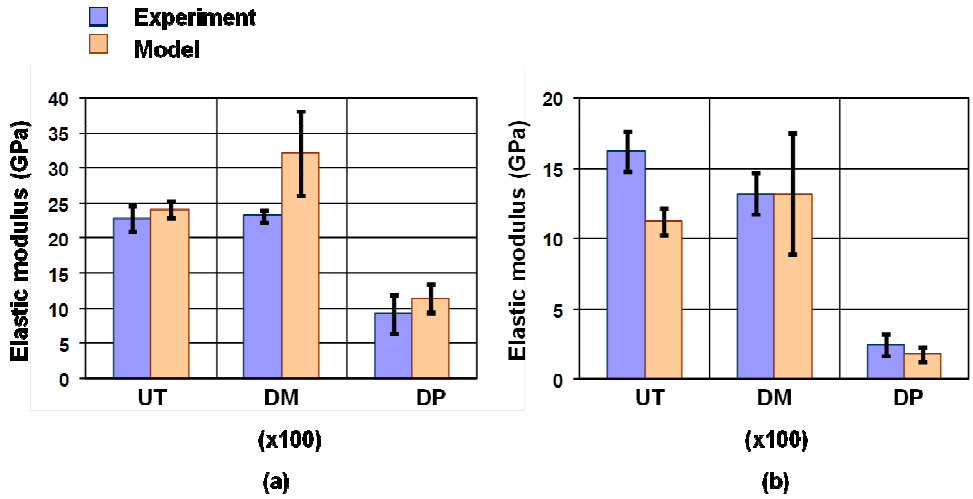


**Figure 3.16** Comparison of the experimental and modeling results for (a) longitudinal, and (b) transverse elastic moduli of untreated (UT), demineralized (DM, magnified by 100X for clarity), and deproteinized (DP) cortical bone. The capped lines show the standard deviation for experimental data and the range for modeling results (due to range in porosity, see Table 3.3).

The other somewhat large discrepancy occurs between the theoretical and experimental longitudinal elastic modulus of DM bone. This can be explained by the fact that only the presence of longitudinal Haversian vascular channels was incorporated in our model, but the existence of Volkmann's canals, that are oriented perpendicular to main Haversian system (see Fig.3.11b), was neglected. Including some voids in the transverse direction (Volkmann's canals) would decrease the computed elastic moduli of DM bone along with considering the off-axis alignment of the Haversian canals. Another reason for the difference of experimental and modeling results for DM bone is a possible degradation of collagen structure during the demineralization process due to enzymatic autolysis [3.21].

Figure 3.17 summarizes the experimental results, obtained from compression testing, for the elastic moduli of UT, DP, and DM trabecular bones tested in A-direction and B-direction, and compares them with modeling results. The mean values reported for theoretical results (Fig. 3.17) were calculated by averaging over the different values of porosity (see Table 3.4). The bars in Fig. 3.17 represent the standard deviation and the range, respectively, for the experimental and modeling data. Experimental and modeling results are in a good agreement. The discrepancies are mainly due to simplifying assumptions and selections made at different stages of modeling and a large variety of trabecular bone density values, even in the limits of one femur head. The main assumption for the modeling part was the using of Gibson and Ashby model for the cellular solid materials at the last modeling step (see **Section *3.2.2.4.2***). This model has several main assumptions: the cellular material assumes to be isotropic with cubic array of cells with same geometry. In the reality, trabecullar bone consists of rod-plate-

structure (see Figs. 3.8 and 3.12) with different dimension cells. Moreover, data summarized in Figs. 3.14 and 3.15 show anisotropic properties of trabecular bone samples for all three bone types (UT, DM, and DP). More detailed μ-CT imaging was performed on the samples from two anatomical directions. For A-direction degree of anisotropy (DA, length of longest divided by shortest mean intercept length vector [3.60], if DA = 1 the material is isotropic) was found to be 1.94, while this number was 1.56 for B-direction. These data clearly proves that trabecular bone behave as anisotropic material. The structure model index (SMI, an indicator of the structure of trabeculae; SMI will be 0 for parallel plates and 3 for cylindrical rods) was important information from this additional μ-CT imaging. For A-direction SMI was found to be 1.04, while for B-direction it was found to be 1.35. These data supported the previous findings about non-uniformity of the trabecular structure for two anatomical directions.

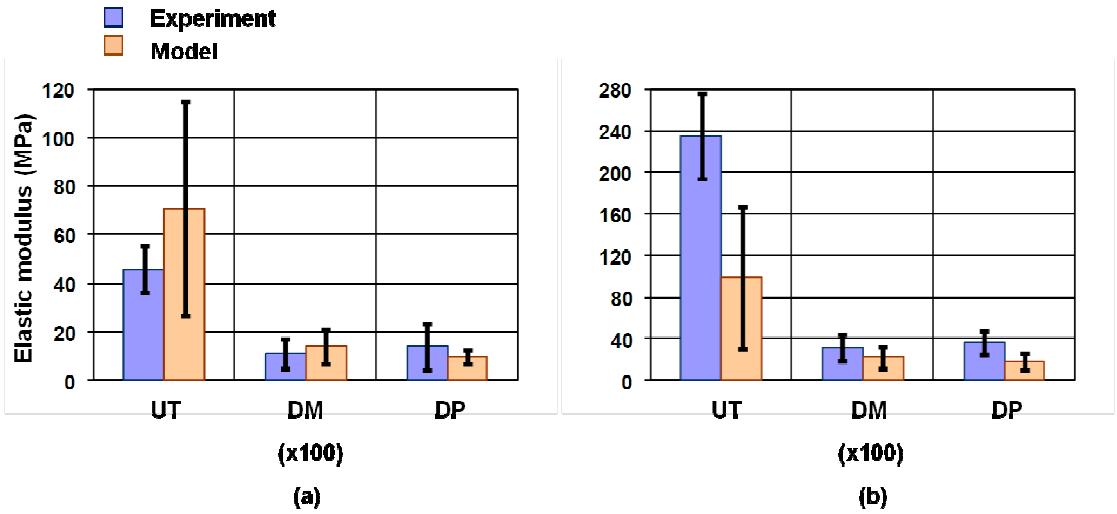


**Figure 3.17** Comparison of the experimental and modeling results for (a) A-direction, and (b) B-direction elastic moduli of untreated (UT), demineralized (DM, magnified by 100X for clarity), and deproteinized (DP) trabecular bone. The capped lines show the standard deviation for experimental data and the range for modeling results (due to range in porosity, see Table 3.4).

### 3.2.4 Conclusions

A new theoretical model was developed that accurately predicts the experimentally measured elastic modulus of cortical and trabecular bovine femur bone. This model assumes that cortical and trabecular bones have a hierarchical structure, are interpenetrating composites of biopolymers and hydroxyapatite minerals, and consist of porosity at different hierarchical levels. A bottom-up approach was employed that incorporated outcomes of the previous hierarchical level as the input for the next one. This model was further verified by the close agreement found between the model and experimental results taken on deproteinized and demineralized bone.

The major findings of this work are as follows:

- This is the first multi-scale model that incorporates experimental observations of bone as an interpenetrating composite combined with interdispersed porosity at different hierarchical levels. These results show the complexity of the bone structure, which is still not well understood, and the open challenges in modeling it.
- The compressive elastic moduli of untreated and treated bones show anisotropy in the elastic modulus between the longitudinal (higher) and transverse (lower) directions. This demonstrates that both the protein and mineral architectures have preferential structures in the longitudinal direction.
- Three-dimensional imaging by micro-computed tomography clearly reveals and quantifies the hierarchical structure of the porosity from lacuna spaces to vascular channels and to resorption cavities. The lacunae spaces are ellipsoids that have the

major axis parallel to the long axis of the bone. The μ-CT images illustrate a complex network of canals, including Haversian and Volkmann's canals, perforating bone structure for cortical bone, and a complex trabeculae network for trabecular bone.

- The multi-scale model using experimental values of porosity and volume fractions of constituents demonstrates that the elastic moduli of the untreated, demineralized, and deproteinized cortical and trabecular bones are in very good agreement with the experimentally measured values.

**Acknowledgements:**

Sub-chapter 3.1, in full, is a reprint of the material as it appears in "Hierarchical structure of porosity in cortical and trabecular bones," in Materials Research Society Symposium Proceeding, Fall 2011. E. Novitskaya; E. Hamed; J. Li; Z. Manilay; I. Jasiuk; J.McKittrick. The dissertation author was the primary investigator and author of this paper.

Sub-chapter 3.2, in part, is a reprint of the material as it appears in "Correlation of multiscale modeling and experimental results for the elastic moduli of cortical and trabecular bone," in Society for Experimental Mechanics Congress Proceedings, 2012. E. Novitskaya; E. Hamed; J. Li; I. Jasiuk; J. McKittrick. The dissertation author was the primary investigator and author of this paper.

### 3.2.5 References


[3.1] Wachter NJ, Krischak GD, Mentzel M, Sarkar MR, Ebinger T, Kinzl L, Claes L, Augat P. Correlation of bone mineral density with strength and microstructural parameters of cortical bone in vitro. Bone 2002;31: 90–95.

[3.2] Dong XN, Guo XE, The dependence of transversely isotropic elasticity of human femoral cortical bone on porosity. J Biomech 2004; 37:1281-1297.

[3.3] Basillais A, Bensamoun B, Chappard C, Brunet-Imbault B, Lemineur G, Ilharreborde B, et al. Three-dimensional characterization of cortical bone microstructure by microcomputed tomography: validation with ultrasonic and microscopic measurements. J Orthop Sci 2007;12:141-148.

[3.4] Wachter NJ, Augat P, Krischak GD, Mentzel M, Kinzl L, Claes L, Prediction of cortical bone porosity in vitro by microcomputed tomography. Calcif Tissue Int 2001;68: 38-42.

[3.5] Cooper DML, Turinsky AL, Sensen CW, Hallgrimsson B, Quantitative 3D analysis of the canal network in cortical bone by micro-computed tomography. Anat Rec 2003; 274B:169-179.

[3.6] Schneider P, Stauber M, Voide R, Stampanoni M, Donahue LR, Müller R, Ultrastructural properties in cortical bone vary greatly in two inbred strains of mice as assessed by synchrotron light based micro- and Nano-CT. J Bone Min Res 2007;22:1557-1570.

[3.7] Van Rietbergen B, Odgaard A, Kabel J, Huiskes R, Relationships between bone morphology and bone elastic properties can be accurately quantified using high-resolution computer reconstructions. J Orthop Res 1998;16:23-28.

[3.8] Fajardo RJ, Muller R, Three-dimensional analysis of nonhuman primate trabecular architecture using micro-computed tomography. Am J Phys Anthropol 2001;115: 327-336.

[3.9] Patel V, Issever AS, Burghardt A, Laib A, Ries M, Majumdar S, MicroCT evaluation of normal and osteoarthritic bone structure in human knee specimens. J Orthop Res; 21:21-26.

[3.10] Hellmich C, Barthelemy JF, Dormieux L. Mineral-collagen interactions in elasticity of bone ultrastructure - a continuum micromechanics approach. Eur J Mech A 2004;23:783-810.

[3.11] Fritsch A, Hellmich C. 'Universal' microstructural patterns in cortical and trabecular, extracellular and extravascular bone materials: Micromechanics-based prediction of anisotropic elasticity. J Theor Biol 2007; 244:597- 620.

[3.12] Nikolov S, Raabe D. Hierarchical modeling of the elastic properties of bone at submicron scales: The role of extrafibrillar mineralization. Biophys J 2008;94:4220-4232.

[3.13] Yoon YJ, Cowin SC. The estimated elastic constants for a single bone osteonal lamella. Biomech Model Mechanobiol 2008;7:1-11.

[3.14] Hamed E, Lee Y, Jasiuk I. Multiscale modeling of elastic properties of cortical bone. Acta Mech 2010;213:131-154.

[3.15] Hamed E, Jasiuk I, Yoo ALee Y, Liszka T. Multiscale modeling of elastic properties of trabecular bone. J R Soc Interface 2012;9:1654–1673.

[3.16] Hamed E, Novitskaya E, Li J, Chen P-Y, Jasiuk I, McKittrick J. Elastic moduli of untreated, demineralized, and deproteinized cortical bone: Validation of a theoretical model of bone as an interpenetrating composite material. Acta Biomater 2012;8:1080-92.

[3.17] Toroian D, Lim JE, Price PA. The size exclusion characteristics of type I collagen - Implications for the role of noncollagenous bone constituents in mineralization. J Biol Chem 2007;282:22437-22447.

[3.18] Chen P-Y, Toroian D, Price PA, McKittrick J. Minerals form a continuum phase in mature cancellous bone. Calcif Tissue Inter 2011;88:351-361.

[3.19] Gibson LJ, Ashby MF. Cellular Solids – Structure and Properties. 2nd Edition ed. Cambridge: Cambridge University Press; 1999, pp.316-331.

[3.20] Olszta MJ, Cheng XG, Jee SS, Kumar R, Kim YY, Kaufman MJ, et al. Bone structure and formation: A new perspective. Mater Sci Eng, R 2007;58:77-116.

[3.21] Novitskaya E, Chen PY, Lee S, Castro-Ceseña A, Hirata G, Lubarda VA, et al. Anisotropy in the compressive mechanical properties of bovine cortical bone and the mineral and protein constituents. Acta Biomater 2011;7:3170-3178.

[3.22] Orgel JPRO, Miller A, Irving TC, Fischetti RF, Hammersley AP, Wess TJ. The in situ supermolecular structure of type I collagen. Structure 2001;9:1061–1070.

[3.23] Parry DAD, Craig AS. Growth and development of collagen fibrils in connective tissue. In: Ruggeri A, Motta PM, editors. Ultrastructure of the connective tissue matrix. Boston: Martinus Nijhoff; 1984. p. 34-63.

[3.24] Miller A. Collagen: the organic matrix of bone. Philos Trans R Soc Lond B Biol Sci 1984;304:455-77.

[3.25] Schmitt FO, Hall CE, Jakus MA. Electron microscope investigations of the structure of collagen. J Cell Comp Physiol 1942;20:11-33.

[3.36] Orgel JPRO, Irving TC, Miller A, Wess TJ. Microfibrillar structure of type I collagen in situ. Proceedings of the National Academy of Sciences of the United States of America 2006;103:9001-5.

[3.27] Currey JD. Bones: structure and mechanics. Princeton: Princeton University Press; 2002.

[3.28] Jackson SA, Cartwright AG, Lewis D. Morphology of bone-mineral crystals. Calcif Tissue Res 1978;25:217-22.

[3.29] Rubin MA, Jasiuk L, Taylor J, Rubin J, Ganey T, Apkarian RP. TEM analysis of the nanostructure of normal and osteoporotic human trabecular bone. Bone 2003;33:270-82.

[3.30] Weiner S, Price PA. Disaggregation of bone into crystals. Calcif Tissue Int 1986;39:365-75.

[3.31] Ziv V, Weiner S. Bone crystal sizes- A comparison of transmission electron microscopic and X-ray diffraction line width broadening techniques. Connect Tissue Res 1994;30:165-75.

[3.32] Hang F, Barber AH. Nano-mechanical properties of individual mineralized collagen fibrils from bone tissue. J R Soc Interface 2011;8:500-5.

[3.33] Landis WJ, Hodgens KJ, Arena J, Song MJ, McEwen BF. Structural relations between collagen and mineral in bone as determined by high voltage electron microscopic tomography. Microsc Res Tech 1996;33:192-202.

[3.34] Landis WJ, Song MJ, Leith A, McEwen L, McEwen BF. Mineral and organic matrix interaction in normally calcifying tendon visualized in 3 dimensions by high-voltage electron-microscopic tomography and graphic image reconstruction. J Struct Biol 1993;110:39-54.

[3.35] Bonar LC, Lees S, Mook HA. Neutron-diffraction studies of collagen in fully mineralized bone. J Mol Biol 1985;181:265-70.

[3.36] Katz EP, Li S. Structure and function of bone collagen fibrils. J Mol Biol 1973;80:1-15.

[3.37] Pidaparti RMV, Chandran A, Takano Y, Turner CH. Bone mineral lies mainly outside collagen fibrils: Predictions of a composite model for osteonal bone. J Biomech 1996;29:909-16.

[3.38] Sasaki N, Tagami A, Goto T, Taniguchi M, Nakata M, Hikichi K. Atomic force microscopic studies on the structure of bovine femoral cortical bone at the collagen fibril-mineral level. J Mater Sci: Mater Med 2002;13:333-340.

[3.39] Remaggi F, Cane V, Palumbo C, Ferretti M. Histomorphometric study on the osteocyte lacuno-canalicular network in animals of different species. I. Woven-fibered and parallel fibered bones. Ital J Anat Embryol 1998;103:145-55.

[3.40] McCreadie BR, Hollister SJ, Schaffler MB, Goldstein SA. Osteocyte lacuna size and shape in women with and without osteoporotic fracture. J Biomech 2004;37:563-72.

[3.41] Reilly GS, Knapp HF, Stemmer A, Niederer P, Knothe Tate ML. Investigation of the morphology of the lacunocanalicular system of cortical bone using atomic force microscopy. Ann of Biomed Engineer 2001;29:1074-81.

[3.42] Giraud-Guille MM. Twisted plywood architecture of collagen fibrils in human compact bone osteons. Calcif Tissue Int 1988;42:167-80.

[3.43] Giraud-Guille MM. Plywood structures in nature. Curr Opin Solid State Mater Sci 1998;3:221-7.

[3.44] Currey JD. Relationship between stiffness and mineral content of bone. J Biomech 1969;2:477-80.

[3.45] Hall RH. Variations with pH of the tensile properties of collagen fibres. J Soc Leather Trades Chem 1951;35:195-210.

[3.46] Gilmore RS, Katz JL. Elastic properties of apatites. J Mater Sci 1982;17:1131-41.

[3.47] Katz JL, Ukraincik K. On the anisotropic elastic properties of hydroxyapatite. J Biomech 1971;4:221-7.

[3.48] Snyders R, Music D, Sigumonrong D, Schelnberger B, Jensen J, Schneider JM. Experimental and *ab initio* study of the mechanical properties of hydroxyapatite. Appl Phys Lett 2007;90;193902-193905.

[3.49] Sun CT, Li S. Three-dimensional effective elastic constants for thick laminates. J Comp Mater 1988;22:629-639.

[3.50] Dong XN, Guo XE. Prediction of cortical bone elastic constants by a two-level micromechanical model using a generalized self-consistent method. J Biomech Eng 2006;128:309-316.

[3.51] Gibson LJ.The mechanical behavior of cancellous bone. J Biomech 1985;18: 317-328.

[3.52] Gibson LJ, Ashby MF. Cellular Solids: Structure and Properties, 2nd ed. Cambridge, University Press, 1997.

[3.53] Chen P-Y, McKittrick J. Compressive mechanical properties of demineralized and deproteinized cancellous bone. J Mech Behav Biomed Mater 2011;4:961-73.

[3.54] Rho JY, Kuhn-Spearing L, Zioupos P. Mechanical properties and the hierarchical structure of bone. Med Eng Phys 1998;20:92-102.

[3.55] Ascenzi A. The micromechanics versus the macromechanics of cortical bone--a comprehensive presentation. J Biomech Eng 1988;110:357-63.

[3.56] Riggs CM, Vaughan LC, Evans GP, Lanyon LE, Boyde A. Mechanical implications of collagen fibre orientation in cortical bone of the equine radius. Anat Embryol (Berl) 1993;187:239-48.

[3.57] Robling AG, Stout SD. Morphology of the drifting osteon. Cells Tissues Organs 1999;164:192-204.

[3.58] Jager I, Fratzl P. Mineralized collagen fibrils: A mechanical model with a staggered arrangement of mineral particles. Biophys J 2000;79:1737-46.

[3.59] Gupta HS, Stachewicz U, Wagermaier W, Roschger P, Wagner HD, Fratzl P. Mechanical modulation at the lamellar level in osteonal bone. J Mater Res 2006;21:1913-21.

[3.60] Odgaard A. Three-dimensional methods for quantification of cancellous bone architecture. Bone 1997;20:315-328.

# Chapter 4 COMPARATIVE STUDY OF YOUNG AND MATURE BOVINE CORTICAL BONE

In this chapter the mechanical properties and microstructure of young and mature bovine femur bone were investigated by optical microscopy and compression testing in the longitudinal and transverse directions for untreated, deproteinized, and demineralized bone. Mature bone was found to be stronger in both directions for the untreated and deproteinized cases. Mature untreated bone was also found to be stiffer and less tough than young bone in both directions. These results are related to the increase in mineralization of mature bone and significant microstructural differences. Young bone was found to be stronger in both directions for the demineralized case, which is attributed to alternations in the collagen network with age. Optical microscopy revealed that mature bone has a more establishedand less porous microstructure compared to young bone.

## 4.1 Introduction and Background

Several groups have investigated mineral contents of young and mature bovine and human bones [4.1-4.3]. Bovine and human bones reach their maturity level at different ages. According to Carter *et al.* [4.4], humans achieve full growth by the age of 16 years, while bovines are fully grown in two years. Therefore, the rate of bone growth is much higher for bovine bones than for human ones. This factor is extremely important for analyzing structure and mechanical properties of bone. In bovines and humans, the bone mineral density increases significantly with age, resulting in corresponding changes in elastic properties, toughness, and fracture risk [4.5, 4.6]. Furthermore, Currey and co-authors [4.3, 4.7] demonstrated that bone from several species becomes more mineralized with increasing age, becoming stiffer and less tough.

In addition, other factors such as collagen deterioration with age were found to influence age-related bone mechanical properties [4.8, 4.9]. Studies have shown strong dependence of bone strength on collagen alignment and collagen content [4.10]. Research on osteogenesis, a bone protein deficiency disease, found in cattle and humans, also showed that a deficiency of proteins decreases bone strength and durability [4.11]. Several interesting results concerning the age related changes of bone microstructure and its influence on bone toughening mechanisms were reported by Nalla *et al.* [4.12], and Ritchie *et al.* [4.13]. They attributed the fracture sensitivity of aged bones to an increasing density of Haversian systems and changes in collagen cross-linking at the nano level. A similar study by Zioupos and Currey [4.14] showed that an increase in stiffness with age lead to a decrease in work of fracture and critical stress intensity factor, which is required to initiate a macrocrack.

Bone deprotenization and demineralization are powerful methods used to separate the two main constituents and allow detailed investigation of properties of the mineral and protein phases separately. Compressive mechanical properties of bone and its main constituents were recently studied for mature bovine cortical bone [4.15] and mature bovine trabecular bone [4.16]. It was shown that both bone types are interpenetrating composite material of the mineral and protein constituents.

Mature bovine cortical bone its main constituents were found to have anisotropic mechanical properties [4.15]. The longitudinal direction was found to be the strongest for demineralized and deproteinized bone due to the preferential collagen fibers orientation in the former case and the mineral crystals preferential orientation in the latter case. To the best of author's knowledge, there is no side-by-side investigation of the anisotropic

properties of mature and young bones and their main constituents. This investigation is the main goal of this chapter.

## 4.2 Materials and Methods

### 4.2.1 Sample preparation

Mature and young bovine femur bones from mid-diaphysis region were purchased from a local butcher shop (La Jolla, CA). The slaughter age was about 18 months for the mature bone samples and about 6 months for young bone samples. All bones were either kept frozen or refrigerated (4˚C) in Hank's balanced saline solution (HBBS). Cross-sectional samples were first roughly cut with a band saw and then precisely shaped with a diamond blade under constant water irrigation into rhomboid parallelepipeds with dimensions 5 x 5 x 7.5 $mm^3$ for compression testing [21]. Samples were cut in two anatomical directions. The longitudinal direction coincided with bone growth direction, and the transverse direction was chosen to be perpendicular to the longitudinal one (Fig. 2.1, page 61).

Additionally, samples for optical imaging, which consisted of the entire mid-diaphysis cross-section (1 cm thick), were prepared using four separate grinding papers and two additional polishing papers. A total of four cross-sectional samples (two for mature and two for young bones) were prepared.

### 4.2.2 Mineral content

Ash content of young and mature bovine samples were determined by heating the samples in an oven for four hours at 105˚C first to evaporate the water, and then for 24

hours at 550˚C to eliminate the collagen content. The weights of the individual samples were measured before and after the heating processes. Weight percent mineral (wt.%) was calculated by dividing the weight after by the weight before heating. Mineral volume percent (vol.%) was calculated by multiplying the wt.% by the ratio of the density of hydoxyapatite to the density of mature cortical bone for mature bone samples or the density of young cortical bone for young bone samples.

### 4.2.3 Deproteinization and demineralization processes

Deproteinization was performed by aging samples in 5.25 wt.% NaOCl (bleach) at 37˚C [4.18]. The bleach solution was replaced daily for two weeks. At the end of the deproteinization process, samples were left overnight under running water to wash away the bleach solution to avoid undesirable chemical side effects. Demineralization was performed by aging the samples in 0.6 N HCl solution at room temperature [4.16]. The acid was replaced daily for ten days. At the end of the demineralization process, samples were left overnight under running water to wash away the acid solution, avoiding undesirable chemical side effects.

### 4.2.4 Structural characterization

Mature and young bone samples from all three groups (untreated (UT), demineralized (DM), and deproteinized (DP)) were analyzed by optical microscopy using a Zeiss Axio imager equipped with a CCD camera (Zeiss Microimaging Inc., Thornwood, NY). Entire cross-sections were analyzed along axes of major angles (0, 45, 90, 135, 180, 225, 270, 315˚) with 0˚ corresponding to lateral (outer) side of the femur (Fig. 4.1). Five photos were taken across each angle of mature cross-sectional sample and

approximately three images across each angle of young cross-sectional sample. Energy-dispersive x-ray spectroscopy (EDS) (FEI-XL30, FEI Company, Hillsboro, OR) was also used for chemical characterization of young and mature samples.

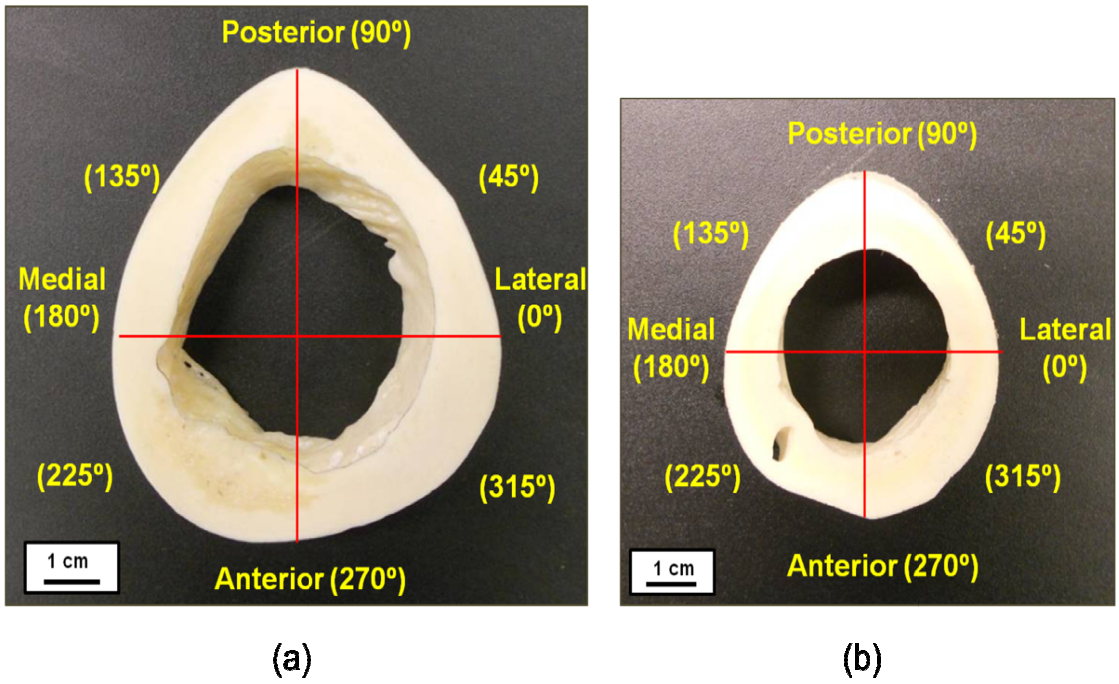


**Figure 4.1** Photographs of cross-sections of (a) mature and (b) young bovine cortical bone.

### 4.2.5 Image processing

An image processor, ImageJ, was used to analyze the porosity of the bone samples. Optical images at 5x and 10x magnifications were individually examined. Porosity values were calculated dividing the sum of the areas of the pores by the total area of the image. Images taken of the cross-sections were stitched together into a continuous image using ArcSoft Panorama Maker Pro, which allowed better analysis of micro- and macrostructure as well as structural changes with respect to a position.

### 4.2.6 Compression testing

Five samples for compression testing were prepared for each of the UT, DP, and DM samples for both young and mature bones in the longitudinal and transverse directions. UT and DP samples were tested with a universal testing machine equipped with a 30 kN load cell (3367 Dual Column Testing System, Instron, Norwood, MA). DM samples were tested with a universal testing machine equipped with a 500 N load cell (3342 Single Column Testing System, Instron, Norwood, MA). Samples were stored in Hank's balanced saline solution for 24 hours prior to testing and were tested in hydrated condition. All samples were tested at a strain rate of $10^{-3}$ $s^{-1}$, and were loaded until failure.

### 4.2.7 Micro-hardness testing

The micro-hardness of two mature and young bone cross-sections was measured using a LECO M-400-H1 hardness testing machine equipped with a Vickers indenter. A load of 100 gf was utilized to indent the exposed surfaces. The Vickers hardness of the bony plates was evaluated by equation:

$$HV = \left(1.854\frac{F}{d^2}\right) \times 9.81$$

where $HV$ is the Vicker's hardness number in MPa, $F$ is the applied load in kgf, and $d$ is the arithmetic mean of the two measured diagonals in mm.

### 4.3 Results and Discussion

Comparisons of young and mature bone microstructures reveal a more undeveloped structure for young bone (Fig. 4.2). Fig. 4.2a shows that mature bone consists of larger secondary osteons (Haversian systems) that are ~ 150-250 µm in diameter. The secondary osteons are uniformly spread throughout the mature bone (Fig. 4.2a). Fig. 4.2b shows that young bone consists of primary osteons that are ~70-90 µm in diameter. Therefore, the microstructure of young bone appears to be under construction and in the developmental stage. In contrast, the overall structure of mature bone is well developed and more uniform. Mature bone has undergone remodeling, which is clearly seen by the presence of the well developed multi-layered secondary osteons and interstitial bone regions (Fig. 4.2a).

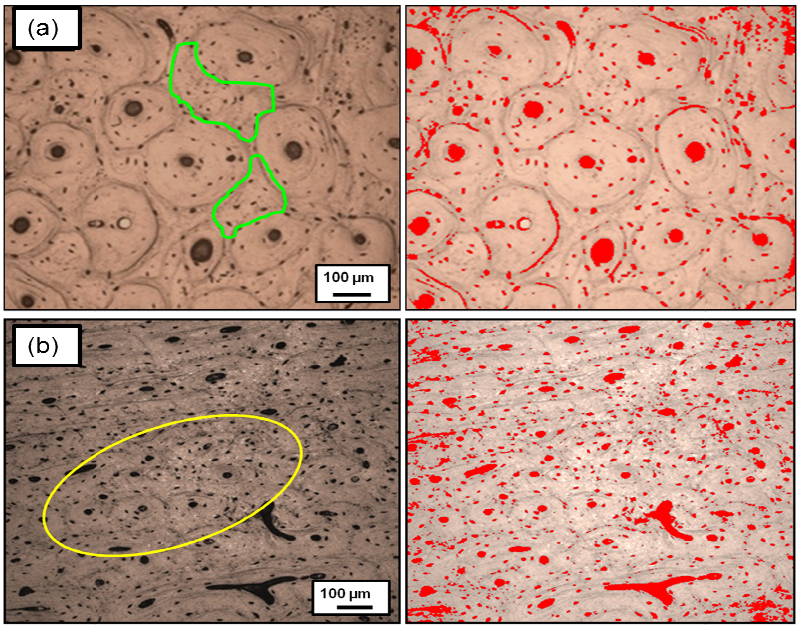


**Figure 4.2** Cross-sectional optical micrographs along with porosity analysis by ImageJ for (a) mature and (b) young. Interstitial bone regions, surrounded by secondary osteons, are enclosed in (a). Area with primary osteons is enclosed in (b).

More detailed microstructural analysis was performed on the entire cross-sections of mature and young bones (Fig. 4.3). Areas with mostly plexiform bone, a mix of plexiform and osteonal bone, and mostly osteonal bone were distinguished for the mature bone. The lateral site of mature bone was made up entirely of layers of plexiform bone with very few osteons (Fig. 4.3a). The medial side of mature bone sample was composed entirely of osteonal bone (Fig. 4.3a). The young bone composed of a disorganized mixture of developing osteonal and plexiform bone (Fig. 4.3b). Both the lateral and medial sides of young bone were composed of the same undeveloped microstructure (Fig. 4.3b). It was previously shown that different bovine femur bone quadrants have different microstructure that mostly related to the rate of bovine bone remodeling [4.19, 4.20]. The distribution of mechanical stress and muscular activity are the most relevant reasons for the differences in the rate of remodeling [4.19].

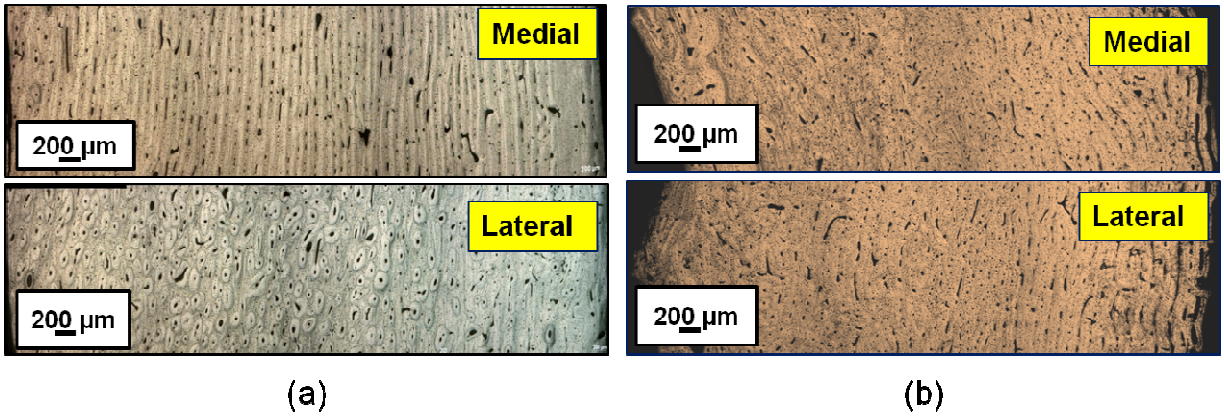


**Figure 4.3** Optical micrographs of (a) mature and (b) young bovine cortical bones in the medial and lateral areas.

Porosity numbers for mature and young bone were first evaluate from Fig. 4.2 that shows optical microscopy images together with images processed by ImageJ software revealing the porosity (red areas). The amount of porosity for young bone is

~8% by area, whereas mature bone is ~5% by area. Since porosity inversely affects strength, the higher porosity of young bone is in agreement with the previous results demonstrating that mature bone is stronger than the young bone. Furthermore, young bone needs more pores for nutrients to pass through in order to support its fast growing tissue.

Detailed porosity evaluation for the different quadrants around the bone cross-section (posterior = 90°, anterior = 270°, lateral = 0° and medial = 180°, Fig. 4.1) was performed for both mature and young bone samples. Representative optical microscopy images of mature and young bovine cortical bone are shown at Fig. 4.4 and Fig. 4.5, correspondingly. It is clear that posterior and anterior quadrants are much more porous compare to the medial and lateral ones for both mature and young bones due to non-uniform load distribution.

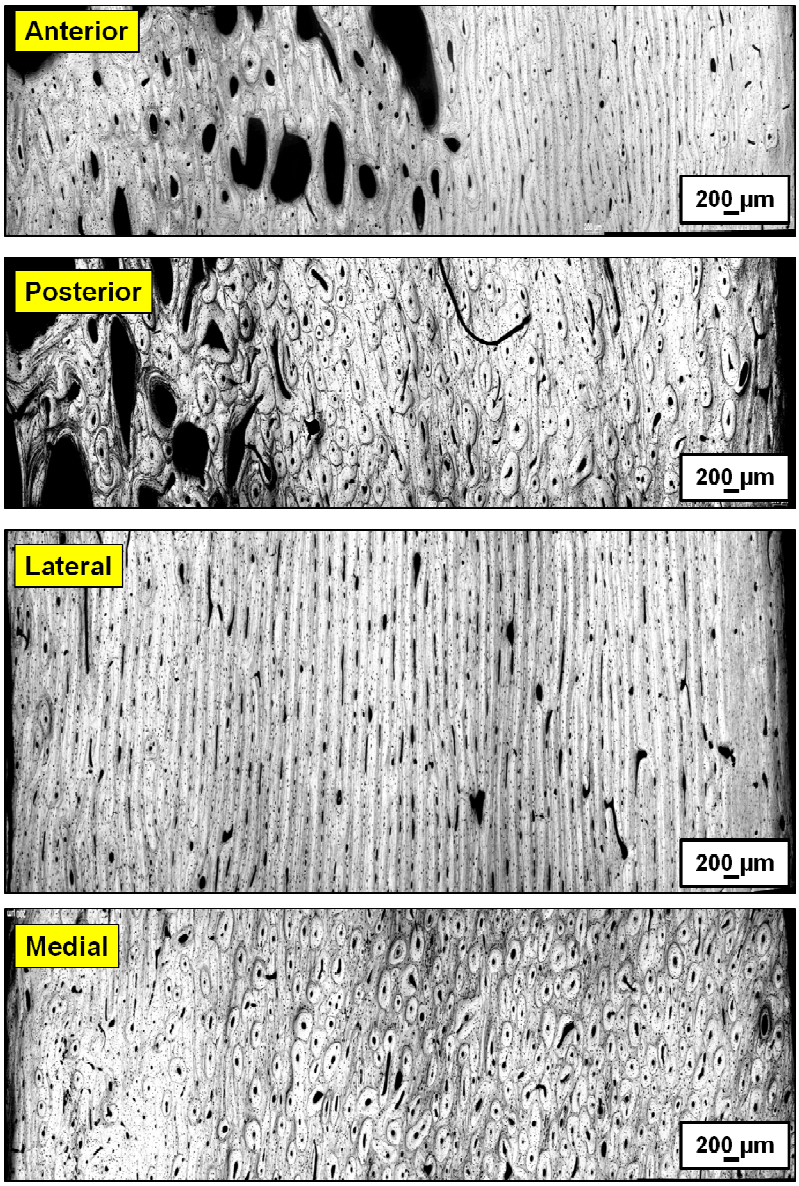


**Figure 4.4** Optical microscopy images of anterior, posterior, lateral, and medial quadrants of mature bovine cortical bone.

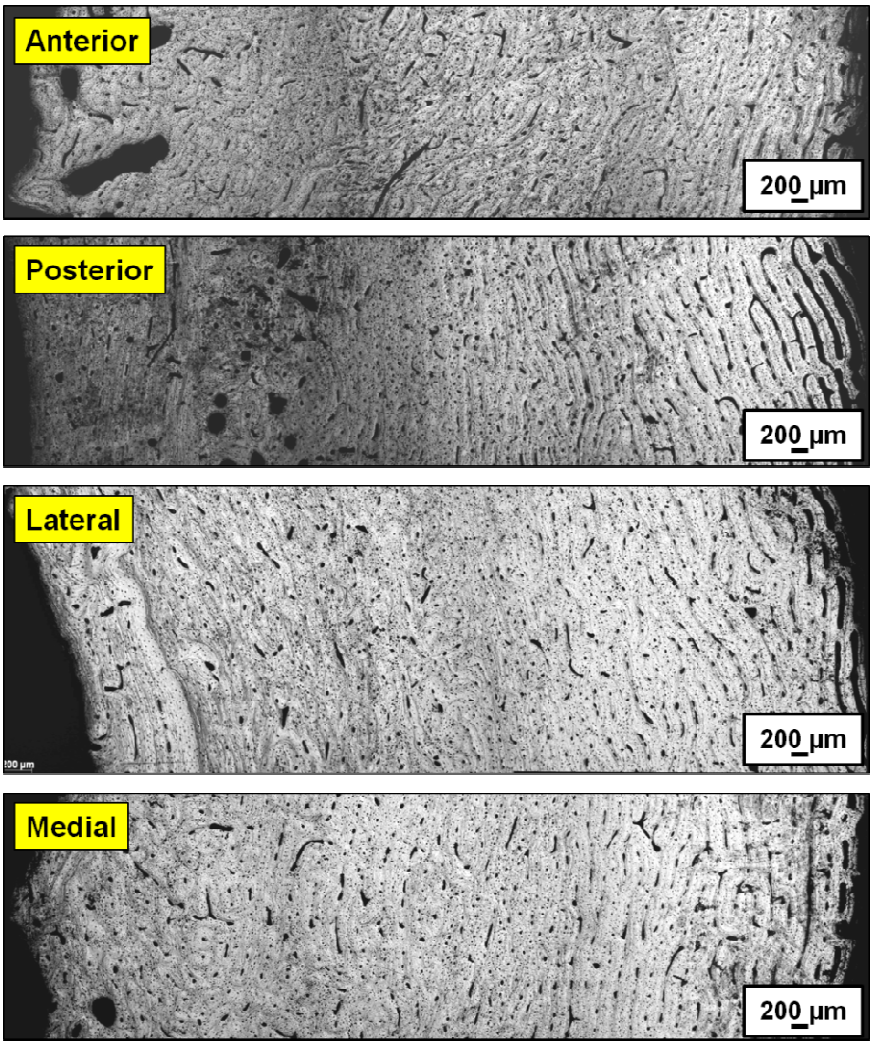


**Figure 4.5** Optical microscopy images of anterior, posterior, lateral, and medial quadrants of young bovine cortical bone.

Figure 4.6 summarized the results of this evaluation, showing that the young bone has larger amount of porosity everywhere around the bone cross-section. Moreover, it shows that porosity distribution has peaks at posterior and anterior regions; these regions correspond to the areas that accommodate more stress and therefore need larger nutrition supplies during animal life conditions. The smallest porosity amount corresponds to the

lateral and medial quadrants for both mature and young bone, showing that those areas of bone are denser and should be stronger in agreement with previous works [4.20].

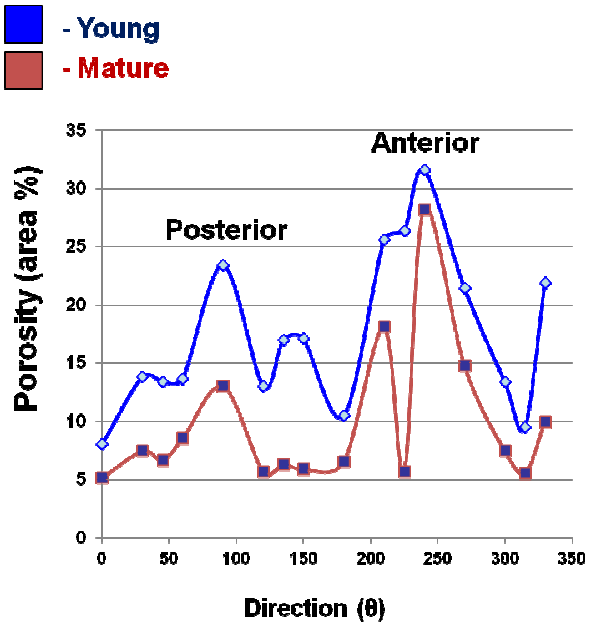


**Figure 4.6** Porosity distribution around bone cross-section for mature and young bone.

To further verify this assumption, micro-hardness measurements were performed around mature and young bone cross-sections. Fig. 4.7 summarized the results of these measurements. Interestingly enough, the areas with minimum porosity (lateral and medial quadrants) for the young bone have higher micro-hardness numbers, while lateral and medial quadrants for the mature bone are still harder compare to posterior and anterior quadrants. Stress redistribution with animal maturation is the possible reason for that: it seems that posterior and anterior quadrants of the bone are only responsible for the initial bone nutrition and weight support. As an animal grows, the anterior and posterior regions are unable to cope with increasing load demand, and then lateral and medial sides accommodate for the needed support. Additionally, these findings confirm the hypothesis

that mature bone is stronger in almost all areas around the bone cross-section: significant differences ($p < 0.05$, using one-way ANOVA software) between mature and young bone micro-hardness numbers were found for posterior, lateral, and medial quadrants.

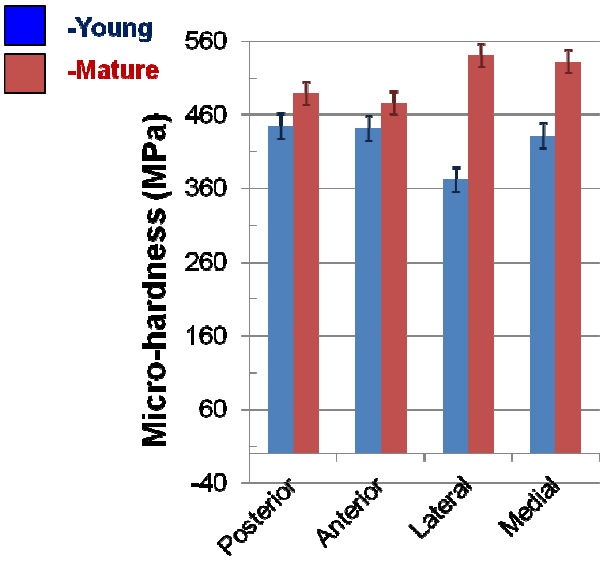


**Figure 4.7** Micro-harness data for different bone quadrants for mature and young bone.

Representative compressive stress-strain curves for UT mature and young bones in the two anatomical directions are shown on Figs. 4.8a and 4.8b. The compressive strength of mature bone is significantly higher than young bone in both directions. Moreover, the toughness (area under the stress-strain curve) of the young bone is significantly higher than that of mature bone. This demonstrates that young bone has a higher ability to absorb energy and plastically deform without fracturing. These results can be, in part, attributed to the change in the mineralization of the bone as it ages. Young bone was found to have a lower mineral content (39±1 vol.%) compared to mature bone (43±1 vol.%). The small difference in a mineral content could be related to a relatively close age difference between the bovine specimens [4.21]. Currey *et al.* [4.7] accounted

the decrease in toughness of aging human femora to the increase in bone mineralization. Moreover, according to Skedros *et al.* [4.26], hypermineralized lamellae surrounding primary osteons help improve toughness by deflecting the cracks that propagate throughout the bone.

Representative compressive stress-strain curves for DP bones in both directions are shown in Figs. 4.8c and 4.8d. In both directions, mature bone exhibits a higher compressive strength. In these figures, the increase in strength of the bone mineral is greater for the longitudinal direction (Fig. 4.8c) due to preferential orientation of mineral crystals, in agreement with [4.15].

Representative compressive stress-strain curves for DM bones in both directions are shown on Figs. 4.8e and 4.8f. The compressive strength and elastic modulus are higher for the young bone. These results suggest that collagen is stiffer and stronger in young bone and that the elasticity and strength become progressively degraded as bone ages. These results are in agreement with other studies [4.8, 4.9], which reported that the deterioration of collagen lowers an overall toughness of the bone by weakening the bridges that connect the collagen framework [4.12, 4.13].

Detailed compression test results for untreated young bone in longitudinal and transverse directions are summarized in Fig. 4.9. It is clear that the compressive strengths vary significantly among five longitudinal samples (Fig. 4.9a), while it is much more uniform for the samples in the transverse direction (Fig. 4.9b). Longitudinal samples with similar compressive strengths were grouped accordingly: L1 and L2 with the higher compressive strengths and L3-L5 with the lower compressive strengths. More detailed observations of the samples show that the first set of the samples (L1 and L2) have a

visible striped pattern of two different colors (white and yellow), while the color of the samples from the second set (L3-L5) was more uniform (yellow). All transversely oriented samples were striped and behaved consistently (Fig. 4.9b). EDS analysis showed that the white areas contain Mg and Na, characteristic of more mature and well developed bone material, while the yellow areas lacked these elements, suggesting that these areas are less developed.

**Table 4.1** Hydrated density, volume % of minerals, compressive strength, and Young's modulus for untreated (UT), deproteinized (DP), and demineralized (DM) mature and young bovine femur bones for longitudinal (L) and transverse (T) directions.

| Sample | Orientation | Density, $g/cm^3$ | Vol. % of minerals | Compressive strength, MPa | Young's modulus, GPa |
|---|---|---|---|---|---|
| UT mature (n = 5) | L | 2.05 ± 0.02 | 43 ± 1 | 184.1 ± 14.7 | 20.5 ± 2.3 |
| | T | 2.07 ± 0.01 | | 156.5 ± 5.3 | 13.0 ± 2.3 |
| UT young (n = 5) | L | 1.79 ± 0.14 | 39 ± 1 | 113.3 ± 39.4 | 6.6 ± 1.9 |
| | T | 1.95 ± 0.02 | | 121.0 ± 3.2 | 5.3 ± 0.1 |
| DP mature (n = 5) | L | 2.00 ± 0.02 | 100 | 11.6 ± 1.1 | 2.5 ± 0.7 |
| | T | 1.98 ± 0.02 | | 10.0 ± 2.1 | 1.9 ± 0.3 |
| DP young (n = 5) | L | 1.79 ± 0.03 | 100 | 6.1 ± 3.1 | 1.5 ± 0.6 |
| | T | 1.78 ± 0.03 | | 3.7 ± 1.6 | 0.5 ± 0.2 |
| DM mature (n = 5) | L | 1.20 ± 0.03 | 0 | 11.1 ± 2.1 | 0.04 ± 0.02 |
| | T | 1.16 ± 0.02 | | 8.9 ± 2.7 | 0.04 ± 0.01 |
| DM young (n = 5) | L | 1.11 ± 0.01 | 0 | 12.7 ± 3.9 | 0.10 ± 0.03 |
| | T | 1.08 ± 0.04 | | 9.9 ± 3.0 | 0.08 ± 0.03 |

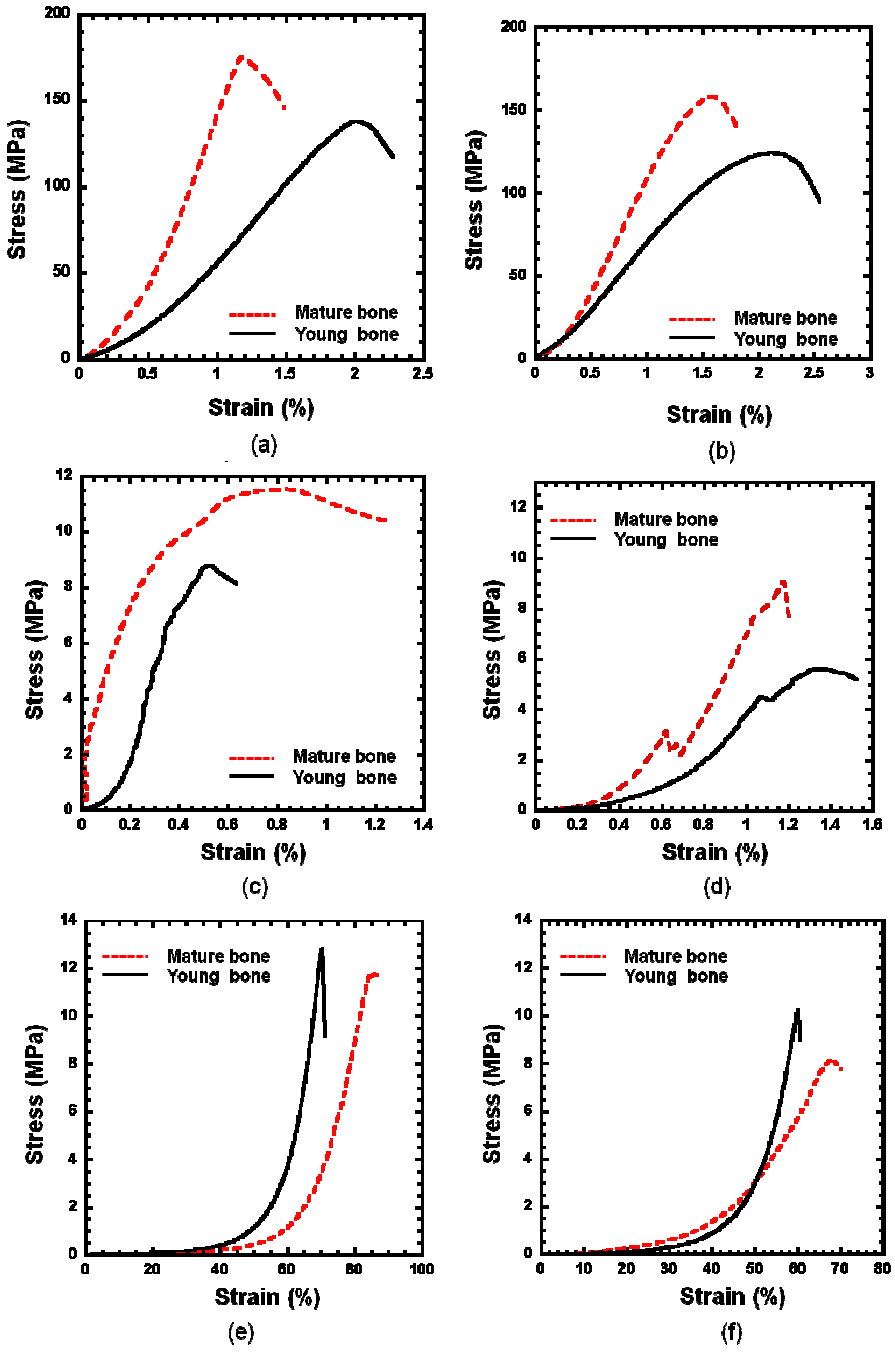


**Figure 4.8** Representative compressive stress-strain curves. Untreated mature (dashed) and young (solid) bones for (a) longitudinal and (b) transverse directions. Deproteinized mature (dashed) and young (solid) bones for (c) longitudinal and (d) transverse directions. Demineralized mature (dashed) and young (solid) bones for (e) longitudinal and (f) transverse directions.

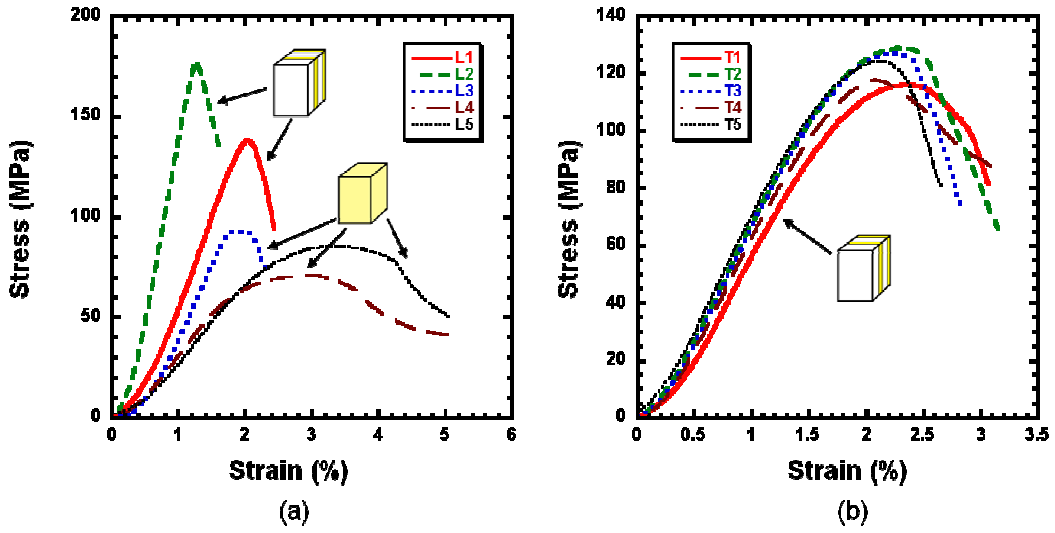


**Figure 4.9** Compressive stress-strain curves of untreated young bone in the (a) longitudinal and (b) transverse directions. Two distinct, visible regions were observed: undeveloped (yellow) and more organized (white). L1 and L2 samples were composed of both regions and L3-L5 consisted only of the yellow regions.

### 4.4 Conclusions

The mechanical properties and microstructure of untreated, deproteinized (mineral), and demineralized (protein) young and mature bovine cortical femur bones were investigated in longitudinal and transverse directions. The main findings are:

- Mature bone has more developed microstructure compared to young bone.
- Bone porosity decreases with maturation.
- Micro-hardness increases with maturation.
- Mature bone is stronger than young bone in both directions for the untreated and deproteinized bone.
- Mature bone is stiffer but has lower toughness than young bone in both directions for the untreated bone.

- Young bone is stiffer and stronger but has lower toughness than mature bone in both directions for the demineralized bone.
- Untreated young bone samples with a higher percentage of developed bone were found to have a higher strength than samples with a lower percentage of developed bone.
- Care must be taken in analyzing microstructure and reporting mechanical properties of bone, due to microstructural differences around the cross-section of the bone.

**Acknowledgements:**

Chapter 4, in part, has been submitted for a publication as it may appear in "A comparative study of young and mature bovine cortical bone," in Acta Biomaterialia, 2012. Z. Manilay; E.E. Novitskaya; E. Sadovnikov; J. McKittrick. The dissertation author was the primary investigator of this paper.

## 4.5 References

[4.1] Riggs BL, Wahner HW, Dunn WL, Bazess RB, Offord KP, Melton LJ. Differential changes in bone mineral density of the appendicular and axial skeleton with aging. J Clin Invest 1981;67:328-225.

[4.2] Boot AM, de Ridder MAJ, Pols HAP, Krenning EP, de Muinck Keizer-Schrama SMPF. Bone mineral density in children and adolescents: Relation to puberty, calcium intake, and physical activity. J Clin Endocrinol and Metabol 1997;82:57-62.

[4.3] Currey JD. Tensile yield in compact bone is determined by strain, post-yield behavior by mineral content. J Biomech 2004;37:549-556.

[4.4] Carter DR, Hayes WC, Scchurman DJ, Fatigue life of compact bone–II. effects of microstructure and density. J Biomech 1976;9:211-218.

[4.5] Aerssens J, Boonen S, Lowet G, Dequeker J. Interspecies differences in bone composition, density, and quality: potential implications for in vivo bone research. Endocrinol 1998;3:0013-7227.

[4.6] Liu XS, Cohen A, Shane E, Yin PT, Stein EM, Rogers H, Kokolus SL, McMahon DJ, Lappe JM, Recker RR, Lang T, Guo XE. Bone density, geometry, microstructure and stiffness: relationships between peripheral and central skeletal sites assessed by DXA, HR-pQCT, and cQCT in premenopausal women. J Bone Miner Res 2010;25:2229–2238.

[4.7] Currey JD, Brear K, Zioupos P. The effects of ageing and changes in mineral content in degrading the toughness of human femora. J Biomech 1996;29:257-260.

[4.8] Danielsen CC, Mosekilde L, Bollerslev J, Mosekilde L. **T**hermal stability of cortical bone collagen in relation to age in normal individuals and in individuals with osteoporosis. Bone 1994;15:91-96.

[4.9] Wang X, Shen X, Li X, Mauli Agrawal C. Age-related changes in the collage network and toughness of bone. Bone 2002;31:1-7.

[4.10] Tzaphlidou M. Bone Architecture: collagen structure and calcium/phosphorus maps. J Biol Phys 2008;34:39–49.

[4.11] Thermine JD, Robey PG, Fisher LW, Shimokawa H, Drum MA, Conn KM, Hawkins GR, Crutz JB, Thompson KG. Osteonectin, bone proteoglycan, and phosphophoryn defects in a form of bovine osteogenesis imperfect. Proc Natl Acad Sci USA 1984;81:2213-2217.

[4.12] Nalla RK, Kruzic JJ, Kirmey JH, Ballooch M, Ager JW, Ritchie RO. Role of microstructure in the aging-related deterioration of the toughness of human cortical bone. Mater Sci Eng C 2006;26:1251-1260.

[4.13] Ritchie RO, Nalla RK, Ager JW, Balooch G, Kinney JH. Fracture and ageing in bone: Toughness and structural characterization. Strain 2006;42:225-232.

[4.14] Zioupos P, Currey JD. Changes in the stiffness, strength, and toughness of human cortical bone with age. Bone 1998;22:57-66.

[4.15] Novitskaya E, Chen PY, Lee S, Castro-Ceseña A, Hirata G, Lubarda VA, McKittrick J. Anisotropy in the compressive mechanical properties of bovine cortical bone and the mineral and protein constituents. Acta Biomater 2011;7:3170-3177.

[4.16] Chen P-Y, Toroian D, Price PA, McKittrick J. Minerals form a continuum phase in mature cancellous bone. Calcif Tissue Inter 2011;88:351-61.

[4.17] Keller TS, Liebscher MAK. Tensile and compression testing of bone. In: An YH, Draughn RA, editors. Mechanical testing of bone and the bone-implant interface. Boca Raton: CRC Press LLC; 2000. p 178-81.

[4.18] Toroian D, Lim JE, Price PA. The size exclusion characteristics of type I collagen - Implications for the role of noncollagenous bone constituents in mineralization. J Biol Chem 2007;282:22437-22447.

[4.19] Lipson SF, Katz JL. The relationship between elastic properties and microstructure of bovine cortical bone. J Biomech 1984;17:231-240.

[4.20] Abdel-Wahab AA, Alam K, Siberschmidt VV. Analysis of anisotropic viscoelastic properties of cortical bone tissue. J Mech Behav Biomed Mater 2011;4:807-820.

[4.21] Nordström A, Tervo T, Högström M. The effect of physical activity on bone accrual, osteoporosis and fracture prevention. Open Bone J 2011;3:11-21.

[4.22] Skedros JG, Durand P, Bloebaum RD. Hypermineralized peripheral lamellae in primary osteons of deer antler: potential analogues of cement lines in mammalian secondary bone. J Bone Miner Res 1995;10:441.

# Chapter 5 MODELING OF THE OSTEOPOTIC DEGRADATION OF ELASTIC PROPERTIES OF TRABECULAR BONE

This chapter will cover the modeling of osteoporotic degradation of trabecular bone. The elastic modulus of trabecular bone was derived based on the measured elastic properties of separate mineral and protein phases. Adopting the mechanics of cellular solids approach, the moduli of elasticity of composite trabecular, deproteinized trabecualr and demineralized trabecular bone were expressed in terms of the trabecular moduli of elasticity and the corresponding density ratios using the power law expressions. The Young's modulus of trabeculae of bone are related to the Young's moduli of deproteinized and demineralized trabeculae through a modified mixture rule, which incorporates an appropriate weight function to account for the mineral/protein interaction effects, and the departure from the ideal mixture rule. Two expressions for the effective modulus of elasticity of trabecular bone were derived: one in terms of the moduli of elasticity of mineral and protein trabeculae, and the other in terms of the moduli of elasticity of deproteinized and demineralized trabecular bone. The material parameters were specified from the results of compressive testing of untreated, deproteinized, and demineralized bovine femur trabecular bone. The osteoporotic decrease of the elastic moduli was analyzed. Two evolution equations were introduced, one for the rate of loss of the mineral content of trabecular bone, and the other for the rate of the protein loss. Both losses are associated with the corresponding density and volume changes, for which appropriate equations are proposed. Based on these, and the evolution equations for morphological parameters accounting for the trabecular microarchitecture, the evolution equations were derived for the elastic moduli of deproteinized, demineralized and

composite trabecular bone. A particular model of osteoporotic degradation was considered in which it is assumed that the relative ratios of the mineral and protein loss are equal to each other during the progression of osteoporosis.

### 5.1 Introduction and Background

Trabecular (cancellous, spongy) bone is a porous inner portion of vertebrae, ribs, skull and the head of the femur, which is surrounded by hard outer layer – cortical (compact) bone. For example, the metaphyses and epiphyses of long bones consist of trabecular compartment surrounded by thin shell of cortical bone; the diaphyses are entirely cortical. Cortical bone predominates in the appendicular skeleton and can resist both tension and compression, while trabecular bone is concentrated in the axial skeleton and is structured to resist compression. While the porosity of cortical bone is in the range of 5–10%, the porosity of trabecular bone is about 40% in the femoral neck, to more than 90% in the elderly spine. Dry trabecular bone can be considered as a composite material consisting of interpenetrating mineral and protein phases [5.1]. This is confirmed by demineralization and deproteinization processes, which result in stand-alone cellular structures of pure mineral (deproteinized bone) or pure protein (demineralized bone), as shown in Fig. 5.1.

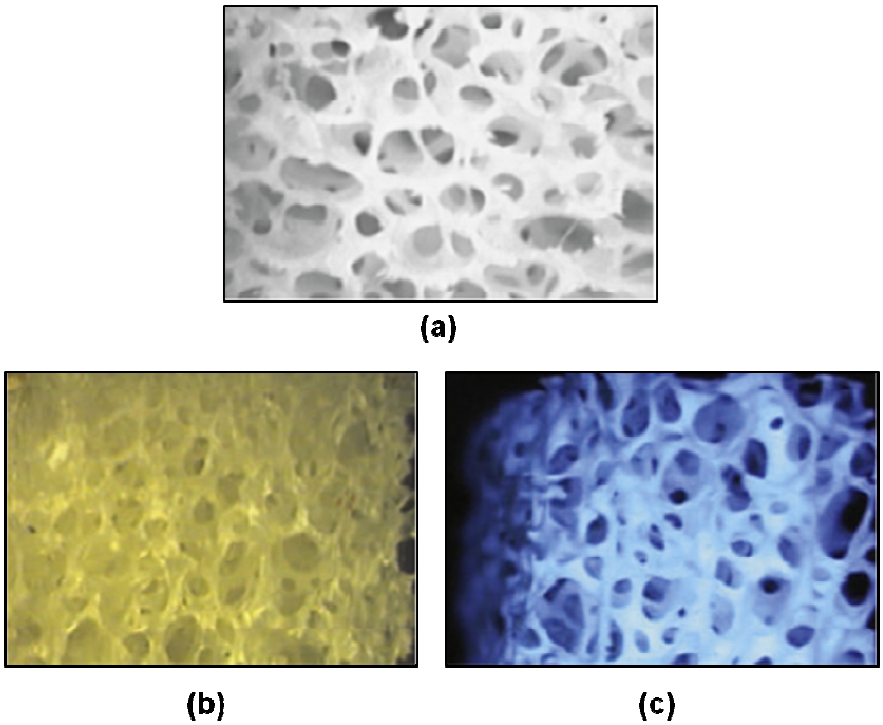


**Figure 5.1** Photographs of cross-sections (5 x 5 mm) of trabecular bovine femur: (a) control/untreated (UT), (b) demineralized (DM), and (c) deproteinized (DP) bone samples (adopted from [5.24]). The volumes of the UT, DM, and DP samples are nearly the same, i.e., $= V_m = V_p$ .

Mechanical properties of trabecular bone are influenced by the trabecular density (fraction of the bone actually occupied by the trabecular bone tissue), the densities of its mineral and protein phases (degree of matrix mineralization and collagen cross-link concentration), their interaction, and the microstructural arrangement of trabecular network (micro-architecture or fabric), [5.2-5.4]. There are other factors that may influence mechanical properties of bone. For example, larger crystals may present in older bone. This increased crystalline size could impair the mechanical properties by permitting earlier crack initiation and decreasing bone ductility [5.5; 5.6]. The elastic stiffness and the strength of trabecular bone are nonlinearly related to the apparent bone

density [5.7; 5.8]. For example, Marcus and Bouxsein [5.9] cite that a 25% decrease in density, associated with 15 years of age-related bone loss, gives rise to 44% decrease of the stiffness of trabecular human bone, with a similar effect on the bone strength. In trabecular bone of the proximal tibia, a decline in apparent density of 25% is associated with a 30–40% reduction in compressive strength and fracture toughness. Microstructural changes of trabecular network due to bone loss, such as thinning or loss of trabecular elements, also exert strong effect on the bone strength. For example, the loss of trabecular connectivity due to the loss of trabecular cross-struts cause a decrease of the buckling strength of isolated trabeculae [5.10], resulting in decrease in strength of the entire bone. In some bones (vertebrae and proximal tibia), the detrimental effect of the decrease of the bone mass on its strength is offset by the development of an increased anisotropy of the trabecular structure porosity increases predominantly in the vertical direction, as the horizontally oriented trabeculae thin and disappear faster than vertically oriented trabeculae (according to Wolffs law, the loaded bone tends to adapt its inner and outer architecture to the environment (loads), so that trabeculae align along stress trajectories to better carry the weight). This helps the load-carrying capacity along vertical (axial) direction, but is accompanied by the decrease in the load carrying capacity in horizontal (transverse) directions, which increases the risk of fracture due to no habitual, off-axis loading [5.11; 5.12]. For example, the ratio of compressive strengths of vertically and horizontally loaded specimens from human lumbar vertebrae increases from approximately 2 at age of 20 to 3.5 at age 80. During this time period, the ash density of vertebral trabecular bone decreases approximately by 50%, with the mechanical properties decrease of as much as 75–90% [5.13]. The objective of the present research is

to derive the elastic properties of trabecular bone based on the measured elastic properties of isolated mineral and protein phases. After deriving the relationships between the mass densities of individual phases and the composite matrix, the approach from the mechanics of cellular solids is adopted to express the moduli of elasticity of composite trabecular, deproteinized and demineralized bones in terms of the trabecular moduli of elasticity and the corresponding density ratios using the power law expressions. The Young's modulus of bone's trabeculae is related to the Young's moduli of deproteinized and demineralized trabeculae by a modified mixture rule, in which an appropriate weight function is incorporated to account for the mineral/protein interaction effects and the corresponding departure from the ideal mixture rule. Two alternative expressions for the effective modulus of elasticity of trabecualar bone were derived, one in terms of the moduli of elasticity of mineral and protein trabeculae, and the other one in terms of the moduli of elasticity of deproteinized and demineralized bone. It was shown that the modulus of elasticity of composite trabecular bone is far from being governed by a simple mixture rule in terms of moduli of elasticity of mineral and protein phases and its volume fractions. The presented analysis was applied to bovine femur trabecular bone. The needed material parameters were specified from the results obtained in compressive testing of trabecular samples from untreated (composite), deproteinized, and demineralized bovine femur bone. Moreover, the osteoporotic deterioration of elastic moduli was presented. Two evolution equations were introduced, one for the rate of loss of the mineral content of trabecular bone, and the other for the rate of the protein loss. Both losses are associated with the corresponding density and volume changes, for which appropriate equations are proposed. Based on these, and the evolution equations for

morphological parameters accounting for the trabecular microarchitecture, the evolution equations are derived for the elastic moduli of deproteinized, demineralized and composite trabecular bone. An osteoporotic degradation was then considered in which it is assumed that the relative ratios of the mineral and protein loss were equal to each other during the progression of osteoporosis.

## 5.2 Materials and Methods

### 5.2.1 Sample preparation

Bovine femur trabecular bone samples were obtained from a local butcher. The age of cattle at slaughter was about 18 months. The bone was carefully cleaned to remove any marrow and lipid components, using pressurized stream of compressed air and water. About 100 samples for compression testing (cubes 5 x 5 x 5 mm) were prepared from close locations of the bone in order to minimize variations in density and mineral content. The samples were first roughly cut by handsaw and then by a diamond blade with the surfaces as parallel as possible. Samples were stored in a refrigerator (T = 4°C) until chemical treatment and testing were performed. The 5 x 5 x 5 mm cubic samples (with mass of about 0.1 g) were the smallest samples that can be smoothly cut and test. There is worse to mention here that smaller cubes, with edge length of about 2 mm and mass about 5 mg, would still be large enough to contain sufficiently many trabeculae to make them statistically equivalent as representative volume elements. Although it would be hard to experiment with them, they may be considered as the smallest representative element for bovine femur trabecular bone to which a continuum constitutive model applies (the lower hierarchical level would be at the length scale of individual trabeculae,

where the study of their individual deformation or fracture could be conducted, for example, by using micro computed tomography, or high resolution magnetic resonance [5.14-5.5], and micro finite element modeling of trabecular microarchitecture [5.16; 5.17], but such analysis is beyond the scope of the present study.

### 5.2.2 Demineralization and deproteinization process

Bone samples were demineralized (DM) by aging in 0.6 N hydrochloric acid (HCl) at room temperature using the procedures outlined in [5.18] and [5.19]. Acid solutions were changed daily in order to avoid saturation that can affect the demineralization process. The whole process took about 4 days. The completeness of demineralization was verified by the mineral absence in the solution using the procedure described by [5.20]. Bone samples were deproteinized (DP) by aging (incubating) in a 2.6 wt.% sodium hypochlorite (NaOCl) solution at 37°C, following the procedure outlined in [5.1] and [5.19]. The solutions were changed daily, and the whole process took about 7 days.

### 5.2.3 Compression testing

Three different sets of the samples were prepared: 40 untreated (UT), 30 demineralized (DM) and 30 deproteinized (DP). UT and DP samples were tested in dry condition. DM samples were subjected to a critical point drying procedure before testing in order to avoid an extensive deformation and shrinkage. Before compression testing the surfaces of the samples were lubricated by petroleum jelly (vaseline) to avoid shearing deformation. Compression testing of untreated bone samples was performed on universal testing machine equipped with 30 kN load cell (Instron 3367 Dual Column Testing

Systems, Norwood, MA). Compression testing of demineralized and deproteinized bone samples was performed on universal testing machine equipped with 500 N load cell (Instron 3342 Single Column System, Norwood, MA). Compression testing for samples from all three groups was performed at a strain rate of $10^{-3}$ $s^{-1}$. An external deflectometer SATEC model I3540 (Epsilon Technology Corp., Jackson, WY) was used in order to measure the small displacement. All samples were loaded until compressive failure.

## 5. 3. Results and Discussions

### 5.3.1 Volume fractions and density relationships

Consider a representative volume element of trabecular bone whose volume is V (the representative volume element (RVE) is small enough to be considered homogeneous in the continuum mechanics sense, but large enough to include sufficiently many trabeculae (or osteons, for cortical bone). Denoting by $V^*$ the volume of its trabeculae (rods and struts), and by $V^0$ the volume of its hollow portion, $V = V^* + V^0$. Cowin [5.21] refers to porosity external to and surrounding the trabeculae as the porosity of the inter-trabecular space. Similarly, if $V_p$ and $V_m$ are the volumes of demineralized (protein) and deproteinized (mineral) phases of the material sample, we can write:

$$V_m = V_m^* + V_m^0, \qquad V_p = V_p^* + V_p^0 \tag{5.1}$$

Assuming that the bonding interactions between the mineral (m) and protein (p) phases do not appreciably affect the volumes, and since trabecular thinning by demineralization and deproteinization dominantly removes trabecular volume inside the sample (which is

an order of magnitude higher that trabecular volume from trabecular elements at the boundary of the sample), it follows that:

$$V = V_m = V_{p,} \qquad V^* = V_m^* + V_p^* \tag{5.2}$$

The volume fractions of trabeculae and inter-trabecular space are $f^* = V^*/V^0$ and $f^o = \frac{V^0}{V} = 1 - f^*$, with similar definitions for $f_m^*$ and $f_p^*$.

The mass densities $\rho$ of composite trabecular, deproteinized and demineralized bone samples are defined such that:

$$m = \rho V = \rho^* V^*, \qquad m_m = \rho_m V_m = \rho_m^* V_m^*, \qquad m_p = \rho_p V_p = \rho_p^* V_p^* \tag{5.3}$$

with the conservation of mass condition $m = m_m + m_p$. In (5.3), $\rho_m^*$ is the density of the mineral phase per unit mineral volume within the trabeculae $V_m^*$ i.e., $\rho_m^* = m_m/V_m^*$. In contrast, $\rho_m$ is the apparent density of the mineral phase per unit bulk volume (including voided intertrabecular space) of the deproteinized trabecular sample $V_m$, i.e., $\rho_m = m_m/V_m$. Similar interpretations apply to densities $\rho_p^*$ and $\rho_p$ of the protein phase. In view of the introduced assumption $V = V_m = V_p$, the conservation of mass yields the additive rule for the trabecular bone density:

$$\rho = \rho_m + \rho_{p,} \tag{5.4}$$

and the mixture rule for the trabecular density:

$$\rho^* = f_m \rho_m^* + f_p \rho_p^* . \tag{5.5}$$

The volume fractions of the mineral and protein portions of trabeculae are defined by:

$$f_m = V_m^*/V^* , \quad f_p = V_p^*/V^* , \quad (f_m + f_p = 1) . \tag{5.6}$$

In view of above definitions and assumptions, the following density relationships can be derived:

$$\begin{aligned} &(\rho_m/\rho_m^*) = f_m(\rho/\rho^*) , \quad (\rho_p/\rho_p^*) = f_p(\rho/\rho^*) , \\ &(\rho/\rho^*) = (\rho_m/\rho_m^*) + (\rho_p/\rho_p^*) . \end{aligned} \tag{5.7}$$

In particular, Eqs. (5.7) specifies the volume fraction of trabeculae, because $(V^*/V) = (\rho/\rho^*)$ . The third equation in (5.7) is obtained by adding the first two.

### 5.3.2 Young's moduli of elasticity

Adopting the approach used in the mechanics of cellular solids (Gibson and Ashby, [5.27]), the effective moduli of elasticity of trabecular bone, and its mineral and protein phases, are related to the moduli of elasticity of the corresponding trabeculae and the density ratios according to:

$$E = E^*(\rho/\rho^*)^n\,, \quad E_m = E_m^*(\rho_m/\rho_m^*)^{n_m}\,, \quad E_p = E_p^*(\rho_p/\rho_p^*)^{n_p}\,. \tag{5.8}$$

These power-law relationships are motivated by the fact that small changes in the density ratios may lead to pronounced changes in the mechanical properties [5.7; 5.17; 5.23-5.26]. The exponents $n,\ n_m, n_p$ depend on the microarchitectural details of trabecular structure (e.g., rod-rod vs. rod-plate like trabeculae). The bone structure of trabeculae is similar to the second (lamellae, lacunae) level of the cortical bone structure. This includes lamellae, lacunae, canaliculi, and cement lines, but generally no vascular channels (like cortical bone). However, lamellae, 2–6 μm thick, are arranged longitudinally within trabecular packets along the trabeculae, while they are arranged concentrically in cortical bone. At the next hierarchical level of structure (below about 0.5 μm), the collagen fibril organization within lamellae, and collagen-mineral structure, are commonly assumed to be the same as for cortical bone. The elastic modulus of such trabeculae ($E^*$) is not a simple weighted sum of the elastic moduli of pure mineral and pure protein $E^* \neq f_m E_m^* + f_p E_p^*$, because of interaction effects between the mineral and protein within each trabecula. A modified mixture rule for Young's modulus of trabeculae was adopted:

$$E^* = \phi f_m E_m^* + f_p E_p^*\,, \quad \phi = \phi(f_m)\,. \tag{5.9}$$

The weight function $\phi = \phi(f_m)$ governs the departure from the ideal mixture rule ($\phi = 1$) and accounts for the effects of interaction between the mineral and protein phase, as well as the differences in micro-porosity or other microarchitectural features of demineralized,

deproteinized, and composite trabeculae. Lucchinetti [5.27] refers to $\phi$ as an ‘‘efficiency or reinforcement’’ parameter. The individual trabecular moduli $E^*, E_m^*, E_p^*$ are themselves dependant on the micro-porosity of UT, DP, and DM trabeculae, but this intrinsic (cortical-bone-type) porosity is much smaller than porosity due to intertrabecular space (BV/TV – bone volume/tissue volume), and for simplicity, it is not explicitly included in the analysis in this section, although it will be considered in **Section 5.3.4**, when dealing with osteoporotic degradation of mechanical properties of bone. The bone marrow around trabeculae is very vascularized by embedded capillaries carrying the blood flow and providing oxygen supply, needed for metabolic bone modeling and remodeling. There is a smaller number of vascular structures within trabeculae themselves [5.28], which also contribute to their microporosity. A simple form $\phi = f_m$ is well-suited to reproduce the experimental data for bovine femur bone. When (5.9) is substituted into (5.8), the effective modulus of elasticity of trabecular bone ($E$) can be expressed in terms of the moduli of elasticity of mineral and protein trabeculae $E_m^*$ and $E_p^*$, as:

$$E = (\phi f_m E_m^* + f_p E_p^*)[(\rho_m/\rho_m^*) + (\rho_p/\rho_p^*)]^n , \tag{5.10}$$

or, in terms of the moduli of elasticity of mineral and protein phase $E_m$ and $E_p$, as:

$$E = \phi f_m^{1-n}(\rho_m/\rho_m^*)^{n-n_m} E_m + f_p^{1-n}(\rho_p/\rho_p^*)^{n-n_p} E_p . \tag{5.11}$$

Clearly, the effective modulus of elasticity of trabecular bone is far from being governed by a mixture rule, i.e., $E \neq f_m E_m + f_p E_p$ . There are other more sophisticated tools to estimate the elastic properties of composites, such as those based on the mean field (self-consistent) or microstructural homogenization methods (5.3; 5.29-5.33), but this study for simplicity adopted a modified mixture rule (5.9), leading to (5.10) and (5.11).

### 5.3.3 Experimental data

The reported modulus of elasticity for a single hydroxyapatite crystal is $E_m$ = 114 GPa [5.34], while collagen has $E_p$= 1.3 GPa [5.35]. The corresponding mass densities are $\rho_m^* = 3.15$ g/cm$^3$ [5.36], and $\rho_p^* = 1.35$ g/cm$^3$ [5.37]. We have tested in our laboratory 20 cortical bone samples from the bovine femur, under dry conditions, and have found that the modulus of elasticity and the mass density were: $E^*$= (20 ± 2) GPa and $\rho^*$= (2.04 ± 0.07) g/cm$^3$. The modulus of elasticity was determined from the slope of the compressive stress/strain curve. On the other hand, the moduli of elasticity and the mass densities of deproteinized, demineralized, and untreated (control) trabecular samples were:

$E_m$ = (295 ± 80) MPa; $\rho_m$= (0.48 ± 0.02) g/cm$^3$;

$E_p$ = (110 ± 35) MPa; $\rho_p$= (0.32 ± 0.02) g/cm$^3$;

$E$ = (1.4 ± 0.3) GPa; $\rho$ = (0.8 ± 0.03) g/cm$^3$.

The volume ratios of the mineral and protein phases were $f_m$= 0.39 and $f_p$= 0.61, as calculated from (5.7) with the mean values of the mass densities $\rho, \rho_m, \rho_p, \rho^*$. The

porosity of the cube specimen, $f^0 = \left(\frac{V^0}{V}\right) = 1 - f^*$, where $f^* = \left(\frac{V^*}{V}\right) = \left(\frac{\rho}{\rho^*}\right)$ is the volume fraction of trabeculae, was about 0.6.

The elastic moduli data for $E, E_m,\ E_p$ were well reproduced from (5.8) by taking $n_m$= 3.15, $n_p$= 1.75, $n$ = 2.84. An alternative $\phi$ that works well is $\phi$= exp $[k(f_m - 1)]$, with $k = 3/2$. For example, $n$ was calculated from the expression $n = \ln\left(\frac{E}{E^*}\right)/\ln\left(\frac{\rho}{\rho^*}\right)$, and similarly for $n_m$ and $n_p$. It is noted that $E^* \neq f_m E_m^* + f_p E_p^*$ and $E \neq f_m E_m + f_p E_p$, so that the mixture rules are far from being obeyed, particularly for trabecular bones, due to their high cellular porosities. The plots of $E^*$ vs. $f_m$, according to (5.9), are shown in Fig. 5.2.

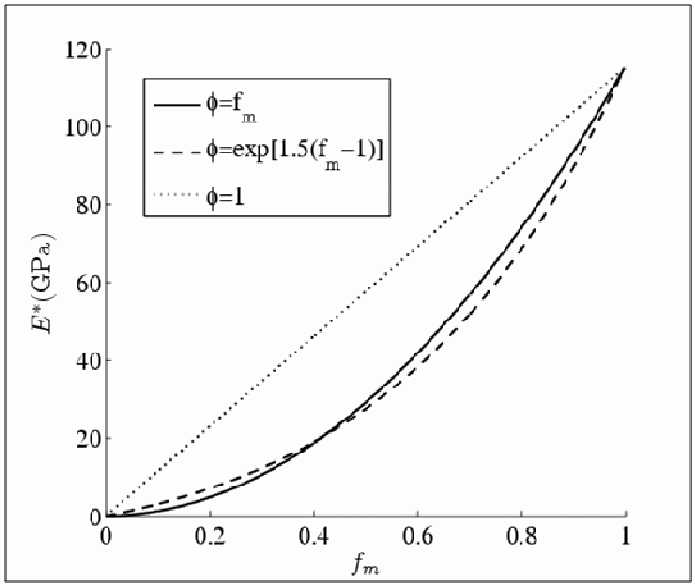


**Figure 5.2** The variation of the trabecular elastic modulus $E^*$ of trabecular bovine femur with mineral fraction $f_m$, according to Eq. (5.9).

### 5.3.4 Osteoporotic degradation

Osteoporosis is a condition of bone loss and microstructural deterioration of bone tissue, which decreases bone strength and increases skeletal fragility, so that fractures may occur under minor traumas, even those associated with normal daily activities. Progression of osteoporosis is caused by a decline in the bone formation activity relative to the resorption activity [5.38]. Since trabecular bone is lighter and more porous than compact bone, it provides more surface area for bone remodeling; it is more metabolically active, and thus more affected by osteoporosis [5.39]. The trabecular packets, found in secondary trabecular bone, are products of bone remodeling, which takes place from the outer surface of trabeculae. Osteoclasts first remove bone, and then osteoblasts deposit new bone at the places where the old bone was removed. Type I osteoporosis signifies a loss of trabecular bone after menopause, caused by the lack of endogenous estrogen, while type II osteoporosis represents a loss of cortical and trabecular bone in men and women as the end result of age-related bone loss, caused by long-term remodeling inefficiency, lack of dietary calcium and vitamin D, and associated mineral absorbtion and handling [5.9]. The calcium level in the body, including the amount of calcium in the bones, is regulated by the parathyroid glands through the secretion of parathyroid hormone. Bone degradation due to mineral loss can be determined from measurement of the bone mineral content (BMC), which can be accomplished by quantitative computed tomography, dual-photon absorptiometry, dual X-ray absorptiometry, and ultrasound [5.40]. In osteoporosis the likelihood of fracture is 10 to 20 times higher than normal. For example, osteoporosis causes about 1700 bone fractures per day in Europe (according to World Health Organization), the femoral

neck fractures being the most frequent [5.41]. It is estimated that osteoporosis is responsible for about 300,000 hip fractures per year in the United States [5.39]. Osteoporosis is a term that describes the loss of calcium from bones due to modification of the remodeling, but in the process of defective remodeling of the bone, in which resorption dominates the deposition, the collagen is lost as well. This results in thinning and resorption of entire individual trabeculae, as shown for an advanced stage of osteoporosis in Fig. 5.3.

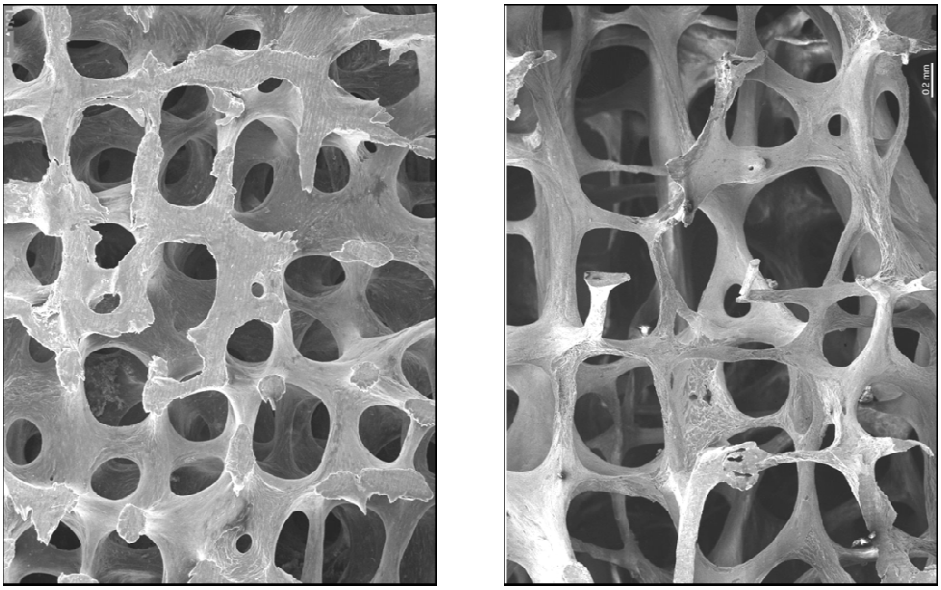


**Figure 5.3** Trabecular bone structure: (a) normal, (b) osteoporotic. The osteoporotic bones contains larger holes as a result of the calcium being dissolved (from www.brsoc.org.uk/gallery, with permission from Prof. Alan Boyde, University of London, UK).

The data on the magnitudes of separate mineral and collagen osteoporotic losses are sparse, although there are reports that suggest that their relative concentrations remain approximately constant during osteoporotic bone loss. For example, Burr [5.5] reported

that there is a decrease in the reducible collagen crosslinks in osteoporosis, but without alteration in collagen concentration. The quality of the osteoporotic collagen was reduced by morphological changes in collagen crosslinks [5.42]. The collagen fibers are narrower, loosely packed and more disorganized which, in turn, leads to decreased strength and abnormal mineralization [5.43]. The effect of decreased collagen cross-linking on the biomechanical properties of bone was previously examined by Knott and Bailey [5.44].

### 5.3.5 A simplified model of osteoporotic degradation

The main assumption for the modeling of osteoporotic degradation of bone properties is that the ratios $m_m/m$ and $\rho_m/\rho$ remains constant. The experimental evidence offers some support for such an assumption [5.5; 5.42]. Since $m = m_m + m_p$, the constancy of the mineral/bone ratio $\frac{m_m}{m}$ also implies the constancy of the protein/bone ratio $\frac{m_p}{m}$. Together, they imply that:

$$\frac{\dot{m}_m}{m_m} = \frac{\dot{m}_p}{m_p} = \frac{\dot{m}}{m}\,, \quad \frac{\dot{\rho}_m}{\rho_m} = \frac{\dot{\rho}_p}{\rho_p} = \frac{\dot{\rho}}{\rho}\,. \tag{5.12}$$

Consistent with the assumed constancy of the mass ratios $\frac{m_m}{m}$ and $\frac{m_p}{m}$, it is reasonable to also adopt the approximation $\psi_m = \psi_p$, so that the density changes contribute to the mass changes in the same way for both the mineral and protein phases. In this case:

$$\dot{f}_m = \dot{f}_p = 0\,, \quad \frac{\dot{V}^*}{V^*} = (1-\psi)\,\frac{\dot{\rho}}{\rho}\,, \tag{5.13}$$

where $\psi$ is a parameter that can be equal to 0 (for the normal bone) or can appropriately vary between 0 and 1 during the progression of osteoporosis. The evolution equation of the composite (compact) bone of each trabeculae in this simplified case:

$$\frac{\dot{E}^*}{E^*} = \frac{\dot{E}^*_m}{E^*_m} = \frac{\dot{E}^*_p}{E^*_p} = \psi \, \frac{\dot{\rho}}{\rho} \, . \tag{5.14}$$

The evolution equations for the elastic moduli of trabecular bone and its mineral and protein components are:

$$\frac{\dot{E}_m}{E_m} = \dot{n}_m \ln\left(\frac{\rho_m}{\rho^*_m}\right) + \left[\psi + n_m(1-\psi)\right] \frac{\dot{\rho}}{\rho} \, , \tag{5.15}$$

$$\frac{\dot{E}_p}{E_p} = \dot{n}_p \ln\left(\frac{\rho_p}{\rho^*_p}\right) + \left[\psi + n_p(1-\psi)\right] \frac{\dot{\rho}}{\rho} \, , \tag{5.16}$$

$$\frac{\dot{E}}{E} = \dot{n} \ln\left(\frac{\rho}{\rho^*}\right) + \left[\psi + n(1-\psi)\right] \frac{\dot{\rho}}{\rho} \, . \tag{5.17}$$

### 5.3.6 Numerical evaluations

The bone mass at a given time of adult life is the peak bone mass attained at skeletal maturity minus the subsequently lost bone mass. Traditional radiographic techniques cannot distinguish osteoporosis until it is severe [5.14], which implies that the rate of osteoporotic bone loss is initially very low, perhaps even zero. Accordingly, the time rate

of bone density proportional to the product of the current density $\rho$, providing an exponential decay, and the time $t$, providing a vanishing rate of bone loss at the onset of osteoporosis ($t = 0$) was introduced. If needed to better reproduce clinical observations, or provide more accurate prognosis, the power $t^k$, with an appropriately adjusted value of $k$, can be used in place of $t$. Thus, the simple evolution equations for the mineral, protein, and composite bone content were proposed:

$$\frac{\dot{\rho}_m}{\rho_m} = \frac{\dot{\rho}_p}{\rho_p} = \frac{\dot{\rho}}{\rho} = -rt\,, \tag{5.18}$$

where $r$ is the coefficient with the dimension (time)$^{-2}$, which accounts for the rate of the mass resorption. If $r$ is assumed to be constant, Eq. (5.18) can be integrated analytically to obtain:

$$\begin{aligned} &\rho_m = \rho_m^0 \exp(-rt^2/2)\,, \quad \rho_p = \rho_p^0 \exp(-rt^2/2)\,, \\ &\rho = \rho^0 \exp(-rt^2/2)\,, \end{aligned} \tag{5.19}$$

where $\rho_m^0, \rho_p^0, \rho^0$ are the corresponding densities at the onset of osteoporosis. Furthermore, we shall take for the simplicity of numerical evaluations that $\psi_m = \psi_p$, which means that the entire mass loss takes place by the reduction of volume (thinning and interruptions of trabeculae), without density changes, i.e., $\dot{\rho}^* = \dot{\rho}_m^* = \dot{\rho}_p^* = 0$. The volume fractions $f_m$ and $f_p$ are constant, while $\dot{V}^*/V^* = -rt$. The elastic moduli of trabeculae at (5.14) vanish $\dot{E}^* = \dot{E}_m^* = \dot{E}_p^* = 0$ (this means that, although the amount of bone is reduced by aging and osteoporosis, the bone of remaining

trabeculae is histologicallly normal, so that the moduli $E_m^*$; $E_p^*$; $E^*$ remain unchanged). Therefore, the expressions (5.15) – (5.17) for the elastic moduli of trabecular bone reduce to:

$$\frac{\dot{E}_m}{E_m} = \dot{n}_m \ln\left(\frac{\rho_m}{\rho_m^*}\right) + n_m \frac{\dot{\rho}}{\rho}\,, \tag{5.20}$$

$$\frac{\dot{E}_p}{E_p} = \dot{n}_p \ln\left(\frac{\rho_p}{\rho_p^*}\right) + n_p \frac{\dot{\rho}}{\rho}\,, \tag{5.21}$$

$$\frac{\dot{E}}{E} = \dot{n} \ln\left(\frac{\rho}{\rho^*}\right) + n \frac{\dot{\rho}}{\rho}\,. \tag{5.22}$$

Their integrated forms, given by (5.7), can be expressed as:

$$E_m = E_m^0 \exp(-r n_m t^2/2)\,, \quad E_m^0 = E_m^*(\rho_m^0/\rho_m^*)^{n_m}\,, \tag{5.23}$$

$$E_p = E_p^0 \exp(-r n_p t^2/2)\,, \quad E_p^0 = E_p^*(\rho_p^0/\rho_p^*)^{n_p}\,, \tag{5.24}$$

$$E = E^0 \exp(-r n t^2/2)\,, \quad E^0 = E^*\,(\rho^0/\rho^*)^n\,. \tag{5.25}$$

For example, if osteoporosis decreases the bone content by 10% in 10 years, from (5.19) the coefficient $r$ is equal to $2.1\text{x}10^{-3}(\text{year})^{-2}$. The corresponding time variation of the mass or density ratios, such that $\rho/\rho^0$, determined from (5.19), is shown in Fig. 5.4.

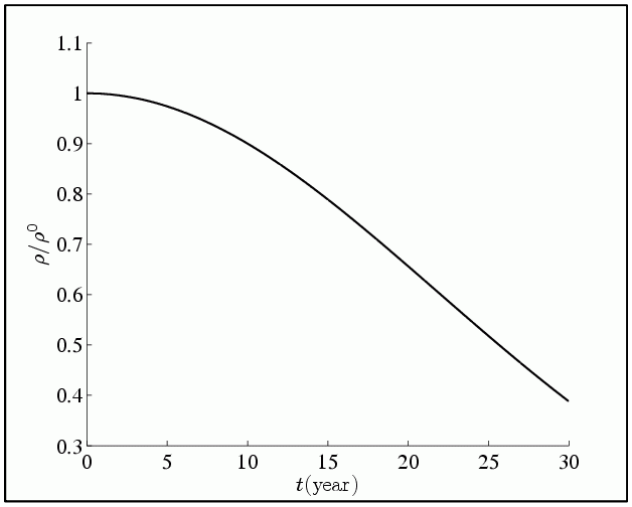


**Figure 5.4** The time variation of the density ratio $\rho/\rho^0$, during 30 years of progression of osteoporosis, according to Eq. (5.18), with the rate coefficient r = 2.1 x $10^{-3}$(year)$^{-2}$.

The predicted bone density decrease after 15 years is 21.1%; after 20 years it is 34.4%, and after 25 years it is 48.2%. Fig. 5.5 shows the osteoporotic degradation of the latter moduli, calculated from (5.23) – (5.25), if the morphological parameters $n_m$ = 3.15, $n_p$ = 1.75, and $n$ = 2.84 did not change with time. These values were determined in **Section 5.3.3** from the density and elastic moduli values of bovine femur bone. The elastic coefficients of human femur are nearly the same as of bovine femur bone ([5.45], Table 18-2, p. 18-6). Human femoral neck samples, obtained from hip replacement surgeries, were tested by Ciarallo *et al.* [5.39]. Comparable to the bovine samples, they found that the compressive strength and the modulus of the human samples are correlated and are within the range of published values for the human femoral neck [5.46]. For example, after 10 years these moduli decrease to $E_m = 0.718E_m^0$, $E_p = 0.832E_p^0$, and $E = 0.742E^0$, while after 20 years they are $E_m = 0.266E_m^0$, $E_p = 0.479E_p^0$, and $E = 0.303E^0$. The different magnitudes of the decrease is due to different trabecular

microarchitectures of deproteinized, demineralized and untreated trabecular bone specimens, and their different microarchitecture, accounted for by different values of the morphological parameters $n_m, n_p, n$ in (5.23) – (5.25).

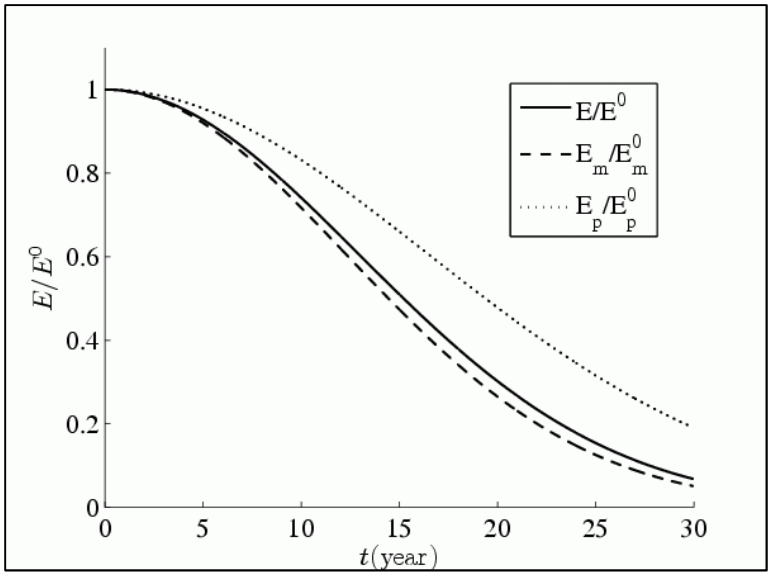


**Figure 5.5** The time variations of the elastic moduli ratios $E/E^0$, $E_m/E_m^0$ , $E_p/E_p^0$ during their osteoporotic degradation, according to (5.23) – (5.25), corresponding to constant values of the morphological parameters $= 2.84$, $n_m = 3.15$ and $n_p = 1.75$ with the rate coefficient $r = 2.1\,x\,10^{-3}$(year)$^{-2}$.

If needed to better match the observed data (e.g., to increase or decrease the rate of osteoporotic deterioration of Young's moduli), the time dependent expressions for the morphological parameters $n_m, n_p$ and $n$ can be included in the analysis. For example, by adopting the rate expression $\dot{n} = -0.012t^{1/2}$ i.e., $n = 2.84 - 0.008t^{3/2}$, so that $n =$ 2.84 and the time rate of $n$ is equal to 0 at $t = 0$, the modulus of elasticity $E$ decreases after 10 years to $E = 0.762E^0$, and after 20 years to $E = 0.409E^0$ (dashed curve in Fig. 5.6). The corresponding decreased values of the morphological parameter $n$ were 2.587 and 2.125. Even less pronounced degradation of elastic modulus is predicted by

adopting a cubic expression $n = 2.84 - 0.0036t^2 + 0.00006t^3$. In this case, the bone's modulus of elasticity decreases after 10 years to $E = 0.766E^0$, and after 20 years to $E = 0.453E^0$ (dotted curve in Fig. 5.6). The corresponding values of the morphological parameter $n$ were $2.541$ and $1.881$. Regarding experimental data for human trabecular bone, it was previously reported in the literature that for the vertebral trabecular bone specimens, a decrease in bone tissue of about 9% over 10 years causes a decrease of the elastic modulus of about 15% in the axial direction (along spine), and about 16% in transverse direction ([5.13], Table 23-1, p. 605).

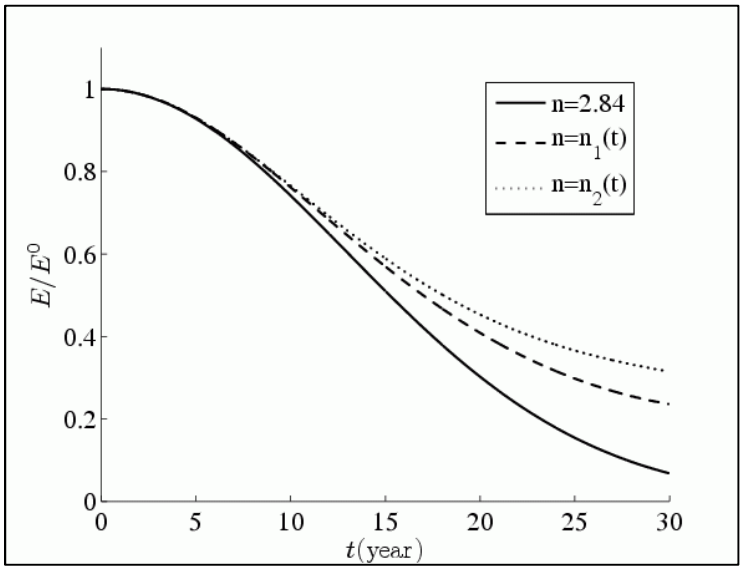


**Figure 5.6** The time variation of the elastic moduli ratio of ftabecular bone $E/E^0$ during odteoporosis degradation, according to (5.25), in the case when the morphological parameter $n = 2.84$ is constant, or equil to time dependent function $n_1(t) = 2.84 - 0.008t^{3/2}$ or $n_2(t) = 2.84 - 0.0036t^2 + 0.00006t^3$.

### 5.4 Conclusions

An analysis of the Young's modulus of trabecular bone based on that of the isolated mineral and protein phases was presented. The Young's modulus of composite

trabeculae is related to the Young's moduli of deproteinized and demineralized trabeculae by a modified mixture rule, in which an appropriate weight function is introduced to account for the mineral/protein interaction effects and the corresponding departure from the ideal mixture rule. Adopting the approach from the mechanics of cellular solids, two alternative expressions for the modulus of elasticity of trabecular bone are derived: one in terms of the moduli of elasticity of mineral and protein trabeculae, and the other in terms of the moduli of elasticity of deproteinized and demineralized bone. The presented analysis is applied to trabecular bovine femur bone. The material parameters are determined experimentally by compression testing of untreated, deproteinized, and demineralized trabecular bovine femur bone. The osteoporotic decrease of the elastic moduli is then analyzed. The evolution equations are introduced for the rate of loss of the mineral content of trabecular bone, and for the protein loss. Both losses are associated with the corresponding density and volume changes, for which appropriate equations are proposed. Based on these, and the evolution equations for morphological parameters accounting for the trabecular microarchitecture, the evolution equations are derived for the elastic moduli of deproteinized, demineralized and composite trabecular bone. A particular model of osteoporotic degradation is considered in which it is assumed that the relative ratios of the mineral and protein loss are equal to each other during the progression of osteoporosis. The rate parameter is adjusted so that the bone content decreases by 10% in 10 years, which yields the decrease of the modulus of elasticity by about 25%. The straightforward adjustment of the morphological parameters of trabecular microarchitecture can modify (slowly) the rate of the elastic moduli degradation if needed to better match the experimental data.

The extension of the presented work is needed to encompass the determination of other elastic properties, the Poisson ratio and the shear modulus of trabecular bone, in terms of the elastic properties of its mineral and protein phases, as well as the effect of stress on the osteoporotic degradation of elastic properties. Decreased physical activity of osteoporotic patients or differences in intensity of load transferred to osteoporotic bone vs. healthy bone exerts their effects on progression of osteoporosis [5.47], [5.48]. Furthermore, the development of elastic anisotropy of trabecular bones during osteoporosis is an essential aspect of the analysis. This requires the description of the trabecular fabric changes (trabecular size and shape changes, trabecular loss of connectivity), dependent on biochemical factors causing the mineral and collagen decay, sustained mechanical loads, and the type of trabecular bone (e.g., [5.49]-[5.55]). For example, trabeculae in vertebrae are mostly rod-like, while in the metaphyses and epiphyses of long bones the trabecular structure consists of a more balanced mixture of the rod- and plate-like trabeculae. These different cellular structures will degrade differently by the progression of resorption cavities, resulting in differences in the degree and the nature of the induced elastic anisotropy. Morita *et al*. [5.38] observed the highest progression rate of osteoporosis in rod/rod trabecular structure; the next highest rate was in plate/bar-like structure, while the plate/plate-like trabecular structure was the least sensitive. The degree of initial elastic anisotropy also varies among different types of trabecular bones. While trabecular bone from the lumbar vertebrae are approximately transversely isotropic, that from the iliac crest and central femoral head are nearly isotropic. This is a consequence of functional differences between different bones: the vertebrae are weight-bearing, whereas the iliac crest is not [5.56]. The biomechanics

study of such aspects of bone behavior is challenging from theoretical, computational, and experimental points of view.

**Acknowledgements:**

Chapter 5, in part, is a reprint of the material as it appears in "Elastic properties of cancellous bone in terms of elastic properties of its mineral and protein phase with application to their osteoporotic degradation," in Mechanics of Materials, 44, 139-150, 2012. V.A. Lubarda; E.E. Novitskaya; S.G. Bodde; J. McKittrick; P.-Y. Chen. The dissertation author was one of the primary investigator of this paper.

## 5.5 References

[5.1] Chen P-Y, McKittrick J. Compressive mechanical properties of demineralized and deproteinized cancellous bone. J Mech Behav Biomed Mater 2011;4:961-973.

[5.2] Boskey AL. Bone mineralization. In: Cowin, SC. (Ed.), Bone Mechanics Handbook. CRC Press, Boca Raton, FL, 200, pp. 5-1–5-33.

[5.3] Hellmich C, Barthelemy J-F, Dormieux L. Mineral-collagen interactions in elasticity of bone ultrastructure - a continuum micromechanics approach. Eur J Mech A/Solids 2004;23:783–810.

[5.4] Fritsch A, Hellmich C. 'Universal' microstructural patterns in cortical and trabecular, extracellular and exrtravascular bone materials: Micromechanics-based prediction of anisotropic elasticity. J Theor Biol 2007;244:597–620.

[5.5] Burr DB. Bone material properties and mineral matrix contributions to fracture risk or age in women and men. J Musculoskel Neuron Interact 2002;2:201–204.

[5.6] Faibish D, Ott SM, Boskey AL. Mineral changes in osteoporosis: A review. Clin Orthop Relat Res 2006;443:28–38.

[5.7] Rice JC, Cowin SC, Bowman JA. On the dependence of the elasticity and strength of cancellous bone on apparent density. J Biomech 1988;21:155–168.

[5.8] Keaveny TM, Morgan EF, Niebur GL, Yeh OC. Biomechanics of trabecular bone. Annu Rev Biomed Eng 2001;3:307–333.

[5.9] Marcus R, Bouxsein M. The nature of osteoporosis. In: Marcus, R, Feldman, D, Nelson, D, Rosen, CJ. (Eds.), Osteoporosis, 3rd ed. Elsevier, Inc, 2008, pp. 27–36.

[5.10] Bell GH, Dunbar O, Beck JS. Variations in strength of vertebrae with age and their relation to osteoporosis. Calc Tiss Res 1967;1:75–86.

[5.11] Ding M, Odgaard A, Linde F, Hvid I. Age-related variations in the microstructure of human tibial cancellous bone. J Orthop Res 2002;20:615–621.

[5.12] Morgan EF, Barnes GL, Einhorn TA. The bone organ system: Form and function. In: Marcus, R, Feldman, D, Nelson, D. Rosen, CJ. (Eds.), Osteoporosis, 3rd ed. Elsevier, Inc, 2008, pp. 3–25.

[5.13] Bouxsein ML. Biomechanics of age-related fractures. In: Marcus R, Feldman D, Nelson D, Rosen, CJ. (Eds.), Osteoporosis, 3rd ed. Elsevier, Inc., 2008, pp. 601–621.

[5.14] Kaufman JJ, Siffert RS. Strength of trabecular bone. In: Cowin, SC. (Ed.), Bone Mechanics Handbook. CRC Press, Boca Raton, FL, 2001, pp. 34-1–34-25.

[5.15] Odgaard A. Quantification of cancellous bone architecture. In: Cowin SC. (Ed.), Bone Mechanics Handbook. CRC Press, Boca Raton, FL, 2001, pp. 14-1–14-19.

[5.16] van Rietbergen B, Weinans H, Huiskes R, Odgaard A. A new method to determine trabecular bone elastic properties and loading using micromechanical finite-element models. J Biomech 1995;28:69–81.

[5.17] van Rietbergen B, Huiskes R. Elastic constants of cancellous bone. In: Cowin SC. (Ed.), Bone Mechanics Handbook. CRC Press, Boca Raton, FL, 2001, pp. 15-1–7-24.

[5.18] Toroian D, Lim JL, Price PA. The size exclusion characteristics of type I collagen: Implications for the role of non-collagenous bone constituents in mineralization. J Biol Chem 2007;282:22437–22484.

[5.19] Chen P-Y, Toroian D, Price PA, McKittrick J. Minerals form a continuum phase in mature cancellous bone. Calcif Tiss Inter 2011;88:351–361.

[5.20] Castro-Cesena AB, Novitskaya EE, Chen P-Y, Hirata GA, McKittrick J. Kinetic studies of bone demineralization at different HCl concentrations and temperatures. Mater Sci Eng C 2011;31:523–530.

[5.21] Cowin SC. Bone poroelasticity. J Biomech 1999;32:217–238.

[5.22] Gibson LJ, Ashby MF. Cellular Solids: Structure and Properties, 2nd ed. Cambridge Univ. Press, Cambridge, England, 1997.

[5.23] Carter DR, Hayes WC. The compressive behavior of bone as a two-phase porous structure. J Bone Joint Surg Am 1977;59:954–962.

[5.24] Ashby MF. The mechanical properties of cellular solids. Metal Mater Trans A 1983;14:1755–1769.

[5.25] Gibson LJ, The mechanical behavior of cancellous bone. J Biomech 1985;18:317–328.

[5.26] Christensen RM. Mechanics of low density materials. J Mech Phys Solids 1986;34:563– 578.

[5.27] Lucchinetti E. Composite models of bone properties. In: Cowin, SC. (Ed.), Bone Mechanics Handbook. CRC Press, Boca Raton, FL, 2001, pp. 12-1–12-19 .

[5.28] Lafage-Proust M-H, Prisby R, Roche B, Vico L. Bone vascularization and remodeling. Joint Bone Spine 2010;77:521–524.

[5.29] Nemat-Nasser S, Hori M. Micromechanics: Overall Properties of Heterogeneous Materials, 2nd ed. North-Holland, Amsterdam, 1999.

[5.30] Zaoui A. Continuum micromechanics: Survey. J Eng Mech (ASCE) 2002;128:808–816.

[5.31] Ostoja-Starzewski M. Microstructural Randomness and Scaling in Mechanics of Materials. Chapman and Hall/CRC Press, Boca Raton, FL, 2007.

[5.32] Fritsch A, Hellmich C, Dormieux L. The role of disc-type crystal shape for micromechanical predictions of elasticity and strength of hydroxyapatite biomaterials. Phil Trans R. Soc A 2010;368:1913–1935.

[5.33] Wang C, Feng L, Jasiuk I. Scale and boundary conditions effects on the apparent elastic moduli of trabecular bone modeled as a periodic cellular solid. J Biomech Eng 2009;131:121008-1-11.

[5.34] Katz JL. Hard tissue as a composite material. I: Bounds on the elastic behavior. J Biomech 1971;4:244–473.

[5.35] Fung YC. Biomechanics: Mechanical Properties of Living Tissues. Springer–Verlag, New York, 1993.

[5.36] Heidemann E, Riess W. Die Veranderungen des Kollagens bei entwasserung mit Aceton + die Konsequenzen Dieser Veranderung fur die Kollagenstruktur. Hoppe-Seyler's Z Physiol Chem 1964;33:101.

[5.37] Potoczek M. Hydroxyapatite foams produced by gelcasting using agarose. Mater Lett 2008;62:1055–1057.

[5.38] Morita M, Ebihara A, Itoman M, Sasada T. Progression of osteoporosis in cancellous bone depending on trabecular structure

. Ann Biomed Eng 1994;22:532–539.

[5.39] Ciarallo A, Barralet J, Tanzer M, Kremer R. An approach to compare the quality of cancellous bone from the femoral necks of healthy and osteoporotic patients through compression testing and microcomputed tomography imaging. McGill J Med 2006;9:102–107.

[5.40] Shah KM, Gob J, Bose K. The relationship between femoral neck strength, bone mineral content and fracture fixation strength: An in vitro study. Osteoporosis Int (Suppl. 1), 1993:S51–S53.

[5.41] Tellache M, Rixrath E, Chabrand P, Hochard C, Pithioux M, Wendling-Mansuy S. Numerical simulation of an osteoporotic femur: Before and after total hip arthroplasty. Eur J Comput Mech 2008;17:785–793.

[5.42] Oxlund K, Mosekild L. Ortoft G. Reduced concentration of collagen reducible cross human trabecular bone with respect to age and osteoporosis. Bone 1996;19:479–494.

[5.43] Bailey AJ, Sims TJ, Knott L. Phenotypic expression of osteoblast collagen in osteoarthritic bone: Production of type I homotrimer. Int J Biochem Cell Biol 2002;34:176–182.

[5.44] Knott L, Bailey, AJ. Collagen cross-links in mineralizing tissues. Review of their chemistry, function, and clinical elevance. Bone 1998;22:181–187.

[5.45] Bronzino JD. (Ed.), The Biomedical Engineering Handbook, vol. 1. CRC Press, Boca Raton, FL, 2000.

[5.46] Martens M, Van Audekercke R, Delport P, De Meester P, Mulier, JC. The mechanical characteristics of cancellous bone at the upper femoral region. J Biomech 1983;16:971–983.

[5.47] van Rietbergen B, Huiskes R, Eckstein F, Ruegsegger P. Trabecular bone tissue strains in the healthy and osteoporotic human femur. J Bone Miner Res 2003;18:1781–1788.

[5.48] Gefen A, Portnoy S, Diamant I. Inhomogeneity of tissue-level strain distributions in individual trabeculae: Mathematical model studies of normal and osteoporosis cases. Med Eng Phys 2008;30:624–630.

[5.49] Fyhrie DP, Carter DR. A unifying principle relating stress to trabecular bone morphology. J Orth Res 1986;4:304–317.

[5.50] Carter DR, Fyhrie DP, Whalen RT. Trabecular bone density and loading history: Regulation of connective tissue biology by mechanical energy. J Biomech 1987;20:785–794.

[5.51] Cowin SC, Sadegh AM, Luo GM. An evolutionary Wolff's law for trabecular architecture. J Biomech Eng. 1992;114:129–136.

[5.52] Sugita H, Oka M, Toguchida J, Nakamura T, Ueo T, Hayami T. Anisotropy of osteoporotic cancellous bone. Bone 1999;24:513–516.

[5.53] Keaveny TM. Strength of trabecular bone. In: Cowin SC. (Ed.), Bone Mechanics Handbook. CRC Press, Boca Raton, FL, 2001, pp. 16-1–16-42.

[5.54] Hart RT. Bone modeling and remodeling: Theories and computation. In: Cowin SC. (Ed.), Bone Mechanics Handbook. CRC Press, Boca Raton, FL, 2001, pp. 31-1–31-42.

[5.55] Hing KA. Bone repair in the twenty-first century: Biology, chemistry or engineering. Phil Trans R. Soc Lond A. 2004;362:2821–2850.

[5.56] Dempster DW. The contribution of trabecular architecture to cancellous bone quality. J Bone Mineral Res 2000;15:20–23.

# Chapter 6 SUMMARY AND RECOMMENDATIONS FOR THE FUTURE RESEACH

Many factors, including those explored in this study, affect the mechanical performance of bone. This dissertation is mostly focused on the analysis of elastic anisotropy of bone and its main constituents along with theoretical modeling of the elastic modulus. Additionally, it covered some aspects related to the maturation of bone and variations in the elastic properties of bone during the progression of osteoporosis. Since bone is a complex and ever changing material, more comprehensive and systematic analysis of correlation between internal bone microstructure and corresponding mechanical properties should be done in future studies.

The anisotropic compressive behavior of untreated (UT), demineralized (DM), and deproteinized (DP) bovine femur cortical bone (sampled from a middle diaphysis region) were investigated, and the reasons for this anisotropy were outlined and discussed. Differences in the internal bone microstructure together with extra level of porosity (after DM and DP) were the main reasons for elastic anisotropy of bone and its main constituents. Additionally, it was found that the anisotropy ratio depends on the location of samples around the cross-section of bone. However, this research did not incorporate other important parameters that could affect the elastic anisotropy of bone. Anisotropic behavior of UT, DM, and DP bone for different taxa (bovine, human), anatomical locations (femur, vertebra, tibia, rib, radius), locations along the same bone (diaphysis, epiphysis), age of bone, strain rate (quasi-static, dynamic), and testing methods (tension, torsion, bending, compression) would help to understand and describe

the complexity of bone tissue for prospective medical applications. There is an enormous parameter space to explore in the future. More experiments will be required to cover the whole range of possible options.

Furthermore, it was found that the weighted sums of the stress-strain curves for DM and DP bone did not add to the whole bone curve. This suggests a strong interaction between the mineral and collagen, which needs to be further examined and quantified.

Initial anisotropy of demineralized bovine femur cortical bone in compressive cyclic loading-unloading within the physiological strain range was studied. It was found that the cyclic loading mostly affects the bone stiffness in the radial and transverse directions, while the longitudinal direction was found to be the least affected. The reasons for that anisotropy were outlined and discussed. Additionally, it was shown that the unloading responses were non-linear for each anatomical direction, giving rise to overall loading-unloading hysteresis and cyclic dissipation of energy. As a future suggestion, closer look at the structure of demineralized bone (pure protein matrix) at submicro- and nano-levels using atomic force microscopy analysis and transmission electron microscopy technique would clarify and possibly explain the nature of sophisticated bone collagen structure at molecular level. This research is of medical interest since many groups have recently investigated synthetic collagen sponge structure and properties for prospective bone substitutes. Moreover, an extension of this work to the case of trabecular bone would provide the entire picture of bone behavior in compressive cyclic loading-unloading compression.

The first theoretical multi-scale model of the elastic response of bone based on experimental observations of bone as an interpenetrating composite material combined

with interdispersed porosity at different levels of hierarchy was developed. It was than verified for UT, DM, and DP cortical and trabecular bovine femur bones. Excellent agreement was found between the theory and experiments for all considered cases. Current version of the model does not include all the complexity of bone structure (the influence of cement lines around bone osteons, the different mineralization of osteonal and interstitial bones, the precise amount and distribution of porosity at different levels of hierarchy). These additional parameters should be incorporated in the future in a more involved modeling of bone. Furthermore, the modification of the existed model to predict other mechanical properties of bone (for example, strength) would become a useful addition to the field of bone modeling. These future modifications of the proposed theoretical multi-scale model will provide an important contribution into the field of bone properties modeling.

A detailed comparative age study of the microstructure and mechanical properties of bovine cortical bone revealed unexpected complexity of internal microstructure of bone. In particular, the dependence of bone microstructure on a load distribution and anatomical position of sample around cross-section of bone was discovered. This result emphasizes the need of careful selection of sample location during a preparation process (e.g., bone samples for mechanical testing should always be taken from the same exact parts of the bone cross-section). Throughout comparative age study of bone internal microstructure, distribution of porosity, and its correlation with mechanical properties of bone for different location along the same bone would map out the bone properties for different anatomical locations and positions along the same bone. This mapping will provide important inputs in the area of sport and reconstructive medicine.

Osteoporotic degradation of trabecular bone elasticity was modeled. Evolution equations for elastic modulus of bone in terms of those of mineral and protein trabeculae and in terms of DM and DP bones were formulated and verified by the analysis of compressive properties of bovine femur trabecular bone (sampled from a femur head). Adopting the mechanics of cellular solids approach, the moduli of elasticity of composite trabecular, DP trabecular and DM trabecular bone were expressed in terms of the trabecular moduli of elasticity and the corresponding density ratios using the power law expressions. An extension of this work is needed to investigate the deterioration of other elastic properties (e.g., shear modulus, Poisson's ratio) in the future. Furthermore, the effect of stress on the osteoporotic degradation of elastic properties of bone should be analyzed. Additionally, the development of elastic anisotropy of trabecular bone during progression of osteoporosis is an essential aspect of analysis of osteoporotic degradation of bone elasticity. The architecture of trabecular bone varies with the anatomical location (rod-rod for vertebrae, rod-plate for a femur head). Different rate of elasticity degradation during the progression of osteoporosis is discovered as well (rod-rod structure degrades much faster compare to rod-plate one, while the plate-plate structure degrades with the least speed). Therefore, the detailed description of the trabecular network changes dependent on biochemical factors (environment, food, exercises), mechanical loads (compressive, torsional), and anatomical locations of bone (vertebrae, femur head, rib) during the progression of osteoporosis will help to clarify the possible prognoses for prevention and cure of osteoporosis in the future.